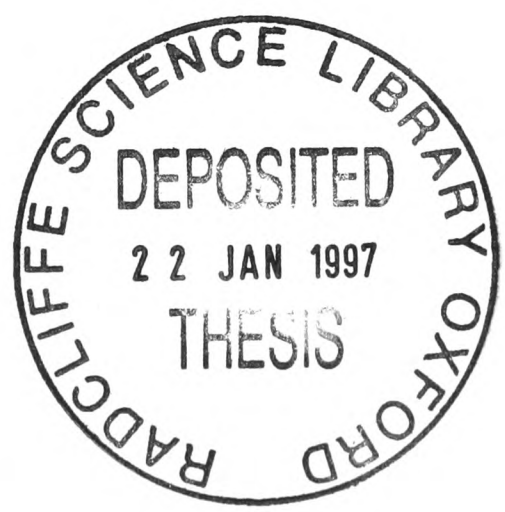
Computer Simulation of Zeolites

A thesis submitted to the Board of the Faculty of Physical Sciences of the University of Oxford in partial fulfillment of the requirements for the degree of Doctor of Philosophy.

Neil Jon Henson

Christ Church

Hilary Term, 1996.



To my parents,

who have always been with me

whether I was two-hundred or

five-thousand miles away

Abstract **D. Phil. Thesis**

Computer Simulation of Zeolites

by Neil J. Henson

Christ Church Hilary Term, 1996

The application of a wide range of computational methods to several problems in zeolite chemistry is explored in this thesis. Symmetry-constrained lattice energy minimisations have been performed on a series of pure silica polymorphs using the shell model for silicates and quantitative agreement is found between the experimental and calculated structures. The computed lattice energies of the silicas are found to be between 8 and 20 $kJmol^{-1}$ less stable than quartz. The energies are found to be directly dependent on the densities of the structures and show good agreement with a recent calorimetric study. A new forcefield for aluminophosphates based on the shell model has been obtained by fitting to the structure and properties of berlinite and lattice energy minimisation calculations have been carried out on a series of aluminium phosphate polymorphs. The experimental structures are reproduced to a reasonable accuracy, especially in cases where high quality crystallographic data are available on calcined structures. In cases where experimental methods give conflicting results regarding the space group symmetry, calculated structures having lower symmetry than those observed in the crystallographic studies are suggested. An approximately linear dependence of lattice energy on density is again observed; the computed lattice energies are found to span a range of 11.7 $kJmol^{-1}$ higher than berlinite, which compares to an experimentally determined range of 9.7 $kJmol^{-1}$. Proton binding calculations have been performed on the structure of H-SAPO-37 to determine the most favourable binding proton sites. The calculations correctly reproduce the sites which have the highest fractional occupancies in a crystallographic study. Molecular dynamics simulation has been used to study the diffusion of xenon in ferrierite and zeolite-L. It was found that at 298K and a loading level of 1.33 atoms per unit cell, diffusion down the ten-ring channel in ferrierite is a more facile process than down the wider twelve-ring channel in zeolite-L ($D=8.90\times10^{-9}$ m^2s^{-1} for ferrierite versus 1.78×10^{-9} for zeolite-L). This effect can be rationalised by consideration of the effect of channel shape on the diffusion pathway. Under the same conditions, the interaction energy was calculated to be more favourable for ferrierite (ΔU=-25.7 $kJmol^{-1}$ versus -20.0 $kJmol^{-1}$). A new forcefield for the interaction of hydrocarbons and aromatics with siliceous zeolites was fitted to thermochemical and crystallographic data. The forcefield successfully reproduced the crystallographically determined positions of pyridine and propylamine in siliceous ferrierite and dodecasil-3C. In addition, quantum mechanical calculations were used to fit a forcefield for the interaction of benzene with cation-containing zeolites. Molecular dynamics calculations were used to study the transport of benzene in siliceous faujasite. The coupling of lattice vibrations to the benzene molecule was found to enhance the mobility (for example, at 298K, $D=0.11\times10^{-9}m^2s^{-1}$ with a fixed lattice compared to $D=0.31\times10^{-9}m^2s^{-1}$ with a flexible lattice). Two diffusion regimes were observed corresponding to intra- and inter-cage benzene mobility which correlate well with hypothetical hopping pathways. Analogous pathways for benzene in cation-containing zeolites have shown that cation sites act as traps for the benzene in Na-X and Na-Y, which reduce the mobility compared to the siliceous case. In Na-X, the pathways are further modified by the addition of extra cation sites that act to reduce the hopping activation energy and therefore enhance the diffusion. This behaviour is consistent with observed trends in experimentally determined diffusivities.

Acknowledgements

There are a large number of people I would like to thank for making this thesis possible. First of all, I would like to acknowledge my supervisor, Professor Tony Cheetham, whose eternal motivation and optimism has been a constant inspiration to me over the last five years. Also, I would like to that Dr. Keith Prout and Professor Richard Catlow who provided guidance during the second year of my D. Phil in Oxford.

My D. Phil research really started in the summer preceding my first year in Oxford when I was given the once-in-a-lifetime opportunity (at least that was what I thought then!) of working for several months in the United States at Mobil Research and Development Corporation in Princeton, NJ. Dr. Brian Peterson proved to be an excellent tutor in computer simulation and gave me the ideal start to my research career during the two summers I spent in CRL. I would also like to thank Dr. John Higgins (now at Air Products) for being an authority on all things crystallographic. Also, Sherry Laney and Andy Kuivenhoven were further responsible to advancing my American education.

The Chemical Crystallography Laboratory in Oxford was my home for almost two years as well as during my Part II as an undergraduate. The Chem Cryst "family" created a great atmosphere for research and a great sense of community spirit throughout the building. I would like to thank Dr. Keith Prout and Dr. David Watkin for making my time in Chem Cryst so pleasant. I learnt a lot of crystallography but I still do not think I could run the CAD4! I owe the members of the Oxford-based Cheetham group a great deal for their help and friendship during the earlier part of my D. Phil. In particular, Julian Gale has been a mentor (and collaborator) to me both in Oxford and at the Royal Institution. Also, I would like to thank Ann, Jo, Angus, Jon, Alex, Nicola, Dave K., Lisa, Lucy, Keith P., Pete, Russ and Anita for making Room 27 a fun place to be, even when I had to make the tea/coffee for 12 people! Dr. Martin Grossel's friendship and support both during my undergraduate and graduate studies in Oxford has been most appreciated. Angus Wilkinson is also responsible for one of my two "experiments" of my D. Phil during a really enjoyable trip to the NSLS at Brookhaven, NY, although I have still to refine the data! I would also like to thank Dave and Helen, Craige, Martine and Mike R. for their friendship during my time in Oxford.

On Fridays, I could often be found at the Royal Institution in London clogging up their

terminals and computers with my calculations. Prof. Richard Catlow's research group adopted me as a part-time member of their clan which allowed me to stay in touch with the theoretical aspects of my work while amongst a group of experimentalists. In particular, I would like to thank Julian, Rob, Dewi, Eddy H., Andy Rohl, Dave Gay, Tim and Ashley for letting me use *ricx* and for the many evenings in the Clarence.

In the summer of 1993, I moved out to the University of California at Santa Barbara to continue the work on my degree, and discover the beaches and rather inclement weather conditions of Southern California. I was fortunate that many of our Oxford group had already made the move which eased the transition somewhat. I would like to thank the many members of the Cheetham group at UCSB for their guidance and friendship of the last three years including Angus ("Prof. Anomalous P. Scattering"), Lucy ("The Juice"), Russ, Jon, Martin ("The Rinman"), Gerardo, Randy, Viktor, Dilia, Branton, Jean-Christophe, Simon ("Arfur Daley"), Uwe ("Dr. Stupid"), Barbara, Alex ("The Flexmeister"), Anne, Luis, Scott, Jason and Raj. Also I would like to thank Dr. Claus Jeppesen who has put up with my constant requests regarding the computer system, and Wendy, Sylvia, Pam and Sonia for always finding solutions to my administrative problems. I have also had the opportunity to work with members of the Chemistry department. I would like to thank Andreas Schneider for his hospitality and friendship on both sides of the Atlantic. Also, I have been lucky to work with Prof. Scott Auerbach for almost two years. Scott's constant enthusiasm and vast knowledge of chemistry have always been inspirational and has always given me something to which to aspire. I have also been fortunate to spend time at several other laboratories during my three years in Santa Barbara. I spent over two months at Los Alamos National Laboratory working in Dr. Tony Redondo's group developing simulation code and attempting to access the CM-5. I would also like to thank Prof. Preston MacDougall for distracting me from time-to-time! In addition, I have made frequent trips to Biosym Technologies (now Molecular Simulations) in San Diego including an eight-week stay while I was still at Oxford. I would like to thank John Newsam, Clive Freeman, Steve Levine, Sean Li, Christophe Kölmel, Alan Gorman, Ron Lindsay and Ton van Daelen for making me feel so welcome in the land of the cubicles! Finally, I spent four days working at the Technical University of Vienna with Michael Stockenhuber and Andreas Jenyts collecting sorption data in the group of Prof. Johannes Lercher. I would like to thank them for their patience

and introduction to Austrian culture.

A fun atmosphere at home often makes research easier, and I have been lucky to have some great roommates over the last five years. In Oxford, I had a great year living on the outskirts of Cowley with Steve, Margarita (who are now happily married!) and Rob. I should also thank the long-suffering D&D group (Steve M., Gary, Paul, Steve F., Rich and Alex) for allowing Molroc and Golin to survive far longer than they should have done and for many great reunions. In Santa Barbara, I could not have hoped for a better pair of roommates in my first year. Allison and Dave McLaren are responsible for some of the best memories I have in Santa Barbara. Also, I would like to thank Rob, Rod (Mr. Teddy Bear!), Song, Tammy, Scott, Anne and Alex for making our household a happy one, and of course, Wayne, the itinerant landlord!

I would like to thank all the people who have taken time out from their busy lives to help in the proofreading of this mighty tome. I must be one of the few graduate students who has a professional proofreader looking over their thesis. Nicola Stedman does this kind of thing all day, and still had time for me. Thanks!! Also, I would like to thank Jean-Christophe (Ch. 1 and 2), Julian (Ch. 2 and 3), Andreas (Ch. 2), Russell (Ch. 2), Martin (Ch. 2 and 6), Scott W. (Ch. 2), Nicola and Alex (Ch. 2,4,5,6 and 8), Scott A. (Ch. 3,7,8 and 9), and Simon (Ch. 5 and 8). Also, Jon has bravely ploughed through the final version of my thesis looking for errors that no-one else could find. In addition, I would like to thank Jean-Christophe for carrying three packets of A4 paper across the Atlantic for me!

Finally I would like to thank my two closest friends of the past few years, Jon and Laurie, for their constant companionship during the writing of this thesis.

Production Notes

This thesis was typeset using LaTeX2ϵ in 11pt Utopia on an SGI Personal Iris 4D/35TG. Graphs were produced with *XMGR* version 3.01 and *GNUPLOT* version 3.4 . Molecular graphics were generated by the *InsightII* software (version 3.0.0) written and distributed by Molecular Simulations Inc. and *PSYCHO* written by Alan Gorman. Extra diagram labelling was performed using *Showcase* version 3.3 .

Contents

1. Aims of Research 1

2. Introduction to Zeolites 3

2.1 The Structure of Zeolites 4

2.1.1 Secondary Building Units 5

2.1.2 Polyhedral Building Units 5

2.1.3 Framework Density 5

2.1.4 Stacking of Layers 6

2.1.5 Channel Structure 7

2.1.6 Heteroatom Substitution 10

2.1.7 Extra-Framework Cations 11

2.2 Synthesis of Zeolites 11

2.3 Methods of Characterisation 14

2.3.1 Diffraction Methods 14

2.3.2 Electron Microscopy 15

2.3.3 Extended X-ray Absorption Fine Structure (EXAFS) 16

2.3.4 Infra-Red Spectroscopy 16

2.3.5 Nuclear Magnetic Resonance 16

2.3.6 Sorption Experiments 18

2.3.7 Diffusion of Molecules in Zeolites 20

2.4 Applications of Zeolites 24

2.4.1 Heterogeneous Catalysis 24

2.4.2 Ion Exchange 28

2.4.3 Sorption and Gas Separation 28

3. Theoretical Methods **29**

3.1 Quantum Mechanical Methods 29

3.1.1 *Ab Initio* Techniques 30

3.1.2 Electron Correlation 36

3.1.3 Semi-Empirical Techniques 36

3.1.4 Density Functional Theory 37

3.1.5 Structural Optimisation 38

3.1.6 Periodic Quantum Mechanical Calculations 39

3.1.7 Applications to Zeolites 39

3.2 Forcefield Methods 43

3.2.1 Potential Energy Functions 43

3.2.2 The Fitting of Forcefield Parameters 52

3.2.3 Perfect Lattice Energy Minimisation 54

3.2.4 Minimisation Methods 57

3.2.5 Defect Lattice Energy Minimisation 59

3.2.6 Free Energy Minimisation 61

3.2.7 Statistical Mechanical Approaches 63

3.2.8 Molecular Dynamics 65

3.2.9 Monte Carlo Simulation 72

3.2.10 Applications to Zeolites 74

3.3 Computational Hardware Development 78

4. Computer Simulation of Silica Polymorphs **83**

4.1 Computational Methods and Forcefields 83

4.2 Structural Models 85

4.3 Results and Discussion 87

4.3.1 Forcefield Comparison 87

4.3.2 Comparison with Structural Data 87

4.3.3 Variation of Lattice Energy with Density 93

4.3.4 Comparison with Thermochemical Data 94

4.3.5 Phonon Spectra 96

5. Computer Simulation of Aluminophosphate Polymorphs **99**

5.1 Derivation of a Forcefield for Aluminophosphates 100

5.1.1 Functional Form 100

5.1.2 Fitting Methodology 101

5.1.3 Structure and Properties of Berlinite 102

5.2 Application to Aluminophosphate Structures 104

5.3 Results and Discussion 104

5.3.1 Structural Reproduction 104

5.3.2 Variation of Lattice Energy with Density 111

5.4 Proton Sitings 112

6. Molecular Dynamics Studies of Xe in Zeolites FER and LTL **116**

6.1 Xenon as a Probe for Diffusion in Zeolites 116

6.2 Computational Studies of Xenon in Zeolites 117

6.3 The Structures of Ferrierite and Zeolite-L 118

6.4 Computational Details 118

6.5 Results and Discussion 120

7. Forcefield Development for Organic Molecules in Zeolites **134**

7.1 Functional Forms for Inorganic-Organic Interactions 134

7.2 Fitting Methodologies 135

7.3 Charge Models for Inorganic-Organic Interactions 137

7.4 Strategies for Fitting to Experimental Data 139

7.4.1 Fitting to Crystallographic Data 139

7.4.2 Fitting to Thermochemical Data 139

7.5 Forcefield Development for Normal Hydrocarbons 141

7.6 Forcefield Development for Aromatic Hydrocarbons 145

7.6.1 Siliceous Faujasite 145

7.6.2 Cation-Containing Faujasites 148

7.7 Application to Templating Effects in Siliceous Ferrierite 154

7.7.1 Background 154
7.7.2 Structural Details 154
7.7.3 Potential Parameter Assignment 155
7.7.4 Docking Calculations 155

8. Computer Simulation of Benzene in Siliceous Faujasite **164**
8.1 Structural Models and Experimental Data 164
8.2 Energy Minimisation of Siliceous Faujasite 166
8.3 Calculation of Preferred Binding Sites 167
8.4 Molecular Dynamics Studies 170
8.5 Hopping Pathways 178
8.6 Conclusions 184

9. Simulation of Benzene in Cation-Containing Faujasites **186**
9.1 Experimental Motivation: NMR Spin Lattice Relaxation 186
9.2 Methods and Models 188
9.2.1 Computational Methodology 188
9.2.2 Cation Sites in Faujasites 190
9.3 Relative Cation Site Stability 193
9.3.1 Methods and Models 193
9.3.2 Results and Discussion 194
9.4 The Behaviour of Benzene in Na-Y 199
9.4.1 Models for Na-Y 199
9.4.2 Docking Calculations 200
9.4.3 Minimum Energy Pathways 201
9.5 Behaviour of Benzene in Na-X 204
9.5.1 Models for Na-X 204
9.5.2 Docking and Minimum Energy Pathways 207
9.5.3 Benzene Hopping in Highly Loaded Systems 218
9.6 Conclusions 221

References **222**

Appendix A . The LFOPC minimisation method 246

Appendix B . The DIZZY program 250

"When the only tool you have is a hammer,
every problem looks like a nail"

Dr. Tony Redondo (of LANL),
a supporter of the multi-disciplinary approach.

"When you actually make a prediction that comes
true, then I'll take your calculations seriously"

Dr. John Higgins (now of Air Products),
A cynic like everyone else knows my work.

"Neil, what do we do?"

Prof. Tony Cheetham,
The original entry in my Frequently Asked Questions list.

". . . if you performed some of these experiments
in the lab you would not get the exact same results shown.
That's the difference between a computer model and
practice in science."

An excerpt from *Run Time Chemistry Explorer*,
a computer-based educational tool.
After writing this thesis, I now know the difference too.

Chapter One

Aims of Research

During the last decade, the use of computational methods to study microscopic processes has grown significantly. This is especially noticeable in the field of molecular biology, where pharmaceutical companies have a considerable investment in computational resources. In the area of materials science, important advances in the development of computational techniques have also been made, although the methods are somewhat less developed than in the pharmaceutical area. The work has primarily focused on the simulation of materials themselves to both reproduce experimental data and to make predictions. The application of computational methods to zeolitic systems is becoming an increasingly important tool in studying the relation between microscopic properties and their relation to both sorption and catalytic applications. A detailed understanding of important processes at the microscopic level is a prerequisite in providing a rational method for computer-aided catalyst and molecular sieve design. The routine application of such methodologies would allow candidate zeolite structures to be screened prior to experimental study, their catalytic activity assessed using a computational algorithm, and the most promising candidates selected for experimental trials. Although the development of such screening techniques still lies in the future, the wide range of computational methods that are currently available can provide a useful insight into the interpretation of both experimental data and the identification of the important fundamental processes at the microscopic level.

The work presented in this thesis will address several important areas in zeolite research, illustrate the relevance of a wide range of computational approaches and show how the results obtained can be used as an aid to the interpretation of experimental data. Initially, the focus will be primarily on the representation and relative stability of zeolite frameworks in the absence of sorbed species. In Chapter 4, currently available forcefields

will be compared and their quality assessed with reference to the reproduction of known silica structures using lattice energy minimisation techniques. In addition, the calculation of the phonon spectrum will be examined as a method of predicting the crystallographic space group adopted by zeolites whose structures are ill-defined. In the case of aluminophosphates, there has been significantly less work performed in forcefield development. In Chapter 5, a new forcefield for the treatment of aluminophosphates will be presented. This forcefield is based on the shell model and is analogous to a previous forcefield for silicates. As in the previous chapter, the quality of the new forcefield will be assessed by comparison with experimentally determined crystal structures. Also, by using a combination of the new forcefield with a silica forcefield, the acid properties of the catalytically important SAPO-37 system will be investigated. The behaviour of sorbed species in the zeolite pore structure is an important aspect of many zeolite applications. In Chapter 6, the subtleties in the transport mechanisms of a relatively simple sorbate (xenon) will be investigated in two zeolites with markedly different channel structures (siliceous ferrierite and zeolite-L) using molecular dynamics methods. Many catalytic applications of zeolites involve the reaction and transport of hydrocarbons within the zeolite pore structure. In Chapter 7, the methods and important issues of fitting a new forcefield to accurately represent the interaction of zeolite frameworks with both saturated and aromatic molecules will be considered. A new forcefield for the treatment of these molecules will be presented and applied to in a study of template molecule siting in ferrierite. In Chapter 8, a more extensive investigation of benzene in siliceous faujasite will be performed using the forcefield fitted in the previous chapter. Monte Carlo docking, molecular dynamics and constrained energy minimisation will be used to probe the dynamics and siting of the benzene molecules in this system. The results will be compared to available experimental data. In the final Chapter, the much more challenging example of the behaviour of benzene in cation-containing faujasites will be presented. By using constrained energy minimisation to propose hypothetical hopping pathways, it will be shown how such calculations can be used to rationalise experimental measurements from an atomic scale perspective.

Chapter Two

Introduction to Zeolites

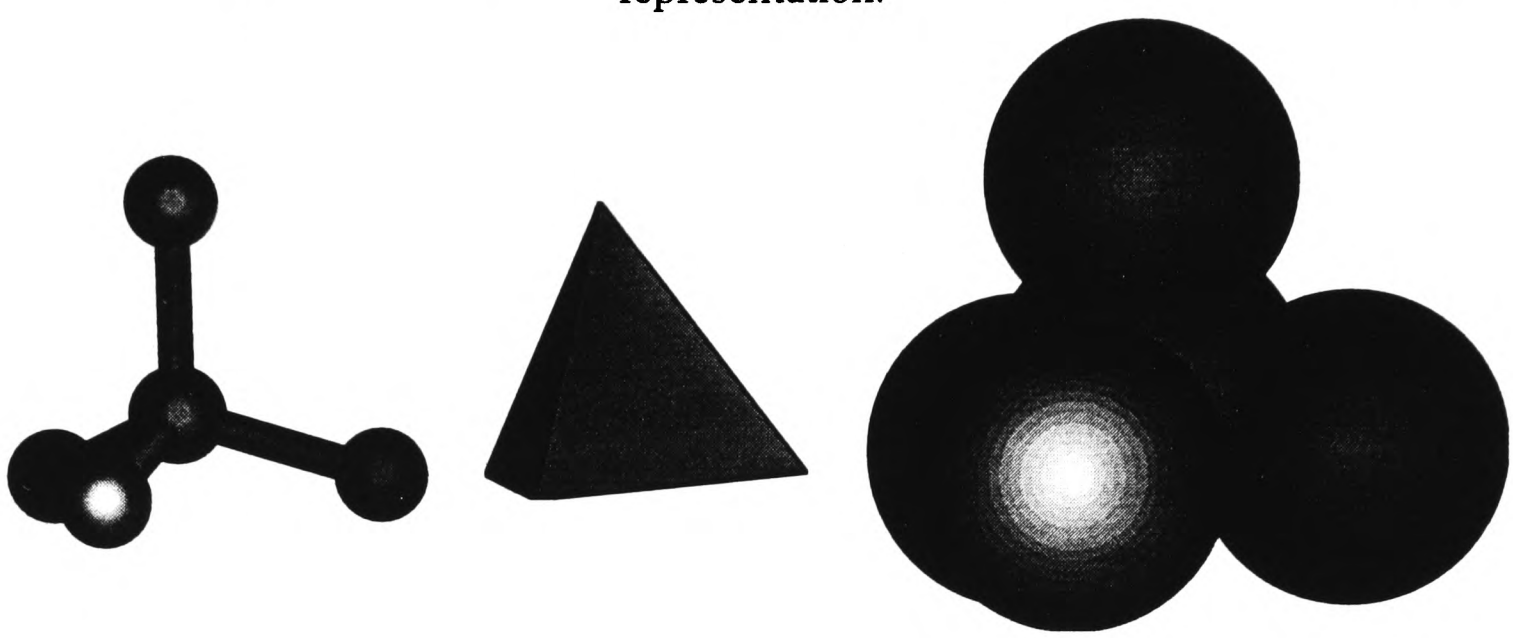
The origin of the word "zeolite" comes from the Greek words $\zeta\epsilon\iota\nu$ and $\lambda\iota\theta o\sigma$ ("boil" and "stone") and was first used by Swedish chemist and mineralogist Axel Fredrick Cronstedt in his paper reporting the discovery of a new class of tectosilicate minerals (that is, constructed from SiO_4 units) in 1756.[1] The original manuscript was recently translated into English and presented at the 9th International Zeolite Conference in Montreal.[2] It is generally thought that the mineral under investigation was stilbite, although this is still a matter for debate.

Zeolites are microporous solid-state materials having channels, cages and windows of molecular dimensions. The zeolite framework consists of an infinite array of corner-sharing TO_4 tetrahedra (see Figure 2.1). Although the tetrahedra are quite rigid, there is considerable flexibility in the bond angles about oxygen (bond angles range from 125° to close to 180° throughout the many known zeolite structures). The tetrahedral atom T can be a wide range of combinations of elements; for example, Si and Al (aluminosilicates), Al and P (aluminophosphates),[3] B and Si (borosilicates),[4] Ga and Si (gallosilicates),[5] Si, Al and P (silicoaluminophosphates),[6] or other metal atoms in combination with Al and P (metalloaluminophosphates).[7] Several of these variants have analogous aluminosilicate structures; however, a number of unique $AlPO_4$ and $GaPO_4$ structures have also been discovered such as the eighteen-ring VPI-5 structure,[8] the twenty-ring cloverite structure,[9] and the twenty-ring JDF-20 structure.[10] A general formula for aluminosilicates can be written as :-

$$M^{n+}_{x/n}[(AlO_2)_x(SiO_2)_y].wH_2O$$

In cases where the identity of the T atoms causes a charge imbalance in the system, the charge neutrality is maintained by the incorporation of protons or extra-framework cations (M). The cations usually occupy sites of relatively low coordination number in the struc-

Figure 2.1: The primary building unit of all zeolite structures after Newsam[11]. Drawn (a) in ball and stick form, (b) as a tetrahedron, and (c) in space-filling representation.



(a) (b) (c)

tures and are, as a consequence, easy to ion-exchange for alternative cations. In aqueous conditions, they are often extensively hydrated. The zeolite pore structure allows the sorption and diffusion of small organic molecules, which are important in many catalytic processes used in industry. In addition, the well defined size and shape of the pore system allows shape-selective behaviour to be observed.

2.1 The Structure of Zeolites

The first synthetic zeolite, levynite, was prepared by St. Claire Deville in 1862[12] from aqueous solutions of potassium silicate and sodium aluminate. Although, a variety of zeolites can be found in natural mineral deposits, the major proportion of known zeolites have been isolated by synthetic procedures. However, significant advances in the understanding of zeolite structure only occurred once improvements in analytical techniques allowed direct examination of samples with diffraction methods. The first crystal structure determination of a zeolite was that of analcime by Taylor in 1930.[13] As of 1991, the latest edition of the *Atlas of Zeolite Structure Types*[14] reports the number of unique zeolite framework types as 85.

A series of rules has been initiated for the classification of zeolite structure types by an IUPAC Commission on Zeolite Nomenclature.[15] Each unique framework structure has

been assigned a three letter code. The coding system is independent of composition, crystallographic symmetry and the identity of the tetrahedral atoms in the structure. Hence many different materials may have the same structure code. For example, Na-X, Na-Y, US-Y, SAPO-37, and CSZ-1 all have the FAU framework code.

A number of different classification schemes have also been proposed to understand zeolite structures, based on structural building units, framework density, and channel structure.

2.1.1 Secondary Building Units

Meier[16] proposed a number of fundamental building blocks, called secondary building units or SBUs (the primary building units being single TO_4 tetrahedra). These consist of four to sixteen TO_4 tetrahedra which, when assembled, can form all the known zeolite structure types. These are shown schematically in Figure 2.2. They have been derived assuming that each framework can be assembled from just one type of SBU. In a few systems, combinations of SBUs are found, for example, lovdarite (formed from spiro-5 and 4), and melanophlogite (formed from 5 and three 5-1's).

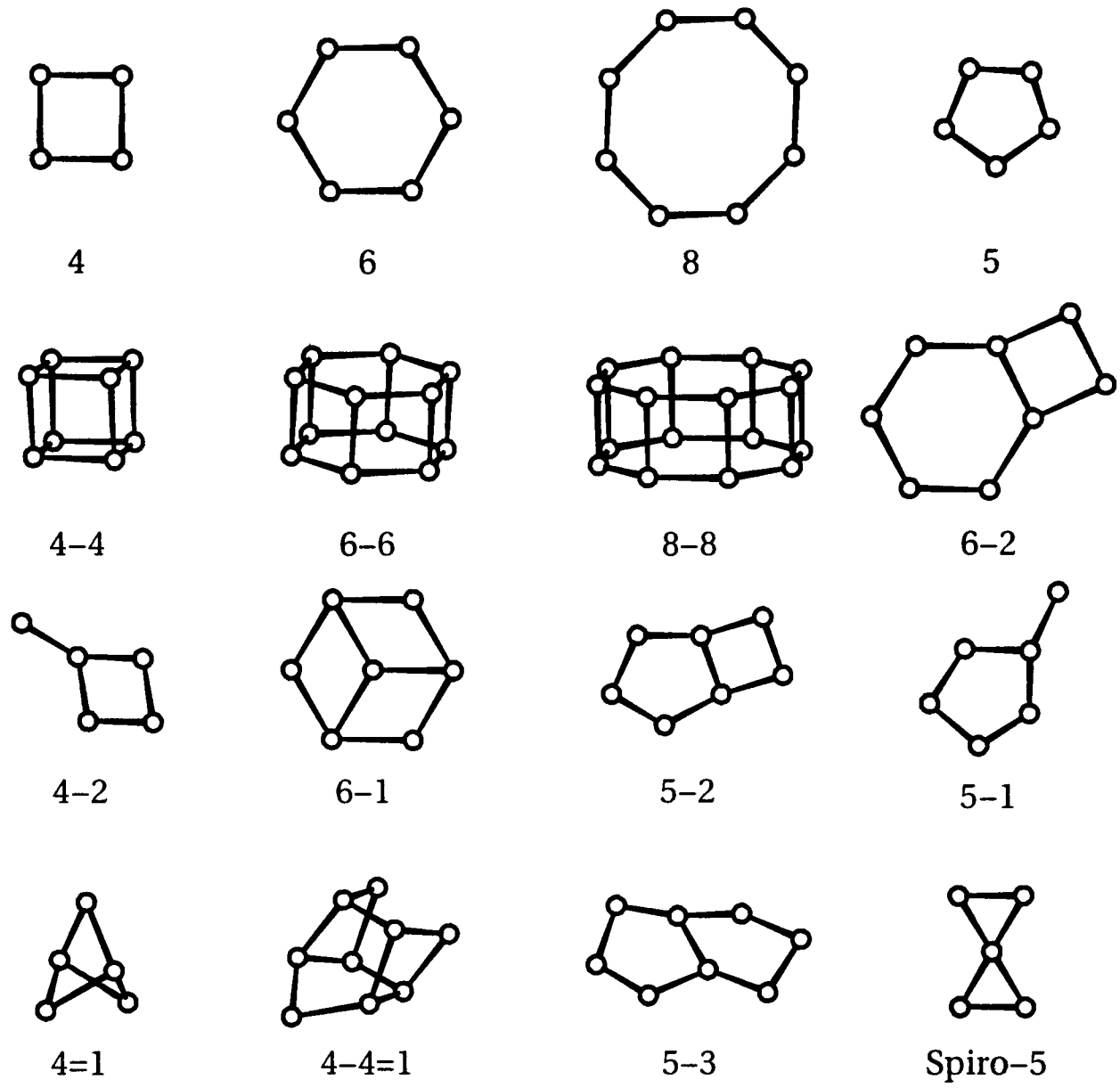
2.1.2 Polyhedral Building Units

An alternative method of considering zeolite structure is the notion that the framework can be assembled from polyhedral building units. Figure 2.3 shows an example of this. The β-cage, or sodalite cage, polyhedral unit can be joined in several ways to create different zeolite frameworks. The sodalite cage can be thought of as a linking of four- and six-rings to form a truncated octahedron, which has an internal diameter of around 6Å. If the sodalite unit is linked by fusing four-rings the structure of sodalite itself is constructed, whereas if the unit is linked by bridging four-rings the structure of zeolite-A is obtained. Finally, if the β-cage is linked by bridging six-rings, the faujasite framework is formed.

2.1.3 Framework Density

This parameter is a measure of the available pore volume in a zeolite structure. It is defined as the number of tetrahedral atoms per 1000Å^3. Most condensed silicate structures, such

Figure 2.2: Secondary building units after Meier and Olson[14].
Each node represents a single T atom. Oxygen atoms are omitted for clarity.

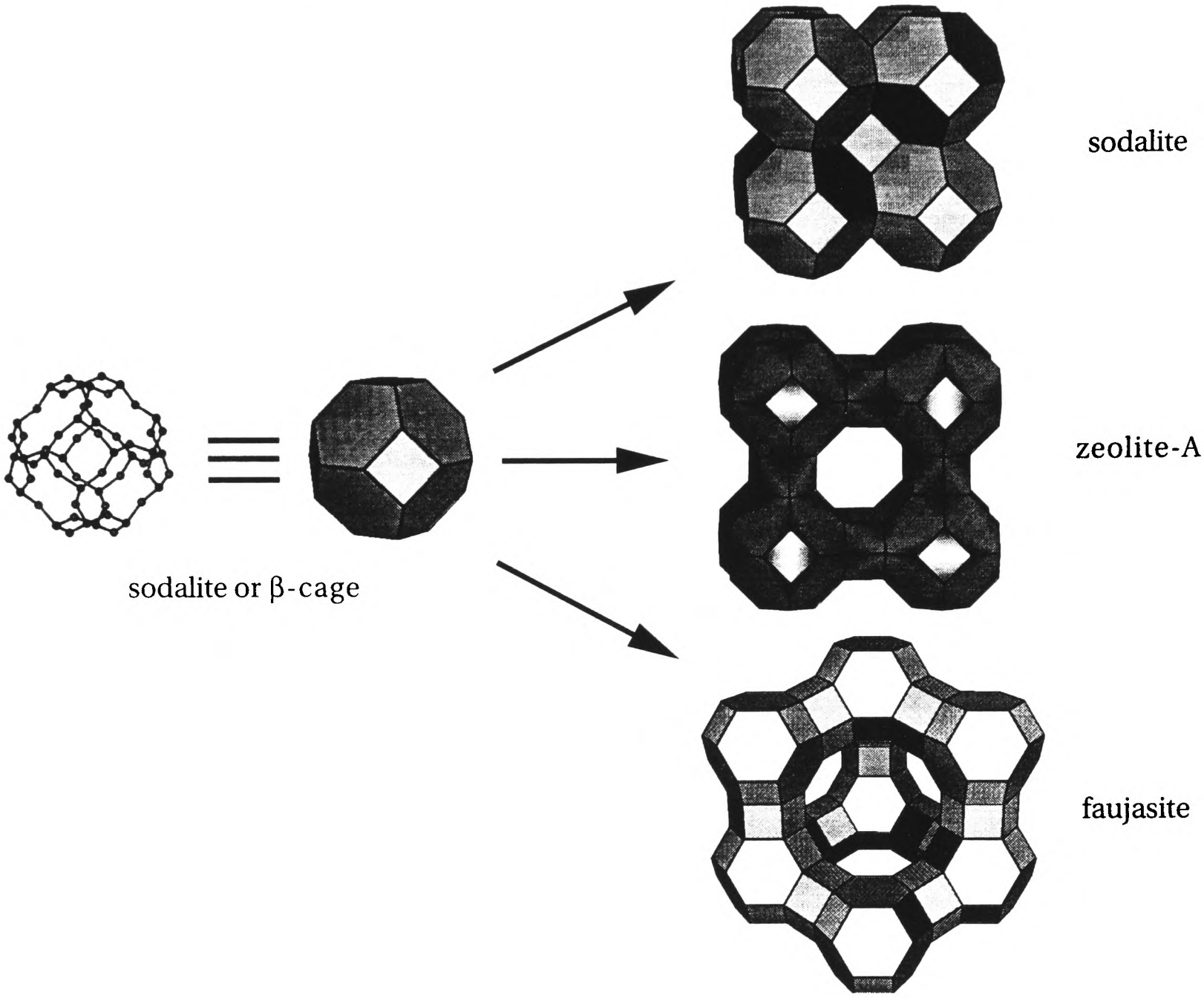


as α-quartz, cristobalite and tridymite, have values around 20, whereas most zeolites range from 12 to 19. Cloverite, which has one of the largest ring systems observed in a zeolite, has a value of 11.1 .

2.1.4 Stacking of Layers

Another useful method of visualising zeolite structures is to view them as being built from layers stacked in various ways. Smith has used this approach to describe many of the possible zeolite structures by viewing them in projection as two-dimensional three-connected nets.[17] Akporiaye and Price have proposed a formalism by which the framework structures can be thought of as a stacking of layers related by symmetry operators.[18] This is particularly useful for rationalising the structure of the pentasil zeolites, which are made up from five-rings. Zeolite-β is a interesting example of the effect of stacking faults on structure.

Figure 2.3: Building the structure of a zeolite from polyhedra.

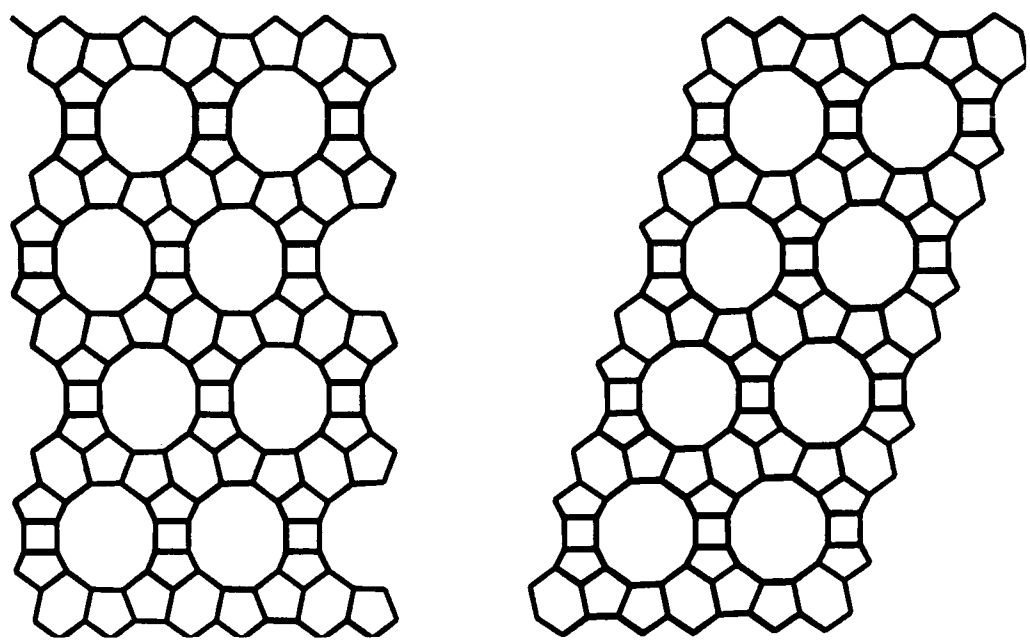


An wide range of zeolite-β polymorphs can be synthesised each member having a different degree of stacking faults in the structure. The two end members are shown in Figure 2.4.

2.1.5 Channel Structure

Apertures circumscribed by more than six tetrahedral (or oxygen) atoms are generally referred to as channels; whereas smaller openings are simply considered to form windows connecting larger cavities. A zeolite channel can be described by a number of parameters. For example, its direction relative to the crystallographic axes, the number of tetrahedral (or oxygen) atoms in the ring, and the free diameter of the channel. A selection of structures and their channel dimensions is shown in Figure 2.5. The diameter of a channel is

Figure 2.4: The stacking of layers to form a zeolite structure



zeolite–β polymorph A zeolite–β polymorph B

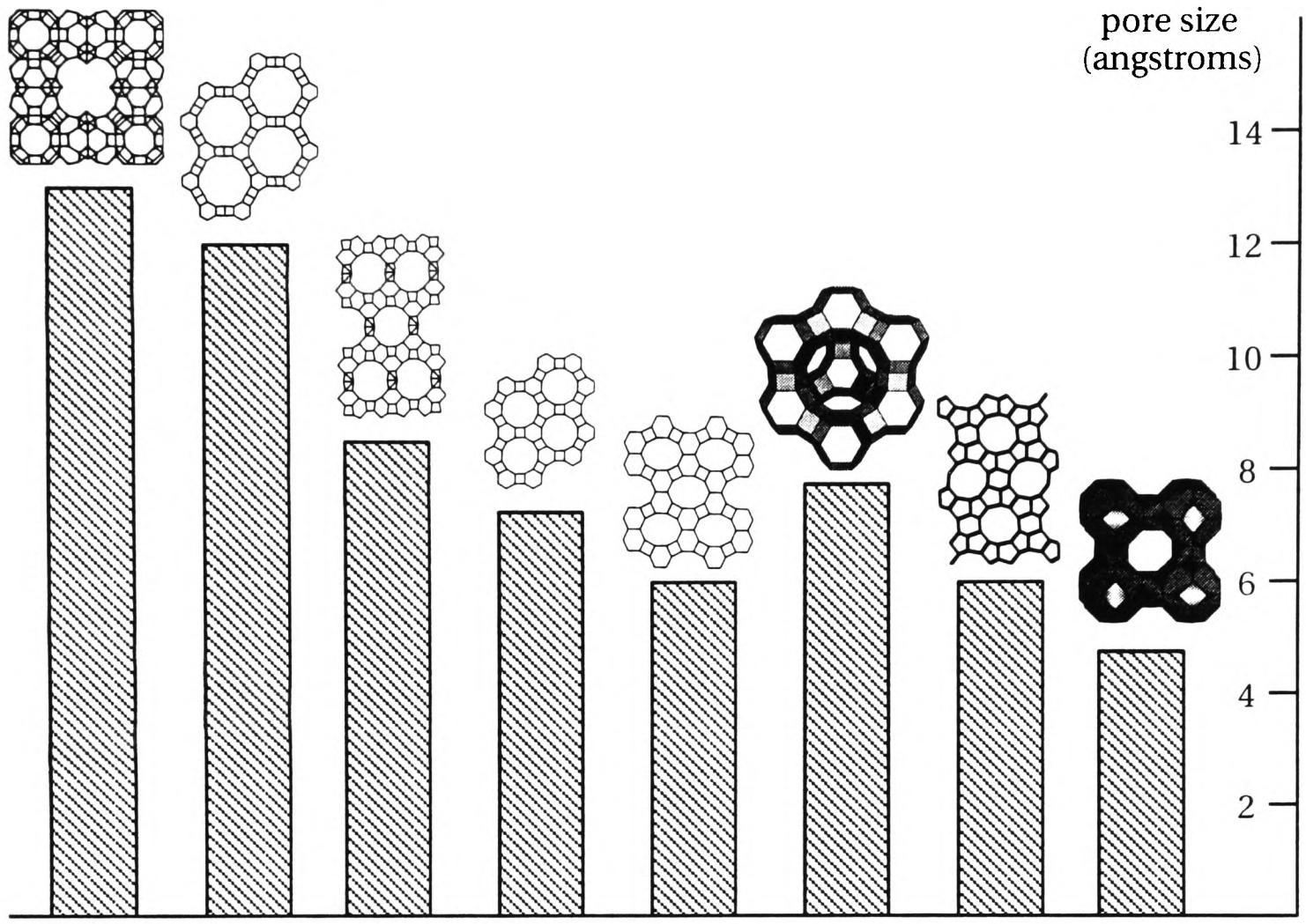
dependent on a number of factors such as the hydration state, temperature, the Si/Al ratio as well as the structure itself. Table 2.1 illustrates how channel size can change between

Table 2.1: Estimated pore size for some common zeolites

Zeolite	Ring Size	Approximate Free Dimension (Å)	
		Minimum	Maximum
Faujasite	12	7.4	7.4
Ferrierite	8	3.4	4.8
Ferrierite	10	4.3	5.5
Mordenite	8	2.9	5.7
Mordenite	12	6.7	7.0
ZSM-5	10	5.4	5.6
Zeolite-A	8	4.1	4.1
Zeolite-L	12	7.1	7.1

different structures. For example, the ten-ring channel size varies considerably from ferrierite to ZSM-5. In the ferrierite structure, the channel has an elliptical shape, whereas in ZSM-5 it is more circular.

Figure 2.5: A comparison of channel size for various zeolites, after Davis[19]. The three-letter IUPAC codes for each zeolite are shown on the abscissa.



-CLO	VFI	AET	AFI	AEL	FAU	MFI	LTA	
20	18	14	12	10	12	10	8	largest ring

The six-ring construct is the largest SBU in which the tetrahedral atoms can lie in the same plane. All other ring systems require some degree of ring puckering to be stable. For example, the twelve-ring (window) in faujasite consists of two sets of oxygen atoms, each of which lies in a distinct plane.

Many zeolites possess multi-dimensional channel systems within a single structure. For example, ZSM-5 has two channel systems, a ten-ring sinusoidal channel running parallel to the a- axis and a ten-ring straight channel parallel to the b- axis. The two channels intersect at various points in the structure.

Brunner and Meier[20] have shown that there is a correlation between framework density and the smallest rings in the structure. This implies that in order for large pore zeolites to be stable, they must also contain a number of smaller ring structures. The presence of narrow T-O-T angles that are necessary to form small ring structures tend to be unfavourable in aluminosilicate zeolites; however, three-membered rings are observed in several hetero-

substituted systems such as the zincosilicate, VPI-7.[21]

One of the most exciting developments in zeolite science in the past five years has been the discovery of the MCM-41 family of zeolites by workers at Mobil.[22] The channel systems in these structures are repeated in the crystallographic sense, although the silicate walls are themselves amorphous. Channel dimensions varying between 16Å to 100Å have been observed, hence their classification as mesoporous materials. Several distinct phases have been identified including cubic, hexagonal and lamellar structures.

2.1.6 Heteroatom Substitution

Zeolites are often synthesised with varying amounts of aluminium and other heteroatoms in their structures. In general, for aluminosilicates there have been few crystal structure determinations with Si/Al ratios greater than one that have shown site preferences and therefore the substitution pattern is commonly random. However, several empirical rules have been proposed to aid the understanding of this phenomenon. Löwenstein[23] noticed that there were no zeolite structures with a Si/Al ratio less than unity, and rationalised this by proposing that $[AlO_2]^-$ units, which possess a net negative charge, would try and locate themselves as far apart as possible in the structure to reduce electrostatic repulsion. Thus, Löwenstein's rule[23] prohibits the presence of Al-O-Al bridges in structures. This rule is obeyed in almost all cases, although there is some evidence for non-Löwensteinian behaviour in sodalites which have been synthesised at high temperatures,[24] although these are limited to condensed non-zeolitic sodalite structures such as $Ca_4(Al_6O_{12})$,[25] and siloxane clusters. In addition, zeolite-A can be synthesised with a Si/Al ratio close to unity in which the Si and Al are fully ordered throughout the structure in accordance with this rule.[26] The faujasite structure can also be synthesised in this state[27] (the Na-LSX composition). Dempsey and co-workers[28] have suggested that this effect also extends to next-nearest neighbours so that the number of Al-O-Si-O-Al linkages assumes a minimum for a given Si/Al ratio. Schröder and Sauer have performed a theoretical study that suggests that Dempsey's rule may not hold in the faujasite structure,[29] although Sato and co-workers have recently shown by ^{29}Si NMR measurements that it does hold for the zeolites ZK-19 and Linde W.[30] The amount of aluminium that is tolerated in a zeolite framework is also structure dependent. For example, in ZSM-5 only relatively low levels of Al are allowed

(down to Si/Al ≈ 6), whereas for faujasite the full range is possible from the Si/Al=1.0 composition[27] to purely siliceous.[31] The strict Al/P alternation present in many aluminophosphate structures precludes the existence of any ring structures containing an odd number of tetrahedral atoms such as five-rings and as such no analogues of the pentasil family are possible. However, it is possible to observe odd-numbered rings in aluminophosphate structures that deviate from the ideal $AlPO_4$ stoichiometry and therefore contain coordination numbers greater than four at aluminium and phosphorus.

2.1.7 Extra-Framework Cations

Once a heteroatom substitution is made into an otherwise siliceous zeolite structure, the charge imbalance is countered by the incorporation of protons or extra-framework cations. The cations can be monovalent, such as Na^+ and K^+, divalent, such as Ca^{2+} and Sr^{2+}, or even trivalent, such as La^{3+}. The introduction of cations into the structure tends to convert the zeolite from being hydrophobic (as in its siliceous form) to hydrophilic, since a large amount of water can coordinate to the cation. Indeed, in the case of La-Y the interaction between water and the cation is so strong that a La-OH bond is formed when dehydration is attempted.[32] It is possible to locate the cation positions by standard crystallographic techniques.

If the zeolite is ion-exchanged for ammonium, NH_4^+, the zeolite can then be deammoniated to produce the protonated form. Protonated zeolites are of importance in catalytic applications due to the high acidity of the proton. Theoretical[33] and crystallographic[34] investigations have shown that the proton is likely to form a bridging hydroxyl group adjacent to the aluminium substitution position. Unlike metal cations which occupy positions in the zeolite structure that are favoured by electrostatic interactions, the approach of a proton to the basic oxygen is not affected by electron-electron repulsion and an O–H bond can form directly.

2.2 Synthesis of Zeolites

Zeolites are generally synthesised from aqueous alkaline gels consisting of sources of silica, alumina and cations. The synthesis is carried out under hydrothermal autogeneous

Figure 2.6: Pyridine encapsulated in the large cage of dodecasil-3C.
Note: The carbon and nitrogen sites in the ring are disordered, hydrogen atoms have been added for convenience.



conditions at temperatures from 60 to 200°C and may require hours to weeks. Many synthetic methods require the presence of structure-directing agents or templates in order to obtain the desired product. These can range from simple hydrated cations to complex organic amines and crown ethers. Figure 2.6 shows the position of pyridine encapsulated in the large cage of the zeolite dodecasil-3C during synthesis, as determined by single-crystal X-ray diffraction.[35] The actual synthetic mechanism and the rôle of the templates is still open to debate; this field has been the subject of a recent review by Davis and Lobo.[19] It is thought that the structure-directing agent organises zeolite structural sub-units and mediates the formation of an amorphous gel. The gel then acts as a source of the reactant species which are dissolved in the liquid phase and are transported to the nucleation centres. The structure of the nucleation centres can be studied by light scattering and small angle neutron scattering experiments. Although many details remain unknown, the centres undoubtedly allow spontaneous zeolite crystal growth to occur by lowering the free-energy of the solution. Low aluminium content zeolites tend to be favoured by the use of large organic templates, which supposedly reflects their hydrophobic character and in addition to the fact that their relatively large size prevents high concentrations of aluminium occurring.

Many syntheses are highly sensitive to conditions such as temperature, pH and the nature of the template. All aluminosilicate zeolites are metastable structures with respect to quartz and alumina. Consequently, zeolite structures tend to convert to structures that are thermodynamically closer to quartz at higher temperatures. The higher temperature preparations tend to form the more thermodynamically stable structure in the series, the final products being quartz and alumina. Subtle changes in the template can often produce different zeolite structures. For example, the crown ether complex Na^+ 15-crown-5 can be used to synthesise the cubic faujasite structure (FAU), whereas if the crown ether is changed to 18-crown-6, the hexagonal faujasite structure (EMT) is the final product.[36]

In order to gain an insight into the mechanism of zeolite formation, *ex situ* NMR measurements have been made on gels.[37] Many different species were detected, including several silicate ring structures, such as four-rings and double six-rings. However, no structures containing more than twelve silicon atoms were observed. This implies that either only an early period in the zeolite formation is being sampled, or these species are the only important moieties needed to build the final structure.

Many applications, notably catalysis, require low aluminium content zeolites. It is possible to post-treat the product from a zeolite synthesis to remove framework aluminium and the charge compensating cations to yield high silica zeolites. The methods employed generally involve two stages. In the first, the zeolite is acid or steam treated, which facilitates the removal of the aluminium. Silicon is then re-inserted into the lattice either by thermal treatment to allow migration from other regions of the structure, or by chemical means. Popular reagents include $SiCl_4$, tetraethylorthosilicate (TEOS), and $(NH_4)_2SiF_6$; the former has recently been used to synthesise a purely siliceous faujasite structure.[31] The synthesis of other heterosubstituted zeolites often requires different conditions than for aluminosilicates. For example, aluminophosphates require relatively acidic conditions with no alkali-metal cations, although alkali-metal cations can be used to synthesise MeAPO structures.

A relatively recent development in zeolite synthesis has been the use of non-aqueous acidic conditions. This was first demonstrated by Flanigen and Patton,[38] and has been extended by Guth and co-workers to synthesise a wide variety of aluminosilicate zeolites in neutral or acidic conditions.[39,40] This method can also be used to synthesise alu-

minophosphate structures.[41] Kupermann and co-workers[42] have demonstrated a procedure that uses hydrogen fluoride in the synthesis of large single crystals (millimeter scale) of zeolites. Siliceous ferrierite has been synthesised using HF, propylamine and pyridine, and this method has also been shown to be useful in the synthesis of aluminophosphates.[43] It is thought that the HF promotes the formation of the zeolite precursors by allowing the silicon and aluminium to assume octahedral coordination with the fluoride ion. In addition, the high solubility of the silicate species in HF causes slow delivery of silicon to the nucleation centres and this promotes the growth of single crystals.

2.3 Methods of Characterisation

2.3.1 Diffraction Methods

The chemistry of zeolite materials cannot be fully understood without detailed structural information. Diffraction methods offer the possibility of extracting a wealth of useful structural data on a zeolitic material. As a consequence of synthetic methods, diffraction studies are almost always limited to powder diffraction studies due to the paucity of single crystals. However, a combination of advances in instrumentation, easier access to synchrotron and neutron sources and improvements in computational power have made the solution of complex structures from powder data possible.

The area of zeolite structure solution from high quality powder data has recently been reviewed by McCusker.[44,45] The Rietveld profile refinement technique[46] is applied extensively to overcome the problem of overlapping peaks which is inherent in a powder diffraction pattern.

Powder neutron diffraction allows the analysis of subtle structural features. For example, the differing scattering powers of Si and Al for neutrons allow these atoms to be distinguished in the structure. This has been shown for a number of structures including the Si/Al ordering in Tl zeolite-A,[47] and studies can also be performed to find the positions of protons[48] and water in zeolite structures. In addition, powder neutron diffraction has been a popular method for the structure solution of aluminophosphate materials from time-of-flight data.[49,50]

Advances in the analysis of powder diffraction data have allowed the extraction of in-

tegrated intensities by a variety of different methods, and created the possibility of solving the structure *ab initio* from powder data using methods commonly applied to single-crystal experiments. This approach has been used in the structure solution of the clathrasil structure sigma-2[51] and $AlPO_4$-18.[52]

There have also been a limited number of diffraction studies that have attempted to locate sorbates in zeolites. This is a much more difficult problem since generally the sorbate must be located at well-defined sorption sites in sufficient concentration to produce a significant contribution to the scattering in the overall pattern. Wright and co-workers located deuterated pyridine in gallozeolite-L, and additionally performed computer simulations which showed good agreement with the diffraction result.[53] Faujasite has been a popular structure for these measurements. Fitch and co-workers[54] located benzene in the structure of Na-Y and pyridine was located in same structure by Goyal and co-workers.[55] The locations of meta- and para-xylene in Ba-Y was determined using a combination of X-ray and neutron powder diffraction,[56] and Klein and co-workers have also located several other aromatic molecules in Na-Y.[57]

2.3.2 Electron Microscopy

Electron microscopy offers the possibility of performing a number of different experiments on zeolite samples. Scanning electron microscopy can be used to investigate the morphology of zeolite crystals. Electron diffraction allows the unit cell and symmetry of a zeolite structure to be determined for a single crystallite and can be compared usefully to X-ray and neutron diffraction experiments. High resolution electron microscopy allows the study of subtle effects not directly accessible by X-ray diffraction methods by imaging the zeolite lattice directly. Thomas has recently reviewed this area.[58] Early work in this area was performed by Thomas and Millard, who investigated the structure of ZSM-5/ZSM-11 intergrowths. Fyfe and co-workers[59] studied several zeolite structures with similar X-ray powder patterns to determine which were unique frameworks. The wide range of intergrowths in the zeolite-β system have also be extensively studied by Newsam and co-workers.[60] Recently, electron microscopy has been used to image metal clusters in a zeolite cavity. For example, Tong and co-workers have looked at platinum clusters in the supercage of Na-Y.[61] Lobo and Davis have shown how, by using electron diffraction in com-

bination with other techniques, the structure of the zeolite CIT-1 could be determined.[62]

2.3.3 Extended X-ray Absorption Fine Structure (EXAFS)

The EXAFS effect arises from oscillations in intensity occurring on the high energy side of an X-ray absorption edge, due to excitations of electrons from core levels to continuum states. The outgoing photoelectron wave is modulated by the backscattering of the photoelectron. The scattering spectrum provides information about the local environment of the absorbing atom and can be Fourier transformed to produce a radial distribution function. This technique has been widely used to analyse the local structure around extra-framework cations and to determine whether a given cation occupies a framework or extra-framework position. Axon and co-workers performed an EXAFS study on an iron-substituted ZSM-5.[63] They determined that iron was four-coordinated to oxygen and also found the distances to the template molecule encapsulated in the channels. The EXAFS data and the Fourier-transformed radial distribution function is shown in Figure 2.7. This system has also been the subject of a recent computational study by Lewis and co-workers.[64]

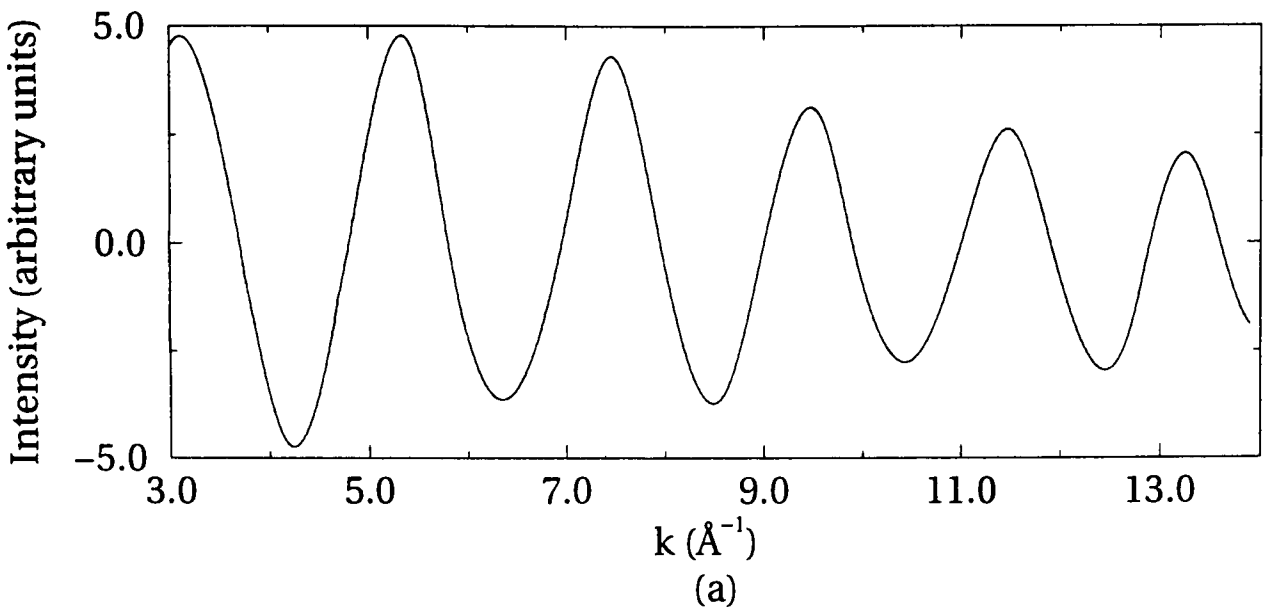
2.3.4 Infra-Red Spectroscopy

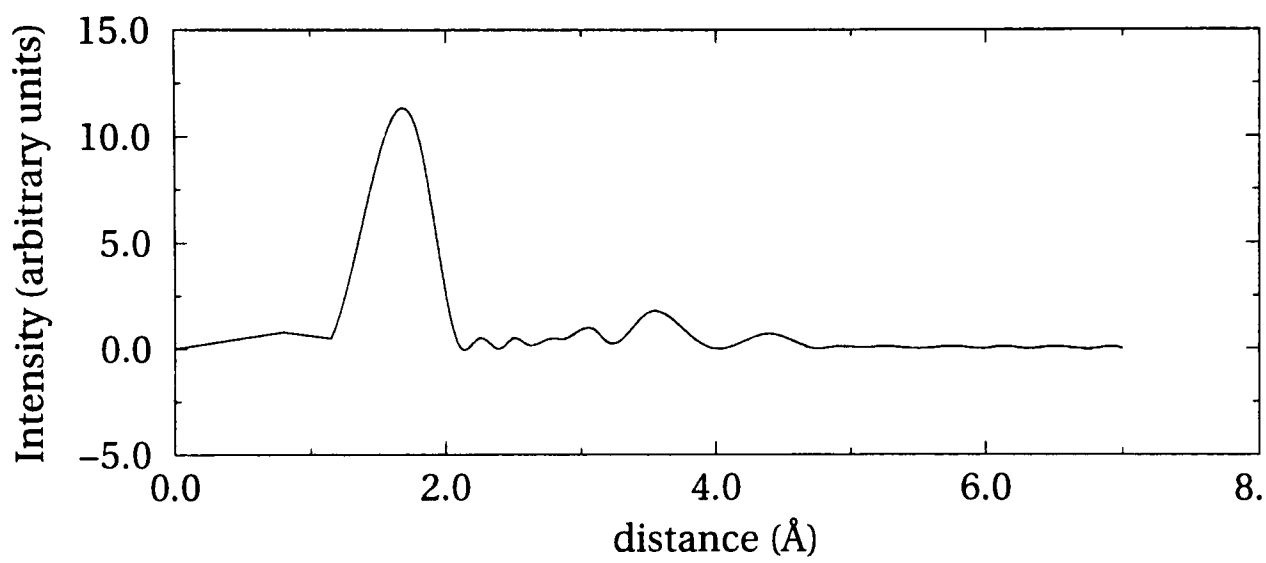
Infra-red spectroscopy can be used to study the vibrational modes of the zeolite framework and of sorbed molecules in the zeolite pores. Framework vibrations have been intensively studied and can now be assigned routinely.[65] The nature of the O–H group in zeolites has also been a popular study in this area as a possible route to the quantification of zeolite acidity.[66] Although, it is common to use probe molecules such as ammonia and carbon monoxide to investigate the behaviour of the acid site in the presence of molecules of varying base strength and modes of interaction.[67] Infra-red methods have also been used extensively to study the nature of sorbate binding in zeolite pores.[68]

2.3.5 Nuclear Magnetic Resonance

Nuclear magnetic resonance can be used to study both the structure of the zeolite itself and also the environment and mobility of molecules moving through the pore structure.

Figure 2.7: (a) EXAFS data and (b) Fourier Transform for Fe-ZSM-5 with template after Axon[63]





[29]Si is a useful probe for aluminosilicate zeolites, especially when coupled with the magic angle spinning technique.[69] The chemical shift is directly dependent on the number of Al atoms surrounding the Si site as well as the degree of condensation around it, and the relative intensities of each of the peaks in a spectrum can be used to measure the Si/Al ratio using the expression :[70]

$$\text{Si/Al ratio} = \frac{\sum_{n=0}^{4} I_{Si(nAl)}}{\sum_{n=0}^{4} \frac{1}{4} n I_{Si(nAl)}} \tag{2.1}$$

It has also been shown that the chemical shift is sensitive to the Si-O-T bond angle.[71] Two-dimensional NMR experiments using COSY (Correlation Spectroscopy)[72] and the INADE-

QUATE pulse sequence (Incredible Natural Abundance Double Quantum Transfer Experiment)[73] provide methods by which T-site connectivities can be directly determined. The application of 2D homonuclear COSY has enabled Fyfe and co-workers to yield the correct connectivities for the structure of ZSM-39.[74]

^{27}Al NMR is a little more problematic since the nuclear quadrupole moment of ^{27}Al tends to broaden the spectra. This has limited measurements to those involving the monitoring of the dealumination process and the detection of extra-framework aluminium. However, the development of dynamical angle spinning (DAS)[75] and double rotation (DOR)[76] methods has allowed further reduction in line broadening, and has found particular application in the study of the varying Al environments found in aluminosilicates and aluminophosphates. Recently, the multiple-quantum magic-angle spinning NMR technique has been developed[77] which also shows promise in the study of quadrupolar nuclei in zeolites.

^{129}Xe is also a useful nucleus for probing a zeolite structure. The large polarisable electron cloud of the Xe atom makes the chemical shift highly sensitive to its environment.[78] A large number of structural effects have been studied using ^{129}Xe NMR including pore structure and reaction sites.[79,80] The technique can also be used to study the behaviour of occluded organic molecules. Chmelka and co-workers have used this method to investigate the properties of benzene in Na-Y.[81]

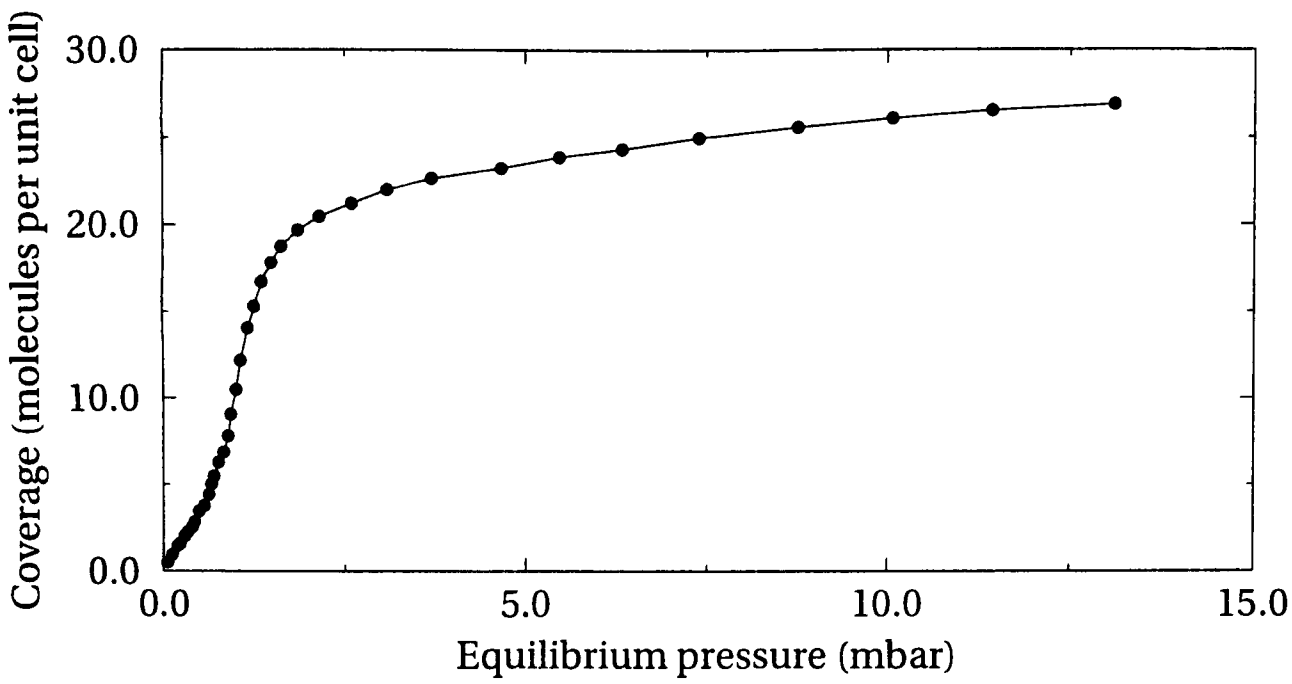
There have been several studies which have attempted to monitor catalytic processes in zeolites by NMR. For example, Anderson and Klinowski detected 29 different organic species in the sorbed phase during the catalytic conversion of methanol to hydrocarbons over ZSM-5.[82]

Other NMR techniques can be used to investigate the transport of molecules in zeolites, as will be detailed in Section 2.3.7.

2.3.6 Sorption Experiments

Sorption experiments are routinely used to probe the pore structure of zeolites, with O_2, Ar, N_2, NH_3, and Xe being useful probe molecules. The sorption isotherm can be routinely fitted to a convenient function form such as the BET isotherm to extract useful information about the available pore volume in the zeolite structure and thermodynamic infor-

Figure 2.8: Sorption Isotherm for Benzene in Siliceous Faujasite at 298K



mation such as the isosteric heat of sorption. In addition, by sorbing a number of different molecules of known kinetic diameter, an estimate of the zeolite channel size can be made. Figure 2.8 shows a typical sorption isotherm for benzene in siliceous faujasite.

In the low pressure regime, the sorption follows Henry's Law for most simple sorbates :-

$$p^* = K_H p \tag{2.2}$$

where p^* is the partial pressure of the gas in the sorbed phase, K_H is the Henry's Law constant, and p is the pressure. By measuring the constant as a function temperature, the isosteric heat of sorption can be obtained from the van't Hoff isochore :-

$$\frac{\partial K_H}{\partial T} = \frac{\Delta H_s}{RT^2} \tag{2.3}$$

where ΔH_s is the isosteric heat. The sorption isotherm tends to be of Brunauer type I form, although the presence of sorption sites of different environments and sorbate-sorbate interactions can cause interesting deviations.[83]

Thermal gravimetric analysis (TGA) and differential scanning calorimetry (DSC) can be used to study the breakdown of the template and the zeolite framework with increasing temperature, in addition to monitoring dehydration. Water tends to be lost in the 90-200°C range, whereas ammonia is retained until around 300°C. The template tends to decom-

pose in the range 375-500°C. At low loading and with low Si/Al zeolites, water is sorbed with isosteric heats ranging from 80-120 $kJmol^{-1}$, whereas for linear hydrocarbons, heat of sorption is roughly 14 $kJmol^{-1}$ per methylene group.

Probe molecules can also be chosen which can interact directly with the acid site in protonated zeolites. For example, zeolite samples can be titrated against known indicators such as ammonia to measure the acidity. Further information can be obtained by the use of an *in situ* technique, for example, NMR or infra-red spectroscopy, to monitor the sorption process more closely. The location of the acid site can be inferred by using the shape selectivity of the zeolite with base probes of different sizes.

2.3.7 Diffusion of Molecules in Zeolites

In most zeolites, the pore structure accessible to molecules has dimensions of the same order of magnitude as the collision cross-section of the molecules themselves.[84] Consequently, the transport of reactant and product molecules is controlled by the continuous interaction between the zeolite and the diffusing species. Unlike the diffusion observed in fluid-filled pores (Brownian diffusion)[85] and diffusion through an aperture (Knudsen diffusion),[86] this diffusional regime, known as configurational diffusion, is not as well understood. However, this effect can be identified by the following experimental characteristics :-

- relatively small magnitudes of the diffusion coefficients
- strong dependence of their values on the size and shape of the diffusing molecules
- relatively high activation energies, typically 20-60 $kJmol^{-1}$
- strong dependence on the concentration of the diffusing molecules

The diffusion of particles down a concentration gradient can be described by Fick's first law :-

$$J(x) = -D(c)\frac{\partial c}{\partial x} \tag{2.4}$$

where $J(x)$ is the flux of matter (the number of particles passing through unit area in unit time), $D(c)$ is the diffusion coefficient and c is the concentration. This definition implies

that the diffusivity is independent of concentration, which is only realised when the system is thermodynamically ideal. A more convenient representation is to reformulate the expression in terms of a gradient in the chemical potential, thus :-

$$J(x) = -B(c)\frac{\partial \mu}{\partial x} \tag{2.5}$$

where B is defined as the mobility. Assuming that the vapour phase is ideal, we can relate the Fickian diffusivity to the mobility by :-

$$D(c) = B(c)RT\frac{d\ln p}{d\ln c} \tag{2.6}$$

where p is the pressure.

Many diffusion experiments in zeolites measure the self-diffusion of molecules, which strictly defines the rate of tracer exchange of marked molecules under equilibrium conditions in a system with no net concentration gradient. This is in general different from the transport diffusivity in the equations above. We can consider the diffusion of a tracer molecule A^* in a mixture of A and A^*. The flux of A is given by :-

$$J_A = -L_{AA}(c_A, c_{A^*})\frac{\partial \mu_A}{\partial x} - L_{AA^*}(c_A, c_{A^*})\frac{\partial \mu_{A^*}}{\partial x} \tag{2.7}$$

Using Equation 2.6 assuming diffusive transport for A, we can write :-

$$J_A = -RTL_{AA}(c_A, 0)\frac{d\ln p_A}{dc_A}\frac{dc_A}{dx} \tag{2.8}$$

where $L_{AA}(c_A, 0) = Bc_A$. This leads to the following relationship between self and transport diffusivities :

$$D(c) = D_{\text{self}}\frac{d\ln p}{d\ln c}\left[1 - \frac{c^2}{c_A c_{A^*}}\frac{L_{AA^*}(c_A, c_{A^*})}{L_{AA}(c_A, 0)}\right]^{-1} \tag{2.9}$$

where $c = c_A + c_{A^*}$ is the concentration of the diffusing species. If we assume that the cross-term, L_{AA^*}, can be neglected, then the equation reduces to :-

$$D(c) = D_{\text{self}} \frac{d \ln p}{d \ln c} \tag{2.10}$$

which is known as the Darken equation. It can be shown that diffusive behaviour can be directly related to the results of a large number of well-defined steps in random directions (or random walk). Using a random-walk analysis, the mean-squared displacement of a particle can be related to the diffusivity by the Einstein relation :-

$$\langle x^2(t) \rangle = 2Dt \tag{2.11}$$

The above equations can be readily extended to two or three dimensions if the diffusive behaviour is isotropic. However, in the case of a zeolite, anisotropic diffusion is expected in any case where the crystal structure is non-cubic, and Fick's Law may be expressed as :-

$$-J_x = D_{xx} \frac{\partial c}{\partial x} + D_{xy} \frac{\partial c}{\partial y} + D_{xz} \frac{\partial c}{\partial z} \tag{2.12}$$

$$-J_y = D_{yx} \frac{\partial c}{\partial x} + D_{yy} \frac{\partial c}{\partial y} + D_{yz} \frac{\partial c}{\partial z} \tag{2.13}$$

$$-J_z = D_{zx} \frac{\partial c}{\partial x} + D_{zy} \frac{\partial c}{\partial y} + D_{zz} \frac{\partial c}{\partial z} \tag{2.14}$$

where D_{ij} is the contribution to the flux in the ith direction from a concentration gradient in the jth direction. The coefficients are expressed as a second-rank tensor :-

$$\mathbf{D} = \begin{bmatrix} D_{xx} & D_{xy} & D_{xz} \\ D_{yx} & D_{yy} & D_{yz} \\ D_{zx} & D_{zy} & D_{zz} \end{bmatrix} \tag{2.15}$$

Most anisotropic problems can be reduced to a corresponding isotropic expression with the appropriate transformation into a rectangular coordinate system.

The measurement of diffusion coefficients by experimental methods can be divided into three areas : the investigation of elementary processes at the atomic level, the study of self-diffusion, and the measurement of transport diffusion.

The transport of molecules within a single crystallite (intracrystalline) can be measured using a variety of spectroscopic techniques. The pulsed field gradient (PFG) NMR technique is the most reliable method of measuring self-diffusivities, since it allows measurements to be made in the micrometre range. For example, Heink and co-workers studied the self-diffusion of *n*-alkanes from methane to heptane in NaCaA,[87] and observed the expected decrease in diffusivity with increasing carbon chain length. Recently, Hong and co-workers have combined the use of Fourier-transform PFG ^{129}Xe NMR to measure the concentrations of individual components in a zeolite during a zeolite-catalysed reaction and conventional PFG NMR to measure the mean-squared displacements.[88] An alternative NMR method which can also examine the diffusion of molecules in zeolites is spin-lattice relaxation. This is based on the relaxation of the longitudinal component of the magnetisation due to the interactions of the molecule with its environment during its diffusional motion. By assuming a hopping length for the motion, activation energies and diffusivities can be extracted. The spin-lattice relaxation method accesses a length scale shorter than the pulsed field gradient approach, and in combination these two techniques offer the opportunity to contrast long and short-range diffusion mechanisms. This method was recently used by Bull and co-workers to investigate the motion of benzene in a range of faujasite samples of varying Si/Al ratio.[89] Quasi-elastic neutron scattering (QENS) can be used to probe the translational and rotational dynamics of molecules sorbed in zeolites. Atomic and molecular motions occurring over a time scale of 10^{-9} to 10^{-12} s broaden the elastic scattering peak of neutrons. The experiments have been mainly limited to molecules containing hydrogen due to its large incoherent scattering cross-section.[90] In cases where the results of PFG NMR and QENS measurements have been compared, the agreement has been encouraging.[91]

In order to measure transport diffusivities on the macroscopic scale it is necessary to introduce a concentration gradient across the sample. The measurements may be made under either steady state or transient conditions. Fourier transform infra-red spectroscopy (FTIR) can be used to study diffusional effects during sorption and desorption processes

by monitoring the intensity of a typical sorbate IR band as a function of time. This method has been used to study the sorption of benzene in H-ZSM-5 and single component diffusivities as a function of temperature have been obtained.[92] The zero-length column (ZLC) chromatographic method has been recently developed by Eic and Ruthven.[93] This has the advantage that only small amounts of sorbate are required and also relatively high diffusivities can be measured. Ruthven[94] has used this method to study Xe and CO_2 diffusion in zeolite 5A, which gave excellent agreement with previous NMR measurements. Torresan and Grenier have reported the technique of surface temperature IR which follows the sorption and desorption rates in zeolite crystals by monitoring the transient response of the surface temperature.[95] Grenier and co-workers have investigated the behaviour of water in Na-X using this method, and, by using large crystals, have obtained diffusivities that compare well with other measurements.[96] The frequency-response method has also been used widely to measure diffusivities in zeolites. Rees and Shen have recently studied the diffusion of hydrocarbons in silicalite-1 at various loadings and temperatures.[97] For the larger molecules, it is possible to extract individual diffusivities in each of the channel systems assuming that the characteristic curves obtained in the experiment result from two independent fluxes.

It is important to realise that many of the techniques detailed above measure diffusivities over a wide range of time and length scales, and may sample quite different transport mechanisms depending on the system in question. For example, it is apparent that when considering macroscopic diffusion, the effects of intercrystalline diffusion can be a significant factor. Table 2.2 summarises the various techniques and their characteristics.

2.4 Applications of Zeolites

2.4.1 Heterogeneous Catalysis

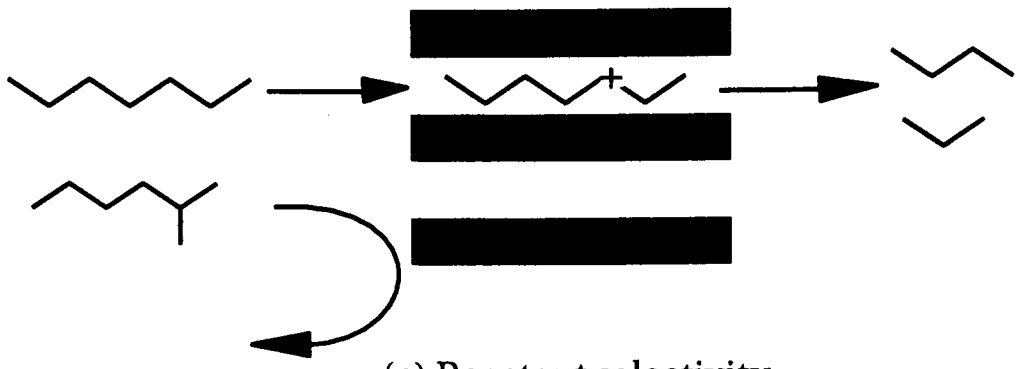
One of the most important applications of zeolites is in the field of industrial catalysis. Zeolites catalyse a wide variety of reactions involving organic molecules. There are several methods by which a zeolite structure is able to catalyse reactions. Firstly, their large internal surface area (typically 300-700m^2g^{-1} or more than 98% of the total surface area) provides a high concentration of active sites, usually the Brønsted acid sites found in proto-

Table 2.2: Experimental techniques for diffusion studies in zeolites.

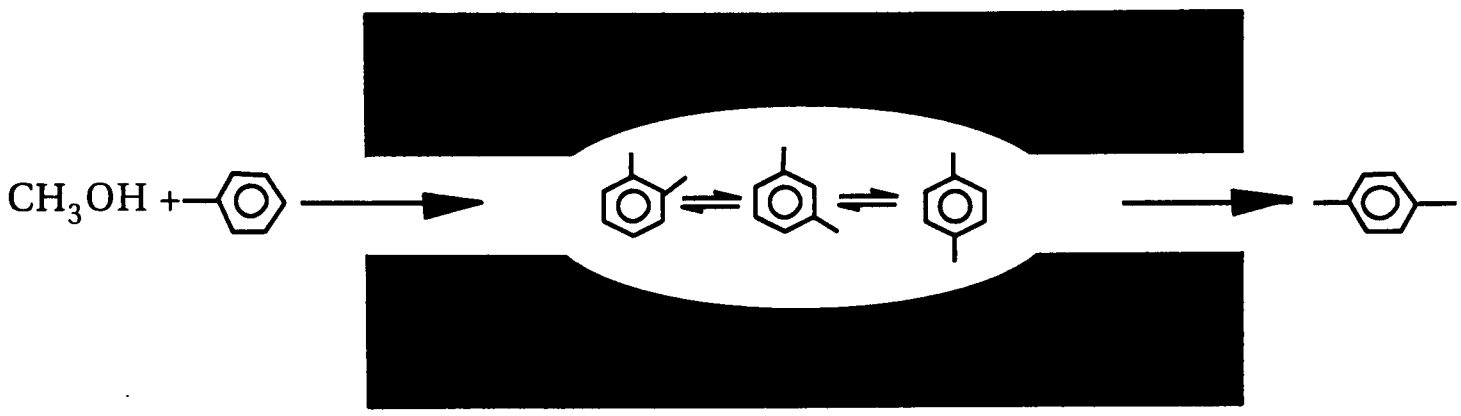
Method	Subject	Space Scale	Time Scale
NMR (line shape, relaxation)	elementary processes	$\leq$nm	$10^{-10}...10^{-1}$ s
Neutron scattering	elementary processes	$\leq$nm	$\leq 10^{-8}$ s
Tracer techniques	self-diffusion	$\geq \mu$m	$\geq$ min
PFG NMR	self-diffusion	μm...mm	ms...s
Transient and steady state measurements	transport diffusion	$\geq \mu$m	$\geq$s

nated zeolites. These are generally located as bridging hydroxyl group, although the small concentration of defect sites undoubtedly contributes to the reactivity. These sites are able to protonate organic molecules such as alkenes to form carbonium ions, or basic groups such as hydroxyl groups and amines. The high thermal stability of many zeolite structures makes them ideal for use in an industrial environment where many processes operate in conditions of high temperature and pressure. The shape selective properties of zeolites can also control the outcome of many reactions inside the pore, either by allowing reactant or product molecules to selectively diffuse through the channels, or by the stabilisation of the transition state (see Figure 2.9). Protonated forms of faujasite are widely used in fluid catalytic cracking.[98] This process converts the predominantly long chain hydrocarbons that are present in crude oil into smaller hydrocarbon molecules useful for gasoline and as feedstocks for synthesis of fine chemicals. Coke is a frequent by-product of this reaction, and causes the deactivation of the catalyst by blocking the pore structure over a period of time. This requires regeneration of the catalyst under an oxidising atmosphere for a prolonged period. Rare-earth cations, such as La^{3+}, are often added to give the catalyst extra structural stability as well as providing extra Brønsted acid sites formed by hydrolysis of the cation. Recently, ferrierite has been shown to be an excellent shape-selective catalyst for the isomerisation of butene to iso-butene.[99] The latter is an important feedstock for the production of methyl tertiary butyl ether (MTBE), which is a commercial oxygenate additive in lead-free motor fuel.

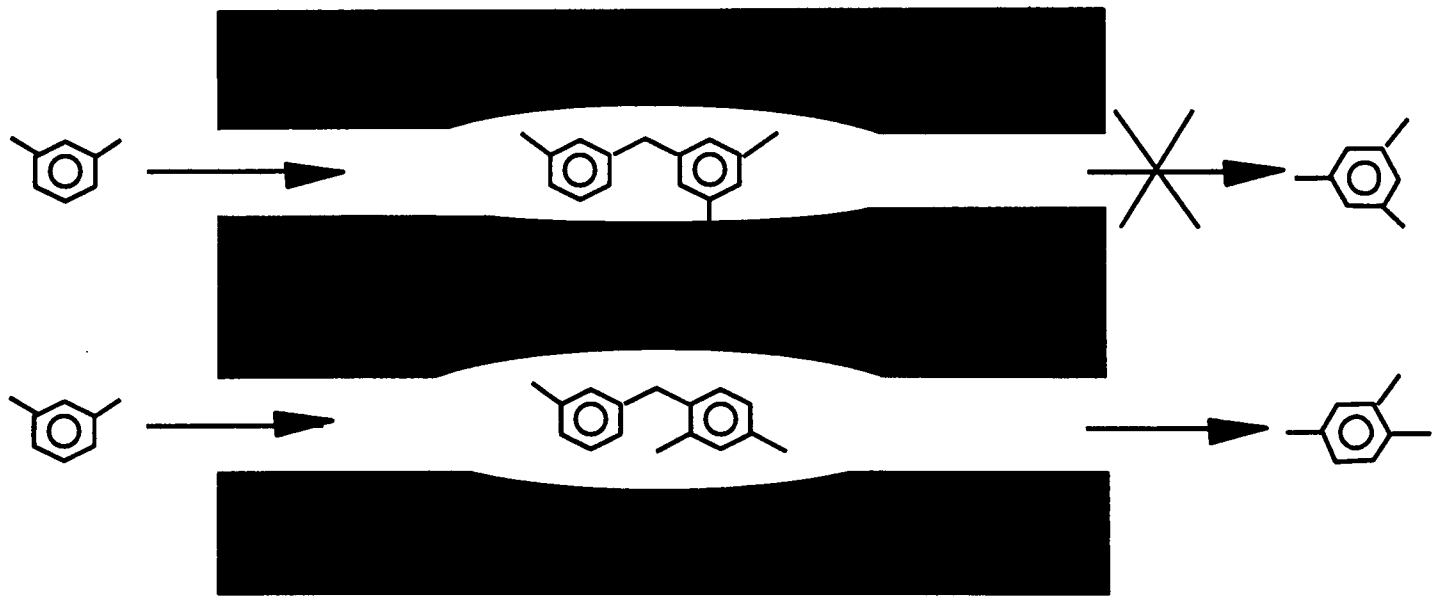
Figure 2.9: Shape selectivity exhibited by zeolites.



(a) Reactant selectivity



(b) Product selectivity



(c) Transition state selectivity

The addition of metal cations to a structure, either as framework species or extra-framework cations, can often modify the catalytic activity. For example, the introduction of Cu^{2+} into ZSM-5 makes it active in the conversion of NO and NO_2, which are common in exhaust gases from automobiles, to nitrogen and oxygen.[100] The addition of small amounts of titanium to silicalite forms titanium-silicalite-1[101] which exhibits activity as an oxidation catalyst using hydrogen peroxide. This process has been recently commercialised to produce catechol and hydroquinone from phenol. In addition, zeolites synthe-

sised with transition metal clusters in their cavities often show catalytic activity with the zeolite effectively acting as a shape-selective support.

The conversion of alcohols to alkenes in zeolite 5A relies on reactant shape-selectivity for its action. Only primary alcohols, rather than branched chain isomers, can enter the small pores of the zeolite and reach the active sites. Under normal conditions, the secondary alcohols, which form the more stable carbonium ion intermediates, would be converted selectively.

Product shape-selectivity is a vital characteristic in the use of ZSM-5 in the isomerisation of xylenes. The *p*-isomer of xylene is an important starting material in the synthesis of polyesters. The isomerisation reaction is known to proceed via a carbonium ion intermediate, creating a thermodynamic equilibrium between the isomers. However, although para-xylene is not the thermodynamically favoured isomer in an equilibrium mixture. It has a much higher diffusivity than the ortho and meta isomers in the pore structure of ZSM-5 on account of its relatively linear shape and can escape from the catalyst more rapidly.

The methanol-to-gasoline (MTG) process[102] is an important method of obtaining gasoline in locations with no direct source of crude oil. In New Zealand it is used routinely as a step in converting the natural gas reserves into petrol for transportation. Mechanistic studies on this system have shown that the important intermediate is dimethyl ether. The smaller channel of the ZSM-5 pore structure prohibits the formation of aromatic species larger than C_9 and C_{10}, thus reducing the amount of coking.

The majority of zeolite catalytic applications are based on zeolites acting as acid catalysts. However, there have been a limited number of reports of base catalytic activity. Hathaway and Davis have synthesised nanophase caesium oxide inside the pores of zeolites, forming excellent base catalysts.[103] Gortsema and co-workers have also commercialised a process using caesium-loaded zeolites to catalyse the formation of 4-methylthiazole, which is an intermediate in the synthesis of an important fungicide.[104]

The chiral crystal structure of polymorph A of zeolite β[60] offers the possibility of asymmetric synthesis. Indeed, the proportion of this chiral polymorph produced by the synthesis procedure can be increased by the use of chiral templates.[19] This new material has been shown to give a 5% enantiomeric excess for the hydration of *trans*-stilbene oxide.[19]

2.4.2 Ion Exchange

The presence of extra-framework cations in the zeolite structure allows efficient ion exchange to occur in aqueous solution. This is exploited in many commercial applications. For example, large amounts of Na zeolite-A are used to soften water by exchanging Na^+ from the zeolite with Ca^{2+} in hard water. This is also a major component of concentrated washing powder formulations, where it replaces sodium tripolyphosphate to reduce the environmentally hazardous phosphate concentration. Ammonium and potassium exchanged zeolites are also frequently added to soil to improve crop yields. Recently, an important use of zeolites as ion-exchangers has been as radioactive decontaminants. Clinoptilolite, for example, was used extensively after the Chernobyl nuclear disaster to leach radioactive ions such as ^{90}Sc and ^{137}Cs from the water supply.[105] In the dehydrated form, zeolites have a high affinity for water, and are used commonly for dehydrating organic solvents prior to synthetic work and in double glazing.

2.4.3 Sorption and Gas Separation

The shape selectivity of a zeolite can also be used to separate gases. Two modes of operation can be envisioned. In the first, which is essentially a thermodynamic effect, the differing affinities of the zeolite for each sorbate effects the separation procedure. Using this principle, it is possible to achieve non-cryogenic separation of O_2 and N_2 with Na-LSX zeolite. In this case, the presence of the quadrupole moment of N_2 causes the molecule to be more strongly bound to the cation. Alternatively, the kinetics of transport through the zeolite pores can be used to achieve the separation. This is essentially the shape selective effect detailed in Section 2.4.1. The Asahi process operates on this principle to separate mixtures of C_8 aromatic isomers (xylenes and ethylbenzene).[83]

Further applications have also been proposed. Herron and co-workers have synthesised a zeolite in which a semiconducting material was formed *in situ* inside the zeolite pore structure.[106] In addition, it is also possible to introduce conducting polymers using similar techniques modifying the physical properties in subtle ways.[107]

Chapter Three

Theoretical Methods

One of the main aims of many computational chemistry methods is a correct representation of the potential energy surface. Using quantum mechanics, an exact expression for the energy as a function of all degrees of freedom in the system is possible, however the solution of this expression is rarely a tractable problem and various approximations must be used. The wide variety of computational methods that are available vary quite considerably in the level of approximation that is employed, ranging from accurate quantum mechanical approaches to the more empirically based atomistic simulation techniques. By a careful consideration of the problem, a technique must be chosen which calculates the desired properties of interest to a given level of accuracy while expending the least amount of computational effort.

In this chapter, the theoretical basis of each of the computational approaches will be discussed along with their relevance to readily accessible experimental data. Finally, the issue of computational hardware development will be addressed and its impact on computational chemistry will be considered.

3.1 Quantum Mechanical Methods

Quantum mechanical methods consider the electronic properties of an atom explicitly by wave mechanics. This allows the study of properties of a system that depend directly on electronic configuration, such as electronic transitions and the important aspects of bond making and bond breaking processes in chemical reactions. Since this treatment is relatively computationally expensive compared to more approximate methods, calculations tend to be limited to clusters of fewer than 200 atoms, even for semi-empirical quantum mechanical methods.

3.1.1 *Ab Initio* Techniques

The time-dependent Schrödinger equation, or Dirac equation, can be written as :-

$$\hat{H}\Psi = i\hbar\left(\frac{\partial\Psi}{\partial t}\right) \tag{3.1}$$

where $\hat{H}$ is the Hamiltonian operator, $\hbar$ is the scaled Planck constant, Ψ is the wavefunction, and t is time.

In the limit that the wavefunction is considered to be a stationary state, the time-independent Schrödinger equation can be written :-

$$\hat{H}\psi = E\psi \tag{3.2}$$

where E is the energy. The Hamiltonian operator can be divided into a number of different terms :-

$$\hat{H} = -\sum_{i=1}^{N_e}\frac{\hbar^2}{2m}\nabla_{\boldsymbol{r_i}}^2 - \sum_{i=1}^{N_e}\sum_{\alpha=1}^{N_n}\frac{Z_\alpha e^2}{|\boldsymbol{r_i}-\boldsymbol{R_\alpha}|} + \sum_{i=1}^{N_e}\sum_{j>i}^{N_e}\frac{e^2}{|\boldsymbol{r_i}-\boldsymbol{r_j}|} + \sum_{\alpha=1}^{N_n}\sum_{\alpha'=1}^{N_n}\frac{Z_\alpha Z_{\alpha'} e^2}{|\boldsymbol{R_\alpha}-\boldsymbol{R_{\alpha'}}|} \tag{3.3}$$

where N_e is the number of electrons, N_n is the number of nuclei, m is the mass of an electron, Z is the nuclear charge, e is the electronic charge, and r and R are position vectors for electrons and nuclei respectively. The four terms represent the electronic kinetic energy, the electronic-nuclear attraction, the electron-electron repulsion, and the nuclear-nuclear repulsion respectively. The kinetic energy operator is the Laplacian :-

$$\nabla^2 = \left(\frac{\partial^2}{\partial x^2}\right) + \left(\frac{\partial^2}{\partial y^2}\right) + \left(\frac{\partial^2}{\partial z^2}\right) \tag{3.4}$$

where x, y and z are the Cartesian axes. Since the electronic motion is considerably faster than nuclear motion, the positions of the nuclei do not respond to changes in the electronic position, and the nuclear-nuclear term can be separated out in Equation 3.3. This is called the *Born-Oppenheimer approximation*, however it has a number of important exceptions in chemical problems, notably the Jahn-Teller effect in transition metal chemistry.

Thus neglecting the nuclear-nuclear term the Hamiltonian can be written as :-

$$\hat{H}' = -\sum_{i=1}^{N_e} \hat{h}(i) + \sum_{i=1}^{N_e} \sum_{j>i}^{N_e} \hat{g}(i,j) \tag{3.5}$$

$$\hat{h}(i) = -\frac{\hbar^2}{2m} \nabla_i^2 - \sum_{\alpha=1}^{N_n} \frac{Z_\alpha e^2}{|\boldsymbol{r_i} - \boldsymbol{R_\alpha}|} \tag{3.6}$$

$$\hat{g}(i,j) = \frac{e^2}{|\boldsymbol{r_i} - \boldsymbol{r_j}|} \tag{3.7}$$

where $\hat{h}(i)$ represents a one-electron many-nuclei term, and $\hat{g}(i,j)$ is a many-electron term. The aim is to solve the Schrödinger equation for the wavefunction, ψ, and the energy, E.

In the case of the hydrogen atom, the many-electron term vanishes and the Schrödinger equation simplifies to :-

$$(\hat{h}(i) - \epsilon_n)\phi_n(\boldsymbol{r_i}) = 0 \tag{3.8}$$

This is one of the few systems for which there is an exact solution to the Schrödinger equation, the hydrogenic wavefunctions having the general form in polar coordinates :-

$$\phi_{\boldsymbol{n}}(\boldsymbol{r_i}, \theta_i, \zeta_i) = \psi(\boldsymbol{r_i})\sigma_{m_s} \tag{3.9}$$

$$= R_n(\boldsymbol{r_i})\Theta_{lm}(\theta_i)\Phi_m(\zeta_i)\sigma_{m_s} \tag{3.10}$$

where n represents a set of quantum numbers describing the wavefunction ($\boldsymbol{n}$ = { n , l , m , m_s }), R_n is a Laguerre polynomial, Θ_{lm} is a associated Legendre polynomial, Φ is a plane wave term, and σ represents the electron spin. Collectively, the wavefunctions ϕ_n are known as *atomic orbitals.*

In the case of many electron systems, no exact solution is possible and a more approximate approach is needed. One starting point is to express the many electron molecular wavefunction as a product of one electron molecular wavefunctions, or *molecular orbitals* thus :-

$$\Psi_{\boldsymbol{N}}(\boldsymbol{r_1}, \boldsymbol{r_2}, \ldots, \boldsymbol{r_{N_e}}) = \psi_{\boldsymbol{n_1}}(\boldsymbol{r_1})\psi_{\boldsymbol{n_2}}(\boldsymbol{r_2}) \ldots \psi_{\boldsymbol{n_{N_e}}}(\boldsymbol{r_{N_e}}) \tag{3.11}$$

This is known as the *Hartree approximation.*[108]

A further complication for many electron systems is provided by the Pauli exclusion principle, which states that the total wavefunction, Ψ_N must be antisymmetric with respect to the simultaneous exchange of any two electrons. This is achieved by the use of the Slater determinant which has the form :-

$$\Psi_N(\boldsymbol{r_1}, \boldsymbol{r_2}, \ldots, \boldsymbol{r_{N_e}}) = \frac{1}{\sqrt{N!}} \begin{vmatrix} \psi_1(1) & \psi_1(2) & \psi_1(3) & \ldots & \psi_1(N) \\ \psi_2(1) & \psi_2(2) & \psi_2(3) & \ldots & \psi_2(N) \\ \psi_3(1) & \psi_3(2) & \psi_3(3) & \ldots & \psi_3(N) \\ \vdots & \vdots & \vdots & \vdots & \vdots \\ \psi_N(1) & \psi_N(2) & \psi_N(3) & \ldots & \psi_N(N) \end{vmatrix} \tag{3.12}$$

where $\psi_i(j)$ represents the electron in spin-orbital i with position vector r_j. The variational theorem states that for any approximate wavefunction, Ψ_N, the calculated approximate energy will be an upper bound to the total energy. The *Hartree Fock method*[109] finds the Slater determinant wavefunction that makes the total energy the lowest.

The energy of the system is given by the following expression :-

$$E(\Psi_N(\boldsymbol{r_1}, \boldsymbol{r_2}, \ldots, \boldsymbol{N_e})) = \frac{\int \Psi^* \hat{H}' \Psi d\boldsymbol{r}}{\int \Psi^* \Psi d\boldsymbol{r}} \equiv \frac{< \Psi | \hat{H}' | \Psi >}{< \Psi | \Psi >} \tag{3.13}$$

Substituting for $\hat{H}'$ from Equation 3.5. The orthogonality of the spin-orbitals reduces the one-electron term to a sum involving integrals over the same wavefunction :-

$$E_1 = \sum_{i=1}^{N} < \psi_i(i) | \hat{h}(i) | \psi_i(i) > \equiv \sum_{i=1}^{N} h_i \tag{3.14}$$

Whereas the many-electron terms can be expressed as :-

$$E_2 = \sum_{i>j}^{N} < \psi_i(i)\psi_j(j)|\hat{g}_{ij}|\psi_i(i)\psi_j(j) > - \sum_{i>j}^{N} < \psi_i(i)\psi_j(j)|\hat{g}_{ij}|\psi_i(j)\psi_j(i) > \quad (3.15)$$

$$\equiv \sum_{i>j}^{N}(J_{ij} - K_{ij}) \quad (3.16)$$

such that the total energy can be written as :-

$$E = \sum_{i=1}^{N} h_i + \sum_{i>j}^{N}(J_{ij} - K_{ij}) \quad (3.17)$$

The J term represents the interaction between two charge distributions, and hence is called the *Coulomb integral* :-

$$J_{ij} = \int \frac{\psi_i(i)^*\psi_j(j)^*\psi_i(i)\psi_j(j)d\boldsymbol{r_i}d\boldsymbol{r_j}}{|\boldsymbol{r_i} - \boldsymbol{r_j}|} \quad (3.18)$$

$$\equiv \int \frac{\rho_i(i)\rho_j(j)d\boldsymbol{r_i}d\boldsymbol{r_j}}{|\boldsymbol{r_i} - \boldsymbol{r_j}|} \quad (3.19)$$

Analogously, the K represents the interaction arising from overlap of two different charge distributions and is known as the *overlap integral* :-

$$K_{ij} = \int \frac{\psi_i(i)^*\psi_j(j)^*\psi_i(j)\psi_j(i)d\boldsymbol{r_i}d\boldsymbol{r_j}}{|\boldsymbol{r_i} - \boldsymbol{r_j}|} \quad (3.20)$$

$$\equiv \int \frac{\rho_{ij}(i)\rho_{ij}(j)^*d\boldsymbol{r_i}d\boldsymbol{r_j}}{|\boldsymbol{r_i} - \boldsymbol{r_j}|} \quad (3.21)$$

These terms can be a four-centre two-electron integral and result directly from the Pauli exclusion principle.

Evaluating these integrals with an initial guess for the molecular wavefunctions, allows the calculation of the Hartree Fock energy, which, by the variational principle, is an upper bound of the lower energy. These expressions can be analytically differentiated in an

attempt to minimise the total energy :-

$$\frac{\partial E}{\partial \psi_i} = \frac{\partial E_1}{\partial \psi_i} + \frac{\partial E_2}{\partial \psi_i} = 0 \tag{3.22}$$

$$= \left[\hat{h}(i) - < \psi_i(i)|\hat{h}(i)|\psi_i(i) >\right] \psi_i(i) \tag{3.23}$$

$$+ \sum_{i \neq j} \left[\int \frac{1}{r_{ij}} \psi_j(j)^2 d\boldsymbol{r_j} - J_{ij}\right] \psi_i(i) \tag{3.24}$$

$$+ \sum_{i \neq j} \left[\left(\int \frac{1}{r_{ij}} \psi_j(j)\psi_i(j) d\boldsymbol{r_j}\right) \psi_j(j) - K_{ij}\psi_i(i)\right] \tag{3.25}$$

or by defining the Fock operators $\hat{J}$ and $\hat{K}$:-

$$\left[\hat{h}(i) + \sum_{j \neq i} (\hat{J_{ij}} - \hat{K_{ij}})\right] \psi_i = \epsilon_i \psi_i \tag{3.26}$$

Since the exchange Fock operator is a function of $\psi_i(j)$, these differential equations necessarily require an iterative solution. This is achieved by assuming a *basis set* for each orbital :-

$$\psi_i = \sum_{\mu} C_{i\mu} \chi_\mu \tag{3.27}$$

where C are orbital coefficients. An initial guess for the orbital coefficients gives a starting point for Ψ which can be then used to define the Fock operators. Equation 3.26 can then be solved to obtain new values for the orbital coefficients. This process is repeated until the coefficients are unchanged from the previous iterative cycle and a self consistent field is obtained.

The basis set representations of Equation 3.26 are called the Hartree Fock Roothaan equations[110] and can be conveniently written as :-

$$(\boldsymbol{H_i} - \boldsymbol{S_i}\epsilon_i)C_i = 0 \tag{3.28}$$

where the Fock matrix, $\boldsymbol{H}$, and the overlap matrix, $\boldsymbol{S}$ are given by :-

$$(\boldsymbol{H})_{\mu\mu'} = \left(\boldsymbol{h}_i + \sum_{j \neq i} \boldsymbol{J}_{ij} - \boldsymbol{K}_{ij} \right)_{\mu\mu'} \tag{3.29}$$

$$(\boldsymbol{S})_{\mu\mu'} = < \chi'_\mu | \chi_\mu > \tag{3.30}$$

The Fock matrix elements can be written explicitly in terms of the basis functions, for example :-

$$F_{\mu\nu} = h_{\mu\nu} + \frac{1}{2} \sum_{\omega\lambda} [< \mu\nu | \omega\lambda > - < \mu\omega | \nu\lambda >] \tag{3.31}$$

Two types of function have been used to model the atomic orbitals (Slater-type orbitals and Gaussian-type orbitals). Slater-type orbitals are of the form :-

$$\chi = N r^{n-1} e^{-\zeta r} Y_l^m(\theta, \zeta) \tag{3.32}$$

where n is the principal quantum number, $Y_l^m(\theta, \zeta)$ is a spherical harmonic function and N is a normalisation constant. whereas Gaussian functions have the form :-

$$\chi = N e^{-\zeta r^2} x^p y^q z^t \tag{3.33}$$

The Slater-type functions are known to be a better representation of the wavefunction, however their analytical integration is more complicated than for Gaussian functions. To improve the speed of the calculation, a series of Gaussian functions may be used to represent a Slater-orbital. One of the simplest basis sets is the STO-3G,[111] which represents the Slater orbitals as a contracted set of three Gaussians. The more Gaussians that are used in the basis set, the more accurate the calculation, however since the computational expense is proportional to the fourth power of the number of basis functions, the minimal basis set that gives the required accuracy is always used. For many systems, it is necessary to include a number of polarisation functions in the basis set to allow for such distortions in the electron cloud that occur during bond breaking and making processes.

For heavier atoms with large numbers of atomic orbitals, the calculation can be simpli-

fied somewhat by representing the core electrons shells by an effective core potential in which the valence electrons move. This approach is known as the *pseudopotential method* and also allows relativistic effects to be partially subsumed.

The most widely used quantum mechanical codes available today are Gaussian-92,[112] GAMESS,[113] CADPAC,[114] and TURBOMOLE[115]

3.1.2 Electron Correlation

In order to obtain accurate values for bond lengths, vibrational frequencies and many other ground state properties as well as representing the dissociation process correctly, a more rigorous treatment of electron correlation needs to be included. There are several generally used methods to include these effects : configuration interaction (CI), perturbation theory, and the coupled cluster method. The first two methods add terms due to excited states to the Hamiltonian. However, in most cases because of the high computational expense, this is limited to only terms up to the quadruplet excitation level. The introduction of correlation corrections greatly increases the computational cost of the calculations, and they now scale at least with the fifth power of the number of basis functions.

3.1.3 Semi-Empirical Techniques

There are many methods that perform the quantum-mechanical calculation using a more approximate approach. These are known as *semi-empirical methods.* For example, the effects of the core electron shells can be completely neglected and the calculation limited to the valence electrons. In addition, the Coulomb and exchange integrals can be approximated by a variety of analytical expressions, which are parameterised to reproduce some experimental quantity of interest. Common approaches are Extended Hückel theory,[116] CNDO (Complete Neglect of Differential Overlap),[117] MNDO (Minimum Neglect of Differential Overlap), AM1[118] and PM3[119] (which attempt to make MNDO more accurate). The AMPAC code[120] implements many of these different techniques within one computational environment.

3.1.4 Density Functional Theory

Density functional theory provides an alternative approach to the solution of the Schrödinger equation by viewing the energy as a functional of the electron density rather than the wavefunction. Recent developments in density functional theory as applied to chemical applications often provide an attractive alternative to Hartree-Fock methods. This technique was first shown to be useful for chemical systems by Hohenberg and Kohn.[121] The basic principle is that that the Hamiltonian is a unique functional of the electron density distribution, $\rho(r)$, which is determined by the external potential, $v(r)$. As with the Hartree-Fock method, the energy obeys the variational principle, that is the correct ground-state electron density distribution is that which minimises the total energy :-

$$\delta(E[\rho(r)] - \mu[\int \rho(r)dr - N]) = 0 \tag{3.34}$$

where μ is the Lagrange multiplier corresponding to the chemical potential and N is the number of electrons in the system.

The energy functional is made up of a number of terms similar to the Hartree-Fock energy :-

$$E_{HK}[\rho(r)] = T[\rho(r)] + V_{ne}[\rho(r)] + V_{ee}[\rho(r)] \tag{3.35}$$

where T is the kinetic energy functional, V_{ne} is the electron-nuclei Coulomb functional and V_{ee} is the electron-electron Coulomb functional. Since there are uncertainties in the values of several of these terms, the total energy is decomposed formally into three terms, a kinetic energy term ($T'[\rho(r)]$), an electrostatic and Coulomb term ($U[\rho(r)]$), and a many-body term $V_{xc}[\rho(r)]$, which contains all the exchange and correlation effects, thus :-

$$E_{HK}[\rho(r)] = T'[\rho(r)] + U[\rho(r)] + V_{xc}[\rho(r)] \tag{3.36}$$

where T' is defined in such a way to represent a system of non-interacting electrons that give the same electron density as the original system.[122] This simplification reduces the

problem to a set of N independent electron equations in the form of the one-electron Schrödinger equation, with the following Hamiltonian :-

$$H_i = -\frac{1}{2}\nabla_i^2 + V_{nuc} + \int \frac{\rho(r')dr'}{|r_i - r'|} + V_{xc} \tag{3.37}$$

where V_{nuc} is the potential due to the atomic nuclei and V_{xc} is the exchange-correlation potential. To achieve a more accurate solution from density functional theory, an improved representation of the exchange-correlation energy is required. Several approximations to this energy are available, of which the *local density approximation*[121,122] is the most common. This is most accurate for cases with fairly constant electron density such as metals and delocalised systems. The exchange correlation term is represented in an analytical form for computational convenience. In chemical applications it is necessary to make gradient corrections to the energy to reproduce the correct ground state properties of interest. Density functional theory has two main advantages over Hartree-Fock methods. Firstly, it includes the effects of electron correlation directly, and, secondly, the calculations scale as the third power of the number of basis functions. However, the choice of basis set is less important than with Hartree Fock methods, instead care must be taken to use an expression for the exchange-correlation energy that is appropriate for the system of interest. Several density functional codes are commercially available including DMol,[123] and DGauss.[124]

3.1.5 Structural Optimisation

Once the potential energy surface is known, derivatives can be calculated either analytically or numerically to obtain the forces acting on the atoms. The derivatives can be used in a further iterative loop to optimise the positions of the atoms using standard techniques (see Section 3.2.4). The second derivative matrix can also be used to obtain vibrational frequencies. This adds a further computational cost to the calculations and tends to limit the system size and richness of basis set that can be used.

3.1.6 Periodic Quantum Mechanical Calculations

The large majority of quantum mechanical calculations that are carried out on chemical systems are on discrete clusters. However, there are a number of codes, notably the Hartree-Fock program CRYSTAL,[125] that perform calculations on periodic systems such as infinite inorganic and organic solids with translational and crystallographic symmetry. The basis functions used must be specially adapted by reoptimisation of the orbital exponents for use in the crystal lattice. The computational cost of such calculations is considerably greater than for clusters, and is limited presently to high symmetry structures with a limited number of atoms in the asymmetric unit.

3.1.7 Applications to Zeolites

Quantum mechanical methods as applied to zeolites have generally focused on the treatment of small clusters that are representative of the zeolite, and the calculation of their structure and properties. The calculation of the energy and derivatives allows the minimum energy configuration of the system to be determined and properties such as vibrational spectra to be calculated. The application of quantum mechanical methods to zeolites has recently been reviewed by Sauer.[33]

The most widely used approach to form the cluster is to cut out a section of the bulk crystal and saturate the dangling bonds with hydrogens. Capping the cluster with hydrogens rather than hydroxyl groups reduces the computational expense of the calculation while retaining similar electronegativities. Calculations have been performed that consider zeolite stability,[126] zeolite acidity,[127,128] water coordination,[129] and framework substitutions.[130] Two questions are important when performing calculations on finite cluster models. Firstly, there are uncertainties due to the approximations in the quantum mechanical technique, and secondly, there are the problems caused by the incompleteness of the model.

Structural Stability

Several studies have considered the implications of the relative energetics of small zeolite clusters on the stability of the zeolite crystal structure. Kramer and co-workers[131] per-

formed quantum chemical calculations on a number of three-, four-, five- and six-ring structures, and concluded that the energies were generally very similar, with the exception of the three-ring unit. This unit is observed only very rarely in zeolite structures, lovdarite and ZSM-18 being examples. In the structure of lovdarite it is stabilised by the presence of beryllium,[132] whereas the synthesis of ZSM-18 has proven to be difficult to reproduce,[133] although recent progress has been made with a new series of templating molecules.[134]

Recent advances in periodic Hartree Fock methods and computational power have allowed calculations to be performed on a number of relatively simple zeolite crystal structures including silicalite,[135] mordenite[136] and chabazite.[137] The studies on silicalite and mordenite were single point energy calculations on the experimental geometry since the CRYSTAL code is not at present capable of calculating derivatives. The electrostatic potential was calculated using the STO-3G basis set. Although no guest molecules are included in the calculations directly, it is possible, by analysis of the electrostatic potential energy map, to postulate favourable locations for sorption. In the chabazite study, the higher quality PS-21G* was used and derivatives calculated by-hand to minimise the structure.

Acid Site Calculations

Many quantum mechanical studies have considered the structure and properties of the zeolite acid site. The calculations can predict the local geometry of the acid site, vibrational spectra, ^{1}H NMR chemical shifts and the proton affinity. The formation of the O-H bond weakens the Si-O and Al-O bonds, and, since the Al-O bond is the weakest, the Al-O bond lengthens by the largest amount. The results are very sensitive to the size of the cluster and the basis set choice. This is illustrated by a recent study of Sauer[138] on the properties of the acid site in boron-substituted zeolite. In this case, the size of cluster, the choice of how the cluster was terminated (with -OH or -H group on boron) and the basis set determines the structure of the acid site. The choice of terminating method is important in producing the correct electrostatic potential at the acid site. These effects have recently been investigated by Brand and co-workers.[139]

The silicalite system has been a popular choice for quantum mechanical investigations of the acid site. Derouane and co-workers[140] and Alvarado-Swaisgood and co-workers[141] examined this problem using clusters, although the number of tetrahedral atoms in the

system require a large number of calculations to thoroughly investigate all configurations. The problems of cluster size and termination has been investigated by several alternative approaches. One method is to embed the quantum mechanical cluster in an infinite array of point charges, which represents the electrostatic effects of the infinite crystal,[142–144] whereas perhaps a more rigorous approach is to use periodic Hartree-Fock techniques. Nicholas and Hess[145] recently performed an elegant study of the acid sites in sodalite using a periodic approach looking at cases in which there are both one and two acid sites in the same β-cage. They found considerable differences between periodic and cluster calculations on the same system.

Knowledge of the systematic errors due to the choice of basis set are often useful in rationalising structural quantities such as bond lengths and angles. For example, the STO-3G and 3-21G basis sets are known to have a large basis set superposition error. This is caused by the basis sets not being completely saturated. During a calculation each atom tends to use basis functions from other atoms to reduce the energy, which causes systematic errors. Minimal basis sets are available that have been specifically designed to reduce this error.[146]

The use of semi-empirical quantum mechanical methods, although less accurate, does allow larger clusters to be considered and the effect of cluster size to be examined more directly. Redondo and co-workers have recently performed semi-empirical calculations on the acid site in ZSM-5 using clusters of over 100 atoms, and allow up to the nth shell of atoms to relax.[147] They show encouraging agreement with previous *ab initio* calculations on the same system.[141] In addition, Gale[148] has studied the effect of cluster size on the relative acid site stability in ZSM-5 using an embedding technique.

Interactions with the Acid Site

The first step in an acid catalysed reaction is the transfer of a proton from the Brønsted acid site to the reactant molecule. Initial calculations considered the transfer of a proton between adjacent bridging hydroxyl groups.[149] The energy for proton hopping was calculated to be 42-62 kJmol^{-1}. Further calculations have also been performed which consider proton transfer to water,[129] ammonia,[150] and methanol.[151] In this last two studies, the cluster was embedded in a large array of point charges to represent long-range elec-

trostatic effects. In the study on methanol in ZSM-5 by Vetrivel and co-workers,[151] the choice of point charges for the array caused the affinity of the zeolite for protons to be greatly exaggerated, and the methanol molecule was predicted to dissociate. Indeed, a semi-empirical calculation using a larger cluster has shown that the more conventional chemistry of the methanol -OH group being protonated is more likely to be the important step.[152] In an alternative approach, Allevena and co-workers used a neutral cluster embedded in an array of point charges in which the charges were determined using an electronegativity equalisation method.[150] Teunissen and co-workers have performed one of the few periodic Hartree Fock calculations on systems of this type with a study of ammonia at the acid site in chabazite.[153]

One of the problems with considering interactions between the acid site and molecules is the correct representation of the dispersive interaction. Since this is essentially caused by intermolecular electron correlation, it is imperative to perform calculations beyond the Hartree Fock level if the dispersive term is thought to be the dominant interaction in the system. Another widely used approach is to use a semi-empirical method in which the effects of electron correlation are to some extent subsumed in the parameterisation. Despite the loss in accuracy, the use of a semi-empirical method allows larger molecules and systems to be considered. Mai and co-workers performed CNDO calculations on the interaction of a variety of aromatic molecules including toluene, xylenes, and methylnapthalenes, with a proton or metal ion in zeolites.[154] Beran and co-workers also considered the interaction between benzene and Na^+ in a six-ring[155] and found the interaction energy to be approximately 130 $kJmol^{-1}$. These studies have concluded that the interaction between an aromatic molecules and a four- or six-ring zeolite cluster is an adequate representation of the sorption complex.

Metal Clusters in Zeolites

There have also been a number of studies investigating the behaviour of metal clusters in zeolites. From the catalytic point-of-view, these kind of systems allow the possibility of using a shape-selective support in reactions that are promoted by metal surfaces. There are also possible applications in the area of quantum-dot research, where the focus is on electronic properties of the cluster. Srdanov and co-workers[156] have looked at the behaviour of

a single electron in various sodalite structures. Ursenbach and co-workers[157] have investigated the behaviour of the Na_4^{3+} cation in Na zeolite-Y using a technique based on density functional theory.

3.2 Forcefield Methods

Atomistic simulation methods attempt to represent the potential energy surface by series of empirical functions that depend on such quantities as distances between atoms, bond lengths and bond angles. They make no attempt to represent electrons in the problem explicitly, rather in most cases they reduce atoms to a single point species and calculate all energies based on this approximation.

3.2.1 Potential Energy Functions

In general, the potential energy of a system based on atoms can be expressed as a sum of two, three and many body terms :

$$E = \sum_{i,j} E_{ij} + \sum_{i,j,k} E_{ijk} + \sum_{i,j,k,l} E_{ijkl} + \ldots \tag{3.38}$$

The sum tends to be truncated at the four-body term in real applications. There are a number of standard functional forms that are commonly used to represent each of the terms in the series.

Two Body Terms

The two body term can be split into a number of different components. The first natural classification is between non-bonding, relatively long range forces, such as Coulombic interactions, and bonded interactions acting over a relatively short distance. The non-bonding term can then be subdivided into further contributions such as dispersive and Coulombic terms.

$$E_{ij} = E_{non-bonded} + E_{bonded} \tag{3.39}$$

$$= E_{dispersive} + E_{polarisation} + E_{Coulombic} + E_{bonded} \tag{3.40}$$

Dispersive contributions are due to the correlated motion of electrons on different atomic centres. This results in an instantaneous dipole being generated on each of the atoms, and it is the interactions of these dipoles, and higher order-multipoles, that gives rise to the dispersive energy. Using perturbation theory it is possible to quantify this term for the general multipole case :-

$$E_{dispersive}(r_{ij}) = \frac{1}{r_{ij}^6} \sum_{n=0} \frac{C_n}{r_{ij}^{2n}} \tag{3.41}$$

where r_{ij} is the internuclear separation, and C_n are the van der Waals coefficients. Since the strength of the instantaneous multipoles is related to the polarisability of the atoms in question, first term in the series, the *London* energy, can be written, exactly as[158] :-

$$E_{London}(r_{ij}) = \left(\frac{3\hbar}{\pi r_{ij}^6}\right) \int_0^\infty \alpha_i(i\omega)\alpha_j(i\omega)d\omega \tag{3.42}$$

where α_i and α_j are the polarisabilities of atoms i and j at imaginary frequency $i\omega$.

Several expressions for the van der Waals coefficients, C_n, have been proposed based on a variation analysis of the dispersive force,[159–161] such as the Slater-Kirkwood formula :-

$$E_{dispersive}(r_{ij}) = \frac{3}{2}\frac{e^2\sqrt{a_0}}{r_{ij}^6} \frac{\alpha_i\alpha_j}{\left(\frac{\alpha_i}{n_i}\right)^{\frac{1}{2}} + \left(\frac{\alpha_j}{n_j}\right)^{\frac{1}{2}}} \tag{3.43}$$

where e is the electronic charge, a_0 is the Bohr radius, and N_i and N_j are the number of electrons in the outer subshell of atoms i and j and the Kirkwood-Müller formula :-

$$E_{dispersive}(r_{ij}) = \frac{6mc^2}{r_{ij}^6} \frac{\alpha_i\alpha_j}{\left(\frac{\alpha_i}{\chi_i}\right) + \left(\frac{\alpha_j}{\chi_j}\right)} \tag{3.44}$$

where m is the reduced mass, c is the speed of light, and χ_i and χ_j are the diamagnetic susceptibilities of atoms i and j. Both these equations give coefficients with considerable errors. In particular, when considering an inorganic solids, the individual ionic polarisabilities are not directly measurable by experimental methods. Also there is some confusion over the choice of N in the Slater-Kirkwood expression, as whether it should refer

to the number of electrons in the valence shell, or in the atom as a whole. However, some progress has been made in the calculation of ionic crystal polarisabilities by *ab initio* quantum mechanical methods.[162] Many studies circumvent this problem by fitting the C_n coefficients to experimental data, as detailed in Section 3.2.2. In this case, it is doubtful that the fitted parameters bear any relation to the contribution of genuine dispersive effects, rather they contain a number of components including covalency.

Two functions forms are generally used to represent dispersive interactions. The first is the Lennard-Jones expression[163] :-

$$E_{ij} = \frac{A_{ij}}{r_{ij}^m} - \frac{C_6}{r_{ij}^n} \tag{3.45}$$

A number of different values for m and n have been tried, although by far the most popular is that with m=12 and n=6. The r^6 term is analogous to that in the expressions for dispersive interactions given above, whereas the r^{12} represents the repulsion felt at short distances due to the overlap of electron clouds and the Pauli exclusion principle. The value of A_{ij} is chosen to produce a minimum in the function at the correct internuclear separation, that is :-

$$\left(\frac{\partial E_{ij}}{\partial r_{ij}}\right)_{r=r_0} = -\frac{mA_{ij}}{r_0^{m+1}} + \frac{nC_6}{r_0^{n+1}} = 0 \tag{3.46}$$

$$A_{ij} = \frac{n}{m} C_6 r_0^{m-n} \tag{3.47}$$

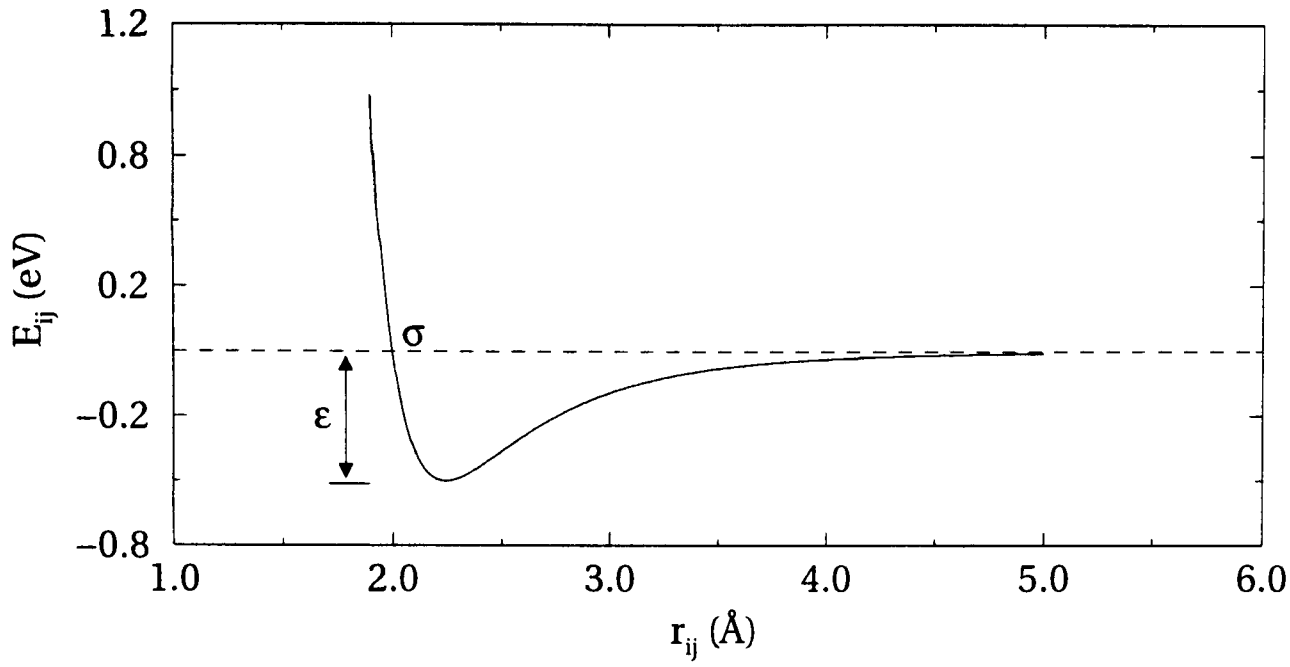
where r_0 is the required minimum, which can commonly be chosen as the sum of the van der Waals radii of the two atoms. An alternative formulation of the Lennard-Jones equation is using a distance and energy parameter :-

$$E_{ij} = 4\epsilon_{ij}\left(\left(\frac{\sigma_{ij}}{r_{ij}^{12}}\right) - \left(\frac{\sigma_{ij}}{r_{ij}^{6}}\right)\right) \tag{3.48}$$

where ϵ_{ij} is the depth of the energy well, and σ_{ij} is the value of r_{ij} when E_{ij} = 0, as illustrated in Figure 3.1. In biological applications, a Lennard-Jones(12-10) potential is often found to be a better representation of hydrogen bonding.

An alternative to the Lennard-Jones potential which is popular in the treatment of ionic

Figure 3.1: Lennard-Jones potential and parameters.



solids, is the Buckingham potential :-

$$E_{ij} = A_{ij} \exp\left(-\frac{r_{ij}}{\rho_{ij}}\right) - \frac{C_6}{r_{ij}^6} \tag{3.49}$$

The exponential repulsive term is thought to be a better representation since it has a similar form to that of the functions used in electronic wave functions. However, this potential fails at short values of r_{ij} since the repulsive term tends to a finite value, while the attractive term goes to negative infinity.

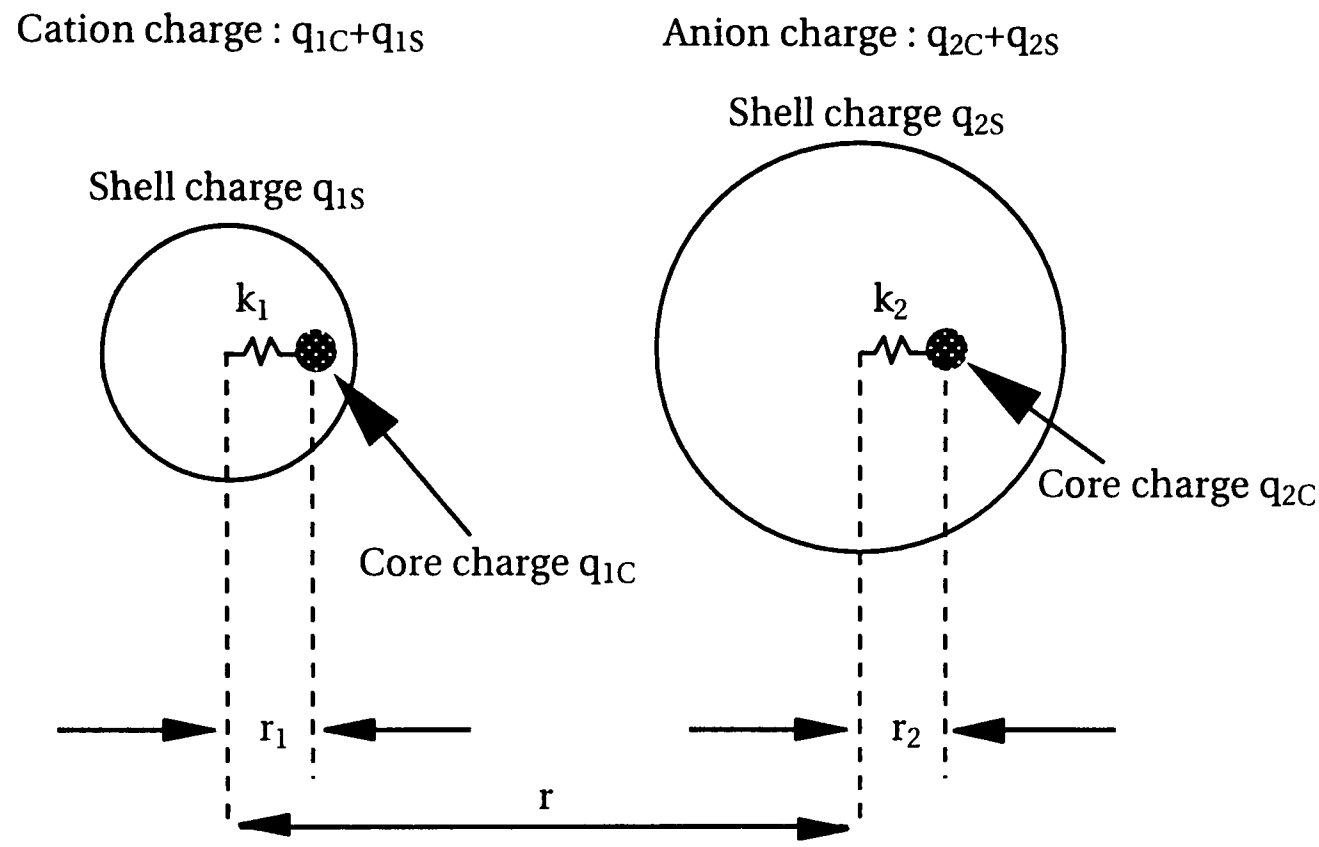
The polarisation energy is related to the induction of a dipole moment by the application of an electric field. In an ionic crystal, the electric field is generated by other species in the crystal, and is given by :-

$$E_{polarisation} = -\frac{1}{2}\sum_i \alpha_i G_i^2 \tag{3.50}$$

where α_i is the polarisability of atom i and G_i is the electric field strength at atom i due to its surroundings.

As with the various expressions for van der Waals coefficients, there is a problem in obtaining values for the polarisabilities of species in crystals. In addition, the polarisability

Figure 3.2: Schematic representation of the shell model.



will not respond to changes in the environment. As the interatomic separation decreases, a point will be reached where the rate of increase of the dipole-induced dipole energy exceeds that of the mutual polarisation energy causing the so-called polarisation catastrophe.[164]

A simple method for avoiding this problem is to use the *shell model* proposed by Dick and Overhauser,[165] which is illustrated in Figure 3.2

Each ion is composed of two parts, a core and a shell, such that the total ionic charge is the sum of the charges on the core (q_C) and shell (q_S). The mass of the ion is centred at the core, while the short-range interactions occur only through the shells. The core and shell are coupled by an harmonic spring of spring constant k_i :-

$$E_{core-shell} = \frac{1}{2} k_i r_{c-s}^2 \tag{3.51}$$

where r_{c-s} is the core-shell separation. The shell is analogous to the valence electron shell of the ion, whereas the core represents the nucleus and core-electronic states. However, since the values for the charge separation are merely variable parameters in the forcefield their magnitudes have no direct meaning. As the core-shell separation charges, the distor-

tion of the electron cloud is varied accordingly. The ionic polarisability is given by :-

$$\alpha_i = \frac{q_{iS}^2}{k_i + r_{c-s}} \tag{3.52}$$

Shell model potentials still show some inadequacies despite being able to reproduce experimental phonon dispersion curves of most materials over a wide range of wavevectors. For example, such potentials are unable to account for the Cauchy violations for FCC crystals such as MgO.[166] To circumvent this problem, Schröder has proposed the *breathing shell model,*[167] which allows for spherically symmetric distortion of the shells. This has also been extended by Sangster[168] to allow for ellipsoidal distortions which are essential to handle d^{10} ions such as Ag(I).

The calculation of the Coulomb energy is the most computationally intensive term in the energy calculation for ionic solids. The summation is simply :-

$$E_{Coulomb} = \frac{1}{2}\sum_{i}^{N}\sum_{j}^{N'}\frac{q_i q_j}{4\pi\epsilon_o r_{ij}} \tag{3.53}$$

This expression assumes that the atoms are represented as point charges, rather than charge clouds, and is only really valid when the atoms are separated by large distances. A general rule for expressions of this type is that such summations are trivially convergent only if the power of the separation is greater than the dimensionality of the system. For the dispersive interaction outlined above this is true, and the potential acts only over a relatively short range. However, this rule does not hold for the Coulombic summation, which is conditionally convergent; that is, convergence is dependent on the order in which the terms are summed, and also dependent on the charge neutrality of the system as a whole. Several methods have been proposed to group the terms in physically meaningful ways that are somewhat system dependent.[169,170] However, for the general system the most popular method to efficiently sum the Coulombic terms is due to Ewald.[171] The essence of the approach is to split up the summation into a short range and a long range component, and Fourier Transform the long range term into reciprocal space. The $1/r$ term can be represented by a Laplace transform which is then split into two ranges bounded by distance η

:-

$$\frac{1}{r} = \frac{2}{\sqrt{\pi}} \int_0^{\infty} e^{-r^2 t^2} dt \tag{3.54}$$

$$= \frac{2}{\sqrt{\pi}} \int_0^{\eta} e^{-r^2 t^2} dt + \frac{2}{\sqrt{\pi}} \int_{\eta}^{\infty} e^{-r^2 t^2} dt \tag{3.55}$$

The long range term is transformed into reciprocal space :-

$$\left(\frac{1}{r}\right)_{long} = \frac{1}{2\pi^2} \frac{8\pi^3}{NV_c} \int_{-\infty}^{\infty} \frac{1}{K^2} e^{-i\boldsymbol{K}.\boldsymbol{r}} e^{-\frac{K^2}{4\eta^2}} d\boldsymbol{K} \tag{3.56}$$

where $\boldsymbol{K}$ are reciprocal space vectors, given by :-

$$\boldsymbol{K} = 2\pi(n_1\boldsymbol{k_1} + n_2\boldsymbol{k_2} + n_3\boldsymbol{k_3}) \tag{3.57}$$

and n_1, n_2, n_3 are integers,N is the number of species in the unit cell of volume V_c . In order to calculate Equation 3.56 computationally, it can be replaced by a sum :-

$$\left(\frac{1}{r}\right)_{long} = \frac{1}{2\pi^2} \frac{8\pi^3}{NV_c} \sum_{\boldsymbol{K}} \frac{1}{K^2} e^{-i\boldsymbol{K}.\boldsymbol{r}} \; e^{-\frac{K^2}{4\eta^2}} \tag{3.58}$$

Thus the total reciprocal space energy is given by :-

$$E_{reciprocal} = \sum_{\boldsymbol{K}} A(K) \sum_i q_i \sum_j q_j \; \cos(\boldsymbol{K}.(\boldsymbol{r_i} - \boldsymbol{r_j})) \tag{3.59}$$

where $A(K)$ is pre-calculated outside the distance loops as :-

$$A(K) = \frac{2\pi}{V_c} \frac{1}{K^2} e^{-\frac{K^2}{4\eta^2}} \tag{3.60}$$

To increase computational speed, Anastasiou and Fincham reduced this expression from a triple sum to a double sum by including complex numbers[172] :-

$$E_{reciprocal} = \sum_{\boldsymbol{K}} A(K) |\sum_i q_i e^{i\boldsymbol{K}.\boldsymbol{r_i}}|^2 \tag{3.61}$$

The real space (short range) integral in the Ewald summation can be evaluated using the

complementary error function :-

$$\frac{2}{\sqrt{\pi}} \int_0^{\eta} e^{-r^2 t^2} dt = \frac{1}{r} \text{ erfc}(\eta r) \tag{3.62}$$

Thus the total Coulombic energy is given by :-

$$E_{Coulombic} = \frac{1}{2} \frac{4\pi}{NV_c} \sum_{\boldsymbol{K}} \frac{1}{K^2} e^{-\frac{K^2}{4\eta^2}} \sum_{i,l_j}^{N} \sum_{j,l_j}^{N'} q_i q_j e^{-i\boldsymbol{K}.\boldsymbol{r}_{ijl_il_j}} + \frac{1}{2} \sum_{i,l_j}^{N} \sum_{j,l_j}^{N'} q_i q_j \frac{1}{r_{ijl_il_j}} \text{ erfc}(\eta r_{ijl_il_j}) \tag{3.63}$$

with the following terms excluded :-

- The $\boldsymbol{K}$=0 term in the first summation
- The $r_{ijl_il_j}$=0 term in the second summation

The value for η, the boundary point between real and reciprocal space summations, must be chosen to give the desired accuracy in each of the summations with the least computational effort. Catlow and Norgett showed that for a given Ewald accuracy A_c (the smallest term in the summation to be included is given by A_c/r), then the cutoffs in real and reciprocal space should be[173] :-

$$r_{max} = \frac{(-\ln A_c)^{\frac{1}{2}}}{\eta_0} \tag{3.64}$$

$$K_{max} = 2\eta_0 (-\ln A_c)^{\frac{1}{2}} \tag{3.65}$$

where the optimal η value is given by :-

$$\eta_0 = \left(\frac{N\pi^3}{V^2} \right)^{\frac{1}{6}} \tag{3.66}$$

The final class of two body terms are those representing bonded interactions, of which two forms are commonly used. The first is a simple harmonic function based on the equilibrium bond length :-

$$E_{bonded}(r_{ij}) = \frac{1}{2} k_{ij} (r_{ij} - r_0)^2 \tag{3.67}$$

where k_{ij} is the force constant for the bond and r_0 is the equilibrium bond distance. Since all covalent bonds have some degree of anharmonicity, many workers add further power series terms to this expression to make the function more realistic. A Morse potential resembles the form of the experimental potential energy surface more closely, and has the general form :-

$$E_{bonded}(r_{ij}) = D_e((1 - e^{-a(r_{ij}-r_0)})^2 - 1) \tag{3.68}$$

where D_e is the depth of the potential minimum and where

$$a = \left(\frac{\mu}{2D_e}\right)^{\frac{1}{2}} \omega \tag{3.69}$$

μ is the reduced mass, and ω is the vibrational frequency. The Morse function allows for the possibility of dissociation at large internuclear separations (as $r_{ij} \rightarrow \infty$, $E \rightarrow 0$).

Three Body Terms

The most widely used three-body potential energy function is the simple harmonic bond angle potential :-

$$E_{three}(\theta_{ijk}) = \frac{1}{2} k_{ijk}(\theta_{ijk} - \theta_0)^2 \tag{3.70}$$

where k_{ijk} is the three body force constant and θ_0 is the equilibrium bond angle.

Four Body Terms

Four body terms are most extensively used to calculate the torsional energy and to model out-of-plane interactions that are needed to simulate planar molecules such as aromatic molecules. A typical function is of the form :-

$$E_{four}(\phi_{ijkl}) = k_{ijkl}(1 + s_{ijkl}\cos(n_{ijkl}\phi_{ijkl})) \tag{3.71}$$

where k_{ijkl} is the four body force constant, s_{ijkl} is the sign of the potential (either ± 1), n_{ijkl} is an integer governing the position of the minimum and ϕ_{ijkl} is the torsion angle.

3.2.2 The Fitting of Forcefield Parameters

Once the form of the potential energy functions that make up the forcefield has been determined, forcefield parameters must be obtained that reproduce experimental quantities of interest to a desired accuracy.

Empirical Fitting to Experimental Data

The most common method of determining forcefield parameters is by least-squared fitting to experimental data. The relevant experimental data that are considered tend to be structural in nature such as the positions of atoms in the asymmetric unit and cell parameters, since these are less sensitive to the form of the potential. However, if a potential is required that can reproduce dielectric and other properties that are more sensitive to derivatives of the energy it is essential to include dielectric, elastic and phonon data in the fitting process. The method tends to be limited to simple prototype structures (such as α-quartz in the case of silicates) as there are rarely reliable experimental data on more complex systems.

Theoretical Determination of Parameters

When there are little high quality experimental data available to which to empirically fit parameters, the values can be obtained directly from theoretical methods.

Although pair potentials cannot be obtained directly from full quantum mechanical calculation, they can be extracted from appropriate formulations. The most commonly used of these is the density functional treatment of the uniform electron gas. Gordon and Kim[174] expressed the energy of a closed shell ion as :-

$$E[\rho] = C_k \int [\rho(\boldsymbol{r})]^{\frac{5}{3}} d\boldsymbol{r} + C_e \int [\rho(\boldsymbol{r})]^{\frac{4}{3}} d\boldsymbol{r} - Z \int \frac{\rho(\boldsymbol{r})}{r} d\boldsymbol{r} + \tag{3.72}$$

$$+\frac{1}{2} \int \int \frac{\rho(\boldsymbol{r})\rho(\boldsymbol{r'})}{|\boldsymbol{r} - \boldsymbol{r'}|} d\boldsymbol{r} d\boldsymbol{r'} + \int \epsilon_C[\rho(\boldsymbol{r})]\rho(\boldsymbol{r}) d\boldsymbol{r}$$

where Z is the nuclear charge and where

$$C_k = \frac{3}{10}(3\pi^2)^{\frac{3}{2}} \tag{3.73}$$

$$C_e = -\frac{3}{4}\left(\frac{3}{\pi}\right)^{\frac{1}{3}} \tag{3.74}$$

The first four terms are the kinetic, exchange and Coulomb energies respectively. The last term is the electron correlation energy which is expanded as an interpolation between the low and high density limits for a homogenous electron gas. For a pair of atoms AB, the total electron density is assumed to be the superposition of the separated ion densities, so that the total energy is then given by :-

$$E_{AB} = E[\rho_{AB}] = E[\rho_A + \rho_B] \tag{3.75}$$

Thus the interaction energy is given by :-

$$V_{AB} = E[\rho_A + \rho_B] - E[\rho_A] - E[\rho_B] \tag{3.76}$$

To reduce the possibility of numerical errors, Gordon and Kim suggested a rearrangement of the terms to give the following expression for the interatomic potential :-

$$V_{AB}(R) = \frac{Z_A Z_B}{R} - Z_B \int \frac{\rho_A(\boldsymbol{r_1})}{r_{1B}} d\boldsymbol{r_1} - Z_A \int \frac{\rho_B(\boldsymbol{r_2})}{r_{2A}} d\boldsymbol{r_2} + \tag{3.77}$$

$$+ \int\int \frac{\rho_A(\boldsymbol{r_1})\rho_B(\boldsymbol{r_2})}{r_{12}} d\boldsymbol{r_1} d\boldsymbol{r_2} + \int [\rho_A(\boldsymbol{r}) + \rho_B(\boldsymbol{r})] E_G[\rho_A(\boldsymbol{r}) + \rho_B(\boldsymbol{r})] d\boldsymbol{r} -$$

$$\rho_A(d\boldsymbol{r}) E_G[\rho_A(d\boldsymbol{r})] - \rho_B(d\boldsymbol{r}) E_G[\rho_B(d\boldsymbol{r})]$$

where :-

$$E_G[\rho(d\boldsymbol{r})] = C_k[\rho(d\boldsymbol{r})]^{\frac{2}{3}} + C_e[\rho(d\boldsymbol{r})]^{\frac{1}{3}} + E_C[\rho(d\boldsymbol{r})] \tag{3.78}$$

where r, r_{1B}, r_{2A} and r_{12} are functions of the internuclear separation, R. By calculating the

energy as a function of the interatomic distance a potential energy curve is obtained that can be fitted to a potential function. Mackrodt and Stewart[175] have shown that, for ions in particular, it is important to solve the corresponding atomic Hartree-Fock equations in an external field of a strength which is equal to the Madelung potential in order to correctly represent the potential energy surface.

The most promising method for deriving interatomic potential energy functions is by using *ab initio* quantum mechanical methods. A large number of single point energy calculations are performed on a cluster possessing a number of the structural features for which the potential parameters are to be derived or on a periodic structure, by varying such internal parameters as bond lengths and bond angles. The potential parameters are then fit to the *ab initio* potential energy hypersurface. This method has an additional advantage that geometries lying far away from the equilibrium state can be explored in order to obtain a more flexible potential. It must be stressed that in order to correctly reproduce the curvature of the potential energy surface and also to obtain accurate bond lengths, post Hartree Fock methods must be used wherever possible. This method has recently been used to derive potentials for silicates,[176,177] alumina,[178] and aluminophosphates.[179]

Once a forcefield has been derived that can reproduce the experimental quantities of interest to the desired accuracy, a number of different types of calculation can be considered.[180] Analytical derivatives can trivially be calculated and structural optimisation of the structures performed. Since the computational cost of atomistic simulations is much less than for quantum mechanical calculations, much larger systems can be considered with or without periodicity included.

3.2.3 Perfect Lattice Energy Minimisation

The simplest calculation that can be performed is the determination of the equilibrium crystal structure of a material with respect to the atomic and crystal structure parameters. Using the terminology of Born and Huang,[181] the lattice energy for a system of s atoms per unit cell, U_l, can be written as a Taylor series expansion that is second order in the total

strain :-

$$U_L(\boldsymbol{R'}) = U_L(\boldsymbol{R}) + \boldsymbol{g}^{\boldsymbol{T}}.\boldsymbol{\delta} + \boldsymbol{\delta}^{\boldsymbol{T}}.\boldsymbol{W}.\boldsymbol{\delta} + O(\delta^3) \tag{3.79}$$

where δ is a generalised (3s+6)-dimensional strain vector consisting of 3s internal components, $\delta\boldsymbol{r}$ and 6 bulk components, $\delta\boldsymbol{\epsilon}$, thus :-

$$\boldsymbol{\delta} = [\delta\boldsymbol{r}, \delta\boldsymbol{\epsilon}] \tag{3.80}$$

$\boldsymbol{g}$ is a vector of first derivatives of the energy :-

$$\boldsymbol{g} = \begin{pmatrix} \dfrac{\partial U_L}{\partial \boldsymbol{r}} \\ \dfrac{\partial U_L}{\partial \boldsymbol{\epsilon}} \end{pmatrix} \tag{3.81}$$

and $\boldsymbol{W}$ is the corresponding matrix of second derivatives :-

$$\boldsymbol{W} = \begin{pmatrix} \dfrac{\partial^2 U_L}{\partial \boldsymbol{r}\partial \boldsymbol{r}} & \dfrac{\partial^2 U_L}{\partial \boldsymbol{r}\partial \boldsymbol{\epsilon}} \\ \dfrac{\partial^2 U_L}{\partial \boldsymbol{\epsilon}\partial \boldsymbol{r}} & \dfrac{\partial^2 U_L}{\partial \boldsymbol{\epsilon}\partial \boldsymbol{\epsilon}} \end{pmatrix} \tag{3.82}$$

Higher terms in the energy expansion are neglected. The configuration, $\boldsymbol{R'} \equiv \boldsymbol{r'_s}$, is related to $\boldsymbol{R}$ by the transformation :-

$$\boldsymbol{r'_s} = \Delta\epsilon.(\boldsymbol{r_s} + \delta\boldsymbol{r_s}) \tag{3.83}$$

in which $\Delta\epsilon$ is the strain matrix formed from the components of the strain tensor :-

$$\Delta\epsilon = \begin{pmatrix} \delta\epsilon_1 & \frac{1}{2}\delta\epsilon_6 & \frac{1}{2}\delta\epsilon_5 \\ \frac{1}{2}\delta\epsilon_6 & \delta\epsilon_2 & \frac{1}{2}\delta\epsilon_4 \\ \frac{1}{2}\delta\epsilon_5 & \frac{1}{2}\delta\epsilon_4 & \delta\epsilon_3 \end{pmatrix} \tag{3.84}$$

The minimisation protocol can either minimise all degrees of freedom (constant pressure), or neglect the bulk lattice strain terms and keep the cell fixed (constant volume).

If U_L is a perfect harmonic function, the displacements required to reach the energy minimum are given by :-

$$\boldsymbol{\delta} = -\boldsymbol{W}^{-1}.\boldsymbol{g} \tag{3.85}$$

Since in most cases this is not true, this equation does produce a configuration that is closer to the minimum provided that $\boldsymbol{W}$ is positive definite. By repeating this procedure iteratively, the final minimum can be reached in a number of steps. The strain derivatives of the energy can be derived assuming that the potential functions are dependent on the square of the separation in which case it can be written :-

$$\boldsymbol{r}' = (\boldsymbol{I} + \boldsymbol{\epsilon}).\boldsymbol{r} \tag{3.86}$$

where $\boldsymbol{I}$ is the unit matrix and $\boldsymbol{\epsilon}$ is the symmetric strain tensor formed from $\{\epsilon_i\}$ analogous to Equation 3.84. Expanding Equation 3.79 in the second derivative matrix :-

$$U_L(\boldsymbol{R}) = U_L(\boldsymbol{R_0}) + \frac{1}{2}\delta\boldsymbol{r}^T.\boldsymbol{W}_{rr}.\delta\boldsymbol{r} + \delta\boldsymbol{\epsilon}.\boldsymbol{W}_{\epsilon r}.\delta\boldsymbol{r} + \frac{1}{2}\delta\boldsymbol{\epsilon}^T.\boldsymbol{W}_{\epsilon\epsilon}.\delta\boldsymbol{\epsilon} \tag{3.87}$$

where :-

$$\boldsymbol{W}_{rr} = \frac{\partial^2 U_L}{\partial r \partial r} \tag{3.88}$$

$$\boldsymbol{W}_{\epsilon r} = \frac{\partial^2 U_L}{\partial \epsilon \partial r} \tag{3.89}$$

$$\boldsymbol{W}_{\epsilon\epsilon} = \frac{\partial^2 U_L}{\partial \epsilon \partial \epsilon} \tag{3.90}$$

From the equilibrium condition :-

$$\frac{\partial U_L}{\partial \delta \boldsymbol{r}} = 0 \tag{3.91}$$

Hence :-

$$\delta \boldsymbol{r} = -(\boldsymbol{W}_{rr}^{-1}\boldsymbol{W}_{\epsilon r}\delta\epsilon) \tag{3.92}$$

So the lattice energy can be expressed as :-

$$U_L(\boldsymbol{R}) = U_L(\boldsymbol{R_0}) + \frac{1}{2}\delta\epsilon^T(\boldsymbol{W}_{\epsilon\epsilon} - \boldsymbol{W}_{\epsilon r}\boldsymbol{W}_{rr}^{-1}\boldsymbol{W}_{r\epsilon})\delta\boldsymbol{\epsilon} \tag{3.93}$$

and the second derivatives or elastic constants become :-

$$\boldsymbol{C} = (\boldsymbol{W}_{\epsilon\epsilon} - \boldsymbol{W}_{\epsilon r}\boldsymbol{W}_{rr}^{T}\boldsymbol{W}_{r\epsilon})/V_c \tag{3.94}$$

where V_c is the cell volume. Once the elastic constants have been determined, the strain can be calculated from Hooke's Law :-

$$\boldsymbol{\epsilon}_j = \boldsymbol{P}_j.\boldsymbol{C}^{-1} \tag{3.95}$$

where $\boldsymbol{P}_j$ is the sum of the static pressure and the applied hydrostatic pressure. The static pressure, $\boldsymbol{P_{Sj}}$, is given by :-

$$\boldsymbol{P_{Sj}} = \frac{dU_L}{d\boldsymbol{r}}.\frac{dr^2}{d\epsilon_j}.\frac{d\boldsymbol{r}}{dr^2} \tag{3.96}$$

Given the strain, it can be substituted into Equation 3.86 to yield new coordinates and cell dimensions. Thus, the minimisation procedure consists of firstly removing the strains on the atoms in the unit cell, and then reducing the bulk lattice strains on the cell.

3.2.4 Minimisation Methods

Several methods of function optimisation are particularly suited to lattice energy minimisation. The function to be minimised, $F(x)$, can be expanded using a Taylor series as :-

$$F(\boldsymbol{x}) = F(\boldsymbol{x}') + \boldsymbol{g}^T.\boldsymbol{\delta} + \frac{1}{2}\boldsymbol{\delta}^T.\boldsymbol{H}.\boldsymbol{\delta} \tag{3.97}$$

where :-

$$\boldsymbol{\delta} = \boldsymbol{x} - \boldsymbol{x}' \tag{3.98}$$

$$\boldsymbol{g} = \frac{\partial F(\boldsymbol{x})}{\partial \boldsymbol{x}} \tag{3.99}$$

$$\boldsymbol{H} = \frac{\partial^2 F(\boldsymbol{x})}{\partial \boldsymbol{x} \partial \boldsymbol{x}} \tag{3.100}$$

Thus the required minimum is given by :-

$$\boldsymbol{\delta} = -\boldsymbol{H}^{-1}.\boldsymbol{g} \tag{3.101}$$

The repeated application of this equation is necessary for convergence. The computational bottleneck in this problem is the inversion of the Hessian matrix, $\boldsymbol{H}$. The inversion process is an $O(n^3)$ problem, which can be quite expensive for systems of the size of most zeolite unit cells. However, several alternative approaches (*variable metric methods*) have been suggested, which are all based on replacing Equation 3.101 by an expression of the form :-

$$\boldsymbol{\delta} = -\lambda \boldsymbol{G}.\boldsymbol{g} \tag{3.102}$$

where $\boldsymbol{G}$ is an approximation to the inverse Hessian matrix and λ is a linear parameter. $\boldsymbol{G}$ is typically initialised with either the exact inverse Hessian or simply the unit matrix, and is then updated with one of several formulae such as Davidon-Fletcher-Powell,[182] Davidon[183] and Broyden-Fletcher-Shanno-Goldfarb[184,185] rather than calculating the inverse directly.

To ensure quadratic convergence a search to determine λ_k is required each cycle. A new set of positions may then be obtained from this approximate Hessian and the iterative cycle repeated until convergence is obtained. Variable metric methods represent the most efficient methods for obtaining the minimum energy in lattice energy calculations; however, a further problem still remains for large systems. Since the Hessian is a symmetric $3N$ x $3N$ matrix, where N is the number of atoms in the problem, storage becomes a problem. Assuming that each atom is a FORTRAN double precision number, then for faujasite,

whose unit cell has 576 atoms, storing the Hessian would require about 12 Megabytes of memory. In such cases, the somewhat simpler though slower *conjugate gradient methods* are used because they only require storage of the first derivatives. The most common algorithm is that of Fletcher and Reeves[186] in which the following update is used :-

$$\boldsymbol{x}_{i+1} = \boldsymbol{x}_i + \alpha_i \boldsymbol{S}_i \tag{3.103}$$

where $\boldsymbol{S}$ is the search vector. It is initialised as the direction of steepest descent and then updated accordingly to the following expressions :-

$$\boldsymbol{S}_n = -\boldsymbol{g}_n + \frac{\boldsymbol{g}_n^T \cdot \boldsymbol{g}_n}{\boldsymbol{g}_{n-1}^T \cdot \boldsymbol{g}_n \cdot \boldsymbol{S}_{n-1}} \tag{3.104}$$

3.2.5 Defect Lattice Energy Minimisation

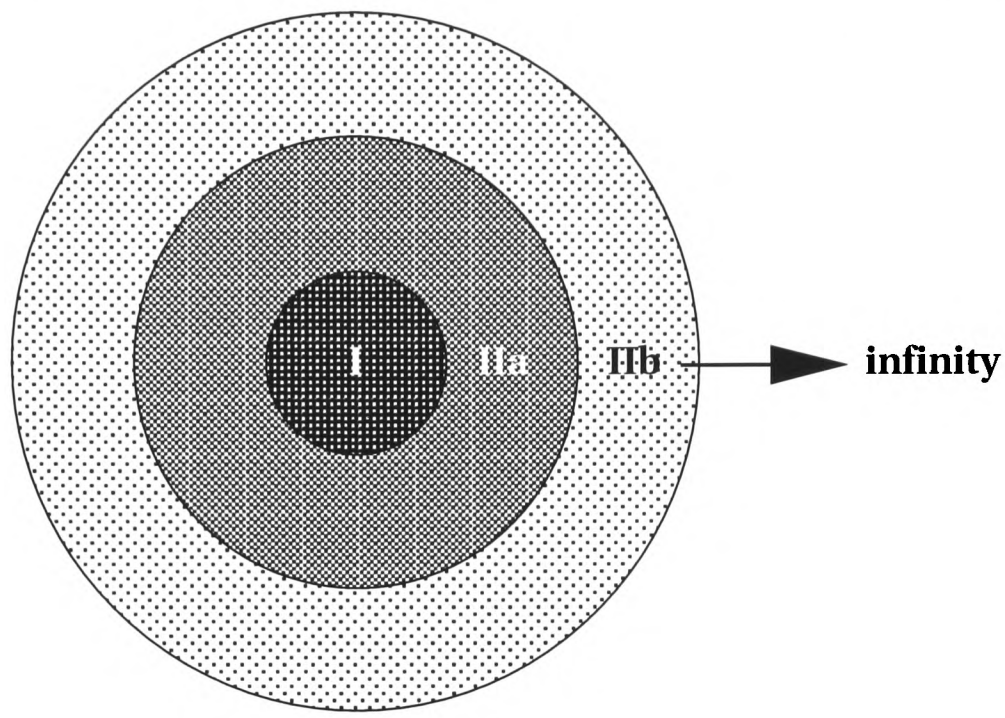
All ionic solids possess defects as part of their structures. The defects may be present in the classical sense as Frenkel or Schottky defects as occur in stoichiometric compounds, or by substitution of one ion for another at a lattice site. The most convenient method for treating a defective lattice is due to Mott and Littleton[187] and is based on the assumption that the total energy of the system is minimised by a relaxation of the ions surrounding the defect. The extent of this relaxation decreases fairly rapidly at distances beyond the defective region. This assumption is implemented in a computational manner by dividing the structure into two regions as shown in Figure 3.3.

In region I the ions are treated explicitly and allow to relax, whereas in region II the displacements of the ions are assumed to be small enough to treated by the harmonic approximation. The total energy is then given by :-

$$E = E_1(\boldsymbol{r}_1) + E_{12}(\boldsymbol{r}_1, \boldsymbol{\zeta}_2) + E_2(\boldsymbol{\zeta}_2) \tag{3.105}$$

where E_1 is the energy of region I, E_{12} is the interaction energy between regions I and II, and E_2 is the energy of region II. r_1 is a vector describing the coordinates of atoms in region I, while ζ_2 represents the displacements in region II. The energy of region II is defined to

Figure 3.3: Schematic representation of the defect calculation method.



be a quadratic function of ζ_2 :-

$$E_2(\zeta_2) = \frac{1}{2}\zeta_2^T.\boldsymbol{A}.\zeta_2 \tag{3.106}$$

The equilibrium condition can be written as :-

$$\frac{\partial E}{\partial \zeta_2} = \frac{\partial E_{12}(\boldsymbol{r}_1, \zeta_2^0)}{\partial \zeta_2} + \boldsymbol{A}.\zeta_2^0 = 0 \tag{3.107}$$

where ζ_2^0 are the equilibrium values of ζ_2. The total energy can then be written as :-

$$E = E_1(\boldsymbol{r}_1) + E_{12}(\boldsymbol{r}_1, \zeta_2) - \frac{1}{2}\left(\frac{\partial E_{12}}{\partial \zeta_2}\right).\zeta_2^0 \tag{3.108}$$

E_1 and E_{12} are evaluated by the techniques as in the case of the non-defective lattice with the region I sites being relaxed.

In the case of charged defects, region II is divided further. Region IIa contains harmonically unrelaxed ions as before, whereas region IIb is replaced by a dielectric continuum. An additional term is added to the energy expression to represent the polarisation energy of the charged defect in the dielectric continuum. This is given by :-

$$E_{polarisation} = -\frac{q^2}{2R}\left(1 - \frac{1}{\epsilon_0}\right) \tag{3.109}$$

where q is the charge of the defect, R is the radius of the spherical cavity surrounding the defect, and ϵ_0 is the dielectric constant. The polarisation of the continuum is given by :-

$$P = \frac{1}{4\pi}\left(1 - \frac{1}{\epsilon_0}\right)\frac{q}{R^2} \tag{3.110}$$

Although this expression only allows for the electrostatic relaxation of the continuum it is a good approximation if the spherical region is large.

3.2.6 Free Energy Minimisation

The previous sections have outlined methods for minimisation of the total internal energy. The method for calculating the free energy is based on the lattice dynamical method of Born and Huang[181] with the assumption that the vibrational motions in a solid can be treated as a set of independent harmonic oscillators whose frequencies vary with cell volume. The aim is to calculate the vibrational frequencies, and thus add a term representing the phonon pressure to the total pressure in Equation 3.95. The structure is then minimised as before.

Using a shell model, the potential energy can be expanded with respect to displacements :-

$$U_L(\boldsymbol{r'}) - U_L(\boldsymbol{r}) = \frac{1}{2}(\boldsymbol{W_{uu}}.\boldsymbol{u}.\boldsymbol{u} + \boldsymbol{W_{uw}}.\boldsymbol{u}.\boldsymbol{w} + \boldsymbol{W_{wu}}.\boldsymbol{w}.\boldsymbol{u} + \boldsymbol{W_{ww}}.\boldsymbol{w}.\boldsymbol{w}) \tag{3.111}$$

where $\boldsymbol{W_{uu}}$ is the second derivative matrix between cores, $\boldsymbol{W_{uw}}$ between core and shell, and $\boldsymbol{W_{ww}}$ between shell and shell.

The displacements can be expressed in terms of the vibrational frequencies using the periodic nature of the crystal :-

$$\boldsymbol{u} = \boldsymbol{u_0}\exp(i(\boldsymbol{q}.\boldsymbol{r} - \omega t)) \tag{3.112}$$

$$\boldsymbol{w} = \boldsymbol{w_0}\exp(i(\boldsymbol{q}.\boldsymbol{r} - \omega t)) \tag{3.113}$$

where q is the wavevector. The second derivative matrices can similarly be expressed in

terms of the wavevector, which gives the following equations of motion :-

$$\omega^2 \boldsymbol{m}.\boldsymbol{u} = \boldsymbol{R}.\boldsymbol{u} + \boldsymbol{T}.\boldsymbol{w} \tag{3.114}$$

$$\text{and } 0 = \boldsymbol{T}.\boldsymbol{u} + \boldsymbol{S}.\boldsymbol{w} \tag{3.115}$$

where $\boldsymbol{R}$ is the matrix for core-core terms, $\boldsymbol{S}$ for shell-shell and $\boldsymbol{T}$ for core-shell, and m is a diagonal matrix of core masses. By substitution, the expressions can be reduced to the eigenvector problem :-

$$\omega^2 \boldsymbol{n} = \boldsymbol{D}.\boldsymbol{n} \tag{3.116}$$

where the dynamical matrix $\boldsymbol{D}$ is given by :-

$$\boldsymbol{D} = \boldsymbol{m}.(\boldsymbol{R} - \boldsymbol{T}.\boldsymbol{S}^{-1}.\boldsymbol{T}).\boldsymbol{u} \tag{3.117}$$

$$\text{and } \boldsymbol{u} = \boldsymbol{m}.\boldsymbol{n} \tag{3.118}$$

The phonon frequencies can be obtained by diagonalising the dynamical matrix. Since the frequencies are dependent on the wavevector, it is necessary to calculate the phonon spectrum over all possible wavevectors. This problem is to some extent alleviated by determining only those frequencies on a three dimensional mesh of point within the Brillouin zone. The thermodynamic properties are found to converge rapidly above 50K with the size of the mesh. Once the phonon spectrum has been calculated the thermodynamic properties can be evaluated such as the kinetic pressure (allowing minimisation to be performed) and the entropy :-

$$S = k \sum_{i}^{3N} \left(-\ln(1 - \exp(\frac{-h\omega_i}{kT})) + \frac{h\omega_i}{kT} \left(\exp(\frac{h\omega_i}{kT}) - 1 \right)^{-1} \right) \tag{3.119}$$

Free-energy minimisation has been successfully applied to the study of several classes of materials including structures encountered in the Earth's crust[188] and high-temperature superconductors.[189]

3.2.7 Statistical Mechanical Approaches

Statistical mechanics provides a link between many of the microscopic properties provided by a computer simulation and the macroscopic properties that are obtained by an experimental measurement. Each experimentally measured quantity can be thought of as a time average taken over a long time interval. More formally for a macroscopic property, A :-

$$A_{obs} = \langle A \rangle_{time} = \langle A(\Gamma(t)) \rangle_{time} = \lim_{t_{obs} \to \infty} \frac{1}{t_{obs}} \int_0^{t_{obs}} A(\Gamma(t)) dt \tag{3.120}$$

where Γ represents the $6N$ dimensional phase space ($3N$ positional variables and $3N$ momenta) of a system with N atoms. In practice the integration is replaced by a sum which has a sufficient number of terms to make the average statistically meaningful :-

$$A_{obs} = \langle A \rangle_{time} = \frac{1}{\tau_{obs}} \sum_{\tau=1}^{\tau_{obs}} A(\Gamma(\tau)) \tag{3.121}$$

where τ is an index running over the succession of steps taken through time. Care must be taken to sample a sufficient region of phase space to yield satisfactory time averages, however many studies have shown that thermodynamically consistent properties which compare well with experimental values can be obtained by using this approximation. As will be seen in later sections, a classical molecular dynamics simulation allows the calculation of such averages by propagating a system through time by the solution of Newton's equations of motion. However, it can be shown that alternative algorithms for generating a series of states in phase space, for example, Monte Carlo simulation, can also produce useful averages. In this case, the average is one over states within an *ensemble* (that is a collection of points in phase space) :-

$$A_{obs} = \langle A \rangle_{ens} = \frac{1}{\tau_{obs}} \sum_{\tau=1}^{\tau_{obs}} A(\Gamma(\tau)) \tag{3.122}$$

The choice of ensemble essentially provides constraints on the generation of configurations in phase space and is governed by the thermodynamic variable that is of interest in the simulation. Four ensembles are commonly used : the microcanonical ensemble (constant-*NVE*), the canonical ensemble (constant-*NVT*), the isothermic-isobaric ensem-

ble (constant-*NPT*) and the grand canonical ensemble (constant-μVT). In each case, the specified thermodynamic quantities are fixed while others can be determined by ensemble averaging. In general, instantaneous values of the non-constrained thermodynamic quantities will fluctuate around their average values. This can be quantified by the calculation of the statistical variance of the quantity :-

$$\sigma^2(A) = \langle \delta A^2 \rangle_{ens} = \langle A^2 \rangle_{ens} - \langle A \rangle_{ens}^2 \tag{3.123}$$

where :-

$$\delta A = A - \langle A \rangle_{ens} \tag{3.124}$$

Apart from providing a measure of the width of the distribution about the average, variances can also be related to useful thermodynamical quantities such as the heat capacity at constant volume, C_v, which is given by :-

$$C_v = \frac{1}{kT^2} \langle \delta H^2 \rangle_{NVT} \tag{3.125}$$

where H represents the enthalpy in the canonical ensemble.

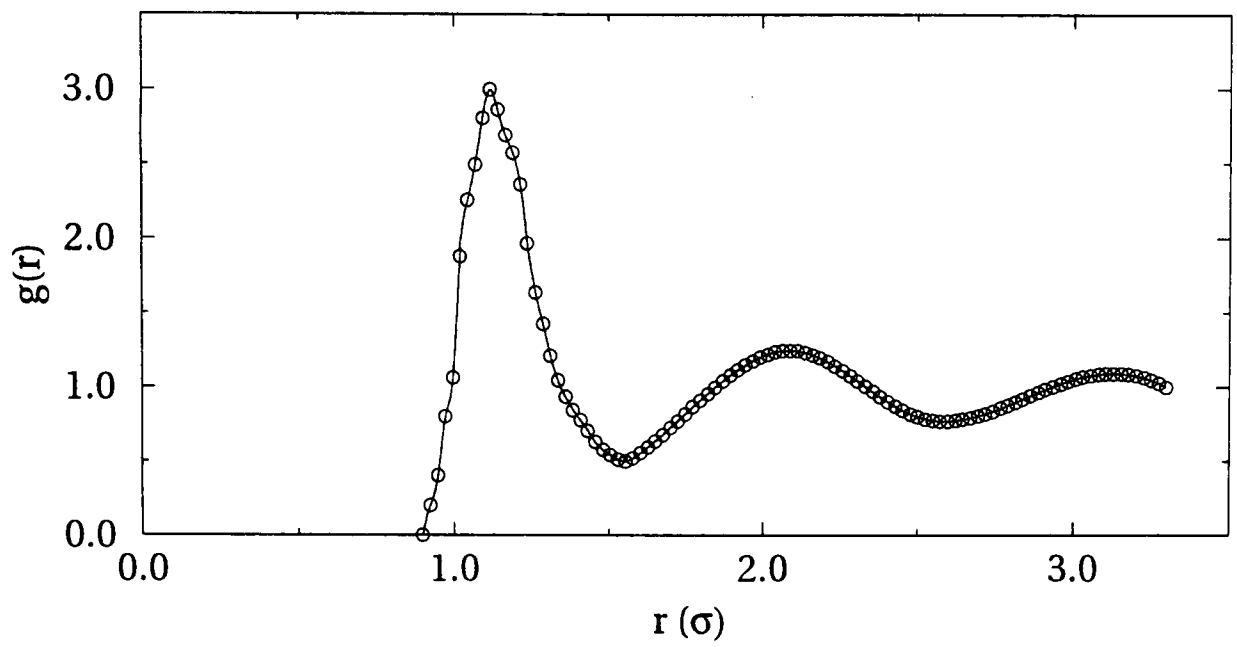
The structure of a system can be investigated by the calculation of distribution functions, such as the pairwise distribution function, $g(r)$. This function gives the probability of finding a pair of atoms at a distance r apart. A typical distribution for a liquid is shown in Figure 3.4. This clearly shows the short-range order associated with the liquid state.

Time correlation functions can also yield useful quantities. The non-normalised correlation function between two different quantities A and B is defined by :-

$$C_{AB}(t) = \langle \delta A(t) \delta B(0) \rangle_{ens} = \langle \delta A(\Gamma(t)) \delta B(\Gamma(0)) \rangle_{ens} \tag{3.126}$$

For the A=B case, the function is called an auto-correlation function and its time integral (from t=0 to t=∞) is the correlation time t_A. The time integrals can often be related directly to macroscopic properties of the system and their Fourier transforms can often be related to experimental spectra. For example, the diffusion coefficient, D, is given (in three

Figure 3.4: Typical pairwise distribution function for a liquid



dimensions) by the time integral of the velocity autocorrelation function :-

$$D = \frac{1}{3}\int_0^\infty \langle \boldsymbol{v}_i(t).\boldsymbol{v}_i(0)\rangle dt \tag{3.127}$$

where $\boldsymbol{v}_i(t)$ is the centre of mass velocity of a single molecule. There is also a related expression which is valid at long times :-

$$2tD = \frac{1}{3}\langle |\boldsymbol{r}_i(t) - \boldsymbol{r}_i(0)|^2\rangle \tag{3.128}$$

where $\boldsymbol{r}_i(t)$ is the molecular position.

3.2.8 Molecular Dynamics

The simplest method of generating a trajectory through phase space is to solve the classical equations of motion. The problem in its most fundamental form for a system of N particles interacting via a potential V is the Lagrangian equation of motion :-

$$\frac{d}{dt}\left(\frac{\partial L}{\partial \dot{q}_k}\right) - \left(\frac{\partial L}{\partial q_k}\right) = 0 \tag{3.129}$$

where the Lagrangian functions $L(\boldsymbol{q}, \dot{\boldsymbol{q}})$ are defined in terms of kinetic and potential energy as follows :-

$$L = K - V \tag{3.130}$$

where H is the Hamiltonian for the system. Moving from generalised coordinates, q_k, and their time derivatives, $\dot{q}_k$, to the Cartesian frame, equation 3.129 becomes the more familiar expression of Newton's second Law of motion :-

$$m_i \ddot{\boldsymbol{r}}_i = \boldsymbol{f}_i \tag{3.131}$$

where m_i is the mass of atom i and $\boldsymbol{f}_i$ is the derivative of the potential energy :-

$$\boldsymbol{f}_i = \nabla_{r_i} L = -\nabla_{r_i} V \tag{3.132}$$

The Hamiltonian is formally written as :-

$$H(\boldsymbol{p}, \boldsymbol{q}) = \sum_k \dot{q}_k p_k - L(\boldsymbol{q}, \dot{\boldsymbol{q}}) \tag{3.133}$$

where p is the momentum. The problem can be reduced to either the solution of a system of $3N$ second-order differential equations (Equation 3.131) or an equivalent set of $6N$ first-order differential equations :-

$$\dot{\boldsymbol{r}}_i = \frac{\boldsymbol{p}_i}{m_i} \tag{3.134}$$

$$\dot{\boldsymbol{p}}_i = -\nabla_{r_i} V = \boldsymbol{f}_i \tag{3.135}$$

The standard numerical techniques that are commonly used to solve these equations are based on finite difference methods. The general principle is that given a set of positions and velocities at some time t, the equivalent set of quantities can be obtained at some later time $t + \delta t$ to a desired accuracy. The value of the time-step, δt, is chosen to be shorter than the time period of the fastest fundamental process in the system and to give an appropriate degree of energy conservation. There are several methods that are commonly used.

One possible method is the *predictor-corrector* algorithm. The first step in this method is to *predict* quantities at some future time $t + \delta t$ based on a Taylor expansion about time t, for example :-

$$\boldsymbol{r}^p = \boldsymbol{r}(t) + \dot{\boldsymbol{r}}(t)\delta t + \frac{1}{2}\ddot{\boldsymbol{r}}(t)\delta t^2 + \ldots \tag{3.136}$$

$$\dot{\boldsymbol{r}}^p = \dot{\boldsymbol{r}}(t) + \ddot{\boldsymbol{r}}(t)\delta t + \ldots \tag{3.137}$$

The additional equations can be written containing terms depending on higher derivatives if desired. Since the above equations do not contain the equations of motion (that is, the values of the forces on the atoms from the forcefield), these approximate quantities need to be *corrected* with a further step. The correction factor can be calculated based on the forces acting on the system at positions $\boldsymbol{r}^p$, and obtain the accelerations, $\ddot{\boldsymbol{r}}^c(t + \delta t)$:-

$$\Delta\ddot{\boldsymbol{r}}(t + \delta t) = \ddot{\boldsymbol{r}}^c(t + \delta t) - \ddot{\boldsymbol{r}}^p(t + \delta t) \tag{3.138}$$

The correction factor can then be use to adjust the remaining variables :-

$$\boldsymbol{r}^c(t + \delta t) = \boldsymbol{r}^p(t + \delta t) + c_0\Delta\ddot{\boldsymbol{r}}(t + \delta t) \tag{3.139}$$

$$\dot{\boldsymbol{r}}^c(t + \delta t) = \dot{\boldsymbol{r}}^p(t + \delta t) + c_0\Delta\ddot{\boldsymbol{r}}(t + \delta t) \tag{3.140}$$

To achieve the desired accuracy and numerical stability, optimal values for c_0 have been suggested.[190,191]

The most widely used algorithm is the Verlet algorithm[192] which is generally attributed to Störmer.[191] This proceeds via a direct solution of the second order equations. The positions are advanced by the expression :-

$$\boldsymbol{r}(t + \delta t) = 2\boldsymbol{r}(t) - \boldsymbol{r}(t - \delta t) + \delta t^2\ddot{\boldsymbol{r}}(t) \tag{3.141}$$

The velocities have been eliminated by the combination of the following expressions :-

$$\boldsymbol{r}(t + \delta t) = \boldsymbol{r}(t) + \dot{\boldsymbol{r}}(t)\delta t + \frac{1}{2}\ddot{\boldsymbol{r}}(t)\delta t^2 \tag{3.142}$$

$$\boldsymbol{r}(t - \delta t) = \boldsymbol{r}(t) - \dot{\boldsymbol{r}}(t)\delta t + \frac{1}{2}\ddot{\boldsymbol{r}}(t)\delta t^2 \tag{3.143}$$

The velocities can be obtained from the following expression :-

$$\dot{\boldsymbol{r}}(t) = \frac{\boldsymbol{r}(t+\delta t) - \boldsymbol{r}(t-\delta t)}{2\delta t} \tag{3.144}$$

This algorithm has the advantage over the predictor-corrector method in that it advances the positions in one step rather than requiring two stages. It is also correctly centred about t making it time-reversible. The Verlet algorithm requires $9N$ words of storage : two sets of coordinates at times t and $t - \delta t$, plus the accelerations. The algorithm has been shown to have excellent energy conserving properties even with large time-steps. For example, in the case of liquid argon, r.m.s. fluctuations that are only 0.01% of the average energy are observed with a time-step of 10fs; these fluctuations increase to 0.2% for a time-step of 40fs.[193,194]

The basic algorithm is problematic in that the velocities at the current time step are not calculated directly. This is an important consideration if the temperature is being constrained in some manner as in the *NVT*-ensemble. To alleviate this problem, a extension to the Verlet method, the *velocity-Verlet* algorithm, has been proposed.[195] This takes the form :-

$$\boldsymbol{r}(t+\delta t) = \boldsymbol{r}(t) + \dot{\boldsymbol{r}}(t)\delta t + \frac{1}{2}\ddot{\boldsymbol{r}}\delta t^2 \tag{3.145}$$

$$\dot{\boldsymbol{r}}(t+\delta t) = \dot{\boldsymbol{r}}(t) + \frac{1}{2}\delta t(\ddot{\boldsymbol{r}}(t) + \ddot{\boldsymbol{r}}(t+\delta t)) \tag{3.146}$$

The velocities are updated in two steps that correspond to the two terms in the last equation. After the coordinates have been updated and the first velocity update is made, the forces and accelerations at time $t + \delta t$ are computed before the last velocity move is made.

In order to perform molecular dynamics calculations on polyatomic molecules, two approaches can be used. Historically, the method of choice was to represent the molecules as rigid bodies with all bond lengths and bond angles fixed. The rationale being that since bond vibrations are relatively fast compared to translational motion, the small time step that would be required to simulate them would not allow sufficient simulation time to be sampled in order to accumulate significant statistical averages. One method involving *quaternions* introducing extra equations of motion for quantities depending on the Eu-

ler angles, as well as for the centres of mass coordinates. A much simpler approach is to use the method of *constraint dynamics* which effectively adds an additional term to Equation 3.131 that constrains bond lengths and angles to their desired values. The RATTLE method[196] uses this approach and is also compatible with the velocity Verlet algorithm. For a pair of atoms i and j constrained to remain a fixed distance apart d_{ij}, the following can be defined :-

$$\sigma_{ij}(\{\boldsymbol{r}(t)\}) \equiv [\boldsymbol{r}_i(t) - \boldsymbol{r}_j(t)]^2 - d_{ij}^2 \tag{3.147}$$

The constraint can be expressed as :-

$$\sigma_{ij}(\{\boldsymbol{r}(t)\}) = 0 \tag{3.148}$$

Additional constraints on the velocities can be derived by differentiation of Equation 3.147 :-

$$[\dot{\boldsymbol{r}}_i(t) - \dot{\boldsymbol{r}}_j(t)].[\boldsymbol{r}_i(t) - \boldsymbol{r}_j(t)] = 0 \tag{3.149}$$

The equations for constrained dynamics are :-

$$m_i\ddot{\boldsymbol{r}}_i = \boldsymbol{f}_i + \boldsymbol{g}_i \tag{3.150}$$

where $\boldsymbol{g}_i$ is the force on atom i due to the constraints. This can be written as :-

$$\boldsymbol{g}_i = -\sum_j{}' \lambda_{ij}(t)\nabla_i\sigma_{ij} \tag{3.151}$$

where the prime denotes a sum over only those atom pairs that are involved in bond constraints with atom i and λ_{ij} are time-dependent Lagrange multipliers determined by the intramolecular forces of the constraints. The lambda values are determined iteratively each time step using the method of Ryckaert and co-workers.[197] However, in recent times, the increase in computer power has allowed bond vibrations to be handled directly by the use of appropriate potential energy functions.

The simplest molecular dynamics calculations operate in the *NVE*-ensemble, allowing the inherent energy conservation properties of the Lagrangian equations and the integration algorithm to conserve the energy. However, most experimental measurements are made under conditions of constant temperature, so simulation in the *NVT*-ensemble is often more appropriate as well as allowing the possibility of investigating the temperature dependent properties of a system. The current temperature of a system can be written as :-

$$T_c = \frac{1}{(3N - N_c)k} \sum_{i=1}^{N} \frac{|\boldsymbol{p}_i|^2}{m_i} \tag{3.152}$$

where N is the number of particles in the systems, N_c is the number of constraints on the system, k is the Boltzmann constant and $\boldsymbol{p}$ the momentum. There are many methods available to constrain the temperature to a constant value.[198] Many of the methods are based on the rescaling of the velocity at each time step. For example, the method of Berendsen and co-workers[199] uses a scaling factor of the form :-

$$\chi = \left(1 + \frac{\delta t}{t_T}\left(\frac{T}{T_c} - 1\right)\right)^{\frac{1}{2}} \tag{3.153}$$

where T_c is the current kinetic temperature and t_T is preset time constant. The rate at which the desired temperature is attained is determined by the time constant.

Simulations can also be performed at constant pressure. The pressure during the simulation is calculated using the *virial theorem of generalised equipartition* :-

$$\langle q_k \frac{\partial H}{\partial q_k} \rangle = kT \tag{3.154}$$

where q_k is the generalised coordinate and H is the Hamiltonian. Using a Cartesian frame and Newton's equations of motion this becomes :-

$$-\sum_{i}^{N} \boldsymbol{r}_i . \boldsymbol{f}_i^{tot} = 3NkT \tag{3.155}$$

where $\boldsymbol{f}_i^{tot}$ represents the sum of intermolecular and external forces. This force can be split

into the interatomic forces, $\boldsymbol{f}_i$, and external forces, $\boldsymbol{f}^{ext}$. The external forces are related to the pressure, P, exerted on the container walls of the system :-

$$\frac{1}{3}\langle\sum_{i}^{N}\boldsymbol{r}_i.\boldsymbol{f}_i^{ext}\rangle = -PV \tag{3.156}$$

If W is defined as the internal virial :-

$$W = \frac{1}{3}\sum_{i}^{N}\boldsymbol{r}_i.\boldsymbol{f}_i \tag{3.157}$$

then Equation 3.155 becomes :-

$$PV = NkT + \langle W\rangle \tag{3.158}$$

Berendsen and co-workers[199] have suggested a method for performing constant pressure MD simulations by coupling to a pressure bath. An extra term is added to the equations of motion to produce a pressure change subject to :-

$$\frac{dP_c}{dt} = \frac{(P - P_c)}{t_p} \tag{3.159}$$

where P_c is the current pressure, P is the desired pressure, and t_p is a time constant. At each step, the unit cell vectors and particle coordinates are scaled by a factor χ :-

$$\chi = 1 - \beta_T\frac{\delta t}{t_p}(P - P_c) \tag{3.160}$$

where β_T is the isothermal compressibility, although this factor is often included in the time constant. This method allows the volume of the simulation cell to change but not its shape. However, Parrinello and Rahman[200] have suggested a method to achieve this allowing phase transitions to be studied by molecular dynamics.

With regards the practical application of molecular dynamics algorithms, the system is initialised in some realistic starting configuration, and velocities are assigned to the particles to reproduce a given temperature using a Maxwell-Boltzmann distribution. The system is allowed to equilibrate for a period, after which configurational averages are accu-

mulated to calculate the thermodynamic quantities of interest. The equilibration of the system can be assessed by monitoring the instantaneous values of the potential energy and the pressure during this period. Equilibration should be continued until all systematic drift in these quantities is eliminated, and oscillation is observed about their mean values.

3.2.9 Monte Carlo Simulation

As with molecular dynamics, Monte Carlo methods aim to generate a trajectory in phase space which samples from a chosen ensemble. The rules regarding the propagation of the system are based on random numbers, hence the term 'Monte Carlo'. In order to generate the next point in the trajectory trial moves are made such that the generated states form what is known as a *Markov chain*, which has the following properties :-

- The outcome of each trial belongs to a finite set of outcomes $\{\Gamma_1, \Gamma_2, \ldots, \Gamma_m, \Gamma_n, \ldots\}$, called the state space.
- The outcome of each trial depends only on the outcome of the trail that immediately precedes it.

The most widely used method to propagate the system is that due to Metropolis and co-workers.[201] State n is generated from state m by picking a random atom and giving it a uniform random displacement along each of the coordinate directions. The energy is calculated with the system in its new state and the energy difference for the move, δV_{mn}, determined. If the move is downhill in energy ($\delta V_{mn} \leq 0$) then the new configuration is accepted as the next point in the trajectory. Whereas if the move is uphill in energy ($\delta V_{mn} > 0$) then the move is accepted with a probability equal to the Boltzmann factor of the energy difference :-

$$\frac{\rho_n}{\rho_m} = \exp(-\frac{\delta V_{mn}}{kT}) \tag{3.161}$$

where ρ_n and ρ_m are the probabilities of the two states. To implement this in a computational environment, a random number between zero and one is obtained each Monte Carlo cycle and its value compared to the Boltzmann probability to determine whether to accept a move which would lead to a higher energy state.

The ensemble average of any quantity, A, is given :-

$$\langle A \rangle_{NVT} = \frac{\int A \exp(-\beta V) d\boldsymbol{r}}{\int \exp(-\beta V) d\boldsymbol{r}} \tag{3.162}$$

$$\approx \frac{\sum_{\tau=1}^{\tau_{max}} A(\tau) \exp(-\beta V(\tau))}{\sum_{\tau=1}^{\tau_{max}} \exp(-\beta V(\tau))} \tag{3.163}$$

where $\beta = 1/kT$. The denominator is the *configurational integral* for the *NVT*-ensemble.

The most common ensemble for Monte Carlo summation is the *NVT*-ensemble; however, a number of other useful ensembles can also be considered. Wood first presented a method for carrying out a simulation in the *NPT*-ensemble.[202] Another useful ensemble for Monte Carlo calculations is the grand canonical ensemble. The simulation is carried out at constant chemical potential, volume and temperature. In this case, ensemble averages are given by :-

$$\langle A \rangle_{\mu VT} = \frac{\sum_{N=0}^{\infty} (N!)^{-1} V^N z^N \int A(\boldsymbol{s}) \exp(-\beta V(\boldsymbol{s})) d\boldsymbol{s}}{Q_{\mu VT}} \tag{3.164}$$

where z for spherical molecules is given by :-

$$z = \left(\frac{2\pi m k T}{h^2} \right)^{\frac{3}{2}} \exp(\beta \mu) \tag{3.165}$$

and $Q_{\mu VT}$ is the grand canonical partition function :-

$$Q_{\mu VT} = \sum_{N} \frac{1}{N!} \frac{1}{h^{3N}} \exp(\mu \beta N) \int \exp(-\beta V(\boldsymbol{s})) d\boldsymbol{s} \tag{3.166}$$

In addition to the Metropolis Monte Carlo move, two additional moves are now possible :-

- a molecule is destroyed
- a molecule is created at a random position in the fluid

To satisfy the condition of microscopic reversibility, the probability of choosing a creation or destruction step is made the same. A useful implementation of the Grand Canonical Monte Carlo (GCMC) method was proposed by Adams.[203,204] In this approach, the chemical potential is split into two terms : an ideal gas term and an excess term :-

$$\mu = \mu^{ex} + \mu^{id} \tag{3.167}$$

$$= (\mu^{ex} + kT \ln\langle N\rangle_{\mu VT}) + kT \ln \frac{1}{V}\left(\frac{2\pi mkT}{h^2}\right)^{\frac{3}{2}} \tag{3.168}$$

$$= kTB + kT \ln \frac{1}{V}\left(\frac{2\pi mkT}{h^2}\right)^{\frac{3}{2}} \tag{3.169}$$

The simulation is carried out at constant B, V and T. Using this scheme, the decisions for creation and destruction are respectively :-

$$\text{create if} \quad \exp \quad (B - \beta\delta V_{mn}) - N \geq \zeta \tag{3.170}$$

$$\text{destroy if} \quad \exp \quad (\beta\delta V_{mn} - B) + (N+1) \geq \zeta \tag{3.171}$$

where ζ is a random number between zero and unity.

As with MD simulations, a period of equilibration is necessary to stabilise the system at some new state after beginning the simulation before averages are accumulated.

3.2.10 Applications to Zeolites

Using the methods outlined in Section 3.2.2, forcefields have been derived for a wide range of solid state materials including silicates,[176,177,205–209] aluminophosphates,[179,210] aluminosilicates,[211] ionic oxides[212] and alkali halides.[213] Bush and co-workers have recently demonstrated an interesting extension to the empirical fitting method by performing simultaneous empirical fits to a large number of different materials containing common structural elements.[214] This ensures that the parameters obtained are optimised for a wide range of different structures. Many of the parameter sets can be usefully combined to allow heteroatom substituted zeolites to be investigated.

Structural Studies

The simplest calculation that can be performed is the investigation of structural effects using lattice energy minimisation. The sophistication of interatomic potentials is sufficient to investigate many subtle structural effects. For example, the monoclinic distortion of silicalite from the room-temperature orthorhombic form has been reproduced by Bell and co-workers.[215] The stacking faults in zeolite-β have been investigated by Tomlinson and co-workers,[216] who found that there is very little thermodynamic difference in energy between the two polymorphs allowing intergrowths between the two structures to occur quite easily. The use of a lattice energy minimisation in conjunction with diffraction techniques can often aid the structure solution of unknown materials. Shannon and co-workers used a computational approach to solve the structure of zeolite NU-87,[217] and recently the structure of MAPO-36 was determined in a similar fashion.[218] In addition to the structures themselves, energy minimisation can also aid in the refinement of sorbate positions as was elegantly demonstrated by Kaszkur and co-workers for dibromobutane in zeolite-Y.[219] The structure of the mesoporous MCM-41 family of porous materials has also been recently simulated using a simple model, which correlates well with experiment.[220] Advances have also been made in the field of crystal structure prediction. Deem and Newsam have demonstrated a method based on simulated annealing that is able to suggest possible zeolite crystal structures based on the limited structural information that is often available from a powder diffraction pattern.[221]

Sorption

The simplest experimentally interesting calculation that can be performed is the determination of the most favourable binding sites for sorption in a zeolite. In early work this was carried out by manually moving the sorbate of interest through the zeolite,[53] though this approach has largely been superseded by energy minimisation methods. One of the limitations of this method is that the final sorbed geometry is strongly dependent on the starting configuration of the system. Also, due to the complicated nature of the potential energy surface, local minima are a significant problem. One technique of dealing with this problem is the docking protocol first demonstrated for zeolites by Freeman and co-workers.[222]

Using this approach, high-temperature dynamics are initially performed on the sorbate to generate a series of thermally accessible configurations. The zeolite-sorbate potential energy surface is then probed by inserting the sorbate into the zeolite at random locations. For configurations that are deemed to have favourable interaction energies according to a predefined criterion, the sorbate position is energy minimised. In this manner, a number of minimised sorbate binding sites are generated, which can then be analysed to determined preferred binding sites. This method has been applied by a number of groups to study the effects of zeolite-template interactions. Santilli and co-workers have used this method to investigate the effect of *inverse shape selectivity*[223] and concluded that the selectivity of a hydrocracking reaction can be related to the binding energies of the various products in the zeolite pores. Cox and co-workers[224] have also extended the docking approach to assess the importance of template-template interactions on the binding energy.

An important consideration when comparing sorption energies obtained from energy minimisation calculations with experimental quantities is that they represent values at zero Kelvin. Although it is possible to introduce the effects of temperature into the minimisation using the techniques outlined in Section 3.2.6, a much easier and less computationally costly approach is to use Monte Carlo or molecular dynamics.

Several Monte Carlo studies have been made to investigate the behaviour of xenon in zeolites using standard NVT ensemble Metropolis methods.[225,226] The heat of sorption as a function of temperature can be calculated using this method, in addition to the sorbate siting preferences. In order to extend this approach to more complicated sorbates, the internal degrees of freedom of the sorbed molecule must also be varied by the Monte Carlo algorithm. This greatly increases the amount of computational time needed both for equilibration and to accumulate meaningful averages. June and co-workers studied the sorptive properties of linear alkanes in silicalite and found that the molecules locate preferentially at the channel intersections.[227] Recently, Smith and Sippman have developed a configurational bias methodology for zeolites that greatly improves the efficiency of such simulations for chain molecules.[228]

The method of Grand Canonical Monte Carlo simulations allows the sorption calculation to be performed at a constant pressure, and, by running simulations at several pressures, a sorption isotherm can be calculated. Woods and Rowlinson used this technique to

study the sorption of xenon in faujasite[229]whereas two more recent studies have looked at the behaviour of Xe in NaA.[230,231] Cracknell and Gubbins have also investigated the sorption of Ar in the aluminophosphates $AlPO_4$-5, $AlPO_4$-8 and VPI-5.[232]

Molecular Dynamics

In addition to allowing the calculation of distribution functions and heats of sorption, molecular dynamics offer the additional advantage of access to the transport properties of the system. MD simulations tend to be more computationally costly than Monte Carlo calculations since they require the derivative of the energy to advance the system through time. Early MD studies in zeolites focused on the study of simple sorbates such as xenon.[233,234] For example, Pickett and co-workers examined the diffusion of xenon in silicalite with the zeolite lattice held rigid.[233] This is a particularly interesting sorbate since self-diffusivities can now be measured routinely with ^{129}Xe pulsed-field gradient NMR[235] and directly compared with values obtained from the simulations. Yashonath and Santikary have also recently looked at the effect of varying both the size of a spherical sorbate and its interaction strength with the zeolite on the mechanism of diffusion in zeolite-Y and zeolite-A.[236] They found a strong correlation between the sorbate diameter and the rate of intercage diffusion. There have also been several studies which considered molecules of more catalytic interest such as small hydrocarbons[237–241] and benzene.[89,242] Demontis and co-workers have made an extensive study of methane in silicalite and have also looked at the effect of adding zeolite lattice dynamics into the model on the transport behaviour. They conclude that allowing the lattice to flex not only affects the mobility of the sorbate but also more subtle properties such as the distribution and clustering of the sorbate in the pore structure.

There are, however, cases in which the application of molecular dynamics can be impractical, because the simulation is unable to sample sufficient time to obtain statistically meaningful results. This is particularly apparent for systems in which the diffusivities of interest are less than $10^{-10}m^2s^{-1}$.[238] Indeed, June and co-workers have estimated that to study a slow moving molecule such as *n*-hexane in silicalite by MD simulation a simulation run of at least 300ns would have to be performed which would require approximately 4000 CPU hours on a large-scale supercomputer.[243] In addition, the inclusion of lattice

dynamics can often cause similar problems due the small time steps required to correctly handle lattice vibrations in the numerical integration of Newton's equations of motion.

Several methods have been demonstrated to probe the diffusion of molecules through zeolites that occurs too slowly for conventional MD methods. The general principles combine techniques in reaction rate theory with conventional forcefield methods. The docking protocol detailed above can be used to probe the zeolite pores for favourable binding sites and then postulate diffusion as occurring via a series of hopping events. By performing a series of energy minimisations along the hopping path, the transition state and thus the activation energy for the hop can be identified. June and co-workers used a transition-state theory approach similar to this to calculate rate constants for the hopping processes and thus diffusion coefficients for the diffusion of Xe and SF_6 in silicalite.[243] An alternative to using transition state theory is to calculate the rate constants directly from the activation energy making realistic estimates for the pre-exponential factor from the reaction rate expression :-

$$\nu = \nu_0 \exp\left(-\frac{E_a}{kT}\right) \tag{3.172}$$

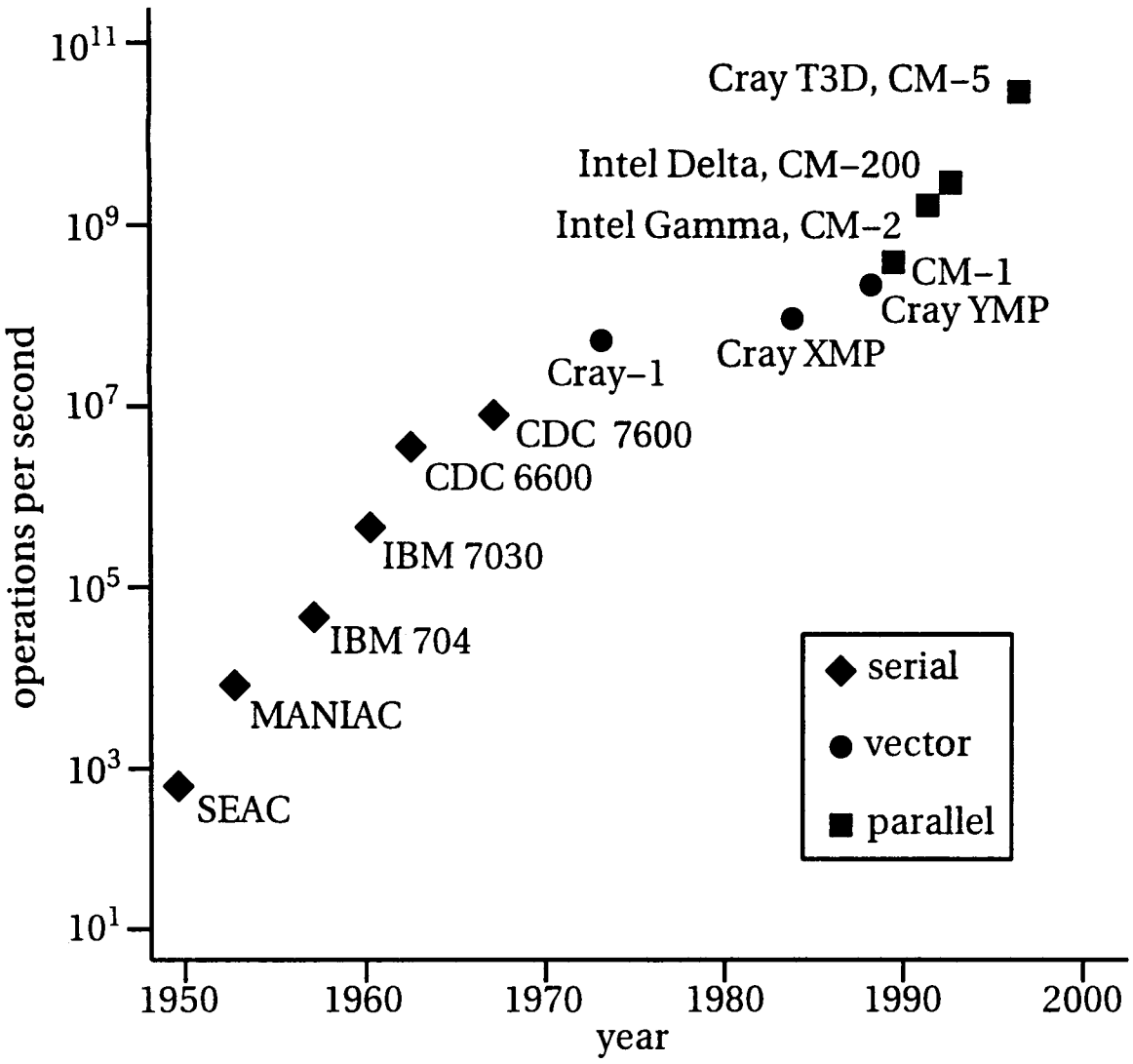
where ν is the reaction rate, ν_0 is the pre-factor, E_a is the activation energy, k is the Boltzmann constant, and T is the temperature. The rate constants can then be used in a *kinetic* Monte Carlo simulation. The most widely used algorithm is based on the Metropolis method. For each kinetic Monte Carlo step an attempted hop is either rejected or accepted based on Arrhenius Boltzmann statistics. A system clock can be updated based on the shortest time scale process in the system. Standard analysis techniques can be applied to determine the diffusion coefficient.

3.3 Computational Hardware Development

Large scale computational hardware development has always been a critical technology in scientific research. The power of available computer hardware has vastly increased since the first silicon chip was fabricated in the late 1950s, and is still increasingly rapidly today.[244] Figure 3.5 shows the development of computer hardware as a function of time.

The construction of the first general purpose digital computer, MANIAC I, under the direc-

Figure 3.5: The growth of computing power. All computers up to the Cray-1 were single processor machines.



tion of Metropolis was located at Los Alamos in 1952 as part of the ongoing nuclear defense program. This was quickly surpassed by MANIAC II, which allowed floating point operations to be performed at a peak rate of 10kflops (1 flop = 1 floating point operation per second). The development of the Very Large Scale Integration (VLSI) method in the early 1980s allowed up to 100000 transistors to be placed on a single silicon chip, vastly reducing the cost of producing microprocessors and causing an explosion in the development of the personal computer industry. In addition, the introduction of vector supercomputers, which allowed the execution of many instructions concurrently on linear data arrays, further pushed forward the boundaries of computer design. The Cray-1, which had a maximum speed of 10 Mflops, was the first successful vector supercomputer and an online memory capacity of 4Mb. Further developments in computer chip design and the introduction of Reduced Instruction Scalable Computing chips have allowed computers with the power of the Cray-1 to become accessible in the desktop workstation environment.

Table 3.1: Performance benchmark ratings in megaflops.

machine	clock speed (MHz)	N=100	N=1000	peak
CRAY C90	238.1	387	902	952
CRAY Y-MP/832	166.7	161	324	333
IBM RS/6000-R24	71.5	142	246	284
SGI POWER CHALLENGE	75.2	101	260	300
CONVEX C4/XA-1	135.0	99	705	810
IBM ES/9000-711 VF	111.1	86	422	563
DEC 7000-710	274.7	53	208	275
DEC 10000-610 Alpha AXP	200	43	155	200
HP 9000/735	99	41	120	198
IBM RISC Sys/6000-580	62.5	38	104	125
HP 9000/715	70	29		
Sun Sparc 20	90	29		
SGI Onyx (R4400)	151.5	26	48.4	75
DEC VAX 9000 410VP	62.5	22	89	125
SGI Indigo2 (R4000)	100	15		
IBM POWERPC 250	66	13		
Gateway 2000 P5-90	90	11		
Apple Power Macintosh 6100/60		9.6		
SGI 4D/25	33	4.3		
SGI Indigo (R3000)	33	4.0		
Gateway 2000 66 80486-DX2	66	2.4		
Compaq Deskpro 486/33l-120 w/487	33	1.4		
IBM-486	33	0.94		
microVAX 3200/3500/3600		0.41		
Apple Macintosh IIsi		0.19		

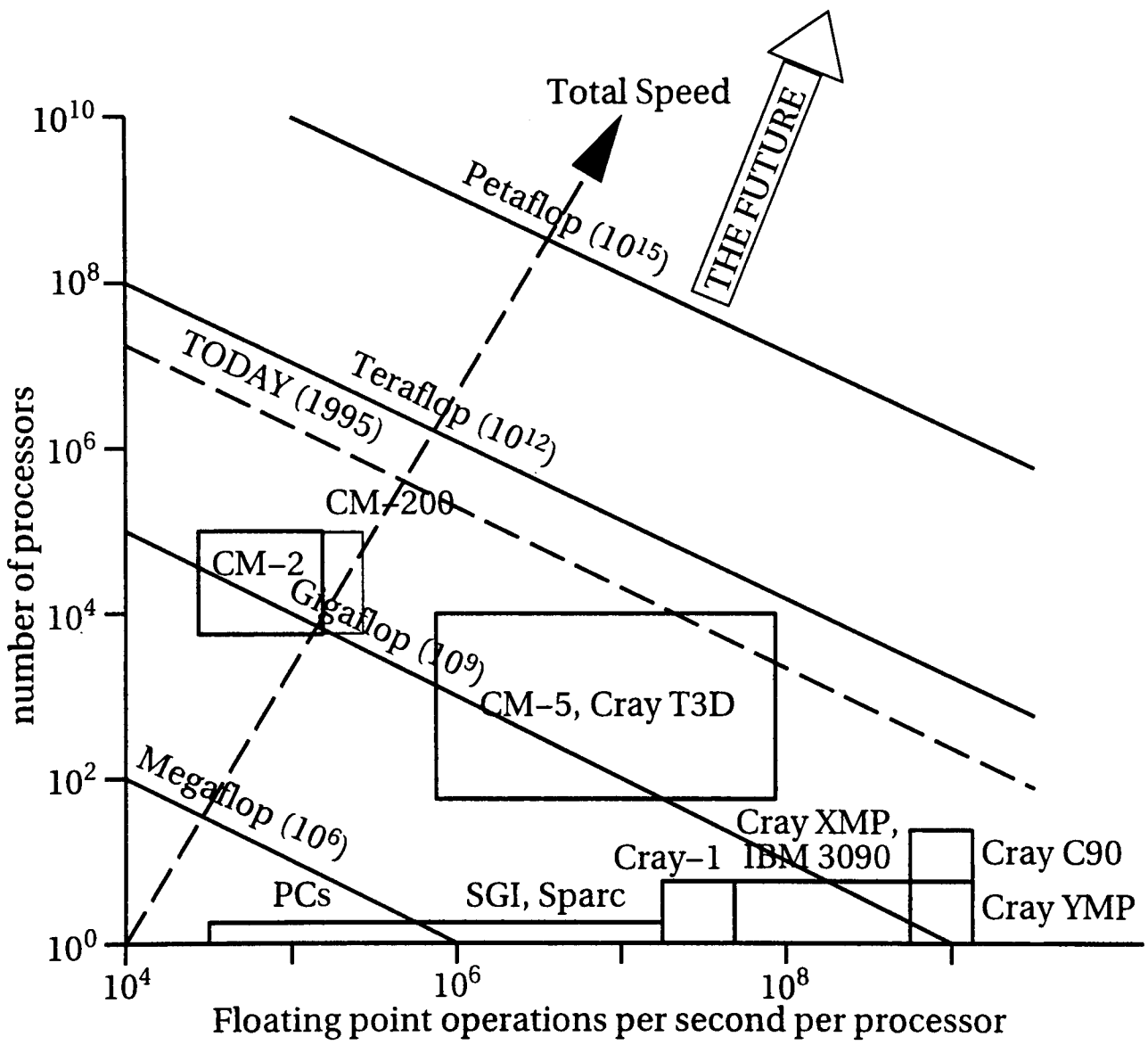
Performance based on LINPAC benchmark for matrices of size N
Peaks values reported by manufacturer

For example, Silicon Graphics' Power Challenge series delivers a maximum performance of 300 Mflops. Performance ratings for a number of commonly available machines are shown in Table 3.1. Undoubtedly the most important computer hardware development in the last decade has been the introduction of massively parallel architectures. These machines consist of large numbers of independent identical processors, or nodes, which can perform calculations in parallel. Early machines were based on the SIMD paradigm (Single Instruction/Multiple Data) and carried out the same instruction on multiple processors simultaneously, although this has been largely superceded by the MIMD approach (Multiple Instruction/Multiple Data). To fully utilise this technology, software algorithms must be redesigned with the interconnectivity of the nodes in mind. The CM-5 (Connection Machines 5) located at Los Alamos consists of 1024 processors each of roughly the performance of a Sun SPARCstation. It has a maximum theoretical performance of 131 Gflops. Large scale molecular dynamics calculations have been performed on up to 38 million Lennard-Jones particles which have realised 40% of the CM-5's power.[245] The bottleneck in computational terms for a machine of this type often becomes the communications between the various nodes rather than the processor speed itself. The speeds of workstations, vector supercomputers and massively parallel supercomputers are compared by plotting the number of processors versus the speed per processor in Figure 3.6.

The PVM (Parallel Virtual Machine)[246] software allows a heterogeneous environment of networked workstations to act as a parallel machine by load-sharing between the various nodes. This is an inferior method compared to a truly massively parallel architecture since the communications are further retarded by the speed of a standard Ethernet connection, although impressive performance can be obtained. This can be further enhanced by using a fast network connection such as HIPPI (High Performance Parallel Interface).[247]

The parallel development of computer architecture and algorithmic performance allows the computational scientist to treat larger and more complicated systems with a greater degree of sophistication. Advances in compiler design can to some extent allow this to occur transparently to the user, although to fully exploit the parallel architectures some degree of software redesign must take place.

Figure 3.6: Supercomputers of today and tomorrow. The solid diagonal lines represent lines of constant total speed. Supercomputer manufacturers are hoping to make parallel machines with teraflop speeds available in the next few years.



Chapter Four

Computer Simulation of Silica Polymorphs

Silica polymorphs represent the simplest structural analogues for zeolite structures and as such provide a useful starting point for computational investigations. The development of a transferable forcefield for silica structures is an important first step in the representation of more complex zeolite structures containing heteroatoms, cations and acid sites. Recent advances in synthetic methods have allowed the preparation of purely siliceous zeolite samples, either in single-crystal or powder form. This has enabled high quality structure determinations to be made on several all-silica structures.[31,248,249] In addition, recent thermochemical studies on a series of silica polymorphs have provided an insight into relative thermodynamic stabilities of these structures.[250] In this chapter, the structures of a wide range of silicas, both zeolitic and condensed phases, are investigated using lattice-energy minimisation techniques. The relative accuracy of a number of different forcefields based both on ionic and covalent models is assessed. A comparison is made with experimental thermochemical data. Phonon spectra are calculated for a number of structures and are used to investigate the validity of the space -group choice in the calculations. The minimised energies of structures in different space groups is compared to investigate this technique as a predictive tool for space-group choice in an experimental structure solution.

4.1 Computational Methods and Forcefields

Several forcefields have been developed to study silica structures. They can be divided into two main groups: ionic based models and covalent based models.

In the ionic model, the main component of the forcefield is a electrostatic one acting between point charges. This interaction is augmented by a repulsive term, commonly of Buckingham form, and an additional attractive dispersive term is often included. Sanders

and co-workers[205] fitted a shell-model potential based on formal charges to the structure and properties of α-quartz. In this work, a term was included to represent the bond angle about silicon correctly. In addition, Vessal[251] has used a similar approach to obtain a rigid-ion partial-charge model. A number of ionic model forcefields that have been fitted to quantum-mechanically derived *ab initio* potential energy surfaces are available. Purton and co-workers[177] have fitted a formal-charge shell model to a potential energy surface obtained from local density functional calculations on silicate clusters. Tsuneyuki and co-workers performed calculations on SiO_4^{4-} tetrahedra embedded in a point-charge array to derive an ion-pair potential.[252,253] Kramer and co-workers fitted a partial-charge rigid-ion model to a combination of calculations on H_4TO_4 molecules (T=Si and Al) and experimental data on α-quartz.[206] Recently, de Boer and co-workers[176] have derived a partial-charge shell model for silica using a similar approach. Several approaches have been developed to simulate silica glass structures have also been used to study zeolitic silica structures. The potential of Vessal and co-workers[209] has been used to study the diffusion of hydrocarbons in silicalite.[254] Also, the potential developed for vitreous silica by Feuston and Garofalini[255] has been used to study the structure of the MCM-41 system.[220]

One of the important distinctions of these forcefields is the choice of formal or partial charges. Historically, Born model potentials tend to be based on the ionic model and as such used formal charges. However, since very few inorganic solids are purely ionic, there is normally some degree of covalency in the system, which manifests itself as an electronic polarisation. This can, to some extent, be corrected by the inclusion of the shell model. *Ab initio* quantum mechanical calculations on both small silicate clusters[33] and periodic solids[135] have shown the true charges to be much lower than the formal values. However, the use of formal charges does allow the potentials to be used to study the effects of heteroatom substitution and the incorporation of extra-framework cations with no ambiguity in the assignment of charges. As a consequence of the fitting method, little significance can be applied to the individual components of the energy using the formal charge approach; for example, the Madelung energy effectively represents an upper limit of the electrostatic contribution to the total energy. However, this is not important if only the differences in the total energy are required. This question will be addressed further with regard to host-guest interactions in zeolites in Chapter 7.

The second approach is to derive a forcefield based on more conventional molecular mechanics functions, such as bond-length and bond-angle potentials. Nicholas and co-workers[208] fitted a potential energy surface determined by *ab initio* methods to a functional form consisting of bond stretching terms, bond angle terms, dihedral terms, electrostatic terms and dispersive terms. de Vos Burchart used a similar functional form to investigate the structures of many siliceous zeolite structures.[207] Hill and Sauer[256] performed high level *ab initio* calculations on silica clusters ranging from two to six silicon atoms in size, and fitted a forcefield to the complicated *cff91* form developed by Biosym.[257,258]

Several of the above forcefields have been chosen in this study and a summary of their potential parameters is given in Table 4.1. All lattice-energy minimisations were performed at constant pressure with the experimental crystal symmetry applied as an additional constraint. The Discover code[259] was used for the forcefields of Hill and Vessal and the GULP software (General Utility Lattice Program) written by Gale[260] was used for all other calculations. The calculations were performed on an SGI Challenge XL with dual R4400 processors.

4.2 Structural Models

A wide range of silica structures were considered, including those with zeolite-type frameworks and also a number of condensed silica polymorphs. In addition, a series of hypothetical structures were included which are analogues to aluminophosphate structures.

The focus of this work was on structures for which there is available thermochemical data on lattice enthalpies (α-quartz, cristobalite, tridymite, silicalite, ZSM-11, ZSM-12, SSZ-24 and faujasite). The following structural data were used for the silicas in question. For silicalite, both the orthorhombic structure described by Flanigen and co-workers[261] and the low temperature monoclinic phase[262] were considered. The structure determinations of Fyfe and co-workers[263,264] were used for ZSM-11 and ZSM-12. In the case of tridymite, both the low- and high-temperature phases were minimised.[265,266] For cristobalite, again, the low-temperature (α) tetragonal[267] and the high-temperature (β) cubic structures[268] were used, and also the tetragonal $I\bar{4}2d$ structure proposed by Wright and Leadbetter[269] for β-cristobalite. The cubic siliceous faujasite structure recently reported

Table 4.1: Potential parameters for silicas[a]

Si–O parameters				
	A (eV)	ρ (Å)	C (eV Å^6)	
Sanders *et al*[205b]	1283.9	0.3205	10.66	
Purton *et al*[177c]	1459.7	0.3112	10.63	
de Boer *et al*[176]	18122.0	0.1734	0.00	
Kramer *et al*[206]	17796.0	0.2049	135.41	
Vessal *et al*[251d]	276.1	-	0.00	
O–O parameters				
	A (eV)	ρ (Å)	C (eV Å^6)	k (eV Å^{-2})
Sanders *et al*	22764.0	0.1490	27.88	74.92
Purton *et al*	5811.0	0.2048	28.76	80.00
de Boer *et al*	266757.0	0.1708	0.00	34.98
Kramer *et al*	1305.9	0.3594	196.09	-
Vessal *et al*	16896.1	-	0.00	-
Charges				
	q(Si)	q(O_{core})	q(O_{shell})	
Sanders *et al*	4.0000	0.8690	-2.8690	
Purton *et al*	4.0000	0.8482	-2.8482	
de Boer *et al*	2.7226	0.6512	-2.0125	
Kramer *et al*	2.4000	-1.2000		
Vessal *et al*	2.4000	-1.2000		

[a]A, ρ, and C are Buckingham potential parameters. k is the core-shell spring constant.
[b]Also O-Si-O potential ($E_{ijk} = \frac{1}{2}k_{ijk}(\theta_{ijk} - \theta_0)^2$), k_{ijk} = 2.097 eV rad^2, θ_0 = 109.47°.
[c]Also O-Si-O potential ($E_{ijk} = \frac{1}{2}k_{ijk}(\theta_{ijk} - \theta_0)^2$), k_{ijk} = 1.568 eV rad^2, θ_0 = 109.47°.
[d]A and C parameters represent Lennard-Jones parameters. Units of A are eV Å^{12}.

by Hriljac and co-workers[31] and also the hexagonal EMT structures described by Newsam and co-workers[270] were examined. The SSZ-24 structure was that determined by Bialek and co-workers.[248] The structures of ferrierite and dodecasil were taken from recent powder and single-crystal studies of those materials.[35,249] All the structures were treated as purely siliceous. In addition, the recently characterised structure of moganite[271] and the

structure of stishovite,[272] a high-density silica polymorph containing octahedral silicon, were also included. The structures of the other silicas considered in this study are detailed elsewhere.[49,52,60,273–281]

4.3 Results and Discussion

4.3.1 Forcefield Comparison

Many of the forcefields considered have been previously used to simulate the structure and properties of α-quartz in order to assess their quality. In order to compare the relative quality of the forcefields with respect to the representation of the zeolite structure, three well characterised siliceous zeolite structures were chosen (SSZ-24, faujasite and ferrierite) and their structures minimised at constant pressure using the experimental space-group symmetry. The results are summarised in Tables 4.2–4.4.

The structural quantities that show the largest variation from structure to structure are the Si–O–Si bond angles, and as such they provide the most stringent test of the potential model. The formal charge shell model of Sanders is still the most accurate method of representing the structures of silicas using the Born model approach. The LDF potential of Purton approaches that of Sanders in quality but reproduces bond angles about oxygen less accurately. The partial-charge shell model generally represents the cell parameters better than other structural quantities; but, the bond lengths are always overestimated.

4.3.2 Comparison with Structural Data

The remainder of the calculations reported in this chapter are based on the Sanders potential. There are a number of important questions to consider when comparing minimised structures with those of experimental structure solutions. One point to note is that the calculations performed here represent minimum energy structures at zero Kelvin. No attempt is made here to assess the effect of temperature on the calculated crystal structures.

As seen in the previous section, the potential in general reproduces structural quantities accurately, especially for high-symmetry structures. In general, the lattice parameters of all the structures considered are reproduced to within 2% of the experimental values. This is

Table 4.2: Comparison of different silica forcefields with experiment for SSZ-24 in space group $P6/mcc$ (e.s.d.'s in parentheses)

	Expt.[248]	Sanders	Purton	Kramer	de Boer	Vessal	Hill
Cell parameters (Å)							
a	13.671	13.679	13.839	13.436	13.680	14.033	13.957
c	8.328	8.466	8.274	8.274	8.505	8.559	8.592
Bond lengths (Å)							
Si(1) – O(1)	1.606(6)	1.596	1.600	1.603	1.623	1.597	1.615
Si(1) – O(2)	1.601(12)	1.599	1.609	1.612	1.611	1.606	1.619
Si(1) – O(3)	1.529(2)	1.585	1.593	1.617	1.593	1.602	1.618
Si(1) – O(4)	1.605(5)	1.604	1.609	1.608	1.628	1.613	1.607
Average :	1.585	1.596	1.603	1.610	1.614	1.605	1.615
Bond angles (°)							
O(1) – Si(1) – O(2)	105.5(2)	107.1	109.0	112.6	104.6	115.0	109.5
O(1) – Si(1) – O(3)	106.1(5)	110.7	110.3	109.2	110.8	110.0	109.4
O(1) – Si(1) – O(4)	105.9(3)	109.8	109.7	110.2	109.9	109.0	109.4
O(2) – Si(1) – O(3)	110.7(5)	109.3	109.4	106.0	109.0	109.5	109.3
O(2) – Si(1) – O(4)	115.8(3)	111.6	109.6	109.7	114.4	103.9	109.3
O(3) – Si(1) – O(4)	112.1(3)	108.4	108.8	109.0	108.1	109.2	109.9
Average :	109.3	109.5	109.5	109.5	109.5	109.4	109.5
Si(1) – O(1) – Si(1)	150.5(2)	148.1	153.9	161.6	140.3	165.6	155.2
Si(1) – O(2) – Si(1)	144.8(4)	149.9	148.8	149.9	151.8	151.3	148.5
Si(1) – O(3) – Si(1)	143.1(4)	148.8	154.5	161.3	140.7	164.7	155.3
Si(1) – O(4) – Si(1)	172.4(7)	177.4	178.5	178.8	176.9	179.4	179.3

Table 4.3: Comparison of different silica forcefields with experiment for faujasite in space group $Fd\bar{3}m$ (e.s.d.'s in parentheses)

	Expt.[31]	Sanders	Purton	Kramer	de Boer	Vessal	Hill
Cell parameter (Å)	24.2576(3)	24.226	24.500	24.745	24.221	24.840	24.542
Bond lengths (Å)							
Si(1) – O(1)	1.607(2)	1.614	1.621	1.614	1.637	1.609	1.616
Si(1) – O(2)	1.597(2)	1.599	1.603	1.608	1.623	1.603	1.612
Si(1) – O(3)	1.604(2)	1.609	1.613	1.618	1.634	1.613	1.618
Si(1) – O(4)	1.614(3)	1.608	1.613	1.606	1.628	1.600	1.612
Average :	1.606	1.607	1.612	1.612	1.631	1.606	1.617
Bond angles (°)							
O(1) – Si(1) – O(2)	110.7(1)	112.0	110.7	108.1	113.0	106.1	109.6
O(1) – Si(1) – O(3)	109.1(1)	109.4	108.2	105.9	111.8	104.1	109.2
O(1) – Si(1) – O(4)	108.2(1)	107.5	110.1	114.3	103.7	118.1	111.2
O(2) – Si(1) – O(3)	108.7(2)	107.6	108.4	109.7	106.7	110.9	109.0
O(2) – Si(1) – O(4)	108.7(2)	108.8	109.4	111.3	108.0	112.0	109.7
O(3) – Si(1) – O(4)	111.5(2)	111.6	111.0	107.3	113.7	105.4	108.2
Average :	109.5	109.5	109.5	109.4	109.5	109.4	109.5
Si(1) – O(1) – Si(1)	138.4(2)	137.6	139.2	141.0	134.6	144.9	138.9
Si(1) – O(2) – Si(1)	149.4(2)	148.9	154.0	160.6	141.6	164.4	161.0
Si(1) – O(3) – Si(1)	145.8(2)	145.9	151.1	156.4	137.6	161.1	159.5
Si(1) – O(4) – Si(1)	141.4(2)	140.8	142.8	149.0	137.8	151.2	137.9

Table 4.4: Comparison of different silica forcefields with experiment for ferrierite in space group $Pnnm$ (e.s.d.'s in parentheses)

	Expt.[249]	Sanders	Purton	Kramer	de Boer	Vessal	Hill
Cell parameters (Å)							
a	14.07025(8)	14.00	14.20	14.38	13.97	14.42	14.33
b	7.41971(4)	7.39	7.60	7.10	7.35	7.61	7.56
c	18.7202(1)	18.58	18.94	19.11	18.38	19.04	19.09
Bond lengths (Å)							
Average Si(1) – O	1.595	1.598	1.602	1.610	1.621	1.605	1.615
Average Si(2) – O	1.610	1.600	1.606	1.610	1.620	1.604	1.615
Average Si(3) – O	1.597	1.599	1.601	1.611	1.624	1.606	1.615
Average Si(4) – O	1.589	1.602	1.603	1.610	1.628	1.605	1.614
Average Si(5) – O	1.609	1.595	1.603	1.610	1.612	1.605	1.616
Bond angles (°)							
Average O – Si(1) – O	107.8	109.5	109.5	109.4	109.9	110.1	109.5
Average O – Si(2) – O	109.5	109.5	109.5	109.5	109.5	109.5	109.5
Average O – Si(3) – O	109.4	109.5	109.5	109.4	109.5	109.4	109.5
Average O – Si(4) – O	109.4	109.5	109.5	109.4	109.4	109.4	109.5
Average O – Si(5) – O	109.4	109.5	109.5	109.4	109.4	109.4	109.5
Si(2)– O(1)– Si(2)	144.6(8)	147.1	149.6	153.4	144.37	157.2	151.7
Si(1)– O(2)– Si(2)	153.7(8)	153.9	159.1	162.5	147.09	163.8	158.1
Si(1)– O(3)– Si(3)	156.8(6)	149.9	158.7	163.2	140.90	165.7	159.2
Si(4)– O(4)– Si(5)	149.2(6)	146.8	150.2	155.2	141.36	158.4	150.6
Si(3)– O(5)– Si(3)	159.5(14)	151.3	168.4	171.9	137.48	173.9	171.8
Si(4)– O(6)– Si(5)	171.9(9)	160.2	180.0	180.0	151.58	180.0	175.4
Si(3)– O(7)– Si(5)	162.4(9)	163.6	155.0	158.8	161.96	160.8	154.8
Si(3)– O(8)– Si(4)	138.3(8)	140.0	154.9	158.8	129.75	160.8	154.7
Si(2)– O(9)– Si(4)	142.3(8)	142.3	150.2	154.5	136.42	157.5	145.8
Si(2)– O(10)– Si(5)	152.3(9)	153.3	150.2	154.5	152.06	157.5	154.9

Table 4.5: Comparison of calculated and experimental cell parameters for silicas (e.s.d.'s in parentheses)

		a(Å)	b(Å)	c(Å)	α(°)	β(°)	γ(°)
α-quartz	(expt.[268])	4.913	4.913	5.406	90.0	90.0	120.0
	(calc.)	4.835	4.835	5.346	90.0	90.0	120.0
α-cristobalite	(expt.[267])	4.97(8)	4.97(8)	6.94(8)	90.0	90.0	90.0
	(calc.)	4.97	4.97	7.00	90.0	90.0	90.0
β-cristobalite	(expt.[268])	5.063	5.063	7.160	90.0	90.0	90.0
	(calc.)	4.995	4.995	7.177	90.0	90.0	90.0
α-tridymite	(expt.[265])	18.494(8)	4.991(2)	23.758(8)	90.0	105.79(2)	90.0
	(calc.)	18.540	4.983	23.824	90.0	105.8	90.0
β-tridymite	(expt.[266])	5.03	5.03	8.22	90.0	90.0	120.0
	(calc.)	5.17	5.17	8.44	90.0	90.0	120.0
ZSM-12	(expt.[264])	24.863(1)	5.012(1)	24.328(1)	90.0	107.7(1)	90.0
	(calc.)	24.954	4.998	24.151	90.0	107.4	90.0
silicalite	(expt.[261])	20.060	13.360	19.800	90.0	90.0	90.0
	(calc.)	20.073	13.335	19.693	90.0	90.0	90.0
mono. silicalite	(expt.[262])	19.879(2)	20.107(2)	23.826(1)	90.0	145.9(1)	90.0
	(calc.)	19.740	19.979	23.656	90.0	145.7	90.0
ferrierite	(expt.[249])	14.07025(8)	7.41971(4)	18.7202(1)	90.0	90.0	90.0
	(calc.)	14.00	7.39	18.58	90.0	90.0	90.0
ZSM-11	(expt.[263])	20.067(1)	20.067(1)	13.411(1)	90.0	90.0	90.0
	(calc.)	19.995	19.995	13.452	90.0	90.0	90.0
SSZ-24	(expt.[248])	13.671	13.671	8.328	90.0	90.0	120.0
	(calc.)	13.679	13.679	8.466	90.0	90.0	120.0
faujasite	(expt.[31])	24.2576(3)	24.2576(3)	24.2576(3)	90.0	90.0	90.0
	(calc.)	24.226	24.226	24.226	90.0	90.0	90.0

summarised in Table 4.5.

In relation to the fractional coordinates of the atoms in the crystallographic asymmetric unit, the agreement with experiment is particularly good for those structures that have been well determined by diffraction measurements, for example the cubic faujasite structure (see Table 4.6). The most difficult structural parameters to reproduce with this class of

Table 4.6: The asymmetric unit of siliceous faujasite : comparison of theory and experiment (units are fractional coordinates; e.s.d.'s in parentheses)

	x	y	z
Si(1)			
experiment	0.94608(8)	0.12530(8)	0.03589(9)
calculated	0.94597	0.12571	0.03590
O(1)			
experiment	0.0000	0.89377(6)	0.10623(6)
calculated	0.0000	0.89309	0.10691
O(2)			
experiment	0.99677(6)	0.99677(6)	0.14066(9)
calculated	0.99773	0.99773	0.14057
O(3)			
experiment	0.07570(6)	0.07570(6)	0.96423(9)
calculated	0.07604	0.07604	0.96423
O(4)			
experiment	0.07063(7)	0.07063(7)	0.32115(10)
calculated	0.07027	0.07027	0.32146

potential are the bond angles about oxygen, since such a wide range of angles is spanned in the various silica structures. However, for faujasite, these also show excellent agreement with experiment, while the agreement is less exact for structures of lower symmetry. This is also a consequence of the forcefield being fitted to the structure of α-quartz, which has a O–Si–O bond angle similar to those observed in faujasite. One approach to improve the reproduction of oxygen bond angles is to add a bond angle term to the forcefield. The Hill

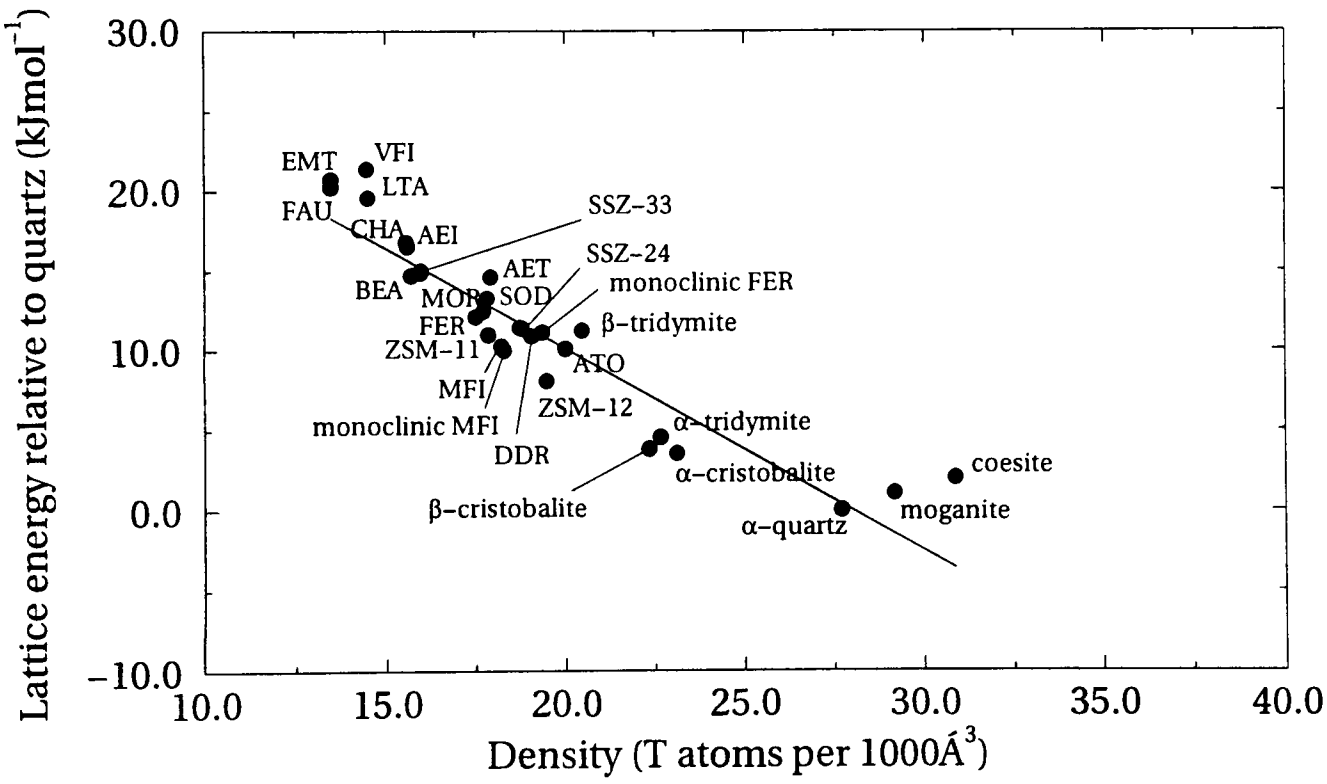
potential contains a quartic bond-angle potential about oxygen having a minimum at θ = 176.3°. However, from Table 4.3 it can be seen that the inclusion of this term does little to improve the bond-angle reproduction over that obtained from the Sanders forcefield.

The Sanders forcefield is unable to represent the structure of stishovite correctly since it contains octahedral silicon. However, this is not an important consideration for zeolite studies since the silicon coordination is restricted to a tetrahedral environment in all known structures.

4.3.3 Variation of Lattice Energy with Density

As has been shown previously,[131,207] the calculated lattice energies of silicas show a direct correlation with the density of the structure (Figure 4.1).

Figure 4.1: Variation of calculated lattice energy with density for silicas (zeolite structures are labelled by their IZA codes).



Kramer and co-workers[206] used an unreasonably large O–O dispersion term in their forcefield, which was found to give an anomalously large range in the minimised lattice energy for the silicas considered. Kramer proposed that an additional correction term be added to the final lattice energy in order to give the correct experimental range. Since the dispersion term in the Sanders potential is more consistent with theoretical estimates of the O–O interaction calculated using coupled Hartree-Fock calculations,[282] this is less of

a problem. To further circumvent cut-off problems, a larger short-range cut-off (12Å) was used than in the work of Kramer and the contribution of interactions beyond this distance was estimated using the continuum approximation.

In the case of tridymite, the low-temperature (α) form is found to be much more stable than the less dense high-temperature (β) phase as would be expected. The proposed tetragonal structure of β-cristobalite is found to be 6 kJmol^{-1} lower in energy than the cubic $Fd\bar{3}m$ structure, in agreement with a previous quantum-mechanical study of this structure.[283]

In an attempt to rationalise the density dependence of the lattice energy, we factorised the total energy into contributions from the Coulombic, short-range attractive, short-range repulsive and three-body terms. The only term that shows a systematic increase with density is the attractive short-range dispersion interaction but the variation is non-linear and consequently does not account for the observed trend. The fitting method that was used to develop the forcefield introduces considerable uncertainty into the physical meaning of the various contributions to the total lattice energy since all forcefield parameters are varied simultaneously to obtain the most accurate reproduction of experimental quantities.

4.3.4 Comparison with Thermochemical Data

A most encouraging aspect of these calculations is that they show good agreement with recent experimental thermochemical data measurements made by Petrovic and co-workers[250] (Figure 4.2). The lattice energy can be related to the heat of formation by a Born-Haber cycle and, to a good approximation, the two quantities differ by a constant term. The experimental data are taken from the work of Petrovic and co-workers[250] for the zeolite structures and from other experimental measurements for the condensed silicas.[284–286] The open framework silicas are predicted to be 8-20 kJmol^{-1} less stable than quartz. Furthermore, when the data on the condensed silicas are included, the experimental values correlate well with density (Figure 4.3). However, the minimised energies of moganite, coesite and stishovite, all of which are denser than α-quartz, are predicted to have higher lattice energies. This correlates with experiment,[250] showing quartz to be the energy minimum in the series, but suggests that the dependence of lattice energy on den-

Figure 4.2: Correlation of the experimental heat of formation with the calculated lattice energy relative to quartz.

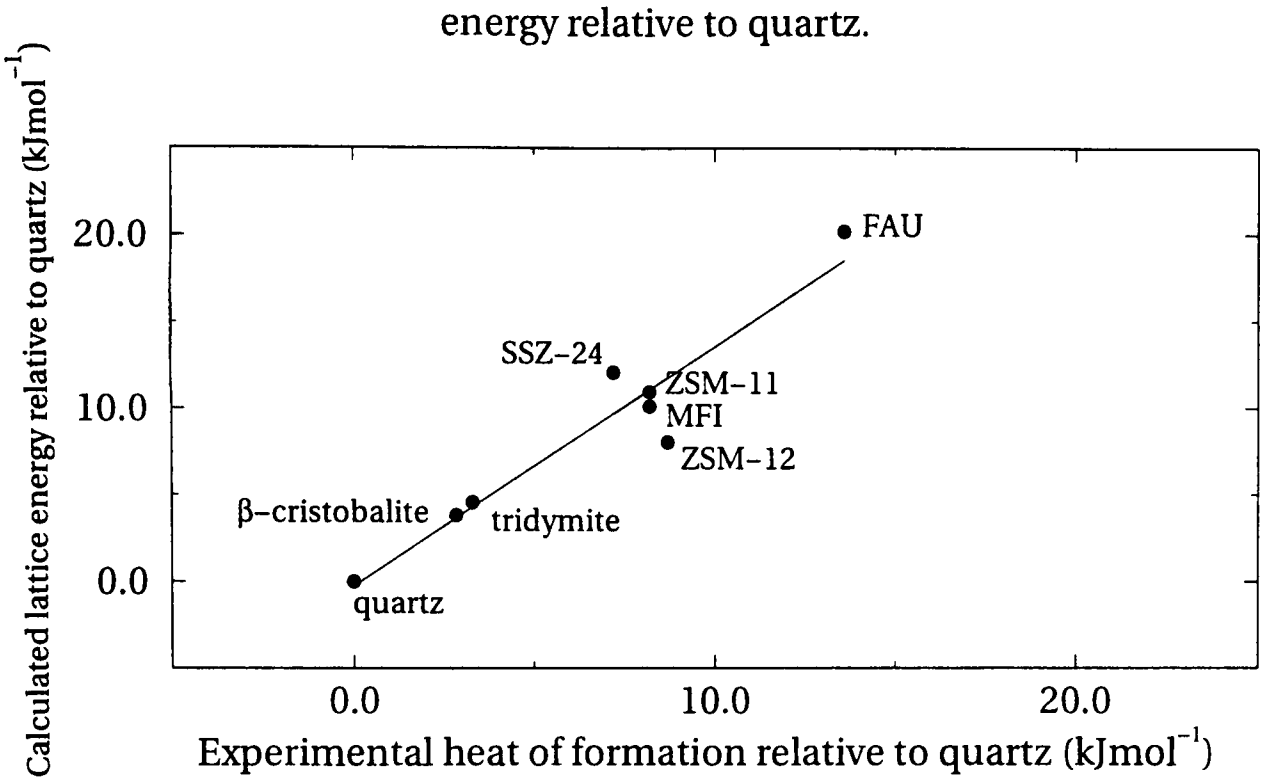
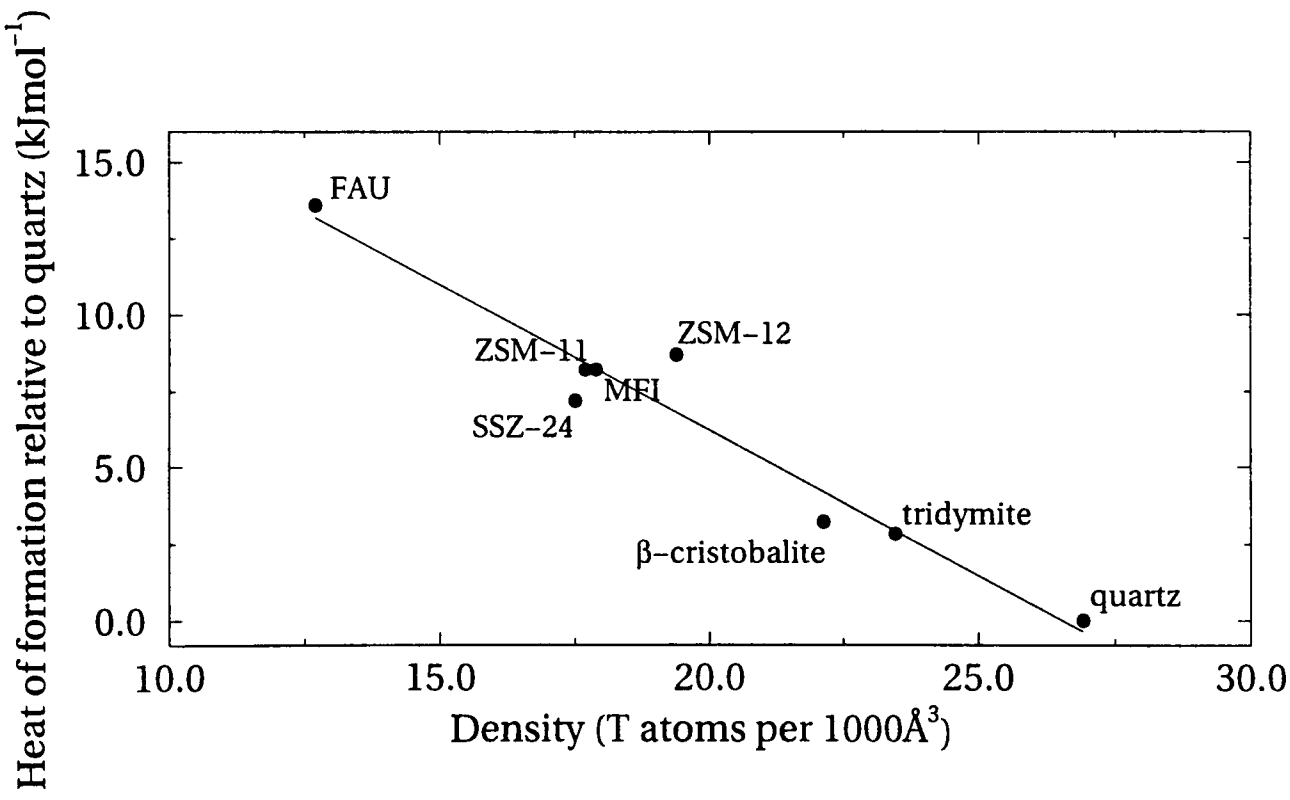


Figure 4.3: Variation in experimental heat of formation with density for silica structures.



sity does not hold for all silica structures. In the case of stishovite, the minimised structure is predicted to be about 100 kJmol^{-1} higher than quartz, which is a large overestimate of experimental value. The deficiencies for this structure are probably due to an inability of the current forcefield to represent six-coordinated silicon correctly.

It would be useful to include structures beyond the lower limit of the density range of those presented here, the recently synthesised mesoporous silicas in the MCM-41 family being good candidates. However, it must be stressed that these are not pure silica materials

Table 4.7: Comparative energies for structures in different space groups.

structure	space group	minimised energy (kJmol^{-1} per T atom)[a]	number of imaginary phonon modes
silicalite	$Pna2_1$	0.23	2
silicalite	$P2_1/c$	0.00	0
ferrierite	$Immm$	0.58	3
ferrierite	$Pnnm$	0.03	2
ferrierite	$P2_1/c$	0.03	5
ferrierite	$P\bar{1}$	0.00	0

[a]relative to most stable structure

and thermochemical data for these systems cannot be considered in this context.

4.3.5 Phonon Spectra

The calculated phonon modes for several of the silica structures at the Γ point have been calculated to characterise each stationary point on the potential energy surface. A minimised structure that gives imaginary frequencies in the phonon spectra is only at a minimum subject to the constraints imposed by the space-group symmetry; it is a saddle point on the unconstrained potential energy surface. The imaginary frequencies can be used to further minimise the structure in $P1$ symmetry, essentially acting as a perturbation which allows the structure to escape the region around the saddle point.

The minimisation of the orthorhombic phase of silicalite in the room- temperature space-group ($Pna2_1$) shows two imaginary frequencies in the calculated phonon spectrum. Relaxing the space group symmetry to $P1$ and allowing the imaginary phonon modes to relax the structure further results in a minimised structure with $P2_1/c$ symmetry, which is the correct low-temperature result. The energy difference between the two structures is small but significant (Table 4.7).

In most cases, the use of the imaginary phonon modes does not introduce sufficient perturbation into the system to allow escape from the region of the potential energy sur-

Table 4.8: Comparison of bond angles about oxygen.

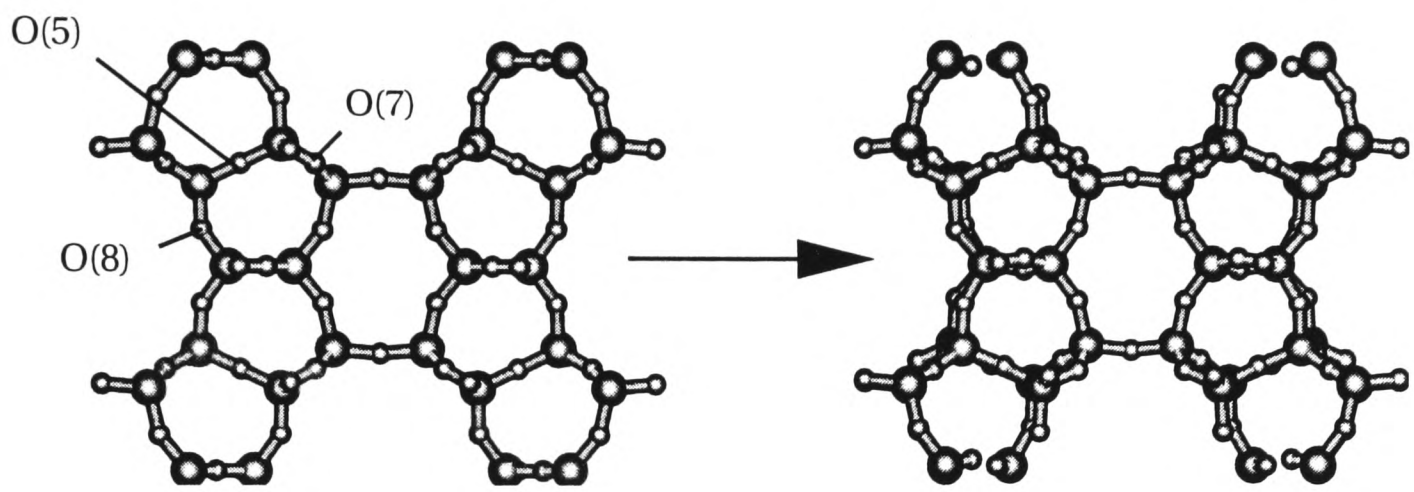
space group	O(1)	O(2)	O(3)	O(4)	O(5)	O(6)	O(7)	O(8)
$Immm$ (expt)	169.3	152.7	153.5	157.9	180.0	153.2	152.9	147.3
$Immm$ (calcd)	165.5	147.0	156.1	157.5	180.0	147.8	153.1	147.8
$Pnnm$ (expt)	159.5	144.6	156.8	153.7	171.9	149.1	162.4/138.2	142.3/152.3
$Pnnm$ (calcd)	151.4	147.1	150.0	153.9	160.3	146.8	163.7/140.1	142.3/153.2

face around the saddle point. Several alternative methods are possible to circumvent this problem. The space group can be manually adjusted to possible maximal non-isomorphic subgroups and the minimisation repeated. This can be quite time consuming if there are a large number of possible subgroups. A more elegant approach is to use the rational-function optimisation method for searching for stationary points on the potential energy surface in combination with the imaginary phonon modes, which is often a better method for finding minima close to saddle points. One of the most popular methods to explore a potential energy surface fully is simulated annealing. Unfortunately, the high frequency of the core-shell vibrations would require too small a time-step to allow sufficient phase space to be sampled and this technique is therefore not currently applicable..

The structure of ferrierite provides an interesting example of the variation in space-group selection. Until recently, the widely used space group for this zeolite was $Immm$.[287,288] However, previous structural studies worked with samples containing significant amounts of aluminium and counter cations. One of the major concerns with this space group is that it requires a bond angle of 180° at the O(5) position, which is believed to be unfavourable in zeolite structures. Recent work by Kuperman and co-workers[42] has allowed the synthesis of large single crystals of siliceous ferrierite to be prepared and the subsequent structure solution of the calcined material yielded the lower-symmetry space group, $Pnnm$.[249] In this structure, the O(5) bond angle is reduced to 171.9°. Further structural studies on the transition-metal loaded ferrierites derived from this synthetic procedure have suggested the possibility of structural refinement in the monoclinic space group, $P2_1/c$.[289]

The reduction in symmetry from $Immm$ to $Pnnm$ represents a difference in energy of

Figure 4.4: The splitting of oxygen sites from $Immm$ to $Pnnm$ structures.



Immm structure *Pnnm* structure

0.58kJmol^{-1}. In addition, the removal of the constraint on the O(5) bond angle in this subgroup splits the O(7) and O(8) positions into two separate oxygen sites, as can be seen in Figure 4.4. In this space group, the bond angles about oxygen are less well reproduced with the current forcefield, especially for angles close to 180° (see Table 4.8). Although moving down in symmetry to $Pnnm$ reduces the minimised lattice energy, several imaginary modes remain in the calculated phonon spectrum. By further reducing the symmetry to $P2_1/c$, additional oxygen sites are split into pairs but there is no extra energy stabilisation and an increase in the number of imaginary phonon frequencies is observed (see Table 4.8). Using the minimised $P2_1/c$ structure as a starting point, the five imaginary phonon modes relax the structure to the low-symmetry $P\bar{1}$ model; the energy stabilisation is only very slight but the imaginary frequencies are eliminated. Clearly, the extra stabilisation afforded by a structure with no imaginary phonon frequencies provides no further insight into the space-group choice used in the crystallographic refinement. It is probable that this subtle effect is currently beyond the sophistication of the Sanders forcefield and further refinements to the forcefield may have to be made before this method can be used as a predictive tool in a crystallographic study.

Chapter Five

Computer Simulation of Aluminophosphate Polymorphs

A large number of microporous aluminium phosphate materials ($AlPO_4$'s) have been synthesised since the first examples were reported by Wilson and co-workers in 1982.[3] They exhibit a wide range of structural characteristics ranging from clathrate-type structures, in which the structure-directing agent is trapped within the aluminophosphate framework, to microporous structures similar to those shown by more traditional aluminosilicate systems. Although many $AlPO_4$ structures have direct aluminosilicate analogues, there are also a large number of unique framework types. Indeed, $AlPO_4$'s and other phosphate derivatives often allow much larger ring structures to be formed, such as the eighteen-ring VPI-5 structure[8] and the twenty-ring structure of cloverite.[9] Whether this is due to the extra stability conferred upon the structure by the Al/P alternation, or merely a consequence of the greater coordination numbers allowed by Al and other heteroatoms during the synthetic phase, is still open to debate. As with more traditional zeolites, framework atoms may be substituted to modify the properties of aluminium phosphates.[7,290] For example, aluminium can be replaced by transition metals to form MeAPOs, such as CoAPO-50,[291] and phosphorus can be substituted by silicon to form the acidic and catalytically active silicoaluminophosphate family (SAPO).[6] Despite their structural diversity and ease of modification, few aluminophosphates have found use in commercial applications, although a large number of systems have been shown to be catalytically active in important industrial processes, such as the use of $AlPO_4$-31 derivatives in the isomerisation of butene.[292]

In the aluminophosphate area, van Beest and co-workers fitted a partial-charge rigid-ion model[179] and investigated the structure and spectra of $AlPO_4$-5,[293] and also the structures of $AlPO_4$-8 and VPI-5.[294] de Vos Burchart and co-workers employed a forcefield based on a covalent model to examine a wide range of aluminophosphates, as well as prob-

ing structures with higher coordinate aluminium.[210] Choi and co-workers used the electronegativity equalisation method to derive a forcefield for $AlPO_4$-5;[295] however, since explicit parameters were obtained for each T–O pair, this somewhat limits the transferability of the forcefield to other systems. In this chapter, a formal-charge shell model for aluminophosphates is derived that is consistent with previous forcefields derived for aluminosilicates by empirical fitting to experimental data on berlinite. Lattice-energy minimisations with symmetry constraints are performed on a wide range of aluminium phosphate polymorphs, including both condensed phases and microporous structures. For several aluminophosphates, structure determinations from powder diffraction data contradict solid-state NMR measurements, suggesting that a lower symmetry space group should have been used in the Rietveld refinement.[296] The extent to which the fitted potential can be used to rationalise such questions is assessed by examining different space groups and checking the consistency with experimental data. As a further test of the quality of the model, calculated lattice energies will be compared to recent thermochemical measurements.[297] In the final section of this paper, the potential is applied to a system of catalytic interest (SAPO-37) and preferred binding sites for protons are calculated for comparison with experimental data.

5.1 Derivation of a Forcefield for Aluminophosphates

5.1.1 Functional Form

The functional form was chosen for compatibility with previously derived forcefields for aluminosilicates.[205,211] The interaction between two ions i and j is given by a Buckingham potential combined with an electrostatic term :-

$$E_{ij} = A_{ij} \exp\left(-\frac{r_{ij}}{\rho_{ij}}\right) - \frac{C_{ij}}{r_{ij}^6} + \frac{q_i q_j}{r_{ij}} \tag{5.1}$$

as in Equations 3.49 and 3.53 . The electrostatic term is summed using the Ewald summation with cut-offs chosen to give accuracy in the electrostatic energy to eight significant figures. The Buckingham terms are evaluated in real space up to a cut-off of 16Å with contributions beyond this distance approximated using the continuum approximation.

The oxygen ions are treated using the shell model of Dick and Overhauser.[165] A mass-

less shell through which all short-range forces act is harmonically coupled to a core from which it is electrostatically screened using the functional form :-

$$E_{core-shell} = \frac{1}{2}k_{ij}(r_{core-shell})^2 \tag{5.2}$$

as in Equation 3.51 . The inclusion of the shell model is essential to simulate the dielectric properties of a material, especially at high frequencies, as well as allowing the covalency of the material to be represented to some degree.

A bond-angle bending term is also included in the form of a harmonic potential :-

$$E_{ijk} = \frac{1}{2}k_{ijk}(\theta_{ijk} - \theta_0)^2 \tag{5.3}$$

as in Equation 3.70 .

5.1.2 Fitting Methodology

The forcefield parameters were determined by a least-squares procedure minimising the sum of squares between the calculated and observed properties. The derivatives of the structural parameters at the experimental geometry are included in the fitting process. In addition, experimental measurements of elastic and dielectric properties are also taken into account to include information on the curvature of the potential energy surface. At each step in the fitting procedure the experimental crystal symmetry is used so as to restrict the fit to the unique structural characteristics of the asymmetric unit. Initially, the oxygen shells are placed at the core positions and during the fit their positions are relaxed in order to remove the forces acting on them. Weighting schemes are often used to emphasise one type of experimental observable over another. Since the first derivative quantities tend to zero at the experimental geometry, only the calculated second-derivative properties are meaningful. Consequently, the structural parameters were favourably weighted.

In the initial fit, the Al–O and O–O parameters were fixed at the values obtained in previous studies[298,299] and the P–O parameters fitted. Although some improvement was possible by allowing the parameters to vary during the fit, it was insufficient to justify abandoning compatibility with existing potentials for aluminosilicates. A three-body potential

centred on phosphorus was also tried but the force constant went to zero during the fitting procedure. The final set of fitted parameters is shown in Table 5.1.

Table 5.1: Fitted parameters for aluminophosphates.

	A_{ij} (eV)	ρ_{ij} (Å)	C_{ij} (eVÅ^{-6})	k_{ij} (eVÅ^{-2})	k_{ijk} (eVrad^{-2})
Al(core) – O(shell)	1460.3	0.2991	0.0	—	—
P(core)–O(shell)	877.34	0.3594	0.0	—	—
O(shell)–O(shell)	22764.0	0.1490	27.88	—	—
O(core)–O(shell)	—	—	—	74.92	—
O(shell)–Al(core)–O(shell)	—	—	—	—	2.09724

5.1.3 Structure and Properties of Berlinite

Using the fitted parameters, the structure of berlinite was lattice energy minimised and elastic, dielectric and piezoelectric constants calculated. The results are compared with experimental data and the values obtained in previous aluminophosphate calculations (Table 5.2). The shell model represents the structural properties much better than the rigid-ion model with the maximum error being less than 1%. The volume is underestimated by 1.2%; however, since the calculation is performed at absolute zero and the crystallographic study was made at room temperature, this discrepancy is expected. The calculated elastic constants are in general too high, especially along the c axis. The partial- charge model is somewhat better in this respect but this is undoubtedly due to the overestimated c parameter. Both of the potential models give permittivities that are too small compared to experiment. This could be improved by refitting the O–O parameters, which are the dominant factor for this property. However, the refit would render the resulting parameter set incompatible with existing forcefields. The calculated piezoelectric stress constants are too low for both models, whereas the strain constants are reproduced better with the partial-charge model.

Table 5.2: Comparison of experimental and calculated structure and properties for berlinite.

	experiment[300–302]	this work	van Beest *et al*[179]	de Vos Burchart *et al*[210]
a (Å)	4.9423	4.9109	4.9991	5.00
c (Å)	10.9446	10.9564	11.1236	10.83
x [Al]	0.4665	0.4670	0.4647	
x [P]	0.4669	0.4698	0.4631	
x [O(1)]	0.4161	0.4083	0.4334	
y [O(1)]	0.2922	0.2891	0.2944	
z [O(1)]	0.3976	0.3972	0.4025	
x [O(2)]	0.4153	0.4179	0.4222	
y [O(2)]	0.2579	0.2600	0.2512	
z [O(2)]	0.8835	0.8822	0.8893	
C_{11} ($10^9 Nm^{-2}$)	63.4	81.8	87.5	
C_{12} ($10^9 Nm^{-2}$)	23.0	15.9	13.0	
C_{13} ($10^9 Nm^{-2}$)	5.8	22.2	19.1	
C_{14} ($10^9 Nm^{-2}$)	-12.1	-10.9	-12.4	
C_{33} ($10^9 Nm^{-2}$)	55.8	106.7	104.0	
C_{44} ($10^9 Nm^{-2}$)	43.2	44.0	48.4	
C_{66} ($10^9 Nm^{-2}$)	30.6	32.9	37.4	
ϵ_{11}^o	5.47	5.25	1.92	
ϵ_{33}^o	5.37	5.42	1.94	
ϵ_{11}^∞	4.60	2.08	1.00	
ϵ_{33}^∞	4.48	2.11	1.00	
d_{11} (10^{12} CN^{-1})	-3.30	-2.30	-1.57	
d_{14} (10^{12} CN^{-1})	1.62	1.09	0.24	
e_{11} (Cm^{-2})	-0.22	-0.34	-0.24	
e_{14} (Cm^{-2})	0.15	0.08	0.17	

5.2 Application to Aluminophosphate Structures

The fitted parameters were then used to investigate a wide range of different aluminophosphate structures.[31,49,52,218,275,276,278,291,300,303–308] In most cases the crystallographic structures can be used directly as starting models, but for several structures a number of hypothetical starting structures were proposed. The structure determined by Pluth and co-workers for $AlPO_4$-17[309] has several partially occupied sites, so a model was derived from the aluminosilicate analogue, erionite.[305] Aluminophosphate models were also derived for : $AlPO_4$-20 (siliceous sodalite[278]), $AlPO_4$-37 (siliceous faujasite[31]) and $AlPO_4$-42 (zeolite-A[276]), since the only structural data available were for their SAPO derivatives. For VPI-5, the structure of $AlPO_4$-54[310] was used as a starting point and the symmetry was lowered to allow for Al/P alternation. Structures that contain Al having coordination numbers of five and six were in general omitted unless there was a trivial way to remove the extra coordinated atoms. No attempt was made to represent the template in these calculations, since the main interest was to assess the stability of the frameworks in the absence of the structure-directing agent. The phonon spectra were calculated at the Γ point to characterise the stationary points.

5.3 Results and Discussion

5.3.1 Structural Reproduction

When making a comparison with experimental crystallographic data it is important to consider a number of effects. Firstly, the calculations represent the minimum energy structures at zero Kelvin, whereas most of the structural determinations were made at room temperature; no attempt is made to include the variation of the lattice parameters with temperature. Second, many of the available crystal structures contain significant amounts of water which may alter the coordination environments of tetrahedral atoms; in several cases the structures are not calcined, so the template molecules are still present in the pores. Furthermore, a survey of the literature reveals that the quality of the structural refinements is not as high as that for many of the silica polymorphs considered in the previous chapter. This is probably due to low crystal quality. In Table 5.3, a comparison of the

Table 5.3: Comparison of minimised structures with previous calculations.

structure	space group	a (Å)	b (Å)	c (Å)	α (°)	β (°)	γ (°)	rel. energy[a] (kJmol^{-1})
$AlPO_4$-5								
expt.[50]	$P6cc$	13.7707(3)	13.7707(3)	8.3789(6)	90.0	90.0	120.0	
expt.[311]	$P6cc$	13.740(5)	13.740(5)	8.474(4)	90.0	90.0	120.0	
expt.[312]	$P6cc$	13.7258(12)	13.7258(12)	8.4835(5)	90.0	90.0	120.0	
this work	$P6cc$	13.83	13.83	8.55	90.0	90.0	120.0	0.92
this work	$P31c$	13.83	13.83	8.55	90.0	90.0	120.0	0.92
this work	$P6$	13.76	13.76	8.39	90.0	90.0	120.0	0.00
theory[293]	$P6cc$	14.18	14.18	8.68	90.0	90.0	120.0	
theory[293]	Cc	13.98	13.98	8.43	90.0	90.0	120.0	
theory[210]	$P6$	13.74	13.74	8.34	90.0	90.0	120.0	
theory[210]	$P6cc$	13.83	13.83	8.33	90.0	90.0	120.0	
$AlPO_4$-8								
expt.[303]	$Cmc2_1$	33.29(2)	14.76(2)	8.257(4)	90.0	90.0	90.0	
expt.[273]	$Cmc2_1$	33.0894(25)	14.6832(13)	8.3630(6)	90.0	90.0	90.0	
this work	$Cmc2_1$	33.35	14.69	8.46	90.0	90.0	90.0	1.16
this work	$Pmn2_1$	33.16	14.63	8.37	90.0	90.0	90.0	0.07
this work	$P2_1$	14.63	18.10	8.36	90.0	66.2	90.0	0.0
theory[293]	$Cmc2_1$	34.27	14.76	8.26	90.0	90.0	90.0	
theory[210]	$Pmn2_1$	34.35	14.32	8.29	90.0	90.0	90.0	
$AlPO_4$-11								
expt.[49]	$Ima2$	18.4845(10)	13.5333(8)	8.3703(4)	90.0	90.0	90.0	
this work	$Ima2$	18.77	13.62	8.47	90.0	90.0	90.0	1.41
this work	$P2$	23.09	8.36	13.55	90.0	126.9	90.0	0.0
theory[210]	$P2$	18.36	13.5	8.29	90.0	90.0	89.79	
$AlPO_4$-18								
expt.[52]	$C2/c$	13.5116(3)	12.6235(2)	18.4394(5)	90.0	90.01	90.0	
this work	$C2/c$	13.68	12.61	18.44	90.0	89.99	90.0	
theory[210]	$C2/c$	13.83	12.72	18.63	90.0	89.5	90.0	
$AlPO_4$-25								
expt.[306]	$Abm2$	9.45	15.20	8.41	90.0	90.0	90.0	
this work	$Abm2$	9.56	15.35	8.53	90.0	90.0	90.0	1.88
this work	$Pca2_1$	9.40	15.33	8.32	90.0	90.0	90.0	0.0
theory[210]	$P2_1$	9.23	15.22	8.12	90.0	90.0	90.0	
VPI-5								
expt.[310]	$P6_3cm$	18.549(1)	18.549(1)	8.404(1)	90.0	90.0	120.0	
expt.[313]	$P6_3cm$	18.524(1)	18.524(1)	8.332(1)	90.0	90.0	120.0	
this work	$P6_3cm$	18.56	18.56	8.56	90.0	90.0	120.0	1.17
this work	$P6_3$	18.41	18.41	8.42	90.0	90.0	120.0	0.0
this work	$P31m$	18.56	18.56	8.56	90.0	90.0	120.0	1.17
theory[210]	$P31m$	18.64	18.64	8.33	90.0	90.0	120.0	
theory[210]	$P31m$	18.64	18.64	8.26	90.0	90.0	120.0	
theory[293]	$Cmc2_1$	19.01	19.01	8.48	90.0	90.0	120.0	

[a]Energy relative to most stable structure per tetrahedral atom

calculated lattice parameters and space groups with previous computational and experimental results is given.

$AlPO_4$-5

There are several inconsistencies in the various experimental methods reported for the $AlPO_4$-5 structure. There have been three notable crystallographic studies, all of which chose the space group $P6cc$. The original structure determination made by Bennett and co-workers was a single crystal X-ray diffraction study on a sample with the tetrapropylammonium hydroxide template.[312] Richardson and co-workers performed a neutron powder diffraction study of a calcined sample, but were unable to refine Al and P sites independently.[50] Qui and co-workers solved the structure of a sample containing tetrapropylammonium fluoride from single crystal X-ray data.[311] The crystal structure of Bennett and co-workers[312] showed three separate peaks for O(2) in the difference Fourier map, indicating some uncertainty in the position of this atom. In addition, solid-state NMR measurements[314,315] suggest that the actual space-group symmetry is lower than that reported in the crystallographic study. Although a minimum energy structure is obtained in the experimental $P6cc$ space group, the calculated phonon spectrum shows nine imaginary vibrational modes. This indicates that the minimisation was forced to end at a saddle point on the potential energy surface due to the symmetry constraints imposed by the space group. Similar results were obtained in previous computational studies on this system. In order to resolve the space-group question, we performed additional minimisations in subgroups of $P6cc$. Using the space group $P6$ a structure 0.92 kJmol^{-1} lower in energy is obtained which has no imaginary phonon modes. This structure reproduces the cell parameters of the Bennett structure for $AlPO_4$-5 to within 1%, and also gives good agreement with the transformed $P6cc$ fractional coordinates (Table 5.4).

With regard to the fractional coordinates, most of the atomic positions are reproduced very well, the maximum shift being about 0.5 Å. The y-coordinate of O(3) shows a shift of 0.4 Å. The range of T-O bond lengths observed is noticeably narrowed on minimisation. The bond angle about O(3) (and, by symmetry, O(4)) is experimentally found to be near to 180°. This angle is reduced by about 23° during the minimisation. The effect of this can be seen clearly in Figure 5.1. The structure minimised in the $P3$ sub group gave a similar en-

Table 5.4: Comparison of experimental and calculated structures for $AlPO_4$-5 in space group $P6$.

Cell parameters :-						
	experiment	calculated				
a (Å)	13.7258(12)	13.758				
c (Å)	8.4835(5)	8.392				
Fractional coordinates :-						
	experiment[a]			calculated		
	x	y	z	x	y	z
Al(1)	0.3377(3)	0.4577(4)	0.5500(3)	0.3368	0.4498	0.5500
Al(2)	0.3377(3)	0.8800(4)	0.0500(3)	0.3382	0.8722	0.0493
P(1)	0.3283(2)	0.4524(3)	0.9220(3)	0.3278	0.4451	0.9247
P(2)	0.3283(2)	0.8759(3)	0.4220(3)	0.3298	0.8709	0.4240
O(1)	0.2137(7)	0.4210(5)	0.9720(4)	0.2101	0.4154	0.9703
O(2)	0.2137(7)	0.7927(5)	0.4720(4)	0.2123	0.7934	0.4823
O(3)	0.3312(10)	0.4555(8)	0.7500	0.3324	0.4218	0.7495
O(4)	0.3312(10)	0.8757(8)	0.2500	0.3393	0.8486	0.2496
O(5)	0.3584(8)	0.3670(7)	0.9740(4)	0.3640	0.3746	1.0195
O(6)	0.3584(8)	0.9914(7)	0.4740(4)	0.3584	0.9917	0.4126
O(7)	0.4126(8)	0.5684(7)	0.9860(4)	0.4077	0.5693	0.9604
O(8)	0.4126(8)	0.8442(7)	0.4860(4)	0.4120	0.8495	0.5190

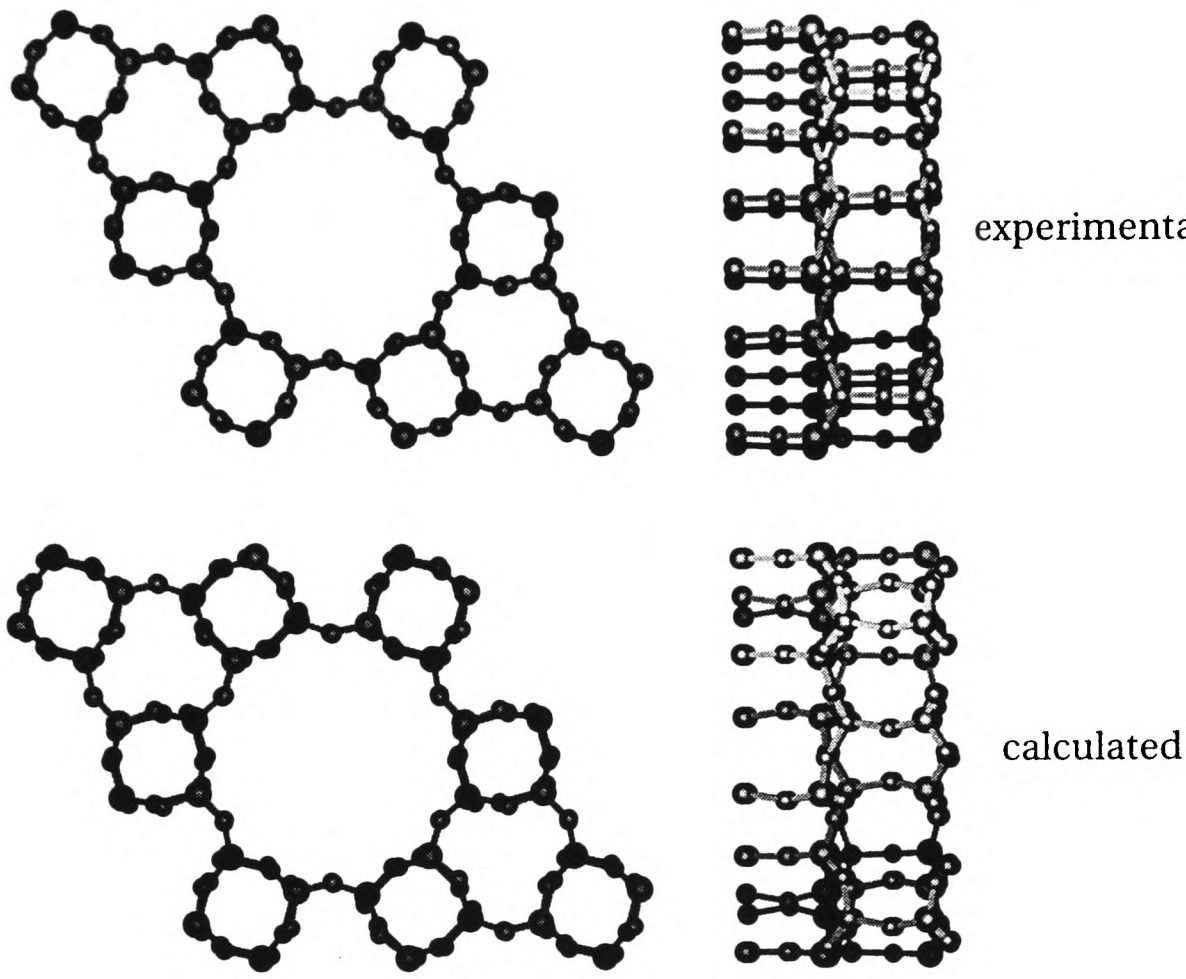
Bond Lengths and Bond Angles :-					
	experiment	calculated		experiment	calculated
mean Al(1)–O	1.710	1.722	Al–O(1)–P	150.2(7)	144.9
mean Al(2)–O	1.710	1.725	Al–O(2)–P	150.2(7)	149.1
mean P(1)–O	1.487	1.517	Al–O(3)–P	178.1(12)	154.6
mean P(2)–O	1.487	1.516	Al–O(4)–P	178.1(12)	154.1
			Al–O(5)–P	148.7(7)	146.6
			Al–O(6)–P	148.7(7)	141.8
			Al–O(7)–P	151.0(9)	143.5
			Al–O(8)–P	151.0(9)	146.5

[a]Fractional coordinates transformed into space group, $P6$

ergy with little change in the phonon spectrum. It must be noted that the NMR studies on this system are consistent with a structure containing three distinct Al and P sites,[314,315] which is inconsistent with any of the diffraction or computational studies at this time. In

keeping with the conclusion of de Man and co-workers,[293] no layer shift on minimisation with the formal charge model is observed. However, the contention of De Man that the un-

Figure 5.1: Comparison of experimental and calculated structures of $AlPO_4$-5.



derestimation of the charges in their model is responsible for the stability of the structures with space-group symmetry lower than experiment is not evident from this work.

$AlPO_4$-8,-11,-18 and -25

In the case of the $AlPO_4$-8, there are two structure determinations in the literature, both in space group $Cmc2_1$. Bennett and co-workers performed a time-of-flight neutron diffraction experiment,[49] whereas Dessau and co-workers used powder X-ray diffraction and a distance- least-squares method to refine their model.[303] Once again, the experimental space group gave imaginary frequencies in the phonon spectrum and the space-group symmetry was reduced. Two subgroups were found to give structures with no imaginary modes: $Pmn2_1$, in agreement with de Vos Burchart and co-workers,[210] and $P2_1$ which had slightly lower energy.

$AlPO_4$-11 also shows a deviation from the experimental space-group symmetry in the

minimised structure (reducing from $Ima2$ to $P2$), producing a structure that is more stable by 1.41 kJmol^{-1}, which is also consistent with the work of de Vos Burchart and co-workers.

Unlike the previous models, the energy minimisation of $AlPO_4$-18 in the experimentally determined space group ($C2/c$) by Simmen and co-workers[52] shows no imaginary frequencies in the phonon spectrum. The three site model is consistent with both the X-ray diffraction study and a recent NMR study.[296]

For the structure of $AlPO_4$-25, a deviation is found from the experimental space-group symmetry ($Abm2$) to lower symmetry ($Pca2_1$). The $P2_1$ model predicted by de Vos Burchart and co-workers also gives a minimised structure with no imaginary phonon modes, and has the same energy as the $Pca2_1$ model.

VPI-5

Several crystallographic papers on VPI-5 are in the literature. The first was determined by Rudolph and Crowder[280] and is for a hydrated system using the space-group $P6_3cm$. There is also a further structure for a hydrated sample in the lower symmetry space group $P6_3$[316] featuring a helical structure of water molecules. In addition, a dehydrated structure from Richardson and co-workers (described as $AlPO_4$-54) employs an average T-site model in the refinement (space group $P6_3$).[310] Minimisations for the dehydrated VPI-5 structure in $P6_3cm$ yielded imaginary vibrational modes, which were eliminated on moving to the lower symmetry space group $P6_3$. The $AlPO_4$-54 cell parameters are reproduced to within less than 1%, while the larger bond angles about oxygen (>165°) are all significantly reduced in the minimised structure. NMR studies on this system[317] have been mainly concerned with the hydrated system in which one of the three Al atoms is clearly octahedrally coordinated.

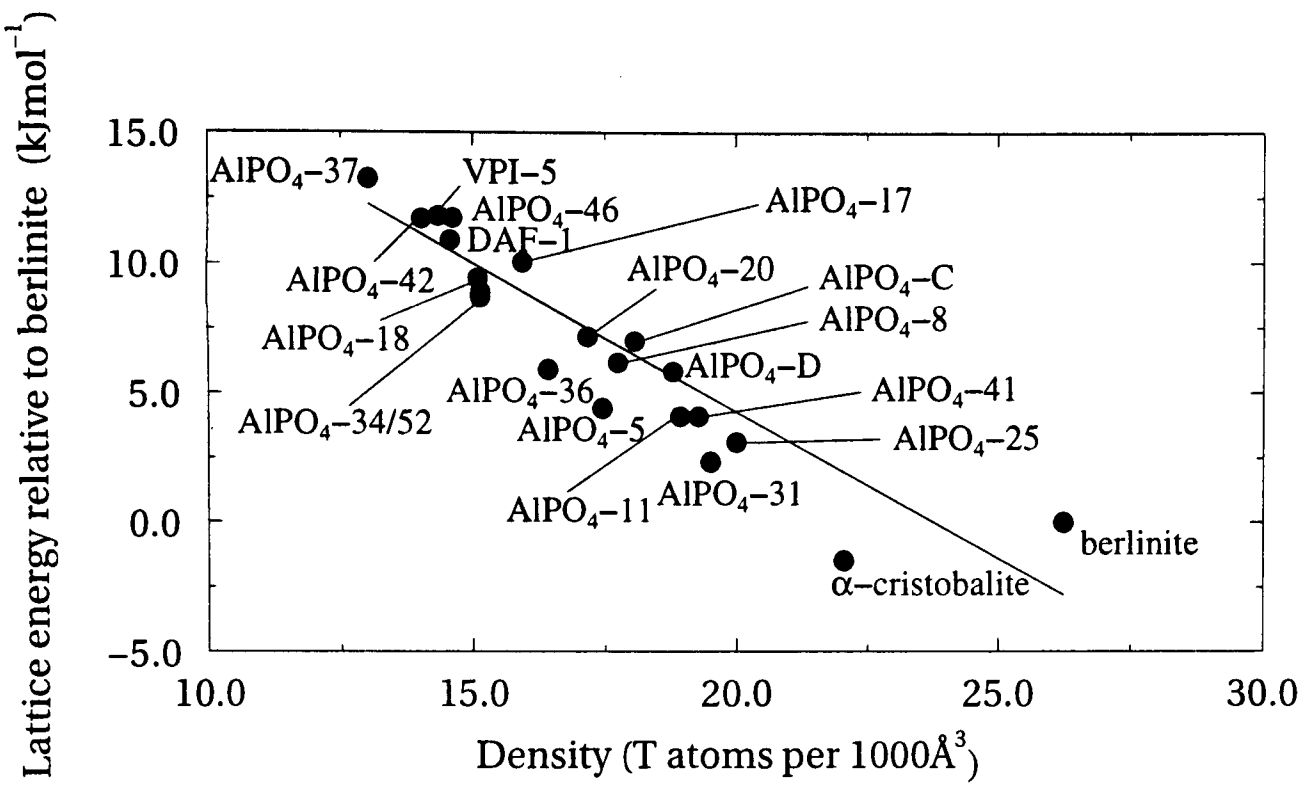
Condensed Phases

Unlike silicates, there is little crystallographic data available on condensed aluminophosphates possessing exclusively tetracoordinate aluminium. Mooney has reported a structure for the low temperature phase of cristobalite.[318] The minimisation energy of this structure was 1.47 kJmol^{-1} more stable than berlinite itself, which is clearly an anomalous

Table 5.5: Comparison of calculated and experimental structural parameters.

structure		space group	a (Å)	b (Å)	c (Å)	α (°)	β (°)	γ (°)
berlinite[300]	(expt)	$P3_121$	4.9423(3)	4.9423(3)	10.9446(13)	90.0	90.0	120.0
	(theory)	$P3_121$	4.91	4.91	10.96	90.0	90.0	120.0
α-cristobalite[318]	(expt)	$C222_1$	7.099(3)	7.099(3)	7.006(3)	90.0	90.0	90.0
	(theory)	$C222_1$	7.13	7.13	7.13	90.0	90.0	90.0
$AlPO_4$-17[305]	(expt)	$P6_3/m$	13.252(4)	13.252(4)	14.810(7)	90.0	90.0	120.0
	(theory)	$P6_3/m$	13.03	13.03	15.35	90.0	90.0	120.0
$AlPO_4$-20[278]	(expt)	$P\bar{4}3n$	8.77	8.77	8.77	90.0	90.0	90.0
	(theory)	$P\bar{4}3n$	8.87	8.87	8.87	90.0	90.0	90.0
$AlPO_4$-31[275]	(expt)	$R\bar{3}$	20.827(1)	20.827(1)	5.003(1)	90.0	90.0	120.0
	(theory)	$R\bar{3}$	20.65	20.65	4.99	90.0	90.0	120.0
$AlPO_4$-34[307]	(expt)	$R3$	13.781(1)	13.781(1)	14.846(2)	90.0	90.0	120.0
	(theory)	$R3$	13.69	13.69	14.64	90.0	90.0	120.0
$AlPO_4$-36[218]	(expt)	$P\bar{1}$	13.162(2)	22.1649(3)	5.189(1)	89.96(2)	92.17(2)	90.02(3)
	(theory)	$P\bar{1}$	13.16	21.51	5.16	90.0	90.9	90.0
$AlPO_4$-37[31]	(expt)	$Fd\bar{3}$	24.2576(3)	24.2576(3)	24.2576(3)	90.0	90.0	90.0
	(theory)	$Fd\bar{3}$	24.52	24.52	24.52	90.0	90.0	90.0
$AlPO_4$-41[308]	(expt)	$P2_1$	13.7915(1)	8.3591(1)	9.7180(1)	90.0	110.59(1)	90.0
	(theory)	$P2_1$	13.59	8.33	9.70	90.0	109.2	90.0
$AlPO_4$-42[276]	(expt)	$R\bar{3}c$	17.40(1)	17.40(1)	42.63(2)	90.0	90.0	120.0
	(theory)	$R\bar{3}c$	16.91	16.91	41.40	90.0	90.0	120.0
$AlPO_4$-46[291]	(expt)	$P31c$	13.23	13.23	26.89	90.0	90.0	120.0
	(theory)	$P31c$	13.10	13.10	26.26	90.0	90.0	120.0
$AlPO_4$-52[319]	(expt)	$P\bar{3}1c$	13.73	13.73	28.95	90.0	90.0	120.0
	(theory)	$P\bar{3}1c$	13.70	13.70	29.23	90.0	90.0	120.0
$AlPO_4$-C[320]	(expt)	$Pbca$	19.816(10)	10.047(10)	8.935(10)	90.0	90.0	90.0
	(theory)	$Pbca$	19.59	10.10	8.95	90.0	90.0	90.0
$AlPO_4$-D[320]	(expt)	$Pca2_1$	19.187(10)	8.576(10)	9.804(10)	90.0	90.0	90.0
	(theory)	$Pca2_1$	20.06	8.39	10.10	90.0	90.0	90.0
DAF-1[321]	(expt)	$P6/mcc$	22.164(1)	22.164(1)	42.482(2)	90.0	90.0	120.0
	(theory)	$P6/mcc$	22.15	22.15	42.53	90.0	90.0	120.0

Figure 5.2: Calculated lattice energy as a function of density. Energy relative to berlinite per tetrahedral atom.



result since berlinite is the most stable of the aluminophosphate polymorphs. Wright and Leadbetter have shown the high temperature phase of cristobalite to have disorder on one of the oxygen sites[269] making this structure unsuitable for consideration in this work. The remaining minimised structures are compared to experimental data in Table 5.5.

5.3.2 Variation of Lattice Energy with Density

As in the previous chapter, the minimised lattice energy shows a linear correlation with density (Figure 5.2). The range of energies observed from $AlPO_4$-37 to berlinite (11.7kJmol^{-1}) is slightly more than for the silicate analogues (10.1kJmol^{-1}). A recent thermochemical study[297] has measured the lattice enthalpies of several aluminophosphate structures. A comparison of experimental versus calculated lattice enthalpies is shown in Table 5.6. The agreement is not as impressive as has been found in the case of silicates (Chapter 4), but the general trend of more dense structures being the most thermodynamically stable is still reproduced. The spread of calculated lattice energies is somewhat larger than experiment, probably due to the use of formal charges in the forcefield. Quantum-mechanical calculations on silicates have shown that the actual charges are considerably less than the formal values.

Table 5.6: Comparison of experimental and calculated lattice energies. Energy is expressed relative to berlinite per tetrahedral atom.

structure	experimental lattice enthalpy ($kJmol^{-1}$)	minimised lattice energy ($kJmol^{-1}$)
berlinite	0.0	0.0
cristobalite	3.0	-1.6
$AlPO_4$-5	7.0	4.4
$AlPO_4$-8	5.4	6.2
$AlPO_4$-11	6.2	4.1
$AlPO_4$-42	7.8	11.7
VPI-5	9.7	10.8

5.4 Proton Sitings

One of the aims of the fitting of a forcefield for aluminophosphates using a formal-charge shell model was to obtain a transferable set of potentials which were compatible with existing forcefields for other systems. With this in mind, the aluminophosphate forcefield was combined with that for silicates derived by Schröder and co-workers[322] to study the siting of protons in the H-SAPO-37 system.

Schröder and co-workers have fitted a forcefield for the prediction of proton siting in aluminosilicate systems,[322] using a combination of the Sanders forcefield for silicates[205] and a potential for the bridging hydroxyl group by Saul and Catlow.[323] This forcefield has been used to study both the H-faujasite system[322] and also H-silicalite.[324] The primitive unit cell of SAPO-37 was constructed from the neutron diffraction study of Bull and co-workers[325] and minimised in the pure $AlPO_4$ form (final cell parameters: a=b=c=17.34Å , α=β=γ=60.0°). Four starting models were created by placing a proton at each of the crystallographically distinct oxygen positions in this minimised structure. Two sets of calculations were performed on SAPO-37. In the first set the system is defined as periodic, and consists of 24 Al species, 23 P species, 95 oxygen species (core plus shell), and a single O–H group in the primitive unit cell of SAPO-37. Since the primitive cell dimension is 17.34Å, interactions between protons in adjacent cells should give only a negligible perturbation to the total energy. A minimisation at constant pressure was performed for each of the four possible positions for the bridging hydroxyl group. In addition to the periodic calculations,

a set of defect calculations was also performed based on the approach of Mott and Littleton.[187] In this method, the proton is represented as an interstitial hydrogen atom bonded to the bridging oxygen group, the centre of the defect cluster being at the silicon position. All atoms lying within a sphere of radius r_2 of the defect centre are treated explicitly, and within an inner sphere of radius r_1 the atoms are allowed to relax during the minimisation. Outside the r_2 boundary, interactions with the defect are handled more approximately as a dielectric response to the defect charge. Several calculations were performed using increasing values of r_1 and r_2. Using values of r_1=13Å and r_2=24Å the energy change on increasing the radii further was found to be less than 0.001 eV for each minimised structure. This corresponds to an inner region of 582 atoms.

Both the periodic and defect-cluster calculations give the same ordering in energies; stability decreasing in the series O(3) $\approx$ O(1) >> O(2) > O(4). The crystallographic study of Bull and co-workers determined the proton occupancies to decrease in the order O(1) > O(2) > O(3), with no occupancy of the O(4) site. Although these calculations predict the stability of the O(1) site, the trend in the occupancies is not reproduced by the calculated proton energies. Since the crystallographic study represents an average structure with protons located at all the occupied bridging positions, individual bond lengths and angles cannot be compared to the results here. In addition, since the O–H bond length was constrained to a value of 0.96Å in the crystallographic refinement, it is difficult to make a direct comparison with the calculated bond length from the simulation. However, the calculated values do show good agreement with a recent neutron diffraction study of the proton positions in H-SAPO-34.[34]

The agreement between the structural properties for the periodic and defect calculations shows the equivalence of the two approaches for this system, the discrepancies in bond lengths and bond angles being less than 0.005Å and 0.4° (Table 5.7). In addition, the relative energies agree to within 0.8 kJmol^{-1} and the calculated O–H stretching frequencies differ by only 2 cm^{-1}. Dzwigaj and co-workers carried out infra-red measurements on H-SAPO-37 and found two O–H stretching frequencies at 3640 cm^{-1} and 3575 cm^{-1}.[326] The calculated O–H stretching frequencies are too large compared to experiment. As Schröder and co-workers observed, the calculated vibrational frequencies with this forcefield model represent harmonic values.[322] Correcting the stretching frequency for anharmonicity cor-

Table 5.7: Geometries of the four bridging hydroxyl groups, energies and O-H stretching frequencies.

	$r_{O\text{-}H}$ (Å)	$r_{Si\text{-}O}$ (Å)	$r_{Al\text{-}O}$ (Å)	$\theta_{Al\text{-}O\text{-}Si}$ (°)	$\theta_{Si\text{-}O\text{-}H}$ (°)	relative energy ($kJmol^{-1}$)	ω (cm^{-1})
periodic							
O(1)	0.998	1.791	1.829	130.7	112.6	1.2	3794
O(2)	1.002	1.779	1.825	142.0	108.8	14.2	3727
O(3)	0.999	1.815	1.821	138.9	106.9	0.0	3766
O(4)	0.999	1.784	1.829	134.4	111.1	17.7	3772
defect cluster							
O(1)	0.998	1.790	1.825	130.7	112.2	1.9	3792
O(2)	1.002	1.779	1.823	141.6	108.7	14.6	3728
O(3)	0.999	1.815	1.820	138.7	107.0	0.0	3765
O(4)	0.999	1.783	1.824	134.2	110.9	18.5	3770

Table 5.8: Comparison of bond angles about oxygen for experimental and minimised structures of SAPO-37. Experimental e.s.d.s are given in brackets.

angle at indicated oxygen	expt	minimised structures with proton at indicated site				minimised $AlPO_4$-37
		O(1)	O(2)	O(3)	O(4)	
O(1)	137.86(30)	130.7	154.7	145.4	138.7	139.6
O(2)	149.79(27)	138.5	142.0	141.6	140.1	148.4
O(3)	144.47(29)	142.6	150.8	138.9	146.3	146.9
O(4)	144.6(4)	134.4	143.6	147.2	134.4	141.6
average		136.6	147.8	143.3	139.9	

responds to subtracting about 150 cm^{-1} from the calculated values, which brings them much closer to those measured by experiment. Clearly, the inability of the simulations to reproduce the correct order of proton occupancies combined with the deficiencies in the calculated O–H frequencies suggest that further work is needed to refine the current forcefield.

It is interesting to note that the empirical rule relating the most favourable binding sites for protons to the bridging oxygen with the smallest angle does not appear to apply completely[327] (see Table 5.8). Bull and co-workers[325] have suggested that in the case of H-

SAPO-37 this effect may be complicated by additional hydrogen-bonding interactions. In the minimisations, the binding of the proton at the bridging oxygen causes a significant contraction in the oxygen angle compared to the minimised structure of the parent $AlPO_4$. In an attempt to relate the oxygen bond angles to the crystallographic study, which essentially represents a mean picture of the system with all the proton sites partially occupied, the bond angles were averaged about each of the bridging oxygens over the four minimised structures. The average angles are found to reproduce the crystallographic values to within 2°, with the notable exception of the O(4) site (Table 5.8).

Chapter Six

Molecular Dynamics Studies of Xe in Zeolites FER and LTL

There is a wide range of levels of computational theory that can be applied to problems in zeolite chemistry; from the exact methods of quantum mechanics, through techniques employing more empirical approaches and the use of forcefields to treatments that eliminate the zeolite completely replacing the potential energy surface by a simple function. When considering the complex behaviour of host-guest interactions in zeolites, the use of a relatively simplistic model can still be fruitful in the investigation of the underlying features that are important to the process. In this chapter, two basic questions are asked with regards to the diffusion of molecules in zeolites. Firstly, the effect of the width of a zeolite channel on the rate at which guest molecules move through zeolite pores is studied, and secondly, the effect of the shape of the pore on the diffusivity is investigated.

6.1 Xenon as a Probe for Diffusion in Zeolites

Xenon is a useful probe in the study of pore structure and transport properties of molecules in zeolites has a number of advantages to both the experimentalist and the computational chemist alike. It is monoatomic and, for the purposes of pore access, spherical. The predicted van der Waals radius for xenon (2.10 Å) is also very similar to that of methane (2.19 Å), so it makes a useful comparison. Thus, it is one of the simplest guest species that can be studied. It is large enough to allow some degree of molecular sieving to take place, that is, it can pass through certain ring sizes but not others. Additionally from the experimental perspective, ^{129}Xe is an important NMR nucleus. In comparison to other possible probes ^{129}Xe has a large chemical shift range due to the highly polarisable electron cloud. Since xenon is a noble gas, there is also no possibility of reactions occurring while making measurements. The initial work performed by Fraissard and co-workers[78] showed that the Xe chemical

shift is sensitive to quantities such as pore and channel dimensions,[79,80] and cation distributions.[328] From a consideration of the chemical shift dependence on sorbate loading, sorption isotherms can be derived,[231] and the behaviour of other guest molecules can be inferred.[81] One of the most exciting developments with regards transport of fluids within zeolite pores is the pulsed-field gradient NMR method which can be used to measure self-diffusivities of Xe directly.[235] These experimental measurements provide the opportunity for a direct comparison with computational results as has been demonstrated recently by Jameson and co-workers[231] and can provide a benchmark to test the validity of the calculations prior to considering systems of greater catalytic interest.

There have also been a limited number of diffraction studies which have located xenon atoms in zeolite pores. The first study was by Wright and co-workers who located xenon in zeolite ρ with neutron diffraction.[329] Recently the application of anomalous scattering has stimulated further interest in this field. Jones and co-workers have used on-edge Kr anomalous scattering to locate krypton atoms in ferrierite[330] and silicalite.[331]

6.2 Computational Studies of Xenon in Zeolites

The first work carried out by Kiselev and co-workers presented a relatively simple model for silicalite to calculate thermodynamic properties such as Henry's constants and isosteric heats of sorption[332] with Slater-Kirkwood type expressions to derive potential parameters.[333] This method is problematic since the values of polarisabilities of species in the zeolite are not directly measurable with experimental techniques. This problem will be discussed in more detail in the next Chapter. The first attempt to perform Xe molecular dynamics in zeolites was made by Yashonath and co-workers in a study of Xe in faujasite,[334] which was followed by studies in other zeolites.[233,242,335] In addition, the technique of Grand Canonical Monte Carlo has been employed by several groups to calculate sorption isotherms which can be compared directly to experiment.[230–232]

6.3 The Structures of Ferrierite and Zeolite-L

The ferrierite structure is based on five-ring building units that are stacked along the c-axis. These units are connected to form ten-ring channels of elliptical cross-section (4.3x5.5Å) that lie parallel to the c-axis and are interconnected by smaller eight-ring channels running parallel to b-axis[336] (see Figure 6.1). In contrast, zeolite-L features 12-ring channels, which define a free aperture of 7.2 to 7.8Å, running parallel to c-axis[287] (see Figure 6.1).

When xenon is the sorbate, both zeolites present essentially one-dimensional channel structures – the eight-ring side channels in ferrierite are too small to allow passage of xenon. This study allows the examination of the effects of channel size and channel shape on the one-dimensional motion of a simple sorbate in a zeolite.

6.4 Computational Details

All calculations were performed with the DIZZY software[337] (Appendix B) developed in Oxford, Princeton and UCSB on the Oxford University Computing Service's C1-XP2 Convex system with two identical C120 processors, and on the MEPSI CRAY-YMP at the Dallas Research Laboratory of Mobil Research and Development Corporation.

Molecular dynamics calculations were carried out with a cut-and-shifted Lennard-Jones (12-6) potential for both the zeolite-sorbate and sorbate-sorbate interactions :

$$E_{ij} = \frac{A_{ij}}{r_{ij}^{12}} - \frac{B_{ij}}{r_{ij}^{6}} - V_c \quad r_c \leq r_{ij} \leq 0 \tag{6.1}$$

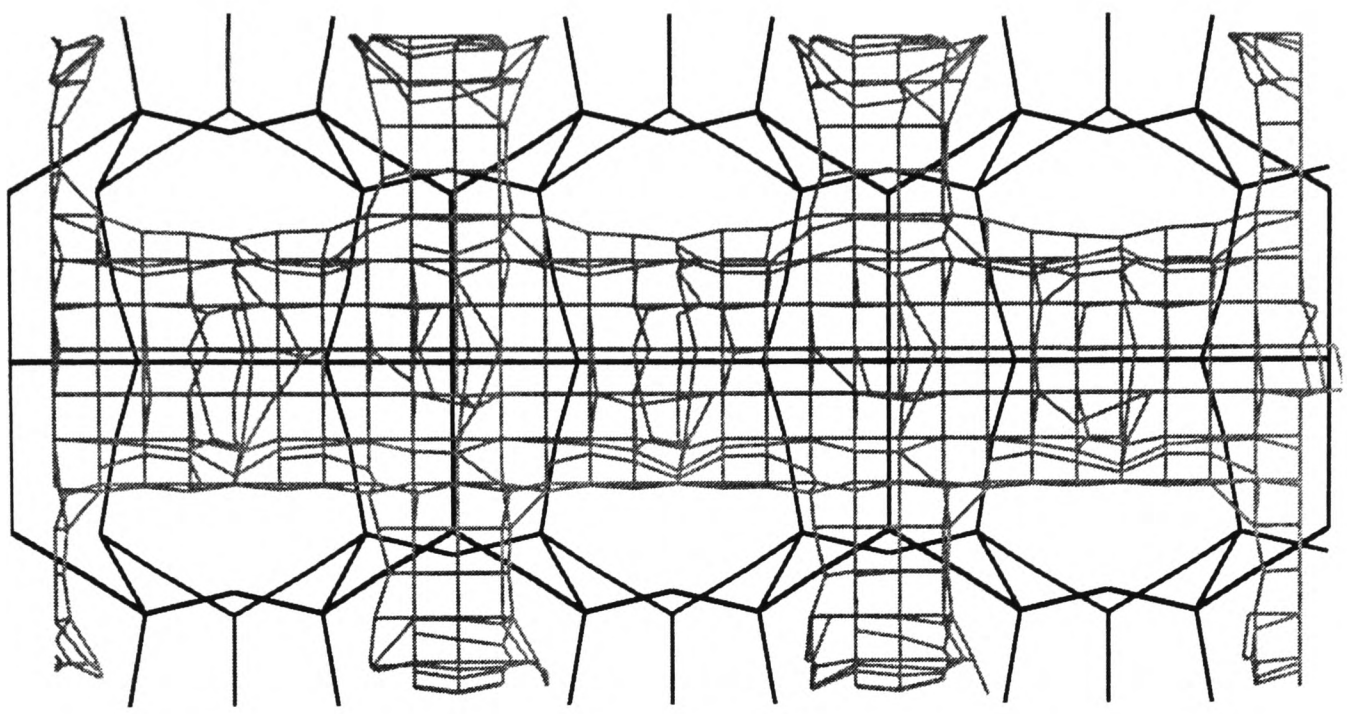
where :

$$V_c = \frac{A_{ij}}{r_c^{12}} - \frac{B_{ij}}{r_c^{6}}$$

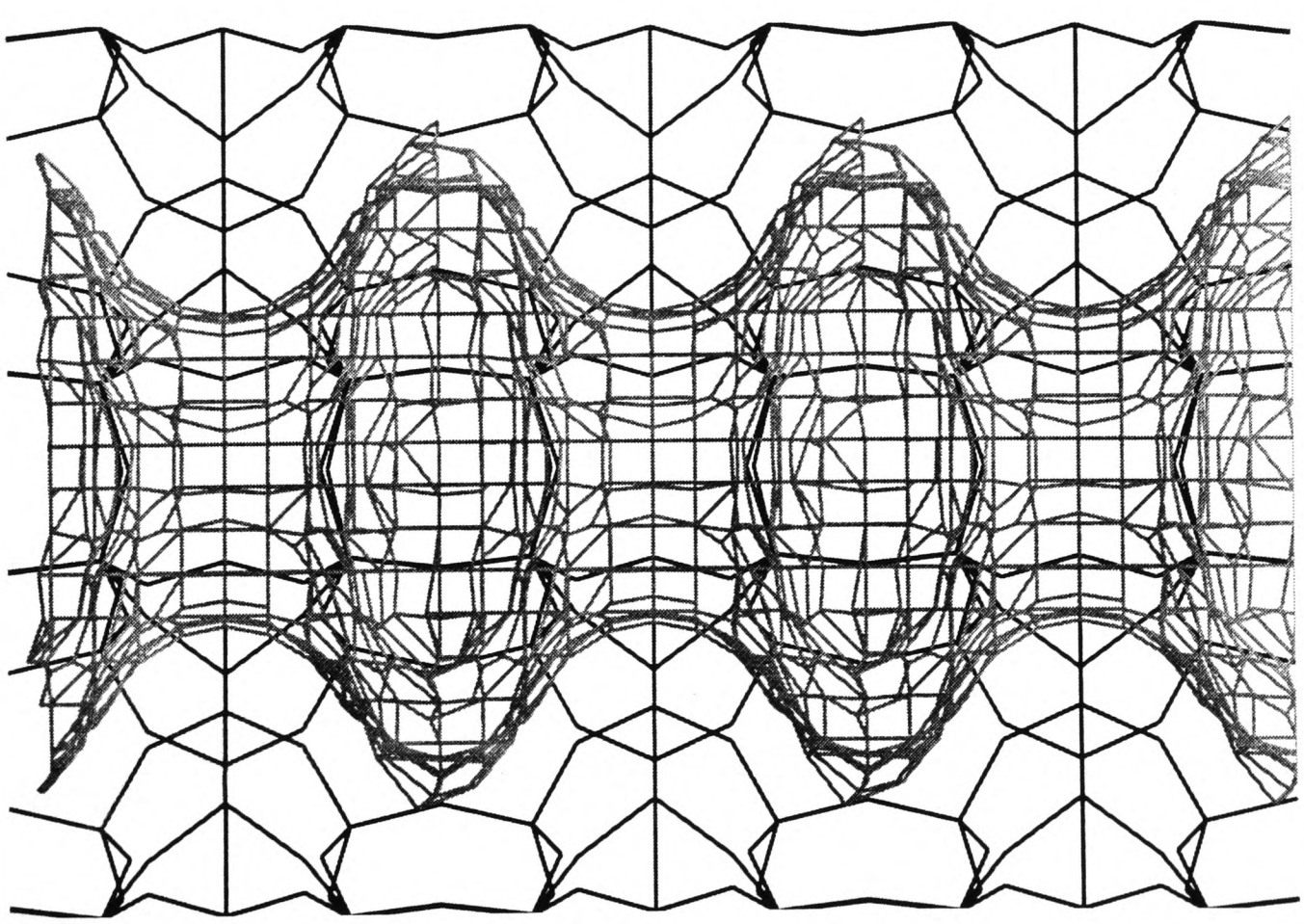
and E_{ij} is the energy between species i and j, A_{ij} and B_{ij} are fitted parameters, r_{ij} is the separation, and r_c is an arbitrary cut-off radius.

The parameters were obtained from the approach of Kiselev and co-workers[332] and are given in Table 6.1. Furthermore, due to the negligible polarisability of the silicon atoms in the framework, it was assumed that interactions with silicon could be neglected, the error

Figure 6.1: Schematic representation of the main channel in (a) ferrierite, and (b) zeolite-L. The net shows the van der Waals surface of the channel



(a)



(b)

being absorbed into the effective polarisability on oxygen. The velocity Verlet algorithm[338]

Table 6.1: Lennard-Jones parameters

	A ($kJÅ^{12}mol^{-1}$)	B ($kJÅ^{6}mol^{-1}$)
Xenon-Zeolite	$8.61x10^{3}$	$1.11x10^{7}$
Xenon-Xenon	$3.36x10^{4}$	$1.51x10^{8}$

was used to integrate Newton's equations of motion within the *NVT* ensemble with a time-step of 5fs. The zeolite structures were modelled as being rigid and purely siliceous. The coordinates of the atoms in the unit cells were taken from recent neutron powder refinements of the two zeolites.[53,288] In the case of ferrierite a 1x2x3 array of unit cells was constructed to form the simulation box, whereas in the case of zeolite-L, a larger 2x2x3 array of unit cells was built and the supercell was transformed into the primitive orthorhombic frame to accelerate the computations. This choice allowed the use of a cut-off for the potentials of 10.5 Å, as well as ensuring that each simulation box contained four main channels. Initially the atoms were placed equidistantly along the centres of the main channels, and the system allowed to equilibrate for a 2000ps period. Using the final configuration of this run as a starting point, five further 600ps simulations (sub-runs) were carried out with the atoms' velocities being randomised over a Gaussian distribution at the beginning of each sub-run. The data obtained from these sub-runs were averaged to obtain the final quantities of interest. The statistical errors in the diffusion coefficient, at the lowest loading level, were estimated to be approximately 25%. A variety of loadings were considered, ranging from two to five atoms per main channel of the zeolite (0.66 to 3.33 atoms per unit cell). The temperature dependent properties of the system were probed by repeating the simulations at a series of temperatures from 200K to 600K.

6.5 Results and Discussion

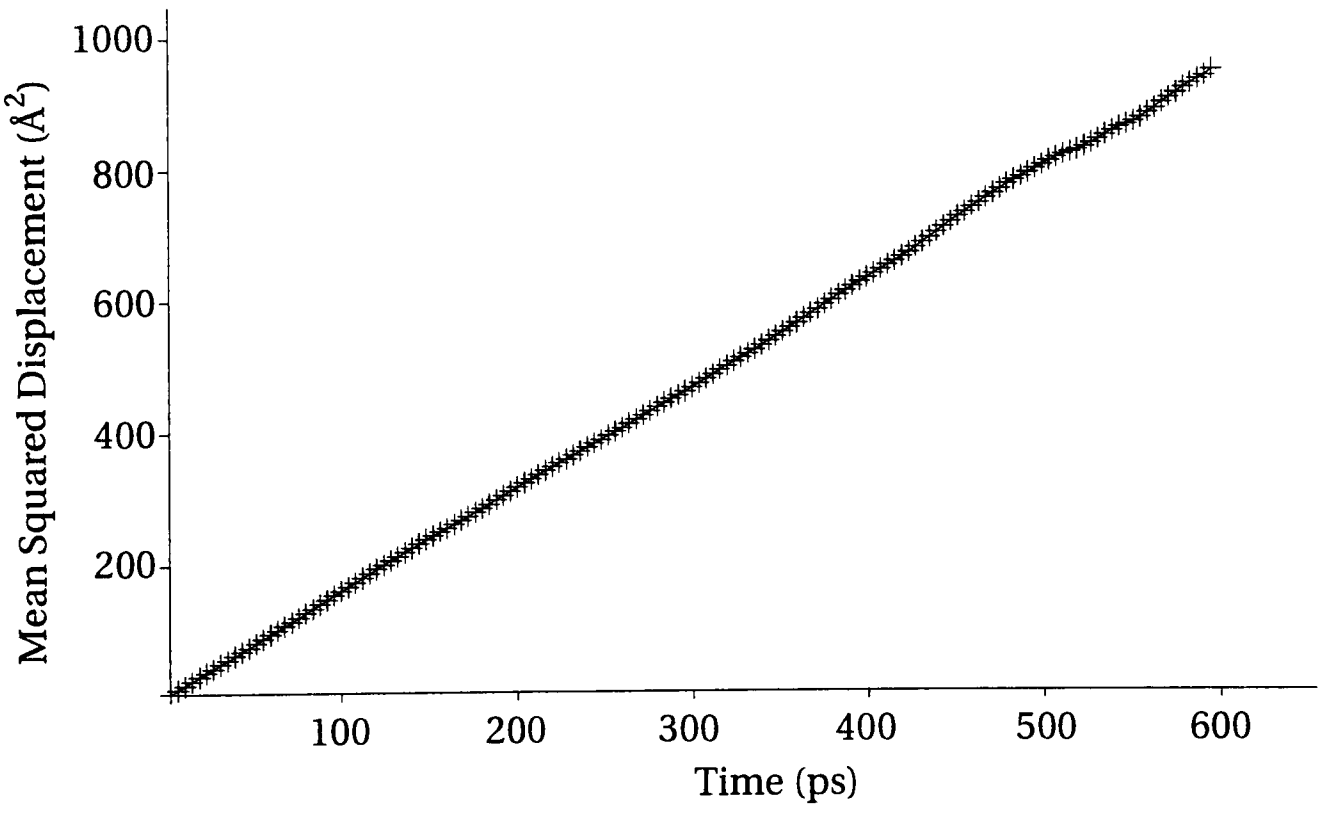
Diffusion coefficients were derived from mean-squared displacements rather than from calculation of the velocity auto-correlation function. To smooth the mean squared displacement data, a multiple-time origin analysis was performed,[335] which utilizes the ex-

pression :

$$\langle r^2 \rangle (n\delta t) = \frac{1}{N} \frac{1}{(N_p - n)} \sum_{i=1}^{N} \sum_{j=1}^{(N_p - n)} \left[r_i \left(t_j + n\delta t \right) - r_i \left(t_j \right) \right]^2 \tag{6.2}$$

where N is the total number of Xe atoms, N_p is the number of points in the data-set and δt is the time interval between points. The fine details of individual trajectories are necessarily omitted in this treatment since only the diffusion coefficients are of direct interest. For long time periods, the mean squared displacement $\langle r^2 \rangle$ shows a linear correlation with time, as illustrated in Figure 6.2, and the diffusion coefficients in each of the simulation box

Figure 6.2: Mean squared displacement plot for xenon diffusion in zeolite-L at 500K with five xenon atoms per main channel



directions can be calculated by a least-squares fit to the Einstein equation :-

$$\langle r^2 \rangle = A + 2Dn\delta t \tag{6.3}$$

where A is a constant and D is the diffusion coefficient in one dimension. Thus the Einstein equation can be give anisotropic diffusion coefficients down each of the channel directions in the zeolite. These coefficients are shown in Table 6.2. As expected, the motion of Xe atoms is dominated by diffusion down the main channel of the zeolite.

Table 6.2: Diffusion coefficients along each cell axis at 298K with three Xe atoms per main channel (e.s.d.'s are shown in brackets)

	D(a) (m^2s^{-1})	D(b) (m^2s^{-1})	D(c) (m^2s^{-1})
Ferrierite	$5.8(195)x10^{-14}$	$1.1(37)x10^{-13}$	$1.5(1)x10^{-8}$
Zeolite-L	$2.4(16)x10^{-11}$	$1.4(12)x10^{-11}$	$3.4(2)x10^{-9}$

From an analysis of the temperature dependence of the diffusivity the mechanism of the diffusion process can be investigated. The calculated diffusion coefficients down the main channel of each zeolite as a function of temperature and loading are shown in Figure 6.3. The diffusivity shows a general increase with temperature reflecting the greater kinetic energy of the atoms, although this behaviour is not apparent for ferrierite at low loadings. This result is probably an artifact due to non-ergodic effects that occur when an atom becomes trapped in a strong binding site. This situation is more likely in ferrierite in which xenon atoms are more strongly bound. An atom bound in this way can only escape if it receives energy from a collision with another particle (the atom could also receive energy from the lattice if it was allowed to flex), which is less likely at low loading. Indeed, at low temperatures the mean-squared displacement often displays steps as a function of time indicating that the jumps between adjacent potential energy minima are not adequately sampled during the simulation, and the averages obtained not as statistically meaningful.

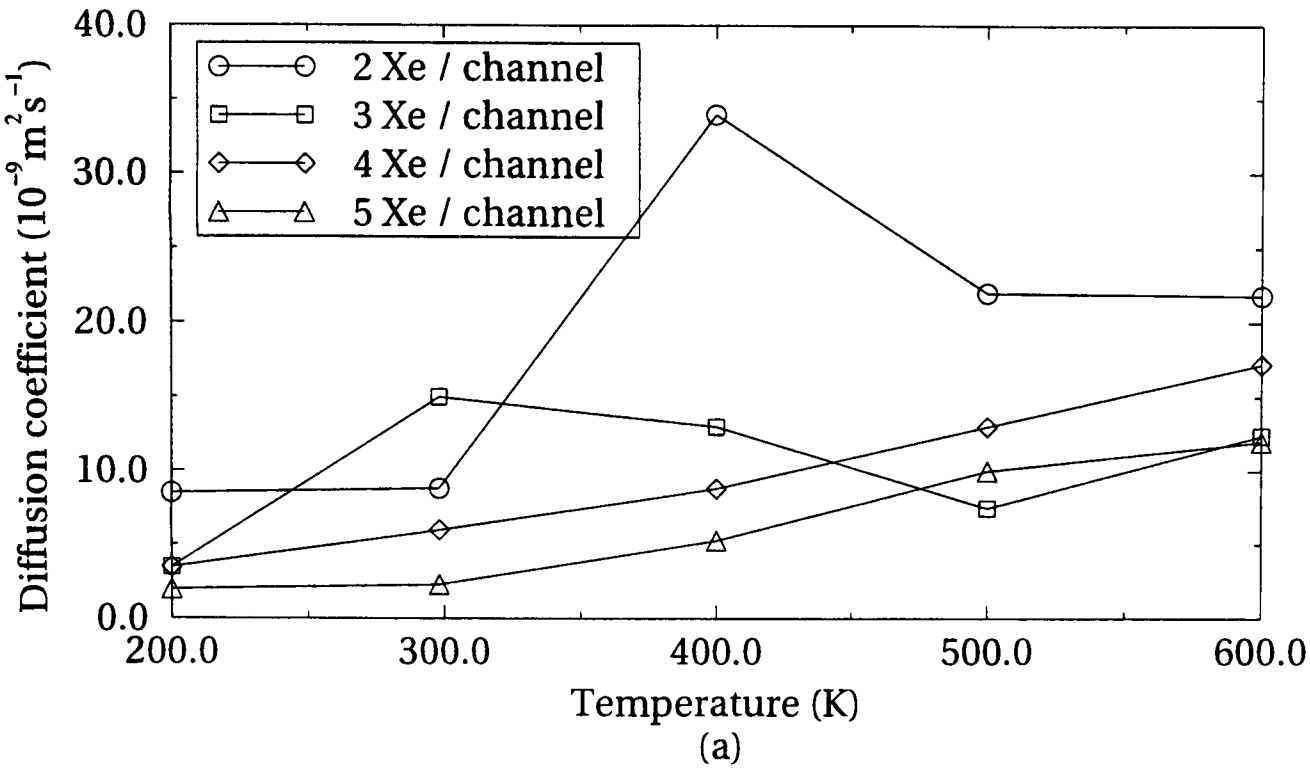
The diffusion data were fitted to an Arrhenius-type expression of the following form :

$$D = D_0 exp\left(-\frac{E_a}{RT}\right) \tag{6.4}$$

where D is the diffusion coefficient, D_0 is the pre-exponential factor, E_a is the activation energy for diffusion, k is the Boltzmann constant and T is the absolute temperature. Typical plots for the two zeolites are shown in Figure 6.4. Although, a good fit to this equation was obtained for zeolite-L at all loading levels, this was only true for ferrierite at high loadings. Again this is probably due to poor statistics at the low loadings as discussed above. Activation energies and pre-exponential factors were extracted from the fits and are given in Table 6.3.

Intuitively, it would be expected that the activation energy would be directly related to

Figure 6.3: Variation in diffusion coefficient with temperature and loading for (a) ferrierite and (b) zeolite-L



the potential energy barriers that a single atom experiences moving down the zeolite pore. To investigate this further, a programmed search of the potential energy surface was performed. The zeolite channel was divided into equally spaced disks and random insertions performed in an appropriate sector of the cross-section based on the point group symmetry of the ring defining the channel.

As will be seen in Chapter 9, although this rather crude method works well for monatomic systems, when molecules are considered more sophisticated algorithms are needed to determine energy profiles such as constrained energy minimisation.

Figure 6.4: Comparative Arrhenius plots for ferrierite and zeolite-L. Points represent calculated diffusion coefficients. The dashed lines are the best fit line to the Arrhenius equation

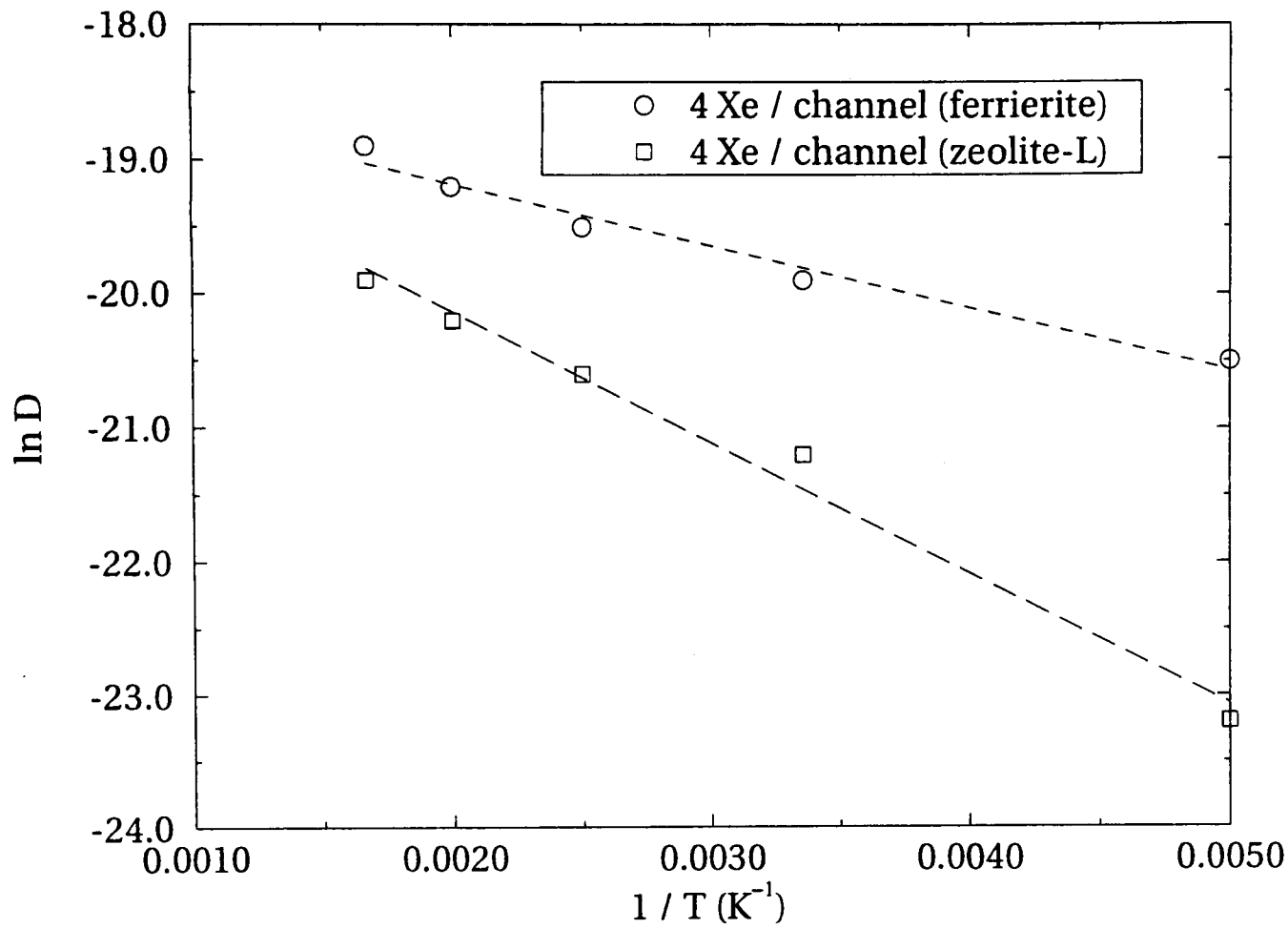


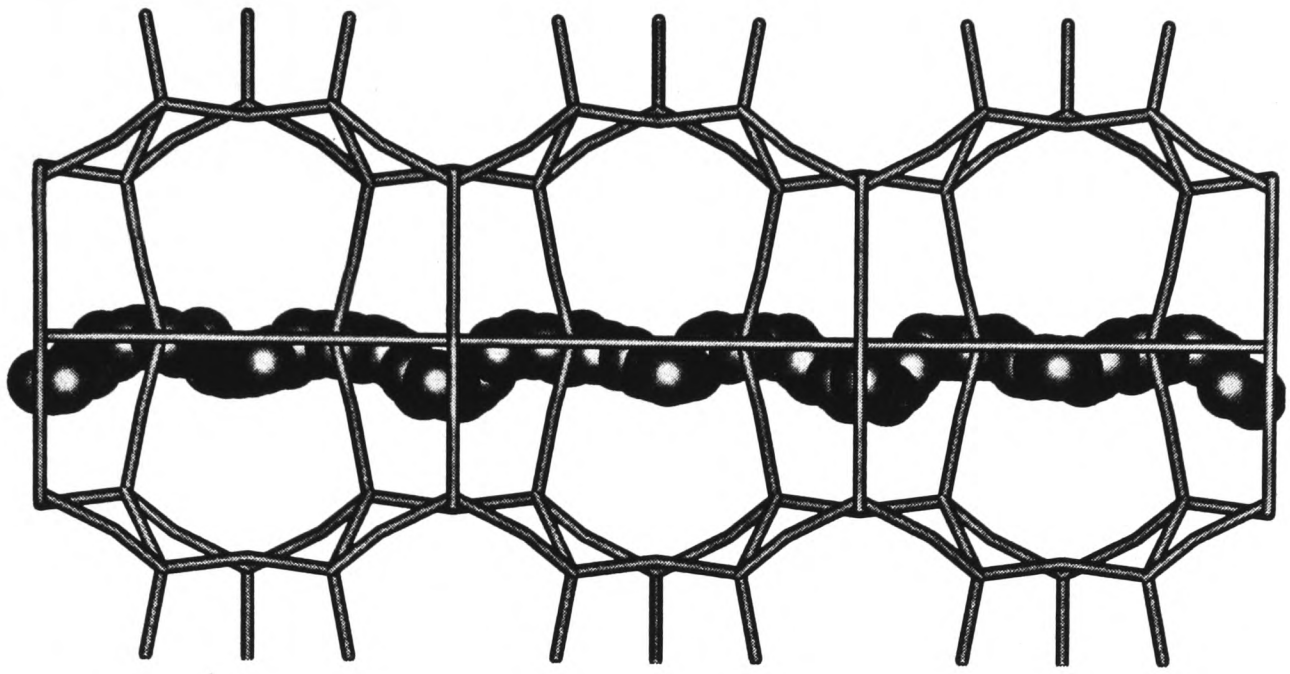
Table 6.3: Variation in pre-exponential factor (D_0) and activation energy (E_a) with loading

Xe atoms per channel	ferrierite		zeolite-L	
	D_0 (m^2s^{-1})	E_a ($kJmol^{-1}$)	D_0 (m^2s^{-1})	E_a ($kJmol^{-1}$)
2	[a]	[a]	$7.9(37)x10^{-8}$	11.5(12)
3	[a]	[a]	$7.0(8)x10^{-8}$	10.4(3)
4	$3.5(5)x10^{-8}$	4.1(3)	$4.9(18)x10^{-8}$	9.3(9)
5	$3.4(14)x10^{-8}$	5.5(9)	$5.2(14)x10^{-8}$	8.9(7)

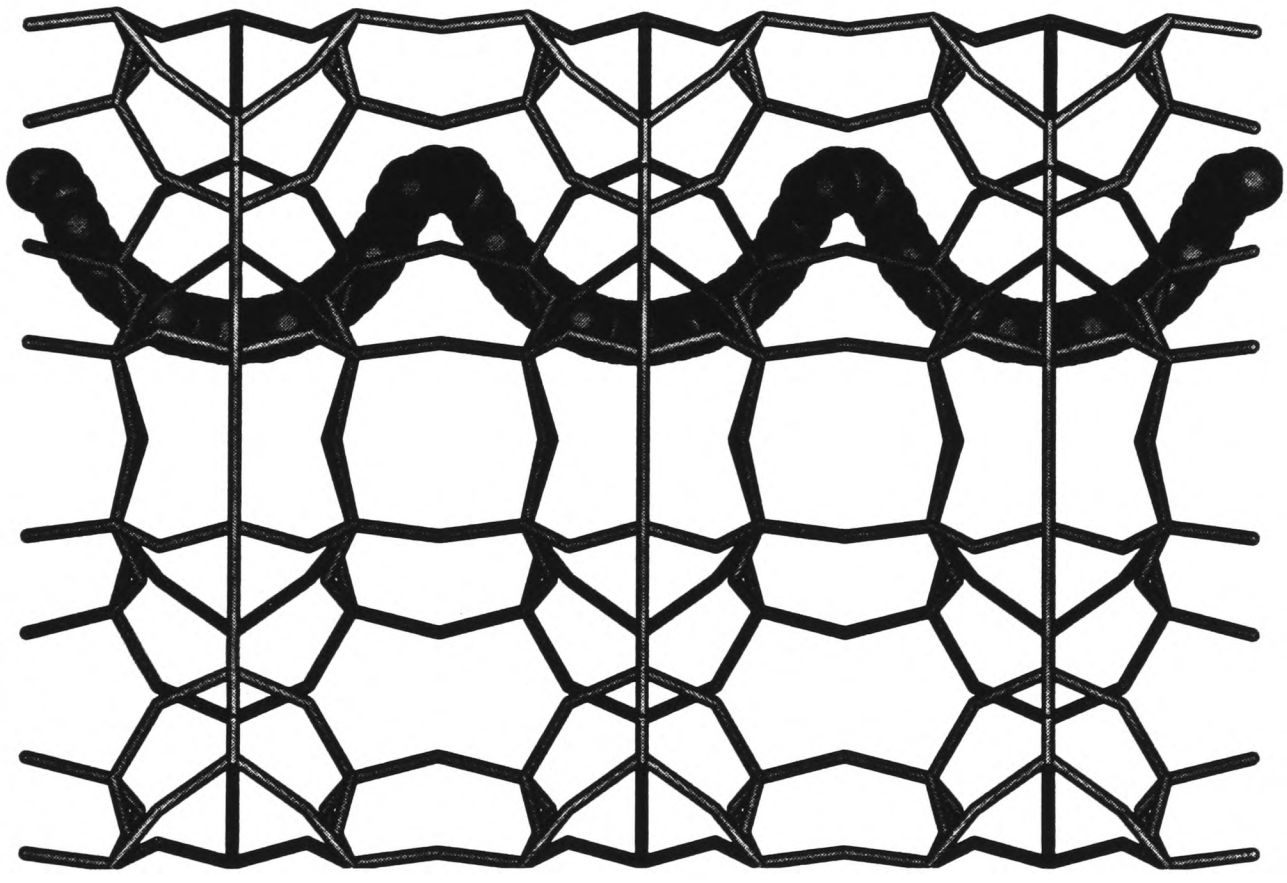
[a]Poor fit to Arrhenius equation

Figure 6.5 shows the predicted energy trajectories down the main channels of ferrierite and zeolite-L. Clearly, the effect of surface curvature has a marked influence on the potential energy surface, as suggested by the work of Derouane.[339–341] In ferrierite, the motion

Figure 6.5: The predicted minimum energy pathways for a single xenon atom moving down the main channel in (a) ferrierite, and (b) zeolite-L



(a)



(b)

is essentially confined to the centre of the channel with only slight perturbations as the probe atom passes the eight-ring side-channel, whereas in zeolite-L the channel is wide enough for the xenon atom to map out the torsions in the channel surface quite distinctly. Clearly, these different pathways suggest two very distinct diffusion mechanisms. In ferrierite, it can be envisaged that xenon atoms have constantly been propelled down the

channel by collisions from behind; resulting in a relatively straight trajectory. In zeolite-L, xenon atoms entering may move around the channel wall to more favourable binding sites rather than following the straighter trajectory. Thus, for atoms to move down the main channel in zeolite-L, they must follow the curve of the channel wall, hence producing a much lower diffusivity than for ferrierite.

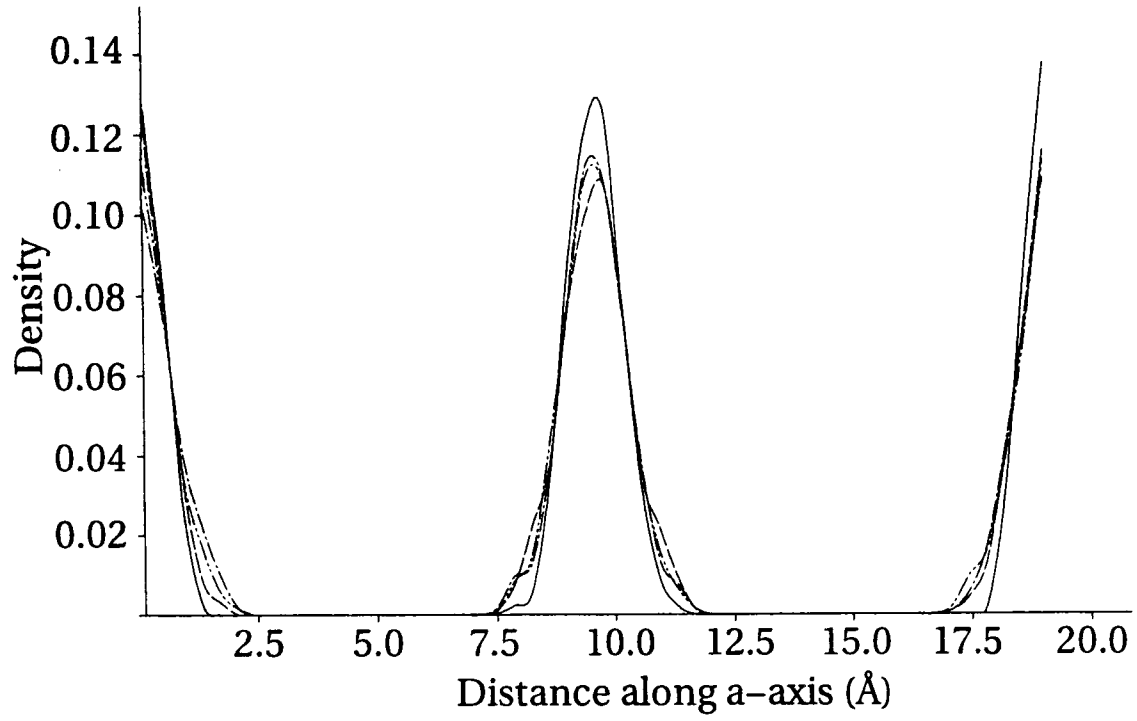
In Table 6.3 it can been seen that, within the statistical errors in the calculations, there is very little difference in the pre-exponential factors for the two zeolites, although the activation energies for zeolite-L appear to be significantly larger. This correlates with the values obtained from the probing of the potential energy surface above (see Figure 6.5). In addition, it can also be noted that there is a slight decrease in the activation energy at higher loadings. At high loading, there exists the possibility of a xenon atom entering a cavity in which there are already other atoms close to the cavity walls, thus requiring the atom to follow a much straighter trajectory as in the case of ferrierite.

When considering the effects of loading on the diffusivity, it would be expected that as the loading increases the transport through the channel should be retarded. However, there are many subtle effects to consider, such as whether the motion is in the Knudsen or configurational regimes as suggested by Tsikoyiannis and co-workers[342,343] and Derouane and co-workers.[339–341] This trend is observed for ferrierite especially at low loading; however, little loading dependence is observed for zeolite-L. The wider sections of the main channel in zeolite-L allow side-by-side passage of xenon atoms and may allow the 'floating' effect proposed by Derouane and co-workers to occur. In this case, the onset of loading effects may require considerably higher loading than for ferrierite.

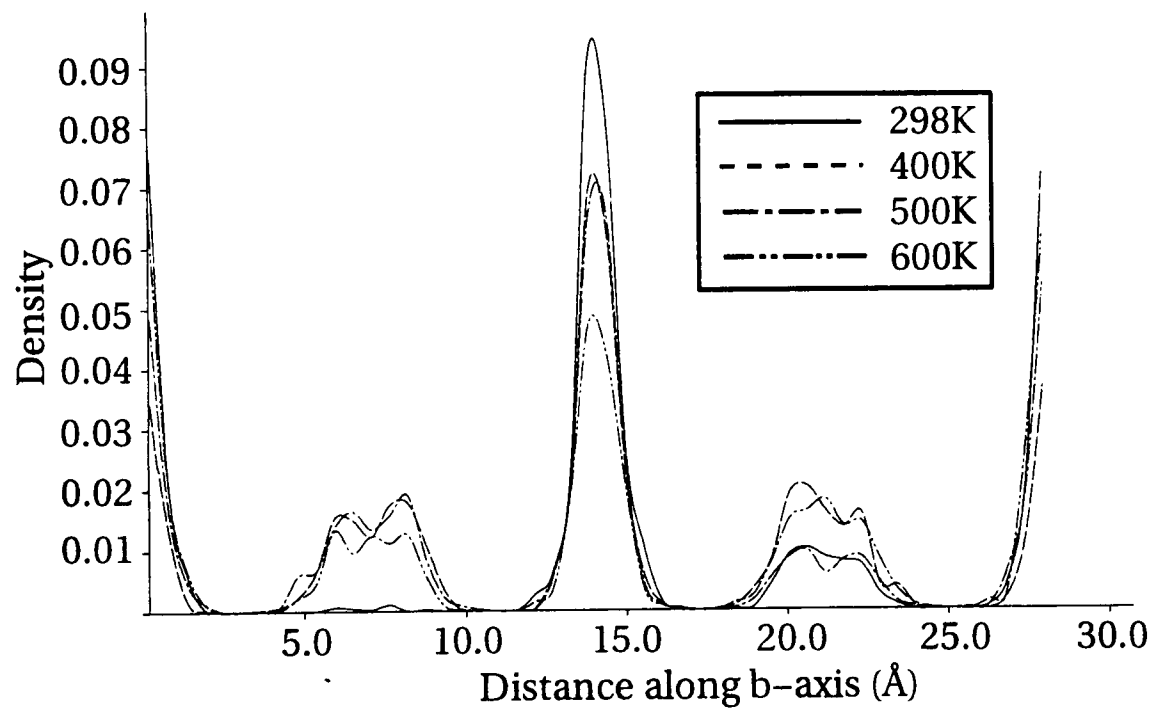
Sorbate distribution functions were calculated to show the variation in Xe density across the three simulation box directions. These are shown in Figures 6.6 and 6.7. Firstly considering the distribution functions along the main channel directions: six peaks are observed in the case of ferrierite, whereas only three are observed for zeolite-L. This further illustrates the effect of the different channel systems on diffusion. Three of the peaks for ferrierite correspond to minima in the centre of main channel, whereas the remaining peaks represent positions adjacent to the entrances to the side channels.

The peaks for zeolite-L also correspond to minima on the potential energy surface. This is further emphasised in Figure 6.8, which shows the projected xenon positions from an

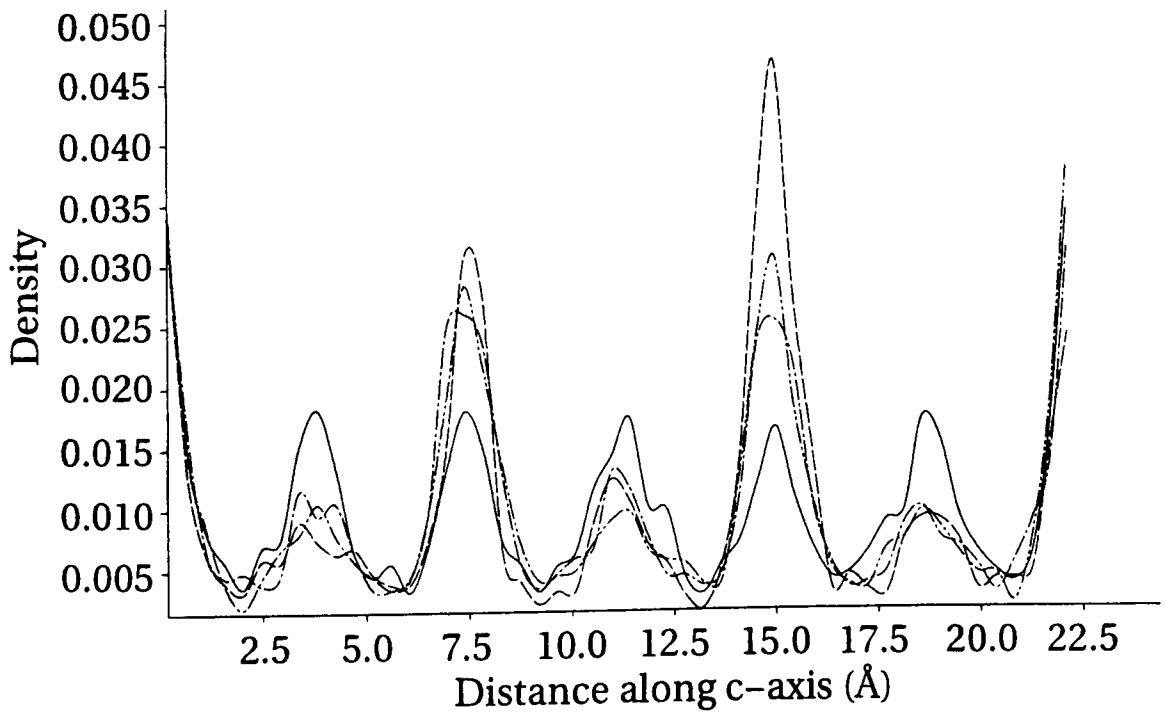
Figure 6.6: Distribution functions for xenon in ferrierite with respect to the (a) a-axis, (b) b-axis, and (c) c-axis of the zeolite unit cell



(a)

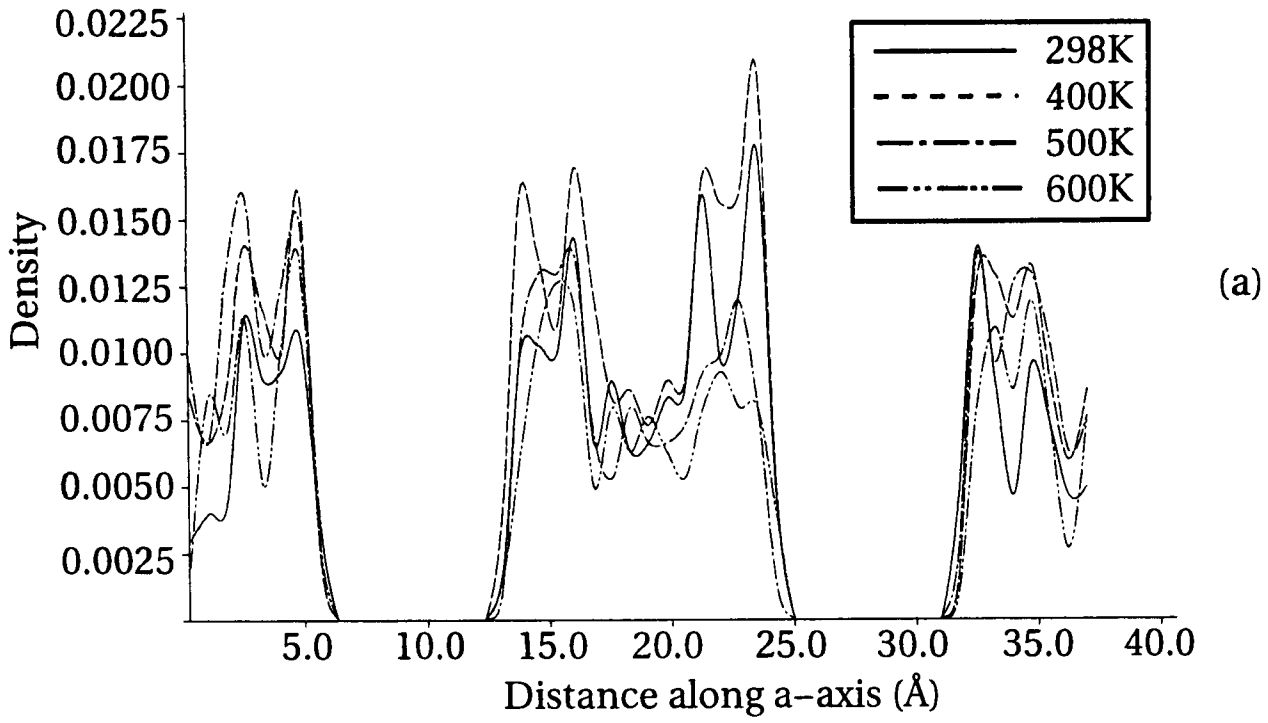


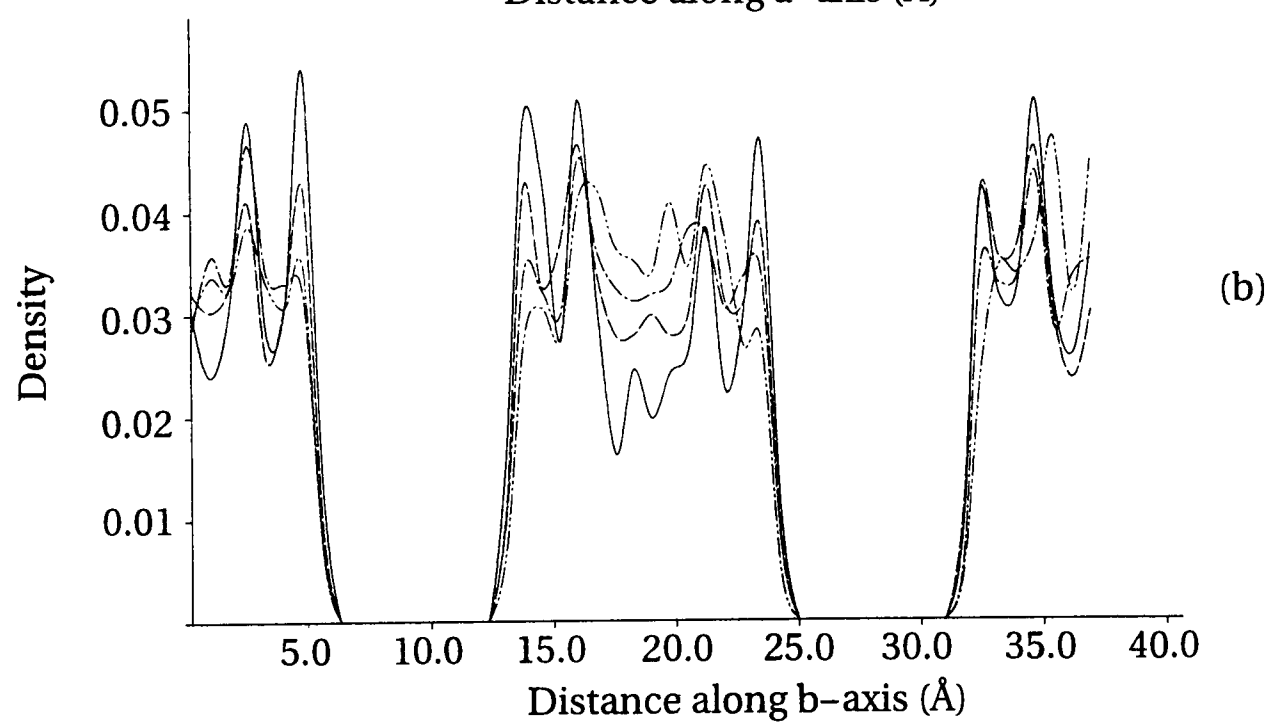
(b)



(c)

Figure 6.7: Distribution functions for xenon in zeolite-L with respect to the (a) a-axis, (b) b-axis, and (c) c-axis of the zeolite unit cell





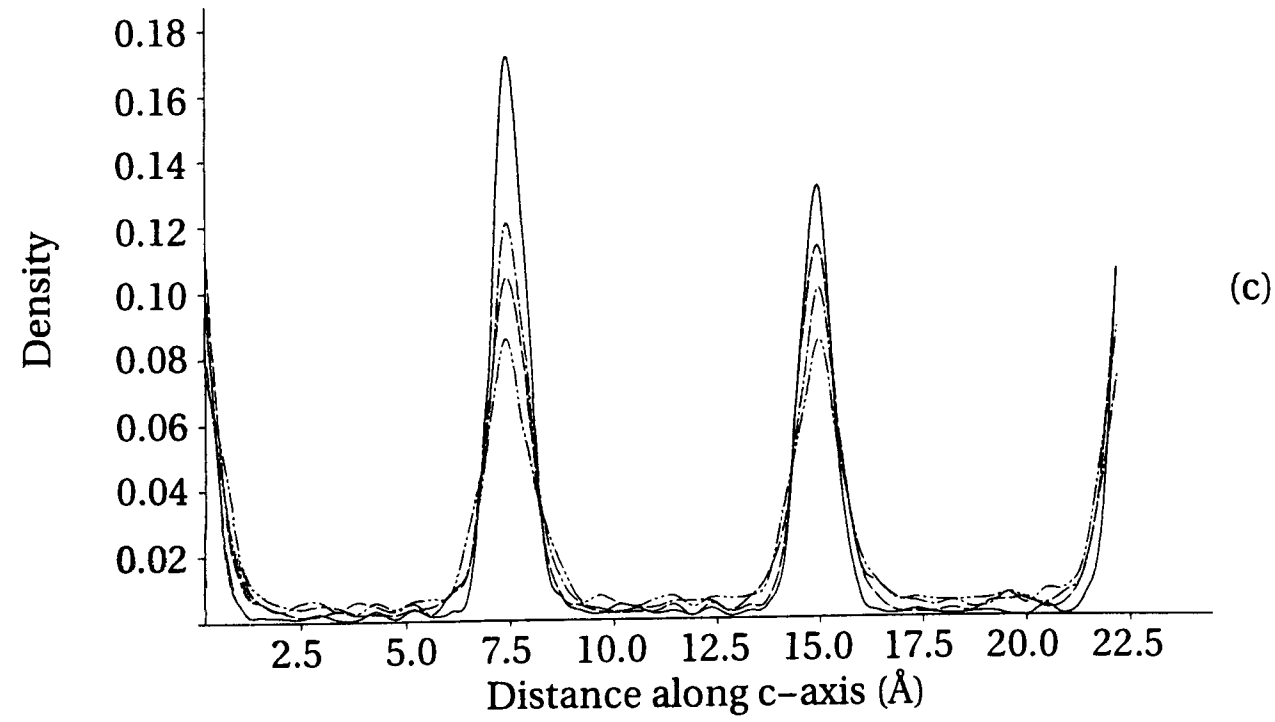
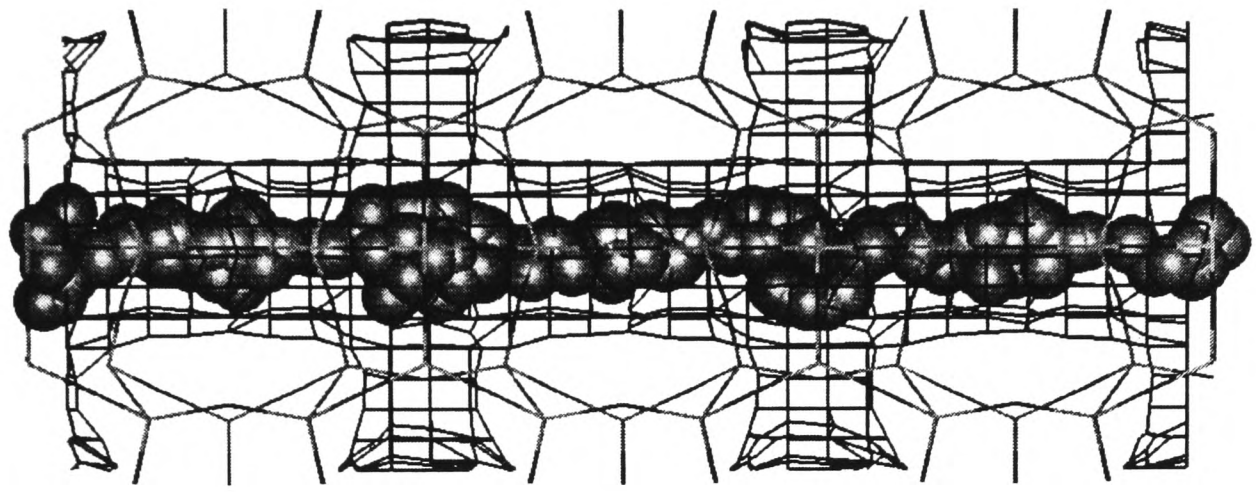
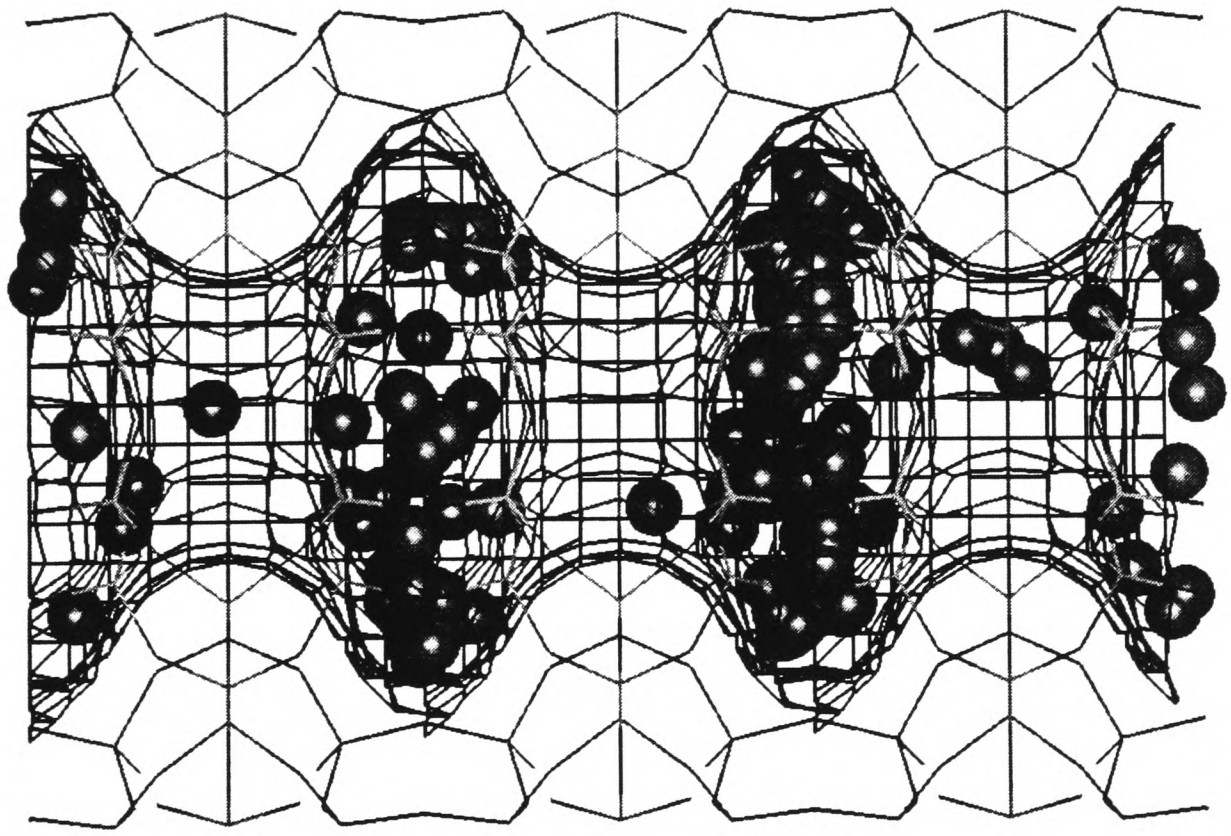


Figure 6.8: Schematic representation of the xenon atom distribution (spheres) with respect to the main channel in (a) ferrierite, and (b) zeolite-L



(a)



(b)

entire run superimposed on the channel structure of each zeolite. The chance of a xenon atom being located in between the energy minima is much higher in ferrierite, suggesting that the sinusoidal shape of the zeolite-L channel confines the atoms efficiently.

The possibility of xenon atom motion between the main channels can also be investigated by reference to the distribution functions along the other simulation box axes. Ferrierite possesses an eight-ring side channel orthogonal to its main 10-ring channel, which could allow interchannel motion to occur, whereas zeolite-L has no direct connection between the channels. However, if the side channel dimensions (3.4x4.8 Å) are compared with the σ parameter used for the Xe-O potential (4.07 Å) in the this work, it would be expected that interchannel crossing is unfavourable even in ferrierite. The distribution functions along the b-axis for ferrierite are shown in Figure 6.6. Although the atoms are confined for the most part to the main channels, there is a small probability of motion into the side channel. This probability increases with increasing temperature. In addition, this effect is more common at higher loading levels, since the atoms are more likely to enter side channels by collisions. Further insight into side channel motion can be obtained by considering the anisotropy of the diffusion as a function of temperature and loading (Table 6.4). Values lying the range 10^{-13} and 10^{-12} m^2s^{-1} merely indicate a "rattling" motion

Table 6.4: Diffusion coefficients (m^2s^{-1}) down the side channel in ferrierite as a function of loading and temperature

temperature (K)	loading (Xe atoms per main channel)			
	2	3	4	5
200	$1.17x10^{-13}$	$6.45x10^{-14}$	$6.11x10^{-14}$	$8.21x10^{-15}$
298	$5.31x10^{-13}$	$1.13x10^{-13}$	$6.12x10^{-12}$	$9.15x10^{-12}$
400	$6.98x10^{-13}$	$7.43x10^{-12}$	$2.15x10^{-11}$	$1.13x10^{-11}$
500	$1.65x10^{-11}$	$1.84x10^{-11}$	$6.09x10^{-11}$	$1.64x10^{-11}$
600	$4.56x10^{-11}$	$6.18x10^{-11}$	$3.88x10^{-11}$	$1.68x10^{-11}$

within the main channel. It can be seen that motion along the side channel is more likely at high temperatures suggesting the greater activation energy of this process. In addition, the diffusivities are consistent with only one or two atoms moving between adjacent main ten-ring channels over the entire duration of the simulation, which further emphasises the rarity of interchannel crossing. Even at the highest loadings, the diffusivities are consistent

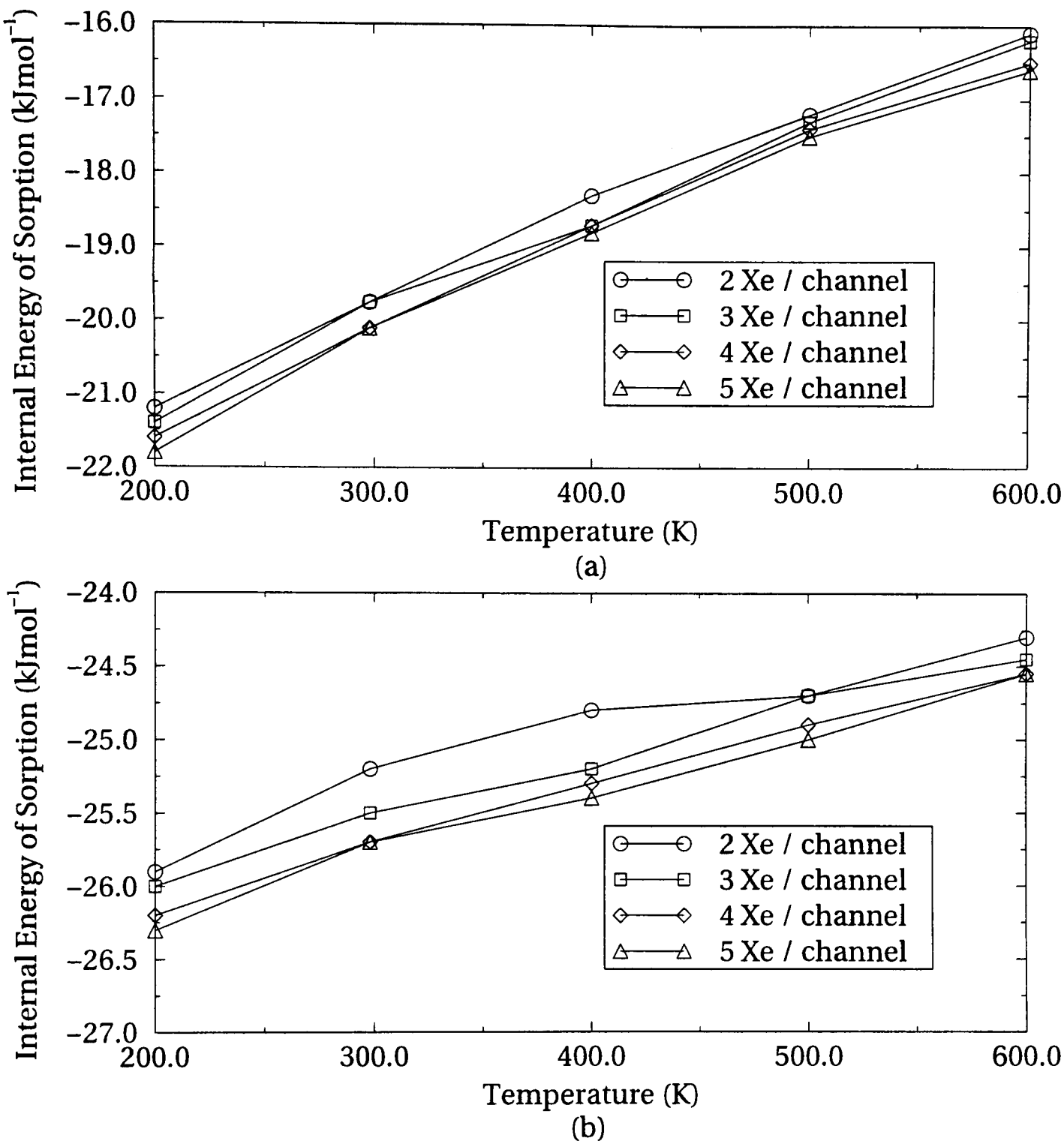
with the Xe atoms that pass through the eight-ring window becoming trapped in the side-channel cage. This may be due to the greater density of Xe atoms blocking their escape as well as the depth of the energy well. From the distribution functions and diffusion coefficients in zeolite-L, it can be concluded that no motion between adjacent 12-ring channels occurs.

In contrast, the resonant diffraction study of Jones and co-workers[330] located several sites for krypton in ferrierite. The site with the highest occupancy is located in the side channel close to the eight-membered ring. Since the van der Waals radius of Kr (1.90Å) is slightly smaller than Xe (2.10Å) it is possible that in the case of Xe this site would be less likely to be observed which is consistent with the results in this computational study. The diffraction study also finds sites in the main channel that are displaced from the centre of the channel slightly which is similar to the slight deviations observed in the minimum energy pathway previously. The Xe absorption edge occurs at a much higher energy than the Kr edge and consequently it is unlikely that a similar experiment on Xe will be performed in the near future.

The density plots across the main channels in zeolite-L show interesting fine structure. At low temperatures, there are five peaks for each channel, the middle one being of considerably lower intensity. The four outer peaks correspond to sites close to the walls of cavity where a greater degree of channel curvature provides more favourable coordination with the oxygen atoms of the zeolite framework. The middle peak corresponds to atoms located in the energetically less-favourable channel centre. As the temperature increases, the intensity of the central peak increases at the expense of the other peaks reflecting the greater kinetic energy of the atoms.

Internal energies of sorption were obtained from the ensemble average interaction energies computed over all the time steps in the simulation for each of the sorbate atoms. For both zeolites, the values are found to increase with temperature (see Figure 6.9). This result again reflects that at high temperatures the atoms possess greater kinetic energies and can therefore probe sites of higher potential energy within the channel. This is also illustrated by the evolution of the potential energy distribution functions with respect to temperature (Figure 6.10). A slight decrease in sorption energies with loading is observed for ferrierite (see Figure 6.9) as a consequence of the additional number of Xe–Xe interactions that are

Figure 6.9: The variation in the internal energy of sorption as a function of loading and temperature for (a) ferrierite and (b) zeolite-L



present. However, over the range of loading studied, this trend is not apparent in zeolite-L. Comparing the data for the two systems, it can be seen that the sorption energies are much lower for zeolite-L. This is due to the smaller diameter of the channel in ferrierite allowing the sorbate atoms to occupy many more sites of higher coordination.

The dynamical and thermochemical results for ferrierite can be usefully compared with data obtained in a previous study of siliceous ZSM-5. In contrast to the two zeolites investigated in this study, ZSM-5 features two interconnecting channels (one straight and one sinusoidal running parallel to the b- and c-crystallographic axes, respectively). The

Figure 6.10: The variation in potential energy distribution function with respect to temperature for zeolite-L with five xenon atoms per main channel

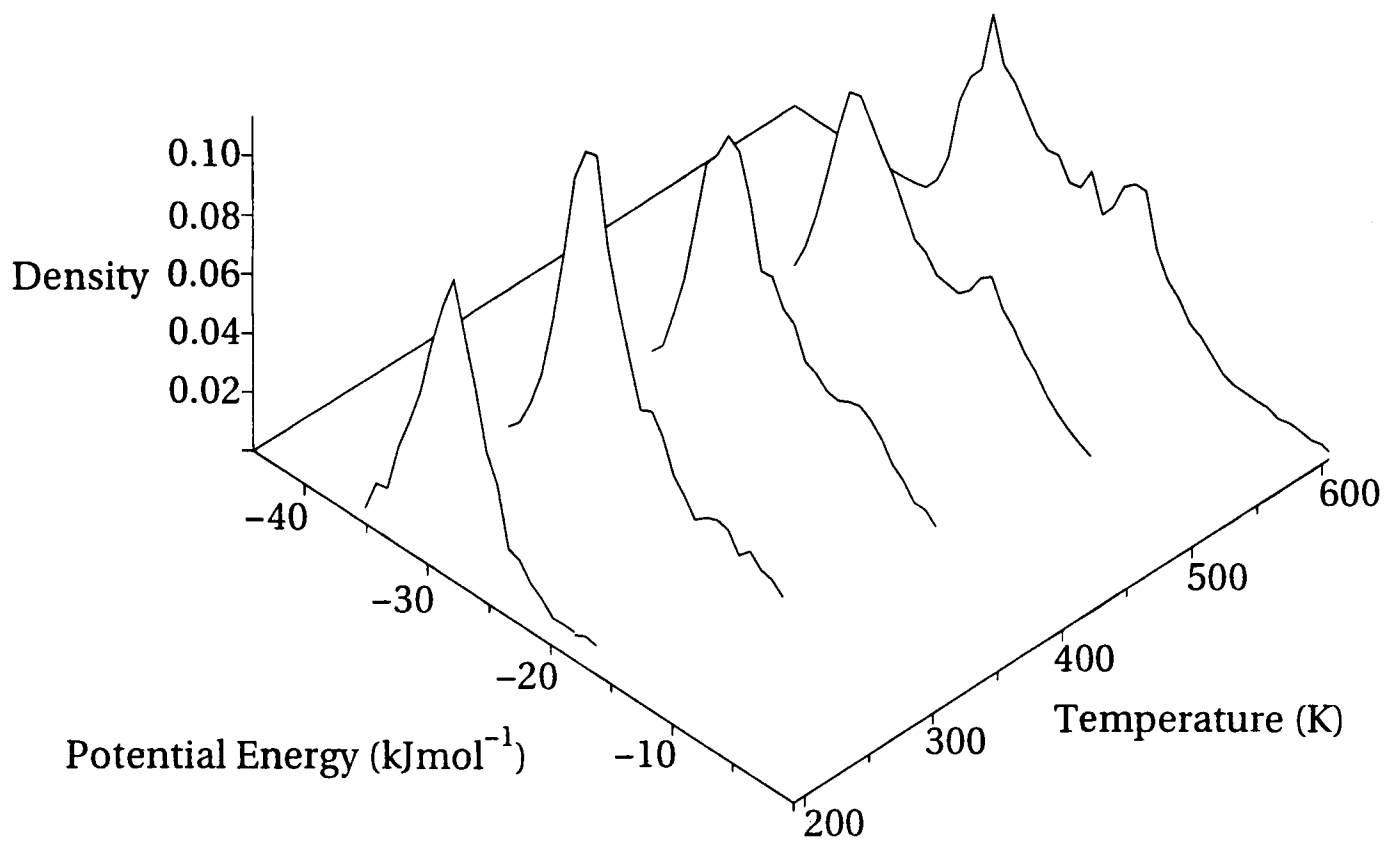


Table 6.5: Comparison of results for ferrierite and zeolite-L with previous simulations of Xe in siliceous ZSM-5 at 298K

zeolite	loading (Xe atoms/channel)	D (m^2s^{-1})	ΔU_{sorb} ($kJmol^{-1}$)	E_a ($kJmol^{-1}$)	D_0 (m^2s^{-1})
ferrierite	3.33	2.5×10^{-9}	-25.7	5.5	3.4×10^{-8}
zeolite-L	1.66	1.6×10^{-9}	-20.0	8.9	5.2×10^{-8}
ZSM-5					
straight channel	4.00	4.0×10^{-9}	-26.9	6.2	3.4×10^{-7}
sinusoidal channel	4.00	1.3×10^{-9}	-26.9	4.7	1.0×10^{-7}

comparison is shown in Table 6.5. At 298K, it can be seen that diffusion is most facile for siliceous ZSM-5 along the straight channel. This is a slightly wider channel than in ferrierite and it does not possess the extreme tortuosity displayed by zeolite-L. The relative sizes of the pre-exponential factors in ZSM-5 reflect the differing shapes of the two channels and can be rationalised using the arguments developed above. On the other hand, the sorption energy of Xe in ZSM-5 is very close to that for ferrierite, a finding that is consistent with channel systems based on the common ten-ring structural element.

Chapter Seven

Forcefield Development for Organic Molecules in Zeolites

A fundamental understanding of sorption phenomenon in microporous materials is essential in many applications involving zeolites, including catalysis, as well as giving an insight into the templating processes that are important during zeolite synthesis. Computational approaches that employ forcefields to represent interactions between the zeolite lattice and small molecules within the pore structures provide a useful method of investigating sorption effects. The first step in any study following these approaches is the development of an appropriate forcefield to correctly describe the interactions at the atomic level. Despite significant advances in the development of forcefields for zeolite lattices, the area of inorganic-organic interactions has not been studied as extensively. In this chapter, relevant methodologies for forcefield development will be examined and their feasibility assessed. Using an appropriate method, forcefield parameters will be derived for the interaction of saturated hydrocarbons in silicalite, by fitting to experimental properties. In addition, an example of how first-principles calculations can be included in the fitting procedure will be illustrated with the derivation of a forcefield for the interaction of aromatic molecules in faujasite-type zeolites.

7.1 Functional Forms for Inorganic-Organic Interactions

During the development of a new forcefield, several important factors must be considered. The transferability of the parameters may be important if the forcefield is to be applied to a number of different systems besides those to which it was originally fitted. Also, if the new forcefield represents an extension of an existing forcefield, compatibility may be an important issue.

A number of different classes of interaction acting between the zeolite and the occluded

molecule may be identified :-

- direct Coulombic interactions
- charge-induced dipole interactions
- charge-multipole interactions
- induced dipole-induced dipole interactions (dispersive interactions)

All these classes of interactions are to varying extents electrostatic in nature. The first class can be included by the assignment of point charges on each of the atoms and treated with the same summation techniques as for zeolite lattices alone. The second class is often ignored, but may be included by a calculation of the polarisation energy from the electric field at the point of interest or subsumed into other terms in the fit. The third class tends to apply to fairly specific systems and is also generally ignored to simplify the form of the potential. The last class is commonly included by the addition of terms into the potential of either Buckingham or Lennard-Jones form.

In addition, if the effects of loading are to be examined, interactions between organic molecules cannot be ignored. A wide range of molecular mechanics forcefields based on covalent models exist to represent bond, angle and torsion intramolecular interactions.[257,344–347] These can conveniently be included into the overall forcefield.

7.2 Fitting Methodologies

Many of the forcefield fitting methodologies detailed in Chapter 2 are also relevant to inorganic-organic interactions. Once again, two general classes of approach can be outlined: derivation of parameters from quantum mechanical calculations and empirical fitting to experimental data.

The first systematic attempt to derive interaction parameters for zeolite-organic molecule interactions was by Kiselev and co-workers.[333] The following functional form was adopted :-

$$E_j = \sum_i \frac{B_{ij}}{r_{ij}^{12}} - \frac{C_{ij}}{r_{ij}^{6}} - \frac{1}{2}\alpha \boldsymbol{E}^2(\boldsymbol{r}) \tag{7.1}$$

which corresponds to a Lennard-Jones term plus a polarisation energy term. The Lennard-Jones parameters were obtained from the Kirkwood-Müller formula assuming effective polarisabilities and magnetic susceptibilities for the atoms in the zeolite and the organic species. Many subsequent studies have used these parameters to successfully examine a wide variety of different systems, although some workers either neglect the polarisation term completely or replace it with an Ewald summation if electrostatic terms are thought to be important.

The method adopted to derive the Lennard-Jones parameters can introduce considerable uncertainty into the forcefield since it is often unclear which values should be used for the polarisabilities. Individual atomic polarisabilities of atoms in a crystal are not directly measurable by experimental techniques, although Fowler has demonstrated a possible route to such values using *ab initio* quantum-mechanical calculations.[282] Recently, Pellenq and Nicholson have proposed a method to measure individual ionic polarisabilities in zeolites based Auger spectroscopy that can be used to calculate improved dispersive parameters.[348] If the Slater-Kirkwood formalism is utilised, the approximate value of the number of electrons in the atom, N, is also debatable. Notably, Pellenq and Nicholson have shown that the Kiselev functional form does not correctly describe polarisability and the zeolite atom partial charges[349] for the sorption of noble gases in zeolite pores.

There have been several studies of the interaction of noble gases with the surfaces of ionic solids by quantum mechanical approaches.[350–352] These works employed perturbation theory to obtain dispersive and induction terms in the forcefield, in addition to *ab initio* Hartree-Fock methods for the Coulombic and repulsive terms. In contrast to those methods for fitting forcefields for handling the zeolite lattice in isolation, cluster models may be less applicable as a route to obtain parameters since long-range electrostatic effects can often play a dominant rôle in the interaction with many organic molecules. Although periodic Hartree-Fock calculations have been performed on a number of siliceous zeolite systems,[135,136] and conclusions made regarding sorption sites,[145] this method is severely restricted by the choice of system size and basis set. Pellenq and co-workers[353] have recently demonstrated the use of the periodic extended Hückel method to derive repulsive parameters for the interaction of Ar in silicalite. This semi-empirical quantum mechanical technique parameterises many of the terms in the secular determinant with ex-

perimental data, and as such is less computationally expensive than Hartree-Fock methods. This study represents the first attempt to parameterise a forcefield for zeolite sorption by a periodic quantum mechanical approach.

Due to the inherent computational costs of quantum mechanical calculations, the prospect of fitting to experimental data is a significantly more attractive one, especially for complicated organic molecules. However, the importance of obtaining high quality experimental data on the system in question must be stressed. Relevant experimental data are diffraction studies that locate the organic molecule in the zeolite structure, preferably at low temperatures where thermal vibrations are reduced, and thermochemical data including isosteric heats of sorption and sorption isotherms.

June and co-workers have demonstrated an approach in which experimental sorption data are included in the fit. Values for Lennard-Jones parameters were used which reproduced the experimentally determined Henry's constant for the sorption of methane in silicalite.[227] Since many of the available experimental thermochemical quantities represent ensemble averages in the computational paradigm, direct fitting of the forcefield parameters is a non-trivial exercise. The calculation of statistically meaningful ensemble averages to compare to analogous experimental values may require hundreds of thousands of simulation steps.

An alternative method is to neglect the effects of temperature, assume that the most favourable binding site for a sorbate dominates the heat of sorption, and attempt to relate this quantity to the binding energy at the site. The various options for fitting to experimental data will be examined in later sections of this chapter.

7.3 Charge Models for Inorganic-Organic Interactions

Although many studies have neglected electrostatic interactions in zeolite sorption simulations, it is clear that for many zeolite systems, especially those containing extra-framework cations, direct Coulombic interactions cannot be ignored. In Chapters 4 and 5 it has been shown that the use of formal charges on the zeolite atoms still remains an effective approximation in the investigation of the relative lattice energetics of microporous materials. Although a number of studies have adopted formal zeolite charges to investigate sorp-

tive properties,[237,254] it is advantageous to adopt a zeolite forcefield having partial charges since this is a more realistic, albeit less accurate, model with respect to the reproduction of structural quantities (see Chapter 4).

Several methods are available to obtain suitable partial charges. Besides arbitrary charge assignment, which is quite prevalent in the literature, the simplest method involves using a quantum mechanical calculation to obtain Mulliken population analyses of the SCF wavefunction.[354] Even for a simple molecule such as methane, the partial charges obtained from this method are strongly dependent on the basis set and the level of approximation chosen. Table 7.1 shows the partial charges obtained for methane from a variety of different calculations, both quantum-mechanical and forcefield based. The cff91 forcefield developed by Biosym has been parameterised to a large database of organic molecules and contains rules for the calculation of partial atomic charges for any organic molecule.[257,258] The MNDO calculation was performed with MOPAC version 6.0, and the Hartree-Fock calculations (basis sets given in brackets) used Turbomole version 2.3 . Further experimental data are needed to decide which charge model is the most realistic; for example, dipole and quadrupole moments can be considered if applicable. An alternative scheme for the calculation of partial charges is to use the SCF wavefunction to calculate the electrostatic potential experienced by protons probing the region around the molecule, and to fit a set of partial charges to the potential energy surface. This calculation was recently carried out for siliceous mordenite and the resulting charges compared favourably with those from a Mulliken analysis.[136]

Table 7.1: Calculated Partial Charges for Methane

Method	Biosym cff91	MNDO	HF (STO-3G)	HF (6-31G**)
q_C	-0.212	0.070	-0.263	-0.472
q_H	0.053	-0.018	0.066	0.118

Several workers have proposed zeolite framework forcefields based on partial charges, including several of the potential models considered in Chapter 4. In order to be able to utilise the selected forcefield to study the sorption effects of molecules in a wide variety of

zeolitic materials, it is important to consider a zeolite forcefield that can treat isomorphous substitutions and extra-framework cations in a consistent manner.

7.4 Strategies for Fitting to Experimental Data

7.4.1 Fitting to Crystallographic Data

Crystallographic experiments represent one of the few methods that are able to determine atomic positions unambiguously and are essential in providing realistic models for atomistic simulation. Although there have been a wide range of structural studies made on the zeolite structures themselves, the location of organic molecules within the pore structure often represents a more challenging experiment. A common problem is disorder arising from the occupation of low symmetry sorption sites. This makes a full structure solution difficult unless high quality single crystal data are available.

Since X-ray and neutron diffraction studies provide a thermally averaged picture of the system, from the modelling point of view this can be related to a structural model with no account taken of thermal properties, such as that obtained by a lattice energy minimisation calculation. As in Chapter 5, the crystallographic data can be used as a basis for a least-squares fit of the forcefield parameters so as to correctly reproduce the experimental structure on minimisation.

In the simplest case, for a system represented by a single Lennard-Jones potential, this procedure can be related to the fitting of the σ parameter in the σ–ϵ representation of that functional form, which controls the position of the minimum of the potential energy function.

7.4.2 Fitting to Thermochemical Data

Thermochemical data, such as that obtained from an experimental sorption isotherm for a probe molecule in a zeolite host, can provide information on the strength of the interaction between the molecule and the zeolite, as well as providing a measure of the available pore volume. In the example given above, thermochemical data such as the isosteric heat of sorption can be used to fit the Lennard-Jones ϵ parameter, which is the depth of the po-

tential energy function. In a complicated forcefield consisting of a number of terms, the position and depth of the actual minimum is a balance between the contributions from different parts of the forcefield.

The easiest and least computationally intense method of fitting to thermochemical data is to assume that the isosteric heat of sorption is entirely due to the occupation of the most stable sorption site for the organic molecule in the zeolite. If the geometry of this site is known from diffraction data then the σ and ϵ values for the appropriate atom pairs can be fitted using standard least-squares methods. In the absence of crystallographic data and given a reasonable guess at suitable forcefield parameters, a docking procedure may be used to locate feasible binding sites. The most favourable binding site can then be used as a basis for the fit to the thermochemical data. However this procedure makes several assumptions. Firstly, there is the assumption that the isosteric heat of sorption can be directly equated to the interaction energy between the zeolite and organic molecule. Secondly, there is no variation in the isosteric heat of sorption with temperature. Finally, no attempt is made to represent the heat of sorption as an ensemble average over states.

From statistical mechanics, the average interaction energy, $\overline{\Delta U}$, between the sorbate and the zeolite lattice at temperature T is given by the ratio of the following configurational integrals :-

$$\overline{\Delta U} = \frac{I_2}{I_1} \tag{7.2}$$

$$I_1 = \int \left(\exp(-\sum_i \frac{E_i}{RT}) \right) d\boldsymbol{q} d\Theta \tag{7.3}$$

$$I_2 = \int \left(\sum_i E_i \right) \exp(-\sum_i \frac{E_i}{RT}) d\boldsymbol{q} d\Theta \tag{7.4}$$

where $\boldsymbol{q}$ represents the centre of mass of the organic molecule, and Θ represents the angular position of the molecule with respect to an arbitrary internal axis system.

In a computer simulation, the integrals are replaced by averages over states in phase space generated with appropriate strategies, such as Monte Carlo or molecular dynamics. Once an average interaction is obtained using a simulation, the isosteric heat of sorption, q_{st}, at low coverage can then be related to the average interaction energy from the following

expression :-

$$q_{st} = \overline{\Delta U} - RT \tag{7.5}$$

Since the simulation allows the calculation of an ensemble average quantity which can be compared with thermochemical values, it is vital that sufficient simulation are performed to ensure that the average is a statistically meaningful quantity. This requirement makes standard least-squares fitting prohibitive since each step may take hours of computer time, and manual adjustment of the potential parameters is therefore a more attractive approach.

An additional parameter that can be employed in the fitting procedure is the Henry's constant, K_h, which can be measured experimentally by taking the slope of the isotherm in the low pressure region. June and co-workers have shown that this is given by the following integral :-

$$K_h(T) = \frac{M_a}{\rho_z N_A V_S} \int \rho_{cm}(\boldsymbol{r}, T) d\boldsymbol{r}\, d\Theta \tag{7.6}$$

where M_a is the molecular weight of the organic, ρ_z is the zeolite density, N_A is Avogadro's number, V_S is the volume of the unit cell, and ρ_{cm} is a density function for the organic molecules in the zeolite.

7.5 Forcefield Development for Normal Hydrocarbons

In order to demonstrate the feasibility of fitting forcefield parameters using these approaches, a relatively simple system was chosen initially. There has been a considerable number of thermochemical measurements made on normal hydrocarbons in silicalite. Isosteric heats of sorption have been obtained for molecules comprising two to six carbon atoms.[355,356] In this section, a forcefield for the interaction of silicalite with methane and propane will be fitted. The transferability of these parameters will then be verified by calculating the heat of sorption of hexane in silicalite.

The silicalite lattice was modelled by the Kramer potential, which combines the desirable qualities of partial charges with an adequate representation of the zeolite structure.

Molecular dynamics simulations were performed on a single unit cell of the orthorhombic phase of silicalite taken from the structure of van Koningsveld and co-workers.[262] In the case of methane, a starting configuration was generated by placing eight molecules at random positions in both the straight and sinusoidal channel systems. All interactions between methane molecules were neglected in order to simulate the infinite dilution limit while improving the statistics of the calculated ensemble averages.

Initial values for the interaction parameters were taken from June and co-workers,[227] who performed Monte-Carlo and molecular dynamics on these systems with a fixed zeolite lattice. An initial molecular dynamics simulation was performed at 298K using the velocity Verlet integration scheme[180] with a time step of 1fs and the thermostating method developed by Berendsen[199] to generate a suitable starting configuration. The system was equilibrated for 10ps following by 10ps data collection period. A simulation was also carried out under the same conditions with all interactions between the methane molecules and zeolite host neglected for calibration purposes. The average interaction energy, $\langle E_{int} \rangle$ between the zeolite and organic molecule is then given by :-

$$\langle E_{int} \rangle = \frac{1}{N} \left(\langle E_{zg} \rangle - \langle E_z \rangle - \langle E_g \rangle \right) \tag{7.7}$$

where N is the number of organic molecules in the system, $\langle E_{zg} \rangle$ is the average energy of a system containing a zeolite interacting with organic molecules, $\langle E_z \rangle$ is the average energy of an isolated zeolite system, and $\langle E_g \rangle$ is the average energy of an isolated system of molecules. Each of the terms can be calculated by acquiring the ensemble average energy during simulations with appropriate systems. The sum of the last two terms can be obtained by performing a single simulation with zeolite and organic molecules in which interactions between zeolite and organic are neglected.

The ϵ values for the O–H and O–C parameters were scaled so as to produce the correct isosteric sorption as calculated using the formulae above. Since $-CH_3$ and $-CH_2$ groups are sufficiently different in their chemical properties from methane it was decided to perform separate fits for ethane and propane to derive parameters for each atom type. Partial charges for each of the atom types were assigned based on Hartree-Fock calculations with the 6-31G** basis set. These are given in Table 7.2. The functional forms adopted in the

Table 7.2: Partial charges for atom types in normal hydrocarbons

	carbon atom types			hydrogen atom types		
	q(CH_4)	q(CH_3)	q(CH_2)	q(CH_4)	q(CH_3)	q(CH_2)
charge	-0.472	-0.333	-0.220	0.118	0.110	0.110

fitted forcefield are summarised in Table 7.3 – a full description of these terms has been given in Chapter 3. The calculated isosteric heats of sorption are shown in Table 7.4 and

Table 7.3: Functional forms

Two-body zeolite	$E_{ij} = \frac{q_i q_j}{r_{ij}} + A_{ij} \exp\left(-\frac{\rho_{ij}}{r_{ij}}\right) - \frac{C_{ij}}{r_{ij}^6}$
Two-body hydrocarbon	$E_{ij} = k_{ij}(r_{ij} - r_o)^2$
Two-body zeolite-hydrocarbon	$E_{ij} = \frac{q_i q_j}{r_{ij}} + 4\epsilon_{ij}\left(\left(\frac{\sigma_{ij}}{r_{ij}}\right)^{12} - \left(\frac{\sigma_{ij}}{r_{ij}}\right)^{6}\right)$
Three-body	$E_{ijk} = k_{ijk}(\theta_{ijk} - \theta_o)^2$
Four-body hydrocarbon	$E_{ijkl} = k_{ijkl}(1 + b_{ijkl}\cos(c_{ijkl}\phi_{ijkl}))$

Table 7.4: Experimental and calculated isosteric heats of sorption for normal hydrocarbons in silicalite at room temperature

	experimental[355,356] ($kJmol^{-1}$)	calculated ($kJmol^{-1}$)
methane	20.0	20.5
ethane	28.3	29.5
propane	37.8	39.0
hexane	66.3	63.6

the final fitted forcefield parameters for hydrocarbons are given in Table 7.5. The interactions between atoms within a single hydrocarbon molecule are handled using standard molecular mechanics functions fitted by Oie and co-workers,[357] and are listed in the table for completeness. As can be seen from the final fitted parameters, there is little difference between the parameters for $-CH_2$ and $-CH_3$, and therefore no justification for adopting

Table 7.5: Forcefield parameters for normal hydrocarbons in zeolites

Two-body zeolite	A_{ij} (eV)	ρ_{ij} (Å)	C_{ij} (eV r^{-6})
Si–O	17796.1	0.205	135.4
O–O	1305.9	0.359	196.1
Zeolite-hydrocarbon	σ_{ij} (Å)	ϵ_{ij} (meV)	
O–C (CH_4)	2.9225	1.1877	
O–C (-CH_3)	2.9225	0.9580	
O–C (-CH_2)	2.9925	0.9590	
O–H (CH_4)	2.5568	0.8362	
O–H (-CH_3)	2.5568	0.6745	
O–H (-CH_2)	2.5568	0.6575	
Two-body hydrocarbon	k_{ij} (eVÅ^{-2})	r_o (Å)	
C–H	31.0	1.07	
C–C	48.9	1.54	
Three-body	k_{ijk} (eV rad^{-2})	θ_o (^{o})	
H–C–H	2.06	109.47	
H–C–C	3.39	109.47	
C–C–C	3.39	109.47	
O–Si–O	2.10	109.47	
Four-body hydrocarbon	k_{ijkl} (eV)	b_{ijkl}	c_{ijkl}
H–C–C–H	0.005	3.0	1.0
H–C–C–C	0.005	3.0	1.0
C–C–C–C	0.005	3.0	1.0

separate atom types for these two structural units exists.

Finally, as a test of the fitted parameters, a similar calculation was performed on hexane in silicalite in order to calculate the heat of sorption. The results of this calculation are also given in Table 7.4, and show good agreement with experiment.

7.6 Forcefield Development for Aromatic Hydrocarbons

This section details the fitting procedure employed to obtain forcefield parameters for the interaction between benzene in faujasite models of varying cation concentrations.

7.6.1 Siliceous Faujasite

There are no relevant crystallographic data on the siting of benzene in siliceous faujasite. A powder neutron diffraction study of benzene in siliceous faujasite failed to locate the sorbate at 4K.[31] This implies that either the most favourable binding site is of low symmetry, or that there are a number of sites closely spaced in energy and the sorbate is disordered over them.

The Kramer forcefield was chosen to model the zeolite framework since, in addition to the use of partial charges for the zeolite atoms, it includes parameters for the incorporation of Al and Na into the model. A number of calculations were carried out to determine suitable partial charges for the benzene molecule. These are summarised in Table 7.6. Snurr and co-workers[358] have suggested charges for benzene (q_C=-0.1530, q_H=0.1530) that approximately reproduce the experimentally determined quadrupole moment (experiment=-2.9x10^{39} C m^2 compared to theory=-3.0x10^{39} C m^2). These charges have also been employed by workers in previous studies of benzene,[242,359,360] and correspond most closely to the 6-31G** derived partial charges.

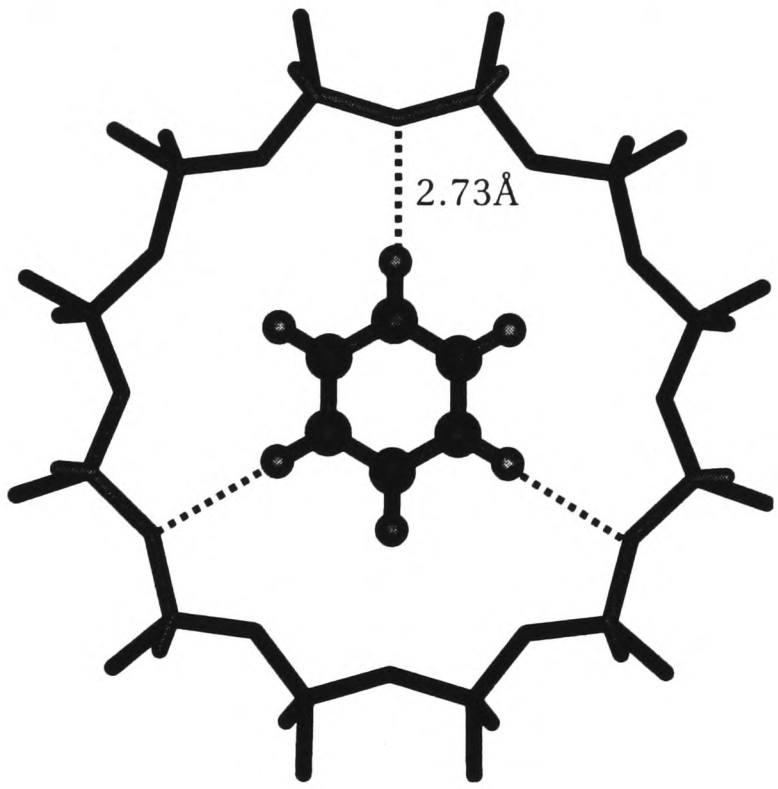
Table 7.6: Calculated Partial Charges for Benzene

Method	Biosym cff91	MNDO	HF (triple-ζ+pol.)	HF (6-31G**)
q_C	-0.120	-0.059	-0.114	-0.148
q_H	0.120	0.059	0.114	0.148

As a convenient starting point for the fitting procedure, the parameters of Snurr and co-workers[358] were adopted. To examine the potential energy surface with this parameter set, an automated Monte-Carlo docking procedure was carried out using the method demonstrated by Freeman and co-workers,[222] and is described in more detail in Chapter 8. The most favourable site was found to be one located above the four-rings in the wall of the

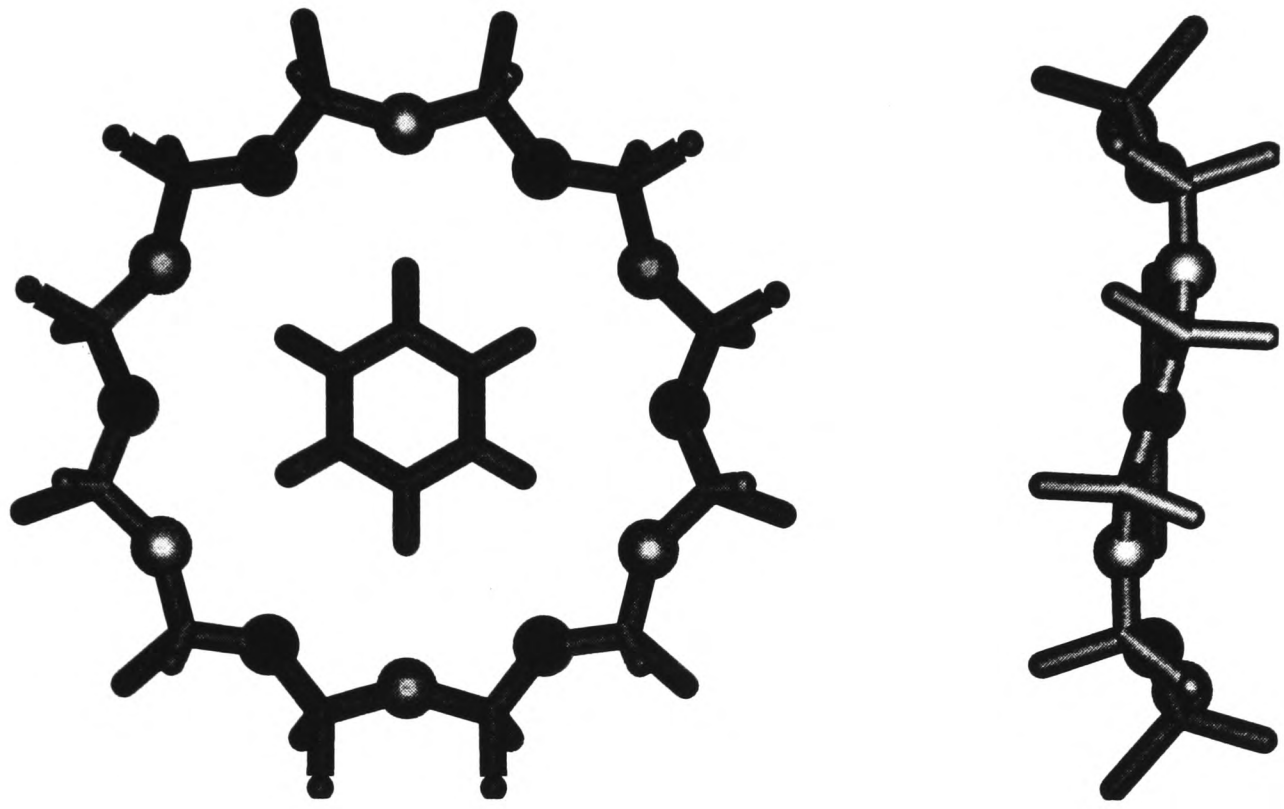
supercage. Since this is a low-symmetry site it is may well be difficult to detect by diffraction methods. In addition, a site located in the twelve-ring window was obtained which was of considerably higher energy. The geometry of this site was similar to a site observed in a neutron diffraction study of benzene in Na-Y.[54] Since the twelve-ring window site is distant from the nearest Na^+ cation site in Na-Y, it is reasonable to assume that this site is relatively unperturbed by the presence of the cation in this structure. Therefore, a close analogy can be drawn between the geometry of this site in Na-Y and the site obtained in the docking calculation, although the failure of the diffraction experiment to locate this binding site in siliceous faujasite suggests that it is insignificantly populated under equivalent conditions. The geometry of the twelve-ring binding site in Na-Y is shown in Figure 7.1. The considerable flexibility of the bond angle about oxygen allows the twelve-ring to devi-

Figure 7.1: Benzene sorption site in the twelve-ring window of Na-Y



ate considerably from planarity to relieve strain. Indeed the oxygen atoms in the ring can be divided into two sets whose members alternate around the ring. The first set lie in a single plane ("in plane"), whereas the second set form two planes of three oxygens straddling the first set ("out of plane"). The benzene is aligned such that it lies in the plane of the in-plane oxygens but the hydrogens point towards the out-of-plane oxygens (Figure 7.2). The hypothetical site with the benzene hydrogens pointing towards the in-plane oxygens would result in a O–H distance of around 2.53Å compared to the slightly larger distance in

Figure 7.2: The twelve-ring window in faujasite showing both "in-plane" oxygens (black) and "out-of-plane" oxygens (grey). (a) View parallel to twelve-ring window, and (b) orthogonal to the benzene plane



(a) (b)

Figure 7.1. Recent quantum mechanical calculations by O'Malley and Braithwaite[361] have suggested that the reason for this subtle differentiation between the two possible sites is the tight steric fit of the benzene in the twelve-ring window.

The Lennard-Jones σ parameters for the O–H and O–C interaction terms in the forcefield can be fitted so as to produce a twelve-ring site of the correct geometry. Docking calculations revealed the possibility of three different geometries in the twelve-ring window depending on the σ parameter values. These sites are all located in the same plane and differ only by the rotational position with respect to the zeolite lattice, and are described below :-

- benzene hydrogens pointing to the in-plane oxygens
- benzene hydrogens pointing to the out-of-plane oxygens
- benzene hydrogens pointing between oxygens

At low values of σ (σ(O–H) < 2.5Å), only the first two geometries are observed with the in-plane configuration being favoured energetically. At intermediate values (2.5Å$< \sigma < 2.7$Å),

all three geometries are observed and are of similar energies. At higher values of σ ($\sigma >$ 2.7Å), the in-plane site is eliminated and the other two sites remain of similar energy. The in-plane site becomes unfavourable when σ becomes significantly greater than the O–H distance between the benzene hydrogens and the zeolite oxygens at that site. The third site in the list offers the possibility of interaction with both sets of oxygens, and more importantly, gives a longer O–H distance with the in-plane oxygen positions at higher values of σ. Since it appears to be impossible to exclude the in-plane site without also creating the third site, which is not observed in either the siliceous faujasite or Na-Y crystal structure determinations, a set of parameters was chosen that gave the minimum σ values while eliminating the in-plane site. During the fitting procedure, the fraction σ(O–H) / σ(O-C) was constrained to a constant value.

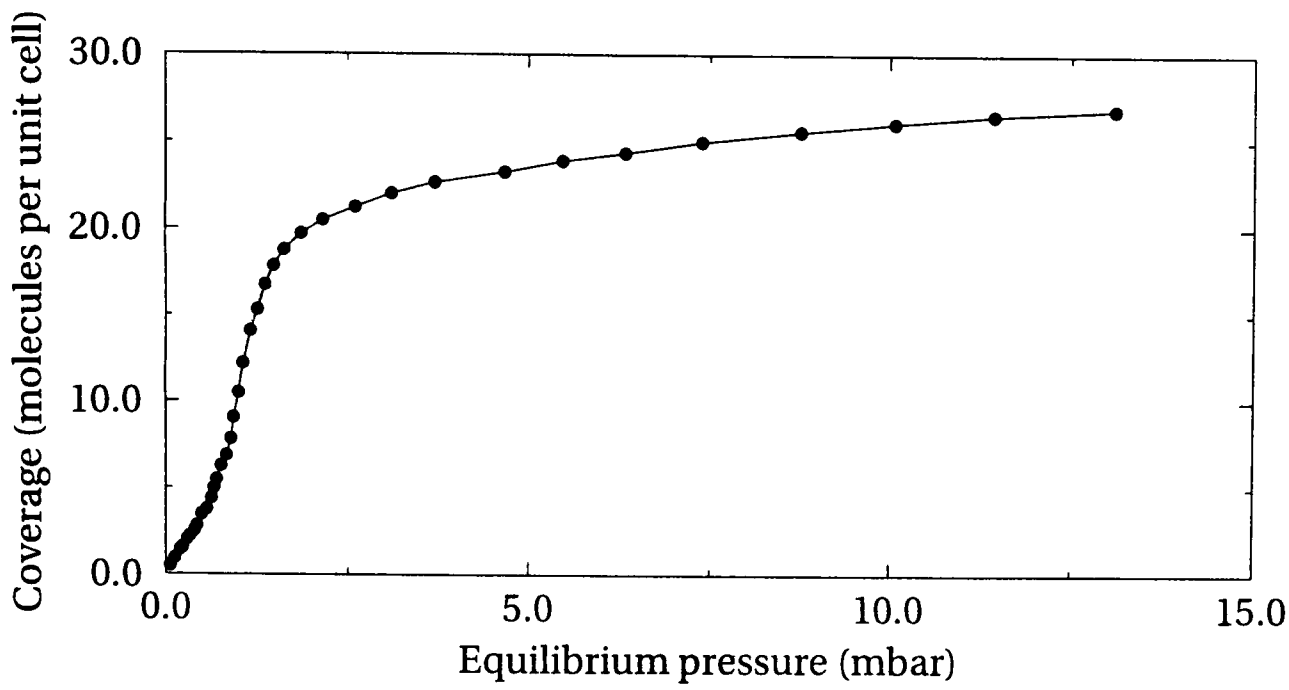
In order to fit the ϵ values, thermochemical measurements on benzene in siliceous faujasite were made.[362] The experimental sorption isotherm is shown in Figure 7.3. The isosteric heat of sorption was 55kJmol^{-1} at 298K. This value is reached at relatively low loadings and remains approximately constant up to a loading of 22 molecules per unit cell (2.75 molecules per super cage). Initially, an attempt was made to fit the ϵ parameters to a system in which the zeolite lattice is held fixed. The structure of siliceous faujasite was minimised at constant volume using the Kramer forcefield to produce a starting configuration for the zeolite. Since the isosteric heat of sorption reaches a constant value at relatively low loadings, the initial fit was made in the infinite dilution limit. To improve the statistics, a single benzene was placed in each of the eight super cages in one unit cell to generate a starting configuration. As in the previous section, molecular dynamics simulations were performed using this configuration with the system being equilibrated for 10ps and then data collected for a further 25ps. The simulation was repeated with varying ϵ parameters until the experimental heat of sorption was reproduced at 298K.

The final forcefield parameters are tabulated in Table 7.6.

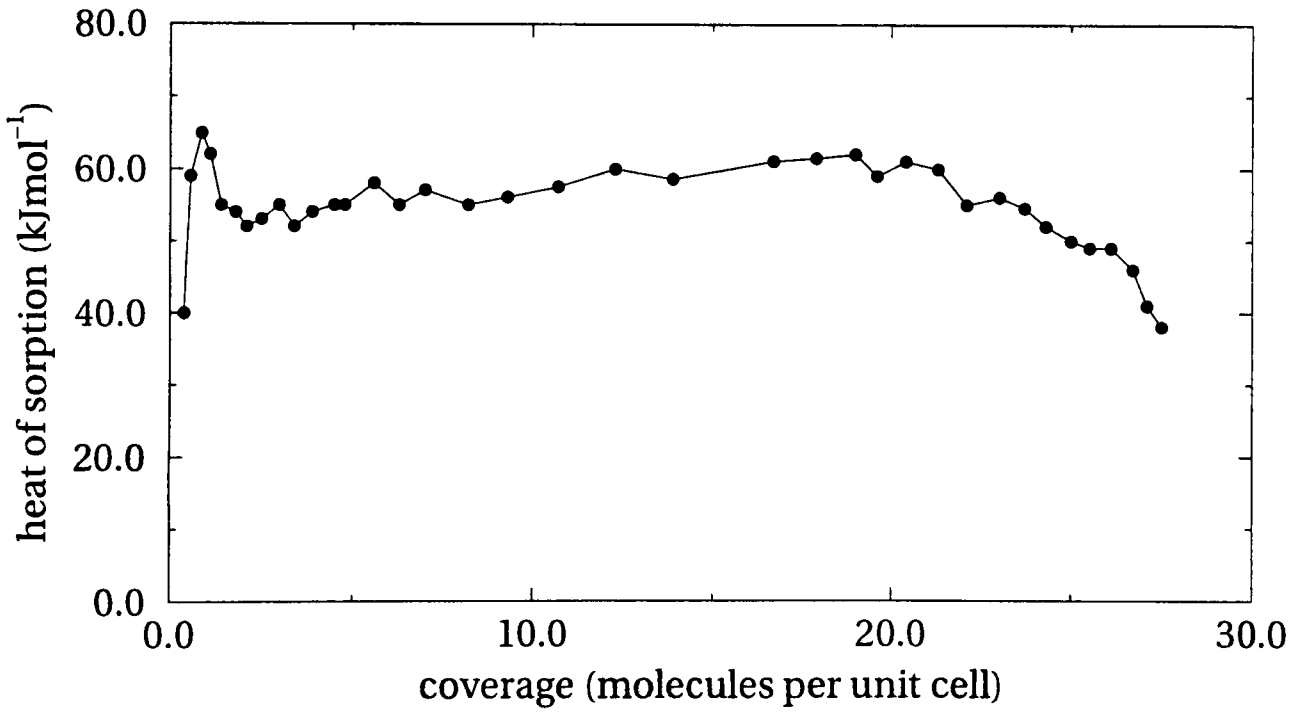
7.6.2 Cation-Containing Faujasites

The neutron diffraction study of benzene in Na-Y at low temperature provides the basis for the fit for this section of the work. Two sites are observed. The dominant sorption site has the benzene bound to a *SII* cation site in the wall of the supercage and is shown in Figure

Figure 7.3: Experimental sorption isotherm for benzene in siliceous faujasite



(a) coverage versus equilibrium pressure



(b) heat of sorption versus coverage

7.4. In addition, there have been numerous thermochemical measurements on this system which give an isosteric heat of sorption lying in the range 70-80 kJmol^{-1}.[326,363,364]

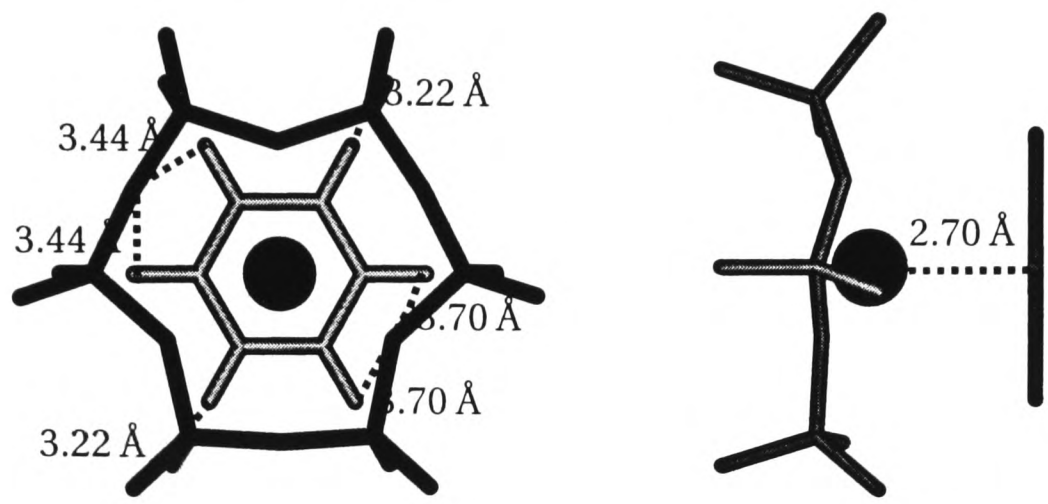
The benzene is bound through the charge-quadrupole interaction at a distance of 2.70Å. The rotational orientation of the benzene molecule is controlled by interactions with oxygen atoms on the neighbouring four-rings; the closest contact being 3.22Å. The

Table 7.7: Forcefield parameters for aromatic hydrocarbons in zeolites

Two-body zeolite	A_{ij} (eV)	ρ_{ij} (Å)	C_{ij} (eV r^{-6})
Si–O	17796.1	0.205	135.4
O–O	1305.9	0.359	196.1
Al–O	16008.5	0.208	175.0
Na-O	3542.2	0.242	0.0
Zeolite-hydrocarbon	σ_{ij} (Å)	ϵ_{ij} (meV)	
O(siliceous)–C	3.1464	6.8309	
O(cation-containing)–C	3.5799	4.0038	
O(siliceous)–H	2.7588	4.5560	
O(cation-containing)–H	3.1358	2.6704	
Na–C	3.2660	4.3538	
Na–H	2.7138	3.1446	
Two-body hydrocarbon	k_{ij} (eVÅ^{-2})	r_o (Å)	
C–H	31.3	1.09	
C–C	48.9	1.39	
Three-body	k_{ijk} (eV rad^{-2})	θ_o (^{o})	
H–C–C	3.44	120.0	
C–C–C	3.44	120.0	
O–Si–O	2.10	109.47	
Four-body hydrocarbon	k_{ijkl} (eV)	b_{ijkl}	c_{ijkl}
H–C–C–H	0.0867	2.0	1.0
H–C–C–C	0.0867	2.0	1.0
C–C–C–C	0.2166	2.0	1.0

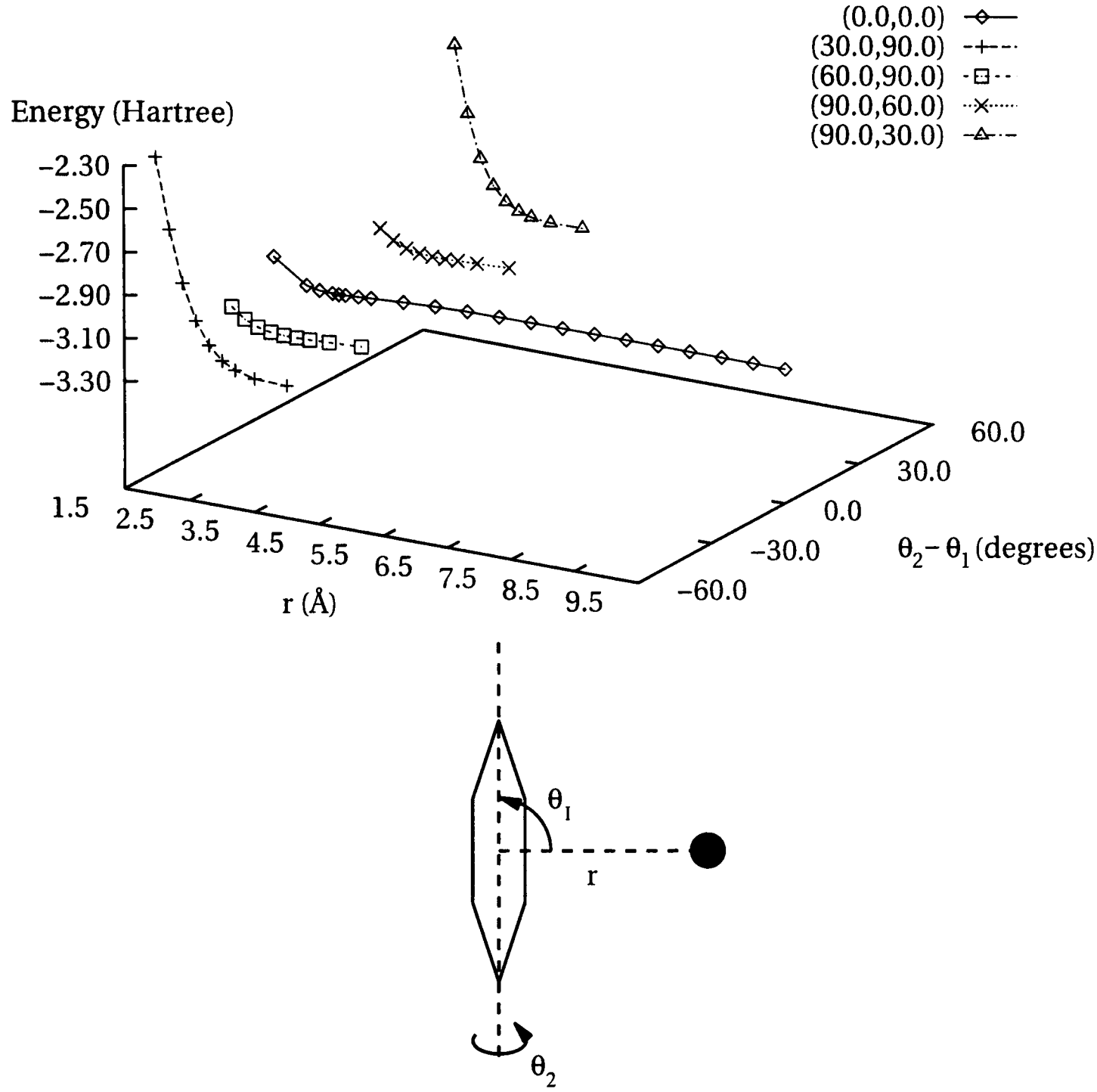
nature of the cation-molecule interaction is a charge-quadrupole term. There is also a sorption site with the benzene located in the twelve-ring window, as was mentioned in the previous section, although the occupancy is much lower until higher loadings are reached. In order to obtain a reasonable starting point for a fit for the benzene-cation interactions, a potential energy surface was calculated using an *ab initio* quantum mechanical approach based on this *SII* cation-benzene geometry. Redondo[365] performed a series of single point

Figure 7.4: The *SII* cation binding site for benzene in Na-Y



energy calculations on a system consisting of a single Na^+ cation at various distances from an isolated benzene molecule using the GAUSSIAN-92 software.[112] All the calculations were performed using the 6-31G** basis set and the MP2 level of electron correlation. Several geometries with the cation located equidistantly from all the carbon atoms in the benzene ring at various distances from 1.5Å to 9.5 Å were considered, in addition to a number of "off-centre" geometries. The potential energy surface obtained is shown in Figure 7.5. In order to ensure that the potential energy surface had its zero point at infinite separation, the central curve was fitted to a cubic spline and extrapolated to its limiting value. This value was then subtracted from all the potential energy points. Both maximum entropy and least-squares fitting methods were employed in an attempt to fit the potential energy surface to a sum of Lennard-Jones potential energy functions acting between the sodium cation and the carbon and hydrogen atoms of the benzene molecule. The first fitting attempts were made using only the "on-centre" geometries. Several Lennard-Jones functional forms were tried, including the (12-4) Lennard-Jones potential, since it is known that charge-quadrupole effects are terms in r^{-4}. However, in both cases, the Na–H term disappears. The results of these fits is shown in Figure 7.6. When several of the "off-centre" terms were added into the fitting procedure, it was found that the Na–C term disappeared. Since the forcefield into which these parameters were to be subsumed contained explicit representations of each atom in the system, it was decided that a necessary feature of the cation-benzene interaction potential would be terms for both benzene atom types. In an

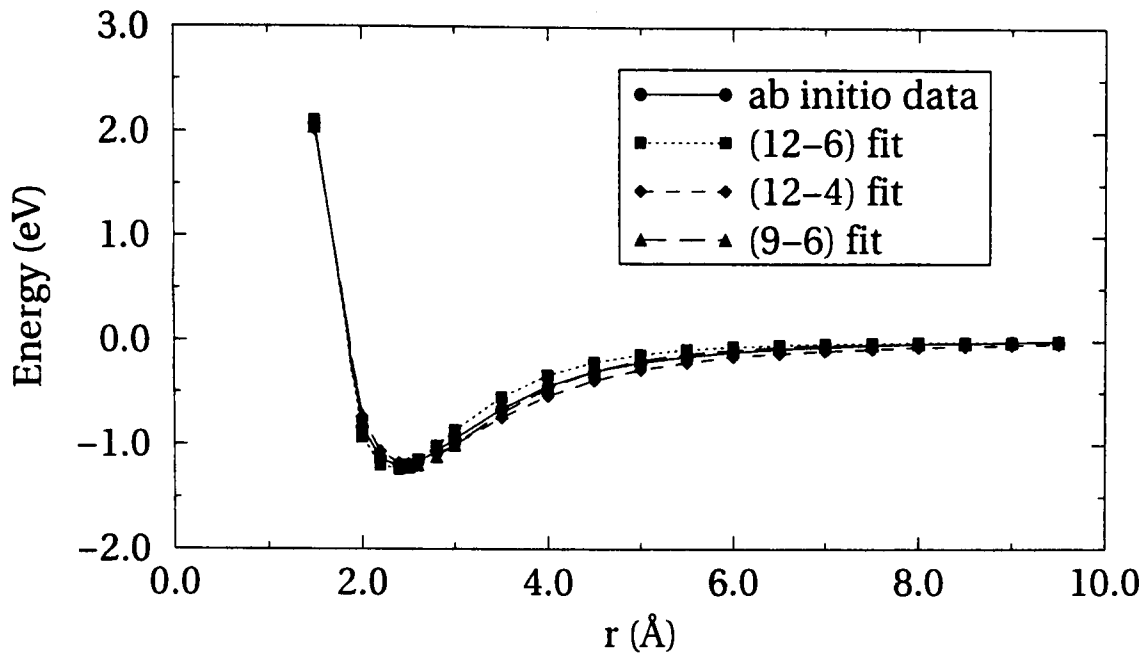
Figure 7.5: *Ab initio* potential energy surface for benzene and Na^+. Curves are labelled according to the values of θ_1 and θ_2 as defined below.



attempt to achieve this, constraints were added to the fitting procedure. In particular, the ratio of σ values in the Lennard-Jones potential were constrained to that used in a previous simulation by Demontis,[239] and the fit repeated. The quality of the fit was degraded with the introduction of these constraints, but convergence was achieved for the (12-6) potential (fitted parameters: Na–C(σ,ϵ)=(2.908Å,0.0254eV), and Na–H(σ,ϵ)=(2.416Å,0.0183eV)).

In comparison with the parameter values obtained for the interaction of benzene with siliceous zeolites, the well-depths are about an order of magnitude deeper, so clearly they need to be adjusted to be compatible with the existing forcefield. In all subsequent fits, detailed below, the ratio of the σ and ϵ values for these parameters will be held constant.

Figure 7.6: Results of fitting procedures to the *ab initio* potential energy surface



Since it is known that the diffusion of benzene in cation-containing faujasites is approximately two orders of magnitude slower than in siliceous faujasite, clearly it is an intractable problem to obtain a meaningful ensemble average for the interaction energy in this system by molecular dynamics. Instead, it was decided to fit the potential parameters to correctly reproduce the crystallographically determined binding sites.

Initially, the forcefield fitted for siliceous faujasite was used as a basis for the fit of the cation-benzene interactions. Although it was possible to achieve an adequate fit for the benzene at the cation binding sites, these parameters were incompatible with a stable window site. It was found that the only way to achieve both stable sites at the cation and window sites was to simultaneously fit the O–H and O–C parameters, as well as the cation-benzene parameters.

In order to introduce some semblance of temperature effects into the potential, a molecular dynamics simulation was performed at room temperature with a starting configuration consisting of each benzene bound to a cation. The system was equilibrated for 10ps, followed by data collection for 10ps as before. This process was also introduced into the fitting procedure until the calculated heat of sorption approximately reproduced the experimental heat of sorption and the crystallographically determined binding sites were stable minima. The final calculated heat of sorption was 79.5 $kJmol^{-1}$, which lies in the range of experimental measurements on this system.

The final fitted forcefield parameters for interaction between aromatics and zeolites are

given in Table 7.7.

7.7 Application to Templating Effects in Siliceous Ferrierite

Although more demanding applications of these forcefields will be given in Chapters 8 and 9, a brief example will be given here to test the applicability of the forcefield parameters on a different system to that on which the fit was performed.

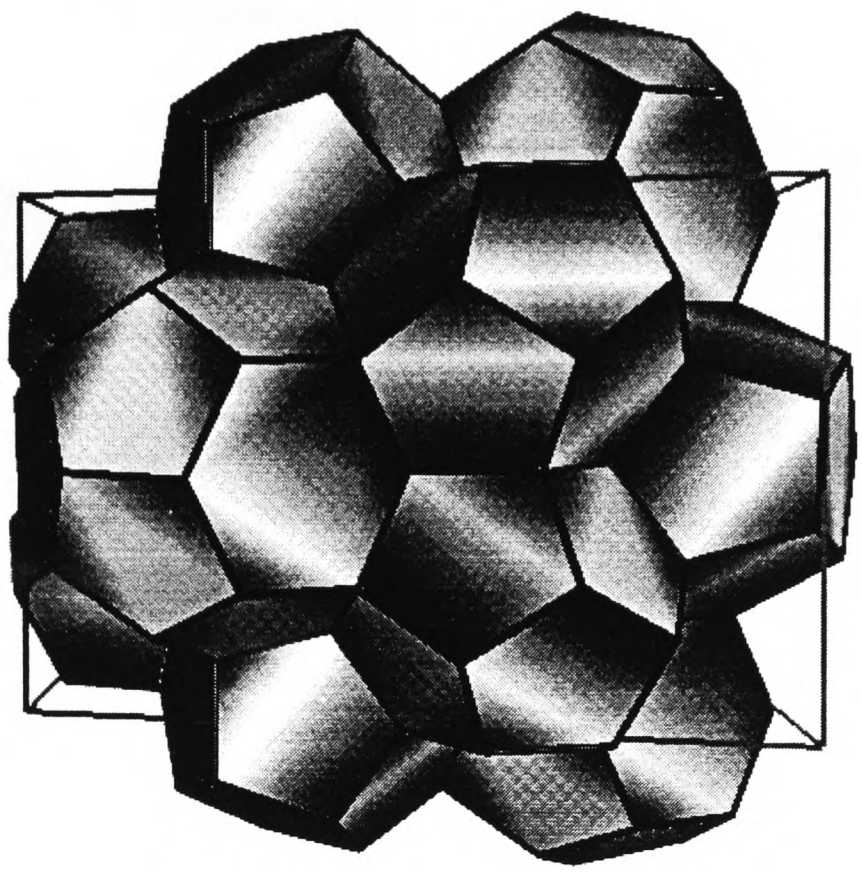
7.7.1 Background

Morris and co-workers[249] have recently performed a detailed study of the synthesis and characterisation of siliceous ferrierite. In this work, a synthetic procedure incorporating a non-aqueous solvent system (HF/pyridine/propylamine) was employed which allowed the extraction of large single crystals of the product following the method first demonstrated by Kuperman and co-workers.[42,43] The ferrierite product is formed in competition with the clathrasil structure, dodecasil-3C, depending on the nature of the synthetic conditions. In subsequent work, Weigel and co-workers[35] performed single crystal X-ray studies on samples of both siliceous ferrierite and dodecasil-3C prior to calcination in an attempt to locate the templates encapsulated in the structures. The ferrierite structure shows the presence of pyridine in both the main and side channels of ferrierite with small amounts of propylamine only in the main channel. Contrastingly, in dodecasil-3C, pyridine is found in the larger cavities with propylamine in the smaller ones. The forcefield developed in the previous sections will be used to investigate the relative binding energies of the various sites of the templates in these zeolite structures.

7.7.2 Structural Details

The structure of zeolite ferrierite was detailed in Chapter 6. It has a channel structure consisting of ten-ring channels with elliptical cross-section (4.3x5.5Å) which lie parallel to the c-axis and are interconnected by smaller eight-ring channels running parallel to b-axis. The structure of the clathrasil dodecasil-3C can be thought of as being made up from two types of cages, one a pentagonal dodecahedron and the other a larger hexadecahedron, that are fused through five-ring faces as shown in Figure 7.7.

Figure 7.7: The structure of dodecasil-3C



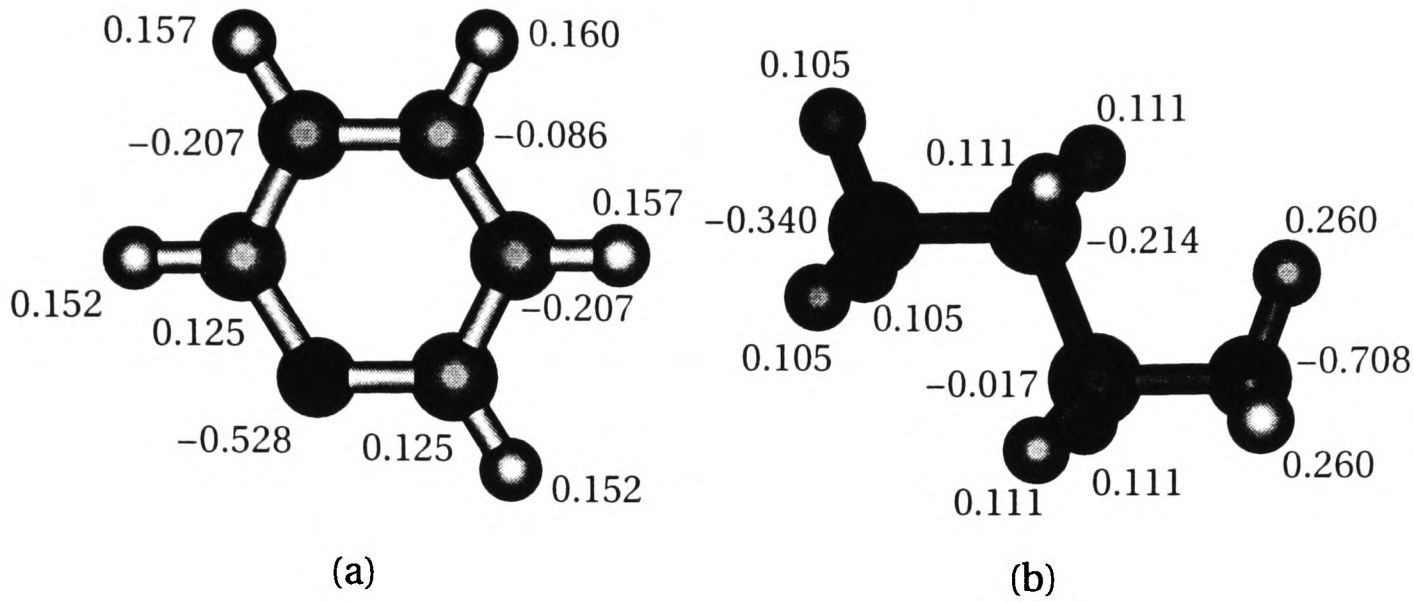
7.7.3 Potential Parameter Assignment

Since there have been no parameters fitted for the interaction of HF with the zeolite framework and the crystallographic studies failed to locate this molecule, it is most convenient to concentrate on the sorption of two nitrogen-containing bases: propylamine and pyridine. In order to generate partial atomic charges for the molecules, a Hartree-Fock calculation was performed, as described previously. The charges were adjusted slightly to retain compatibility with the previous fitted forcefields for hydrocarbons and aromatic molecules. The results are shown in Figure 7.8. The atoms in pyridine were assigned the same potential parameters as those fitted for benzene, in the hope that the partial charge assignment would be sufficient to distinguish between the two molecules. Similarly, the atoms in propylamine were assigned the same dispersive parameters as those used for butane.

7.7.4 Docking Calculations

The following models for the two zeolite structures were chosen. Since the structural refinement of Weigel and co-workers adopted the same space group ($Pnmm$) as that for the siliceous ferrierite structure used by Morris and co-workers, the latter was chosen as the

Figure 7.8: Partial charge assignment for (a) pyridine and (b) propylamine from a Mulliken population analysis



starting point for the calculations here. The $I\bar{4}2d$ model of the dodecasil-3C structure by Weigel and co-workers was used, which is consistent with a previous structural study of Chae and co-workers.[366] The calculations performed in Chapter 4 have shown that there is a small difference in the thermodynamic stability between these two systems in the absence of template molecules (lattice energies relative to α-quartz: ferrierite, +11.3 kJmol^{-1} compared to dodecasil-3C, +10.8 kJmol^{-1}), although the dodecasil-3C would be expected to be the final product if thermodynamic control was the driving force during synthesis.

Docking calculations were performed to probe the relative binding energies of the template molecules in each of the zeolite frameworks, using the methods detailed in Chapter 8. The zeolite structures were initially minimised at constant pressure to obtain a starting point for the docking calculations. In each case, the cells expand during the minimisation procedure (Table 7.8). This is most marked in the case of dodecasil-3C, where a 5.4% cell expansion is observed. The changes in the cell parameters correspond to only small changes in gross structural features such as channel and cage diameters and therefore the main structural components are maintained which is sufficient for the docking calculations.

A 2x1x1 supercell was constructed from the minimised cell of ferrierite to facilitate the inclusion of a longer short-range cutoff that could not have been employed with the crystallographic unit cell. A conformational database was created for the propylamine

Table 7.8: Results of lattice energy minimisation of ferrierite and dodecasil-3C in the absence of template molecules showing changes in cell parameters and unit cell volume on minimisation

	experiment			calculated			% change in volume
	a (Å)	b (Å)	c (Å)	a (Å)	b (Å)	c (Å)	
ferrierite	18.83	14.10	7.43	19.01	14.18	7.52	+2.2
dodecasil-3C	13.64	13.64	19.51	13.88	19.85	13.96	+5.4

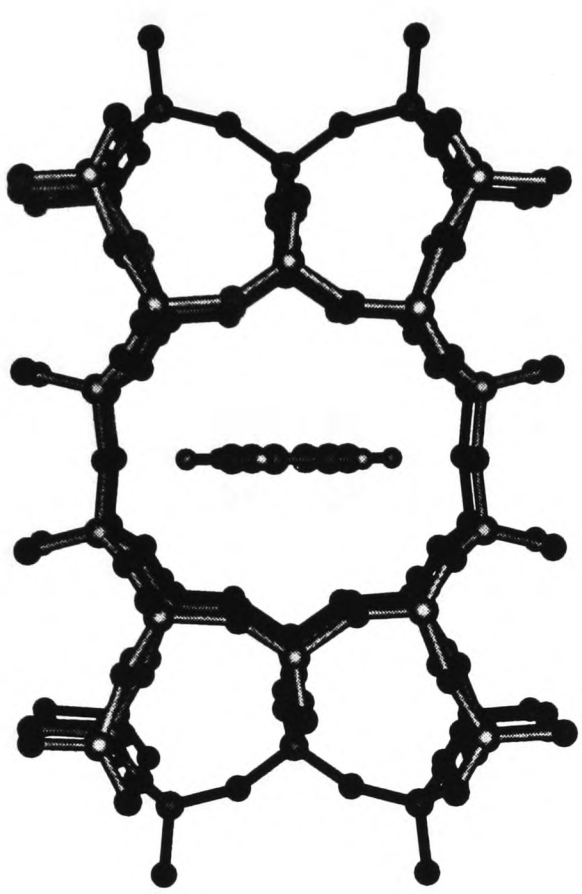
molecule using a high temperature molecular dynamics simulation to fully explore the conformational potential energy surface. Twenty docked configurations were obtained for each of the template molecules in each of the silica structures by random insertion followed by minimisation of the template position with the zeolite held fixed. After subsequent analysis, representative binding sites were identified for each template molecule and all atomic positions further relaxed to obtain the final binding energies. Binding sites are calculated for each of the molecules in both the ten-ring and eight-ring channels in ferrierite, and also in the small and large cages of the dodecasil-3C structure. However, no site is found for the pyridine in the small cage of dodecasil since the cage is too small to accommodate the molecule. The calculated binding energies for the docked template molecules are shown in Table 7.9. The predicted orientation of the pyridine in the ten-ring channel of

Table 7.9: Calculated binding energies for docked template molecules in ferrierite and dodecasil-3C ($kJmol^{-1}$)

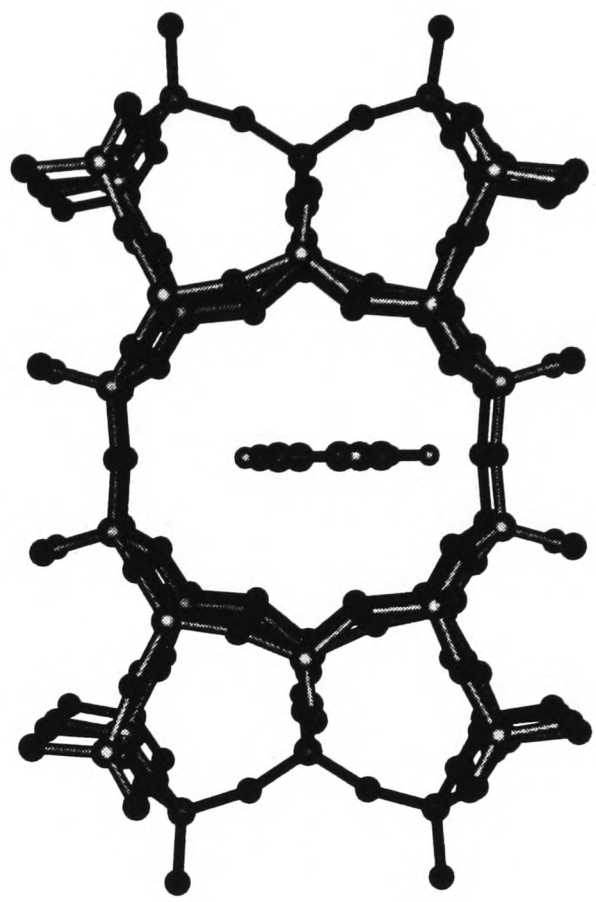
	ferrierite		dodecasil	
molecule	eight-ring channel	ten-ring channel	small cage	large cage
pyridine	78	62	no site	76
propylamine	79	70	78	73

ferrierite reproduces the crystallographic positions quite closely, clearly showing the tilting of the molecules with respect to the zeolite framework (Figure 7.9), but there are noticeable differences in the propylamine positions (Figure 7.10). The thermal ellipsoids on the ring atoms of the pyridine from the single-crystal study are sufficiently different to be able to locate the nitrogen atom of the pyridine ring unambiguously with the nitrogen atom

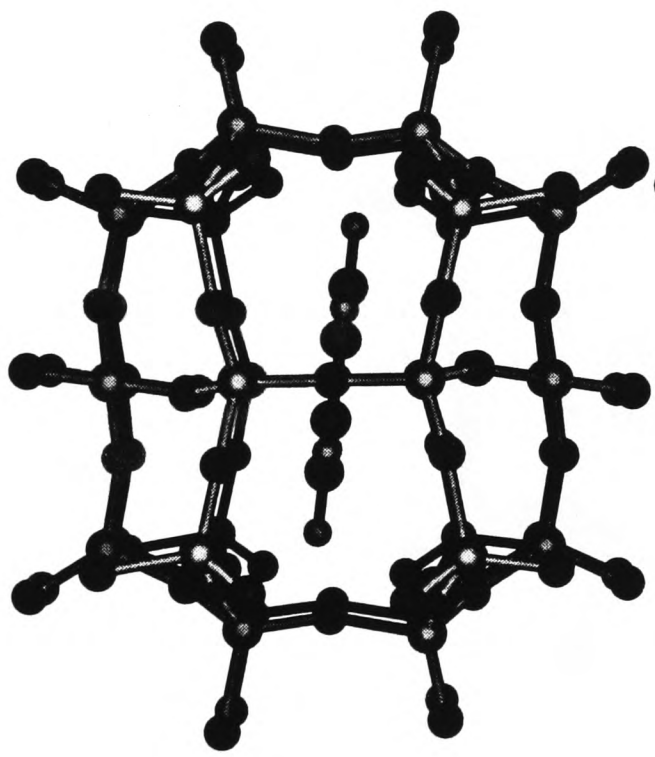
Figure 7.9: Comparison of experimental and calculated sorption sites for pyridine in siliceous ferrierite



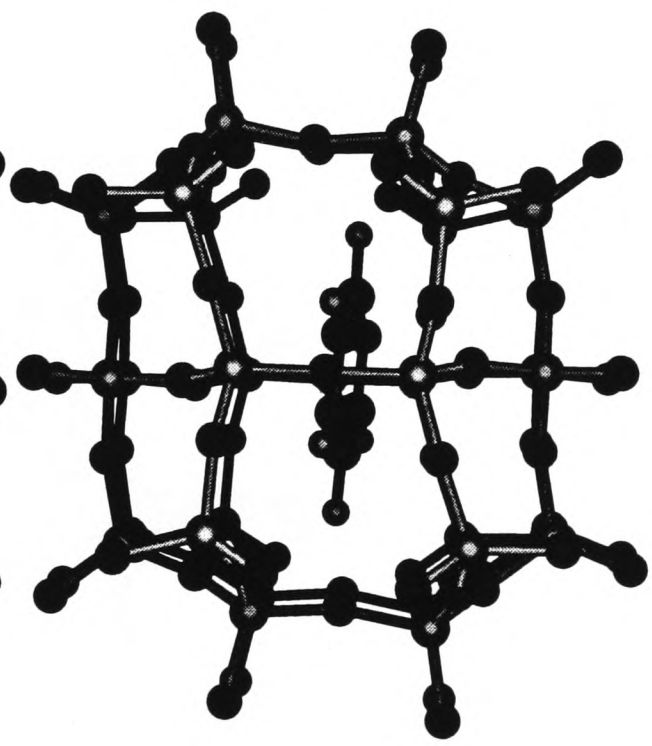
(a) ten-ring site: experiment



(b) ten-ring site: calculated

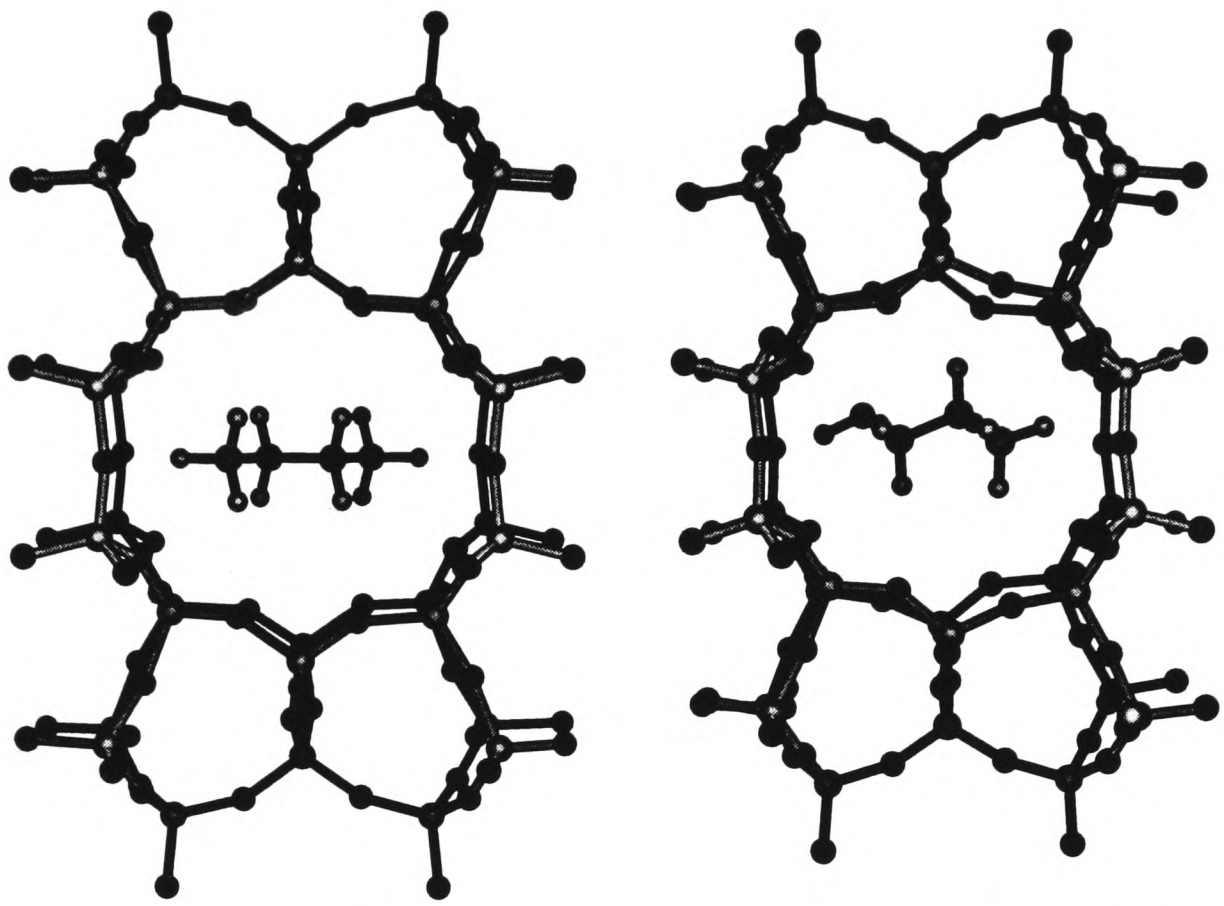


(c) eight-ring site: experiment



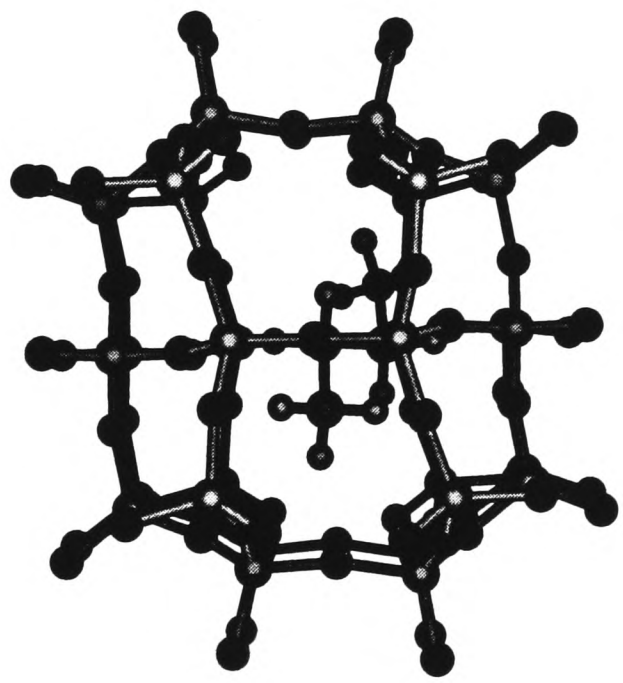
(d) eight-ring site: calculated

Figure 7.10: Comparison of experimental and calculated sorption sites for propylamine in siliceous ferrierite



(a) ten-ring site: experiment

(b) ten-ring site: calculated



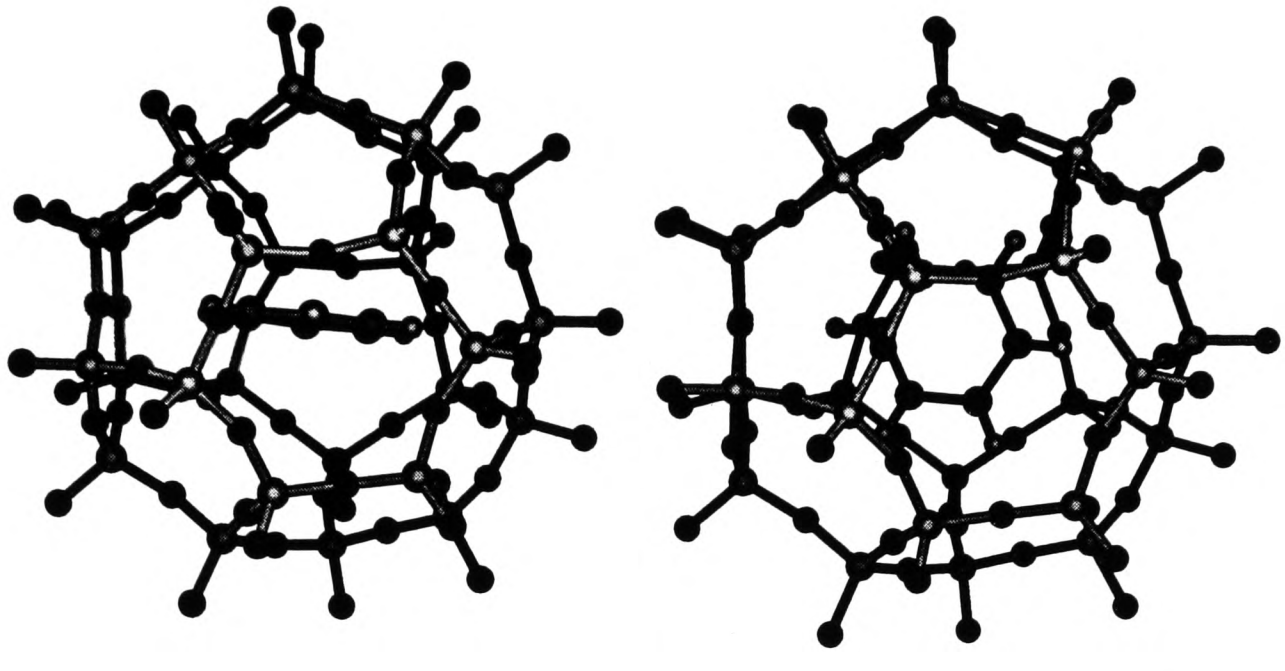
(c) eight-ring site: calculated

pointed towards the ten-ring channel. The docking calculation predict both this site and the alternative rotamer with the nitrogen pointed into the small cage. The latter is predicted to be about 4kJmol^{-1} more stable than the experimental position. The refinement is unable to locate the nitrogen atom for the second pyridine binding site in the main channel. The docking calculation only predicts one site in the main channel with the same orientation as the experimental geometry; the nitrogen atom points towards the side channel.

There is only a small amount of propylamine located in the crystallographic study (12% occupancy of propylamine compared to 90% occupancy of pyridine in the refinement), and all the refined propylamine positions lie in the same plane as the pyridine atoms in the main channel. Although in the study of Weigel and co-workers, there was some electron density lying outside this plane in the difference Fourier map, further propylamine binding sites could not be refined independently. Therefore it is probable that there are several disordered binding sites for propylamine in the main channel of extremely low occupancy, which is not inconsistent with the docking calculations. Although the refinement is not able to refine the nitrogen atom of the amine independently of the other heavy atoms in the hydrocarbon chain, the relevant orientation of the molecule indicates that the amine nitrogen points towards the side channel which is consistent with the docking results. It is probable that this is due to the relatively negatively charged nitrogen atom assuming a position to minimise repulsive interactions with nearby framework oxygen atoms as in the case of pyridine. This is also the case for the calculated propylamine binding site in the side channel.

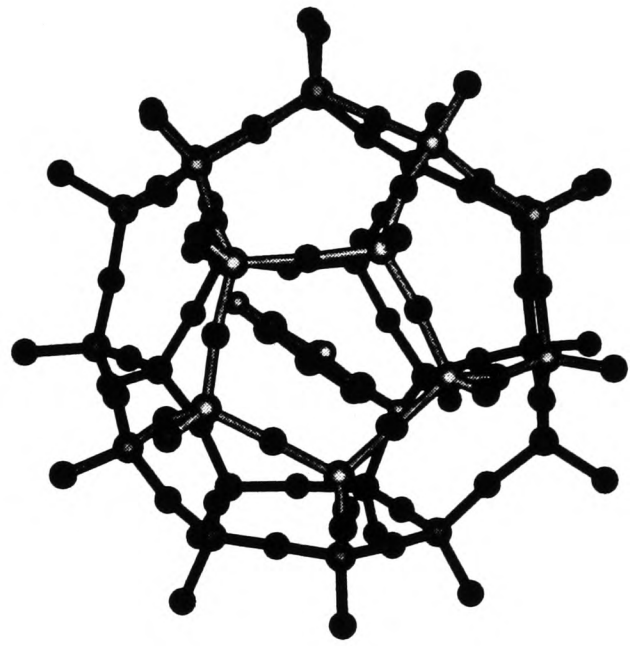
In the case of dodecasil, the structural study indicates that 80% of the large cages contain pyridine, and 25% of the smaller cages contain propylamine. There are two separate orientations for each of the molecules. The docking results are consistent with exclusive occupancy of the small cage by propylamine with pyridine being found in the large cage, although the agreement between the calculated and experimental orientations is not as exact as for ferrierite. The comparison with the experimental sorption sites is shown in Figures 7.11 and 7.12. The calculated binding site for pyridine in the large cage lies away from the centre of the cavity by about 0.86Å in order to optimise distances between the hydrogen atoms of the pyridine and the oxygen atoms of the framework. The refined position lies at the exact centre of the cage although this is to some extent a consequence of

Figure 7.11: Comparison of experimental and calculated sorption sites for pyridine in siliceous dodecasil-3C



(a) experiment : large cage site A

(b) experiment : large cage site B

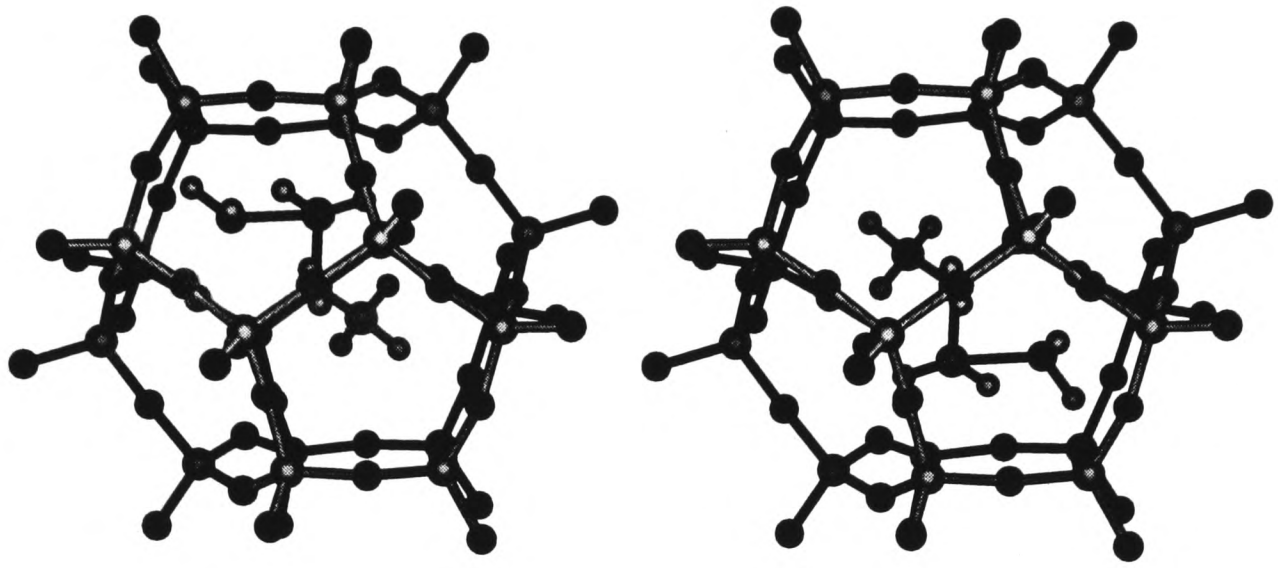


(c) calculated : large cage site

the space group choice, and does not preclude the possibility of several sites lying slightly off-centre.

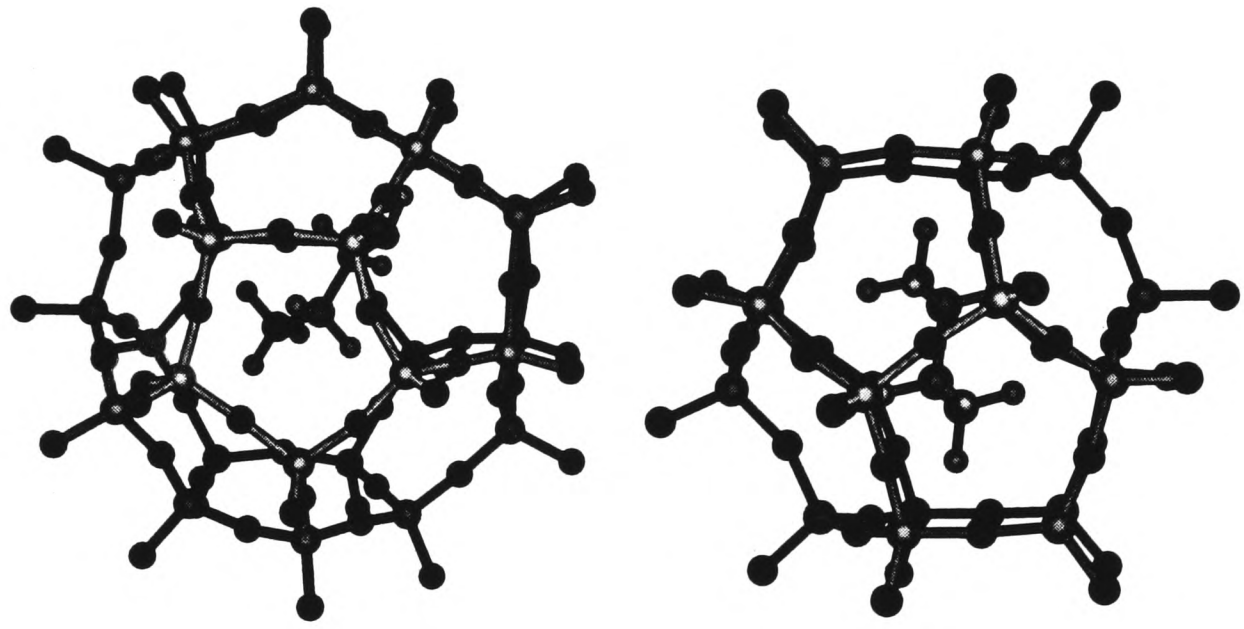
With the presence of both template molecules in the synthetic conditions, it is probable that some degree of competitive sorption, as well as the templating effects, occurs in the two zeolite framework. The calculations here represent the infinite dilution and make no

Figure 7.12: Comparison of experimental and calculated sorption sites for propylamine in siliceous dodecasil-3C



(a) experiment : small cage site A

(b) experiment : small cage site B



(c) calculated : large cage site

(d) calculated : small cage site

attempt to investigate this effect.

The calculated binding energies of the template molecules in each of the zeolite structures are very similar, which would suggest that thermodynamic factors are unlikely to be the driving force determining the relationship between the obtained product and reaction conditions during synthesis. It is possible that entropic factors and other kinetic effects not directly considered in the calculations are responsible for the templating process. Nev-

ertheless, the agreement between the docking calculations and the experimentally determined sites is encouraging.

Chapter Eight

Computer Simulation of Benzene in Siliceous Faujasite

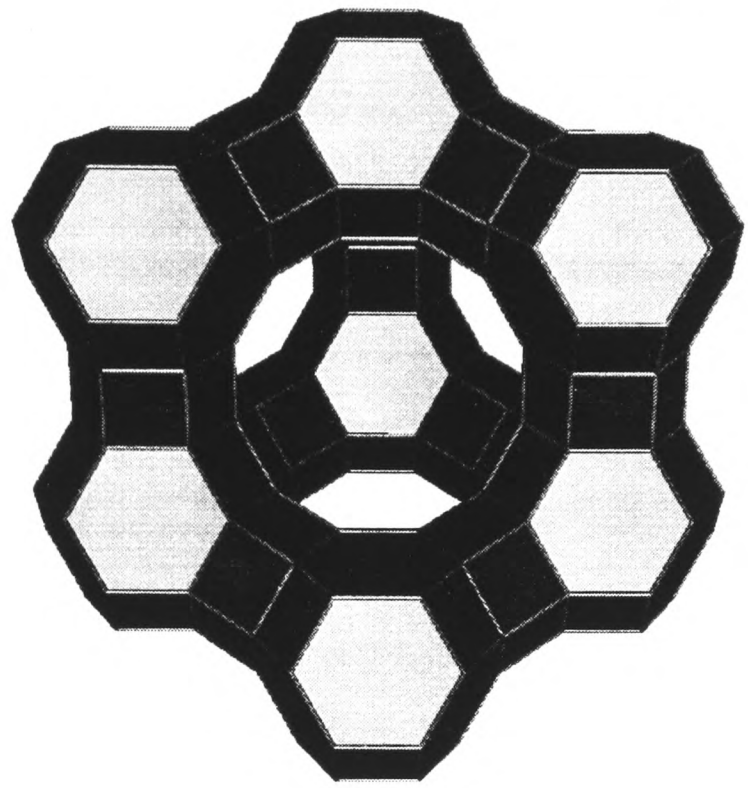
Rare-earth and high silica faujasites are widely used as catalysts in of commercial procedures. For example, an acidic form of faujasite is an important catalyst for the fluid catalytic cracking process[98] in the manufacture of gasoline, showing both good selectivity and high conversion rates. The properties and behaviour of hydrocarbon molecules within the zeolite pore are crucial to an understanding of the catalytic process. For example, the phenomenon of shape selectivity can be directly related to the relative diffusivities of the reactant and product molecules in the zeolite pores.

Siliceous faujasite represents a convenient starting model for a systematic study of the faujasite system both from an experimental and computational standpoint. Since the structure contains no aluminium or extra-framework cations, the dynamical properties of sorbed species are controlled predominantly by the hydrophobicity of the zeolite pore structure. In this chapter, the behaviour of a model probe molecule, benzene, will be examined with a number of different computational approaches. Monte Carlo docking calculations are performed to obtain preferred binding sites, and classical molecular dynamics calculations and constrained energy minimisation are utilised to investigate transport properties. In each case, the results obtained are used to compare with and rationalise available experimental data.

8.1 Structural Models and Experimental Data

The faujasite framework structure is shown in Figure 8.1. The structure can be thought of as being made up of sodalite cages, fused through their six-ring faces (diameter 2.2Å) by hexagonal prisms (double six-rings) (Figure 2.3). This creates large spherical cavities, or supercages, of approximate diameter 13Å. Access to the supercages is afforded by twelve-

Figure 8.1: The structure of the faujasite framework



ring windows with a free aperture of 7.3Å in diameter, which are tetrahedrally distributed about the centre of the supercage. The largest molecule that can be sorbed into the faujasite structure is tributylamine, which has a kinetic diameter of 8.1Å.[14]

The siliceous form of the faujasite framework can be prepared experimentally by a post-synthetic modification method from a cation-substituted faujasite, as detailed in Chapter 2. A neutron diffraction study of this structure has been carried out by Hriljac and co-workers.[31] In addition, an analogous study was made on a sample with benzene sorbed. The data set was collected at 4K in an attempt to restrict the molecular motion that may complicate a structural refinement. Although the framework refines to a model which gives reasonable bond lengths and bond angles, attempts to locate the benzene sorption site were unsuccessful. Since the refined cell parameter was greater than in the unloaded zeolite (24.3210Å vs. 24.258Å), it was inferred that although benzene was indeed present in the structure, it was disordered over a number of different sorption sites of similar binding energy.

The transport properties of benzene in siliceous faujasite have been studied by Bull and co-workers.[89] In this work, the technique of ^{2}H NMR spin lattice (T_1) relaxation was chosen. The experimental method probes the rate of molecular reorientation of the benzene

molecule by monitoring how the interaction with the deuterium quadrupole is averaged as a function of time. This effect manifests itself in the line shape of the NMR spectra. The lineshape of the NMR spectra as a function of temperature indicated that the motion of the benzene molecule was essentially isotropic at all temperatures studied (from 155K to 300K). The existence of the isotropic signal at temperatures considerably lower than the melting point of benzene (278.5K) suggests that the sorbate would also be present under the conditions of the neutron diffraction experiment. The relaxation times measured in the NMR experiment were used to obtain the diffusivity and activation energy for the transport process. The measured diffusion coefficient at 298K was $4.5\pm3.3\text{x}10^{-10}$ m^2s^{-1} and the activation energy was 10.2 ± 0.8 $kJmol^{-1}$. However, it must be pointed out that without further experimental measurements on this system it is unclear as to whether the experiment is truly measuring a diffusive process or merely one in which the molecular reorientation occurs without overall translation motion in the zeolite pores. The activation energy and pre-exponential factor may indeed reflect this reorientational motion rather than the diffusion process. Recently, further measurements have also been made on this system. Nesbitt and Mann have performed pulsed-field-gradient NMR experiments and measured an activation energy of $38.6kJmol^{-1}$ with a room-temperature diffusion coefficient of $3.34\text{x}10^{-10}m^2s^{-1}$.[367] The diffusion coefficient is comparable with the value from the spin-lattice relaxation experiment, but the activation energy is noticeably higher.

8.2 Energy Minimisation of Siliceous Faujasite

As the first step in the study of this system, calculations were performed on the unloaded zeolite with the structure of Hriljac and co-workers as the starting model. In order to assess the quality of the forcefield for the zeolite, a lattice energy minimisation calculation was also performed. The final structure showed a 4.8% increase in cell volume, with the cell parameter increasing to 24.638Å. All subsequent calculations are performed with the cell parameters fixed at this minimum energy position in order to simplify the simulations.

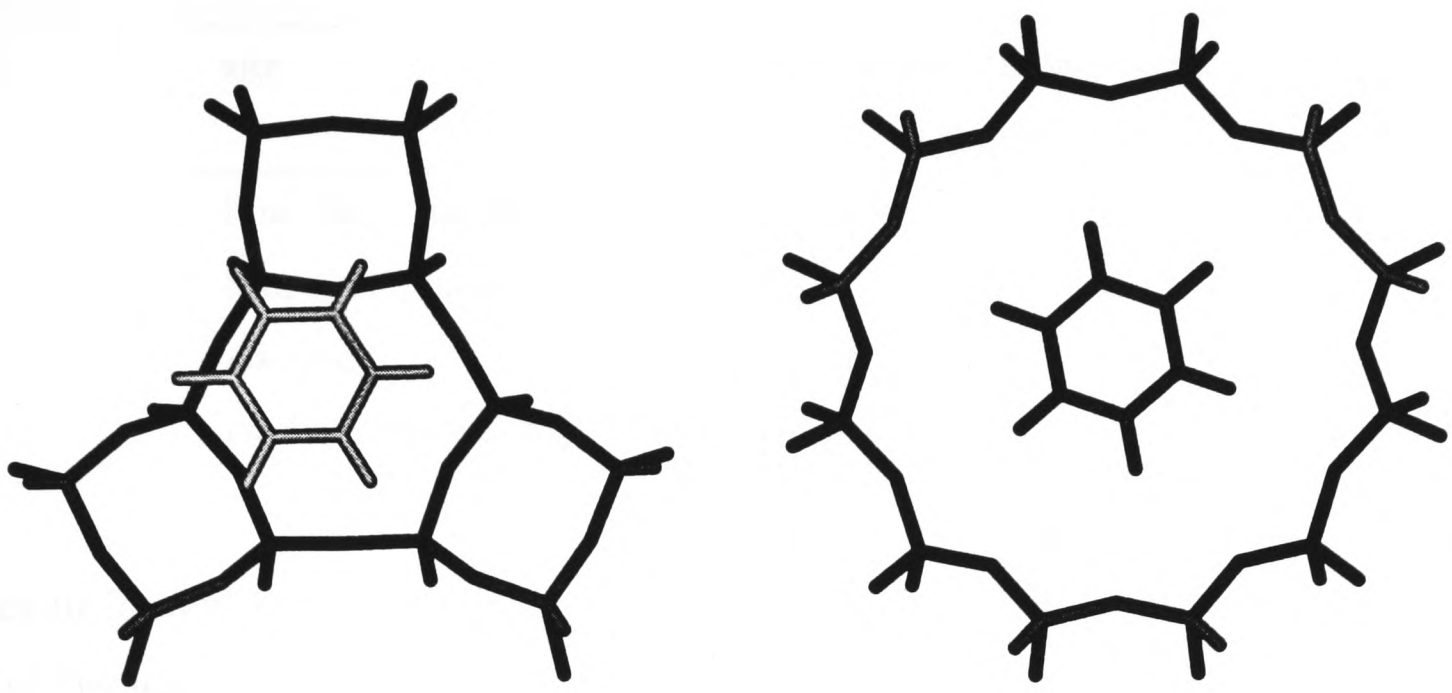
8.3 Calculation of Preferred Binding Sites

To analyse the siliceous faujasite structure for possible binding sites for the sorbate, a modified docking procedure was developed based on the method demonstrated by Freeman and co-workers.[222] Since the benzene molecule is relatively rigid with respect to distortions of the ring away from planarity, the initial guest dynamics step is omitted. This step is performed to obtain a large number of thermally accessible conformations in cases where the sorbate has many internal degrees of freedom. The modified algorithm can be described by the following steps :-

- loop (20)
  - insert sorbate into random position with random orientation
  - calculate energy
  - compare energy to some arbitrary cut-off value
    - * if less favourable, repeat insertion
    - * if more favourable, continue
  - minimise sorbate position with zeolite lattice fixed
  - store minimised configuration and final energy
  - loop (9)
    - * perform 500 cycles of high temperature dynamics on sorbate in zeolite
    - * minimise sorbate position with zeolite lattice fixed
    - * store minimised configuration and final energy
  - end loop
- end loop

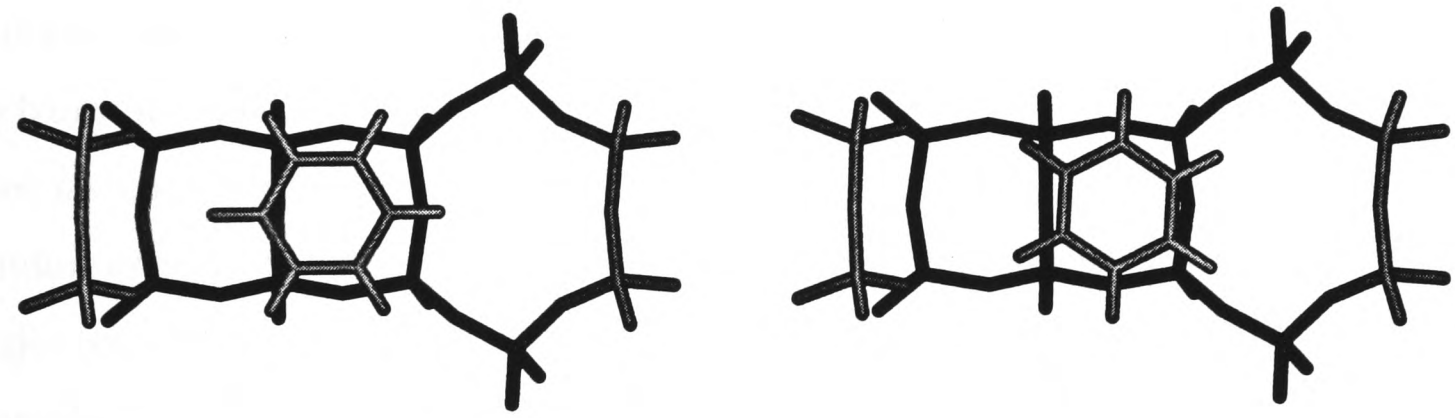
Since the system consists contains approximately 600 atoms, the memory requirements for a minimisation method based on the storage of the Hessian matrix are prohibitive. It was therefore decided to employ a minimisation method using only first derivatives. The dynamical minimisation method, LFOPC, as developed by Snymann[368] (Appendix A) is attractive in that it is both quite efficient for the optimisation of high-dimensional functions

Figure 8.2: Calculated sorption sites for benzene in siliceous faujasite



(a) six-ring site

(b) window site



(c) four-ring site "parallel"

(d) four-ring site "perpendicular"

and is also compatible with other dynamical functionality in the existing software. The introduction of a high-temperature dynamics phase into the docking algorithm reduces the possibility of local minima and saddle points in the final configurations that are inherent in the Snymann method. Thus the docking method generates a large number of minimum energy sites for the sorbate which should fully characterise the zeolite-sorbate potential energy surface.

The sorption sites generated by the docking procedure are shown in Figure 8.2. The relative energies of the binding sites are shown in Table 8.1. The most favourable binding

Table 8.1: Relative binding energies of calculated sorption sites for benzene in siliceous faujasite

site	fixed lattice	flexible lattice
	($kJmol^{-1}$)	
four-ring ("perpendicular")	54.7	56.3
four-ring ("parallel")	51.7	53.3
six-ring	48.6	50.4
twelve-ring (window)	43.4	43.8

sites are located above the four-rings in the wall of the supercage. Two sites are found, the most favourable being oriented such that opposite C–C bonds in the benzene ring lie perpendicular to a line drawn between adjacent six-rings (Figure 8.2(d)). However, the energy difference between the two four-ring binding sites suggests that they have approximately the same energy given the errors in the forcefield. There is also a site located in the vicinity of the six-ring, although in the absence of a cation, the benzene appears to prefer a geometry lying off-centre and closer to the adjacent four-ring. The window site is found to be the least favourable binding site in this system. The contribution of electrostatic terms to the binding energy varies from 7% for the six-ring site to 20% for the window site, and thus the major contribution comes from the dispersive terms in the forcefield, as might be expected from the hydrophobicity of the zeolite.

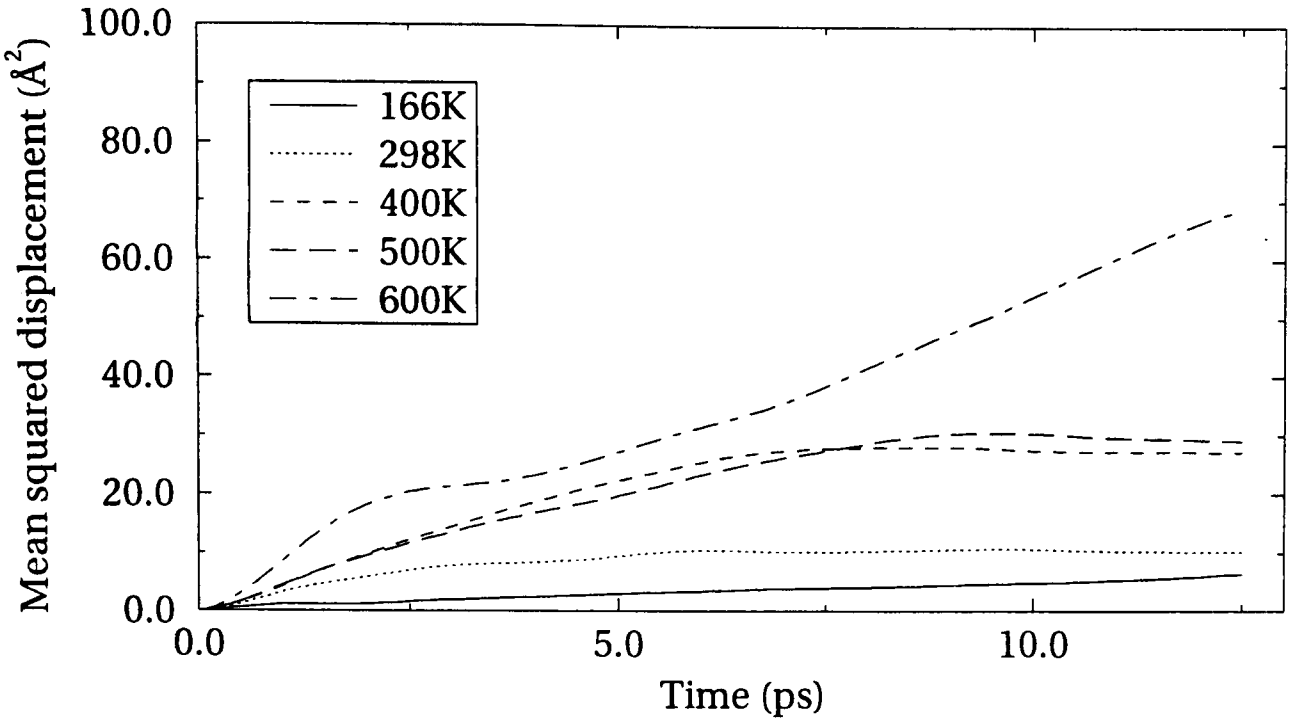
In order to assess the effect of lattice relaxation on the binding energies and geometries, further minimisations were performed using the four minimised configurations as starting points. The effect on the binding energetics is shown in Table 8.1. Both the interatomic distances and the interaction energies are only slightly perturbed from the fixed-lattice sorbate binding sites, suggesting that the effects of lattice relaxation in this case are negligible. It is interesting to note that the effect on the window binding site is significantly less than for the other sites, despite the fact benzene is is known to be quite a tight fit in the window.

8.4 Molecular Dynamics Studies

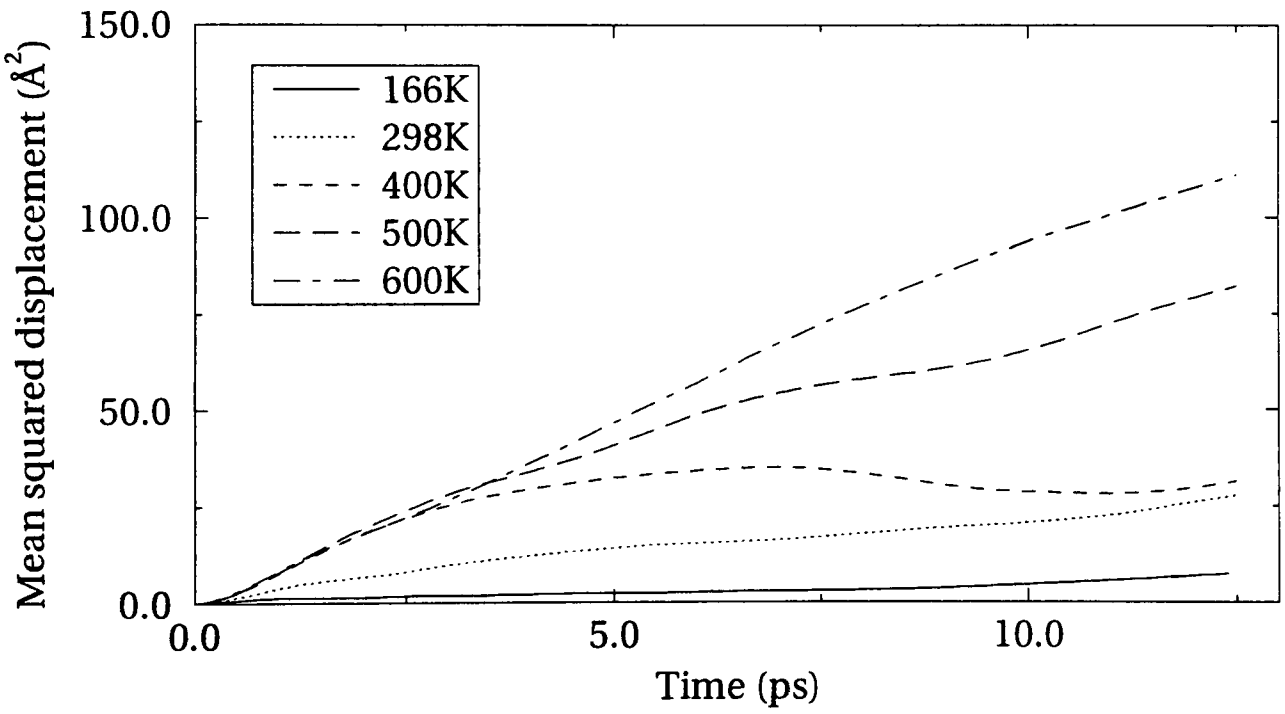
A more direct computational approach to the study of transport phenomena is by molecular dynamics. Based on earlier analyses,[243] the diffusion coefficients measured experimentally for this system represent a time scale that is at the limit of what can be reasonably investigated by classical molecular dynamics techniques.

Molecular dynamics simulations were performed in the NVT ensemble employing the same model for the zeolite as in the docking calculations. Since the experimental studies considered an experimental loading of approximately one benzene molecule per supercage, the calculations focused on the infinite dilution limit. The initial configuration for the system was generated by inserting a single benzene molecule in each of the eight supercages in the faujasite unit cell. All interactions between benzene molecules were neglected in order to simulate infinite dilution, while allowing ensemble averages to be calculated by averaging over all eight molecules to improve the statistics. In order to assess the importance of framework motion on the diffusivity, simulations with both a fixed and flexible lattice were performed. The velocity-Verlet integration scheme[338] was used with a time-step of 1fs, which was found to give energy conservation to 0.001% during an NVE simulation. Simulations were performed at 166, 298, 400, 500 and 600K with the Berendsen method[199] to constrain the temperature to a constant value (Berendsen τ parameter=1.0fs). The system was allowed to equilibrate for a 5ps period and then data were collected over a 25ps period. All the calculations were performed with the DIZZY software (Appendix B) running on a 90MHz Power Challenge XL with dual R8000 processors and 128Mb of main memory.[337] The flexible lattice calculations took 9.8 secs per time step with the majority of the computational time being spent in the calculation of the electrostatic terms in the forcefield. The diffusion coefficients were calculated both from the mean squared displacement and the velocity autocorrelation function as a function of time. A multiple-time-origin analysis was used in both methods (Equation 6.2). The resulting curves are shown in Figures 8.3 and 8.4. The mean squared displacement data were fitted to the Einstein relation, and the velocity autocorrelation function data were integrated in order to obtain diffusivities. It is clear from Figure 8.4 that none of the velocity autocorrelation functions have decayed to zero during the simulations, and therefore there

Figure 8.3: Mean squared displacement of benzene molecules as a function of time averaged over all molecules and using a multiple time origin analysis



(a) fixed lattice

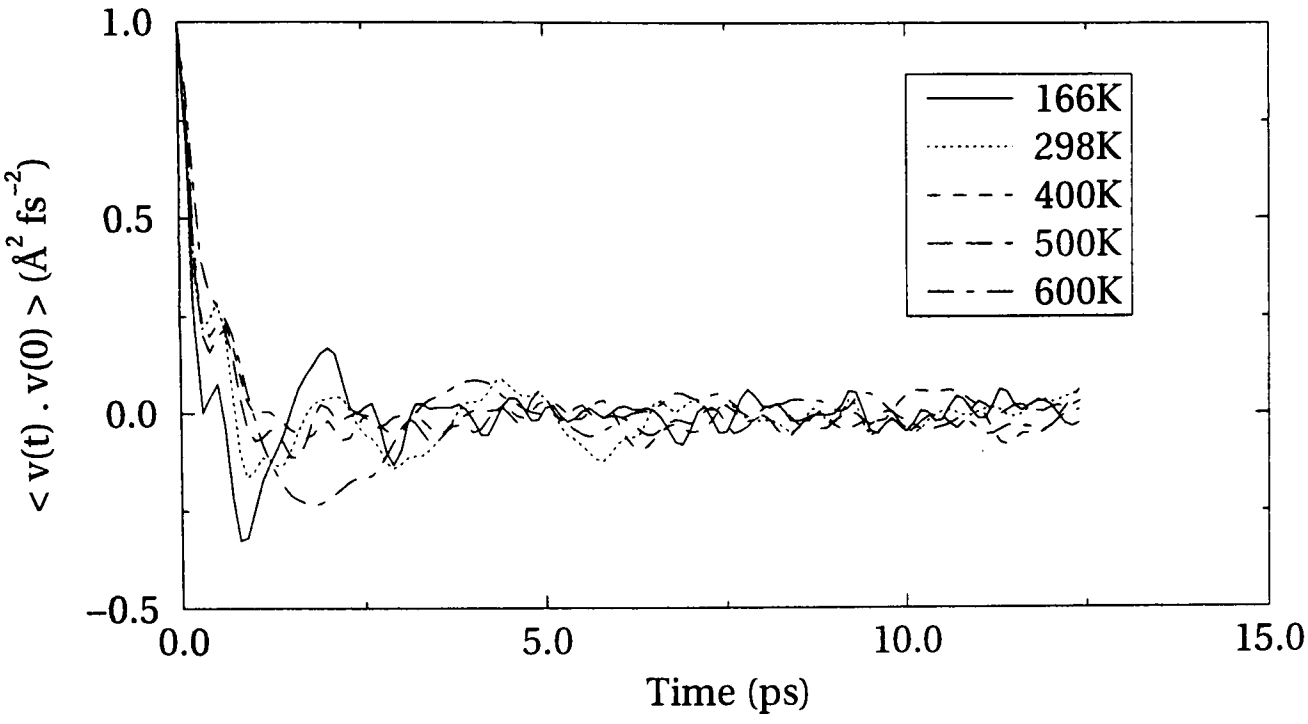


(b) flexible lattice

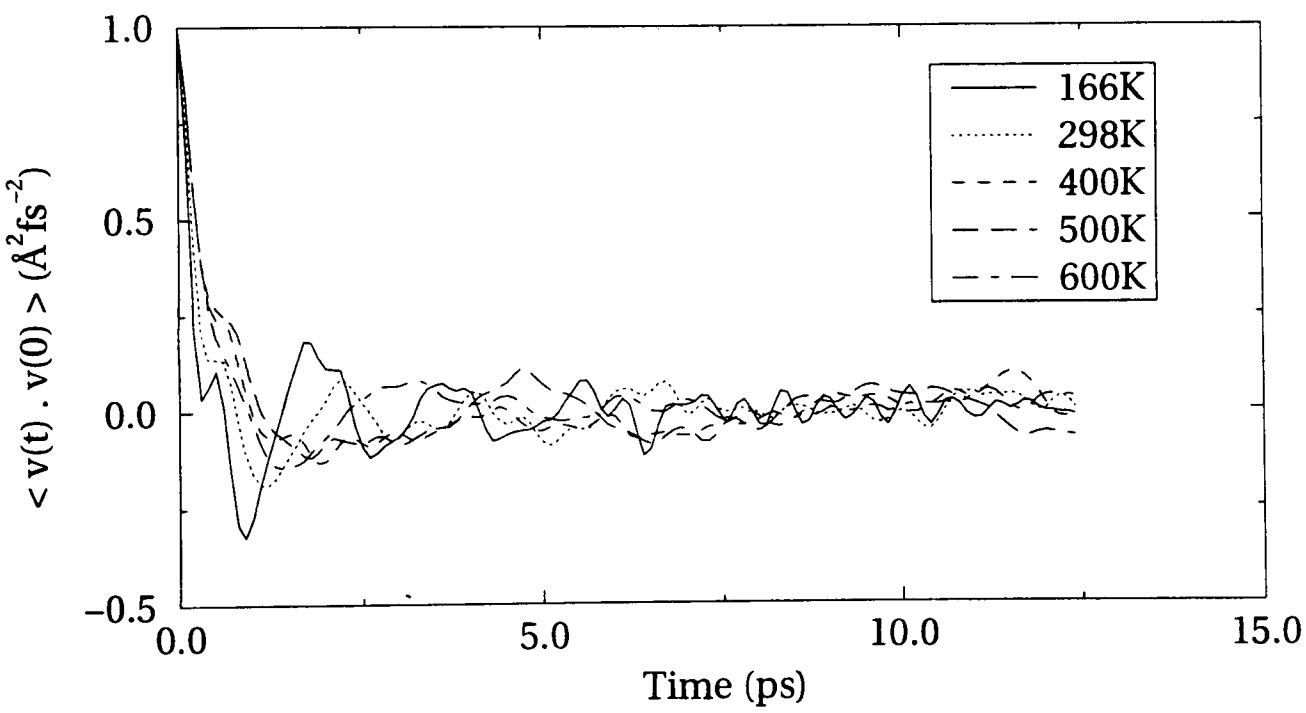
are undoubtedly significant errors in the integrals. In this case, the values obtained from the mean squared displacement plots are probably more reliable.

It can be seen that the inclusion of lattice flexibility in the simulation enhances the sorbate mobility. The effect of lattice flexibility on the diffusivity is to some degree a balance between how the lattice vibrations couple to the sorbate motion at both the sorbate binding sites and at the transition state points in the diffusion pathway. Since motion of the

Figure 8.4: Velocity autocorrelation function of benzene molecules as a function of time averaged over all molecules and using a multiple time origin analysis



(a) fixed lattice



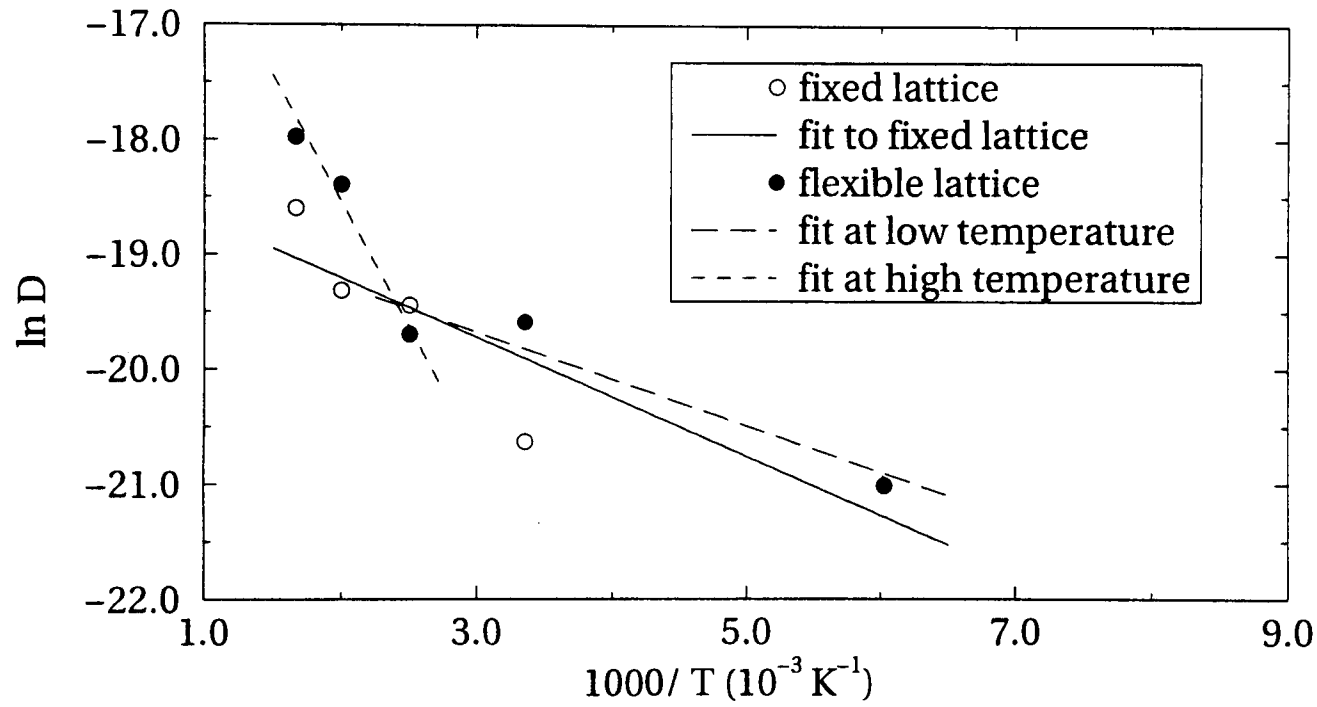
(b) flexible lattice

sorbate through the twelve-ring window is essential to long-range transport in the pore structure, the vibrations of the window undoubtedly play an important role in this process. It might be expected that, as the sorbate is quite a tight fit in the twelve-ring window, any vibrations that tend to distort the shape of the window significantly affect the probability of the sorbate successfully traversing the window into an adjacent supercage; this is a predominantly entropic effect. However, the results presented here suggest that twelve-ring

Table 8.2: Calculated diffusivities for benzene in siliceous faujasite using the Einstein relation (D_{msd}) and the velocity autocorrelation function (D_{vacf})

	fixed lattice		flexible lattice	
	D_{msd} (10^{-8} m^2s^{-1})	D_{vacf} (10^{-8} m^2s^{-1})	D_{msd} (10^{-8} m^2s^{-1})	D_{vacf} (10^{-8} m^2s^{-1})
166K	0.075(1)	0.12	0.076(2)	0.15
298K	0.11(3)	0.11	0.311(5)	0.42
400K	0.36(3)	0.55	0.28(2)	0.54
500K	0.41(1)	0.30	1.03(1)	1.00
600K	0.84(1)	0.60	1.550(8)	2.01

Figure 8.5: Arrhenius plot for the motion of benzene in siliceous faujasite



distortions do not adversely retard the motion of the sorbate through the window.

The calculated diffusivities as a function of temperature are shown in Table 8.2. The temperature variation of the diffusivity was further investigated by plotting the data as an Arrhenius plot (see Figure 8.5). The calculated pre-exponential factors and activation energies resulting from straight line fits to the Arrhenius plot are summarised in Table 8.3. For the fixed lattice, the best fit obtained is that utilising all the points and gives E_a=4.2(12) kJmol^{-1} and D_o=1.23x10^{-8} m^{2}s^{-1} (ln D_o=-18.2(5)). However, in the case of the flexible lattice simulations, the plot clearly shows the presence of two separate rate processes. At low

Table 8.3: Comparison of measured and calculated pre-exponential factors (D_o) and activation energies (E_a) for the motion of benzene in siliceous faujasite

	D_o (m^2s^{-1})	E_a ($kJmol^{-1}$)
experiment (T_1 NMR)[89]	$2.2x10^{-8}$	10.2±0.8
experiment (PFG NMR)[367]	-	38.6
fixed lattice	$1.23x10^{-8}$	4.2±1.2
flexible lattice (low temperature)	$9.4x10^{-9}$	3.4±1.1
flexible lattice (high temperature)	$5.7x10^{-7}$	17.4±3.2

temperatures, the data fits approximately to a straight line with E_a=3.4(11) $kJmol^{-1}$ and D_o=$9.4x10^{-9}$ m^2s^{-1} (ln D_o=-18.5(5)), whereas at high temperature a further process with E_a=17.4(32) $kJmol^{-1}$ and D_o=$5.7x10^{-7}m^2s^{-1}$ (ln D_o=-14.3(8)) becomes dominant. At 400K, the system is in a state in which both processes are contributing to the sorbate transport. This is indicated by the curious shape of the mean squared displacement plot at this temperature. The barrier height for the low temperature process is of the same order as the average thermal energy at this temperature (kT(400K) = 3.3 $kJmol^{-1}$). The calculated pre-exponential factors are within an order of magnitude of those measured in the T_1 relaxation NMR experiment, although the diffusivities at 298K are reproduced less exactly. However, as was mentioned previously it remains unclear as to whether the NMR experiment is probing benzene transport in this system.

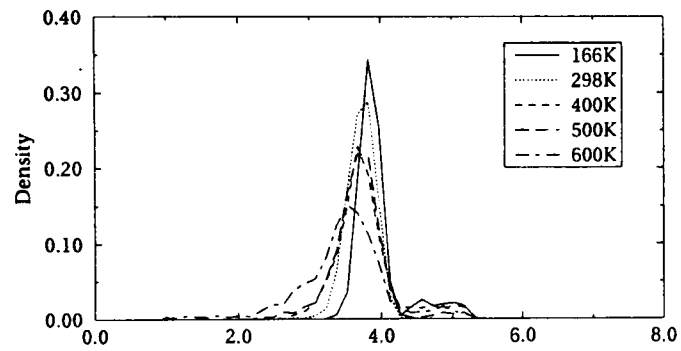
The calculated heats of sorption are shown in Table 8.4. In the case of the flexible lattice simulations, the heats of sorption are calculated as in the previous chapter, whereas for the fixed lattice case, the values simply reflect the average interaction energy between zeolite and sorbate during the dynamics runs. The general trend of decreasing sorption heat with increasing temperature is clearly seen, although the 400K simulation value once again indicates a deviation from this trend.

In a further attempt to investigate the effects of temperature on the transport mechanism, zeolite-benzene distribution functions were calculated. These are shown in Figure 8.6. Two distribution functions are considered. The first is a radial distribution function referenced to the centre of the supercage ("cage centre-benzene"). This shows that

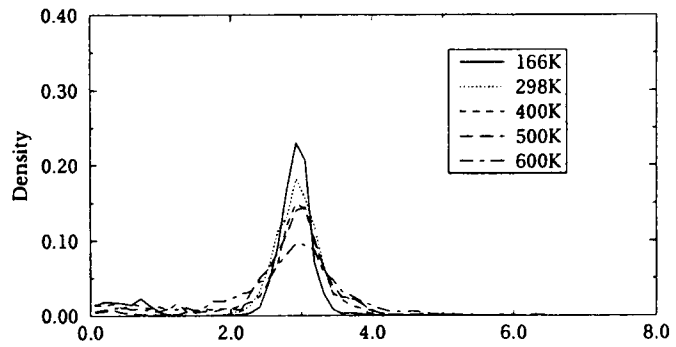
Table 8.4: Calculated heats of sorption as a function of temperature

temperature (K)	sorption heat ($kJmol^{-1}$)	
	fixed lattice	flexible lattice
166	50.9	56.3
298	48.3	53.6
400	46.6	41.1
500	47.8	44.0
600	39.4	40.1

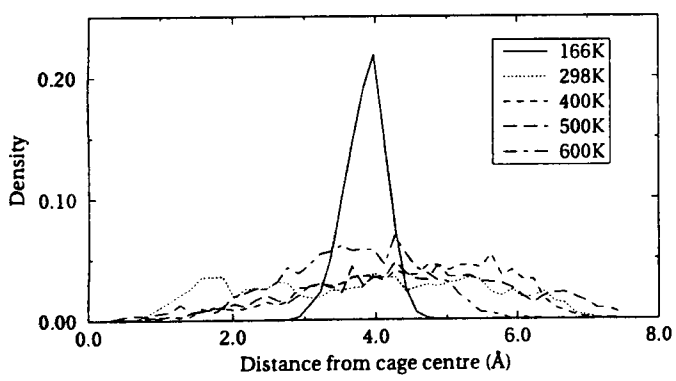
Figure 8.6: Calculated zeolite-benzene distribution functions



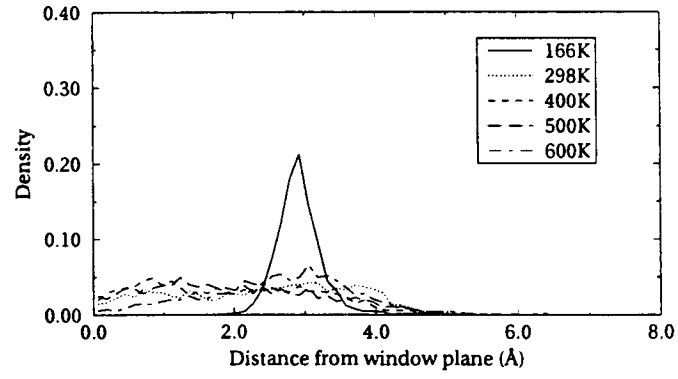
(a) fixed lattice : cage centre–benzene



(b) fixed lattice : cage window–benzene



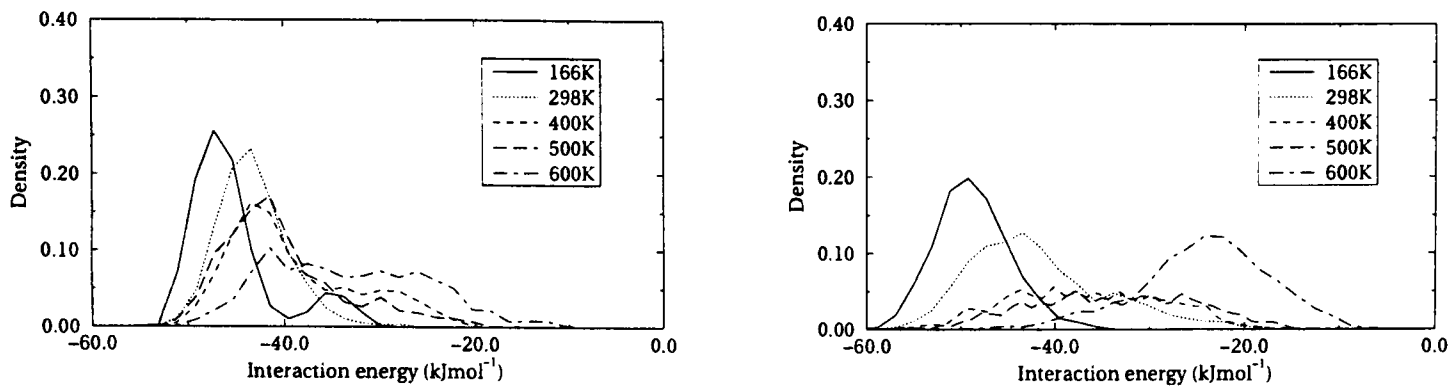
(c) flexible lattice : cage centre–benzene



(d) flexible lattice : cage window–benzene

the benzene molecules are essentially confined to the supercage walls at all temperatures. However, the peak is noticeably broadened with increasing temperature (Figure 8.6(a)). The second distribution is based on the distance of a benzene molecule from the plane of the twelve-ring window ("cage window-benzene"). Again, the main peak around 3Å

Figure 8.7: Calculated benzene molecular energy distribution functions



(a) fixed lattice

(b) flexible lattice

is indicative of benzene molecules at the supercage walls (Figure 8.6(b)). The density in the region of the window plane appears to vary little with temperature and, therefore, cannot be related directly to trends in the diffusivities. Since the time spent in the window is considerably less than in the region of the supercage walls, this suggests that the sampling time for the distribution function would have to be increased to correctly represent any trends close to the window plane. It is noted that the density in the region of the window is finite for the 166K simulation and zero for the 298K simulation. This suggests that the equilibration period in the 166K simulation may have trapped a molecule in the region of the window, which then diffuses into the supercage over the course of the simulation. This is confirmed by a graphical examination of the trajectory . The distribution functions for the flexible lattice simulations are somewhat ambiguous in that they have the same reference point as in the fixed lattice simulations (Figures 8.6(c) and 8.6(d)). Since the lattice is in motion, the centre of the cage and the window plane are constantly changing and it is problematic to define the reference points. However, it is interesting to note that at the lowest temperature considered the lattice appears to be moving insufficiently (i.e. it is essentially fixed) to noticeably affect the distribution functions.

The molecular energy distribution functions are plotted in Figure 8.7. These show the distribution of energies of single benzene molecules averaged over the duration of the simulation. For the fixed lattice simulation, the main peak is shifted to higher energy as the temperature increases, such that at 600K the maximum has moved by approximately 7 kJmol^{-1}. The distribution is also considerably flatter at the higher temperatures. It is in-

Table 8.5: Probabilities of different window transitions as function of temperature

	fixed lattice			flexible lattice		
	# hops	% reverse	% translational	# hops	% reverse	% translational
166K	18	100	0	0	0	0
298K	0	0	0	10	100	0
400K	14	90	10	40	94	6
500K	5	100	0	41	70	30
600K	8	66	33	13	17	83

teresting to note the presence of a second peak at higher energy in the 166K curve. This correlates with the hypothesis suggested above that a molecule is trapped in the region of the window site at the completion of the equilibration phase. No corresponding peak is observed at other temperatures. The flexible lattice plot shows contrasting behaviour. Whereas the significant peak is once again shifted to higher energies with increasing temperatures, two regimes are clearly observed. At the intermediate temperatures, 400K and 500K, the peak is completely broadened, only to be replaced by a new peak at considerably higher energies at 600K. This presumably reflects the transition between intra- and inter-cage motion. This adds further support to the idea that in the case of the fixed lattice, the two distinct regions in the Arrhenius plot corresponding to differing transport mechanisms are less well defined.

Further analysis into the sorbate motion as a function of temperature can be made by calculating the number of times during the simulation that a benzene molecules jumps through a window. Two types of motion can be identified here. In the first, the molecule moves through a window and then, at some later time, moves back into the original supercage ("reverse hop"); in the second, the molecule moves into another supercage during the next window transitional period ("translational hop"). These events were calculated and are summarised in Table 8.5. This table further emphasises that there is no significant long-range translational motion of the sorbate at any temperature below 600K in the fixed lattice simulations and below 400K in the flexible lattice simulations. The analysis also suggests that longer simulations are necessary to improve the statistics in the case of the fixed

lattice runs since there is no systematic increase in the number of window transitions as a function of temperature.

8.5 Hopping Pathways

In a simplified picture, the transport process of a sorbate through a zeolite can be thought of as a series of hops between binding sites. The energetics of the hopping process can be investigated by calculating the minimum energy paths between the two binding sites to obtain the transition state position for the hop and thus the activation energy. This method neglects any factors due to entropic and dynamical effects which could be included by the application of transition state theory[369] or correlation function theory.[370]

The hopping trajectory is defined by drawing a straight line between the centres of mass of benzene molecules bound at each of the two binding sites. The minimum energy pathway is calculated with a constrained energy minimisation method. This procedure drags the benzene from one site to another by constraining a single component of the benzene centre of mass, while allowing all other degrees of freedom to relax. A hopping vector, $\boldsymbol{r}_{ab}$, can be defined between the centres of mass of a benzene molecule lying at each of two binding sites a and b. Intermediate points along this vector can be defined simply as :-

$$\boldsymbol{r}_{ab}(\lambda) = \boldsymbol{r}_a + \lambda \boldsymbol{r}_{ab} \tag{8.1}$$

where λ ranges from 0 to 1. For a given value of λ, the centre of mass of benzene is constrained to lie in a plane defined as containing the intermediate point, $\boldsymbol{r}_{ab}(\lambda)$, and orthogonal to the hopping vector, $\boldsymbol{r}_{ab}$. The constraint is applied by the inclusion of a constraint potential, V_{cons}, to the forcefield, of the following form :-

$$V_{cons} = \frac{1}{2} k_{cons} \left\{ [\boldsymbol{r}(t) - \boldsymbol{r}_{ab}(\lambda)] \cdot \frac{\boldsymbol{r}_{ab}}{|\boldsymbol{r}_{ab}|} \right\}^2 \tag{8.2}$$

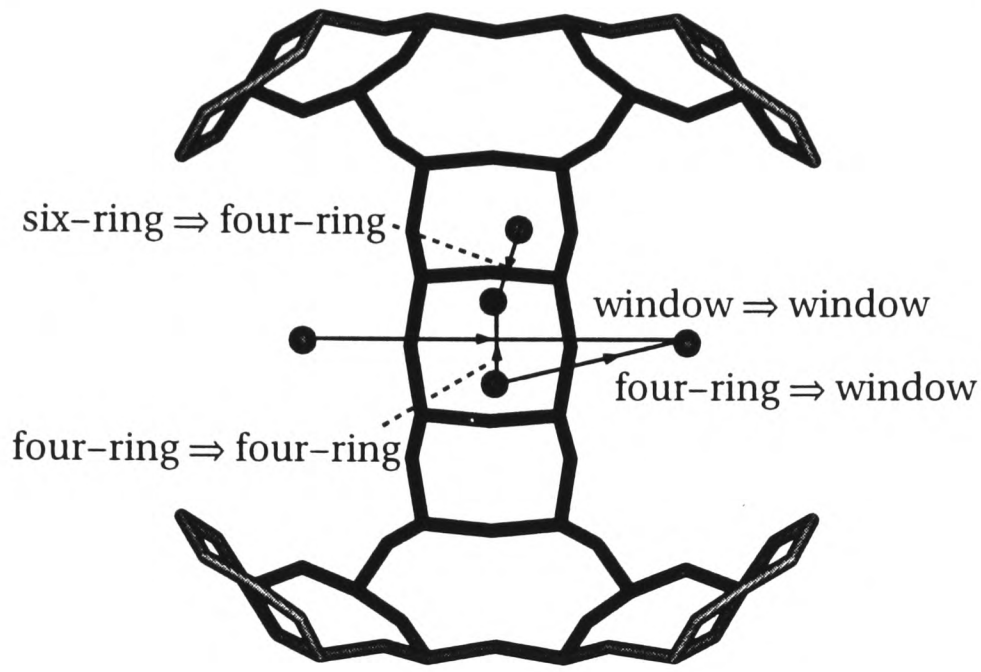
where $\boldsymbol{r}(t)$ is the instantaneous benzene centre of mass position. The force constant is typically 1 eV Å^{-2}. Each point on the pathway is annealed with the techniques outlined in the section 8.3. The resulting final configuration is used as the starting point for the next value of λ.

The reaction coordinate for the hopping process can be usefully defined following the approach of Auerbach.[371] Two separate reaction coordinates are defined that reduce the multidimensional space describing the position of the benzene to a single coordinate; one is based on the full dimensional space of the benzene atomic coordinates, whereas the second, simpler form, is derived from the benzene centre of mass positions. The 36-dimensional space of the atomic coordinates are denoted as $\mathcal{R}$, and the three-dimensional benzene centre of mass is denoted as r. The full-dimensional hopping path is the sequence of configurations $[\mathcal{R}_0,\mathcal{R}_1,\mathcal{R}_2,\ldots,\mathcal{R}_N]$. The partial hopping path length, L_n, is defined by $L_n = L_{n-1} + |\mathcal{R}_n - \mathcal{R}_{n-1}|$, where $L_0 = 0$. The reaction coordinate for the i_{th} configuration, Q_i, is given by $Q_i = L_i - L_N/2$. Thus the values increase monotonically along the minimum energy pathway. The six-fold symmetry of the benzene molecule is taken into account by permuting over the atom indices to obtain the physically meaningful shortest distance. The centre-of-mass reaction coordinate is defined in a similar way utilising the three-dimensional centre of mass positions $[r_0,r_1,r_2,\ldots,r_N]$. This is a particularly convenient approach since any difference between the two reaction coordinates is indicative of benzene reorientation along the minimum energy pathway.

The faujasite pore structure necessarily creates two classes of benzene transport each with different length scales. Over short length scales, the benzene molecule simply moves around the walls of a single supercage (*intracage* motion). This type of motion is accessible to NMR spin-lattice relaxation experiments. In order for longer length scale diffusion to occur, the benzene molecules must make hops between adjacent supercages passing through the twelve-ring windows (*intercage* motion) The rate of this process determines the intracrystalline diffusion constant measured by pulsed-field-gradient NMR.

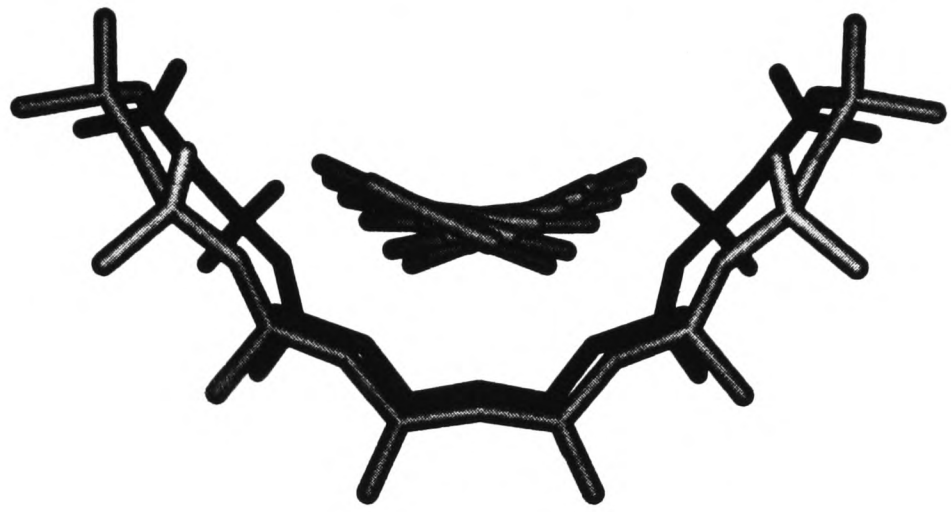
The docking calculations in the earlier section of this chapter determined a number of different binding sites. The minimum energy pathways between the following sites have been calculated : four-ring $\rightarrow$ four-ring, four-ring $\rightarrow$ six-ring, window $\rightarrow$ window, four-ring $\rightarrow$ window and six-ring $\rightarrow$ window. The first two pathways represent intracage motion, whereas the latter two are important for long length scale motion. The pathway vectors are shown schematically in Figure 8.8. Since the two possible four-ring sites are very similar in energy, and differ only in their relative rotational position, only the most-stable ("perpendicular") site is considered here.

Figure 8.8: Schematic representation of possible hopping pathways for benzene in siliceous faujasite. Shaded circles represent centre of mass positions of benzene

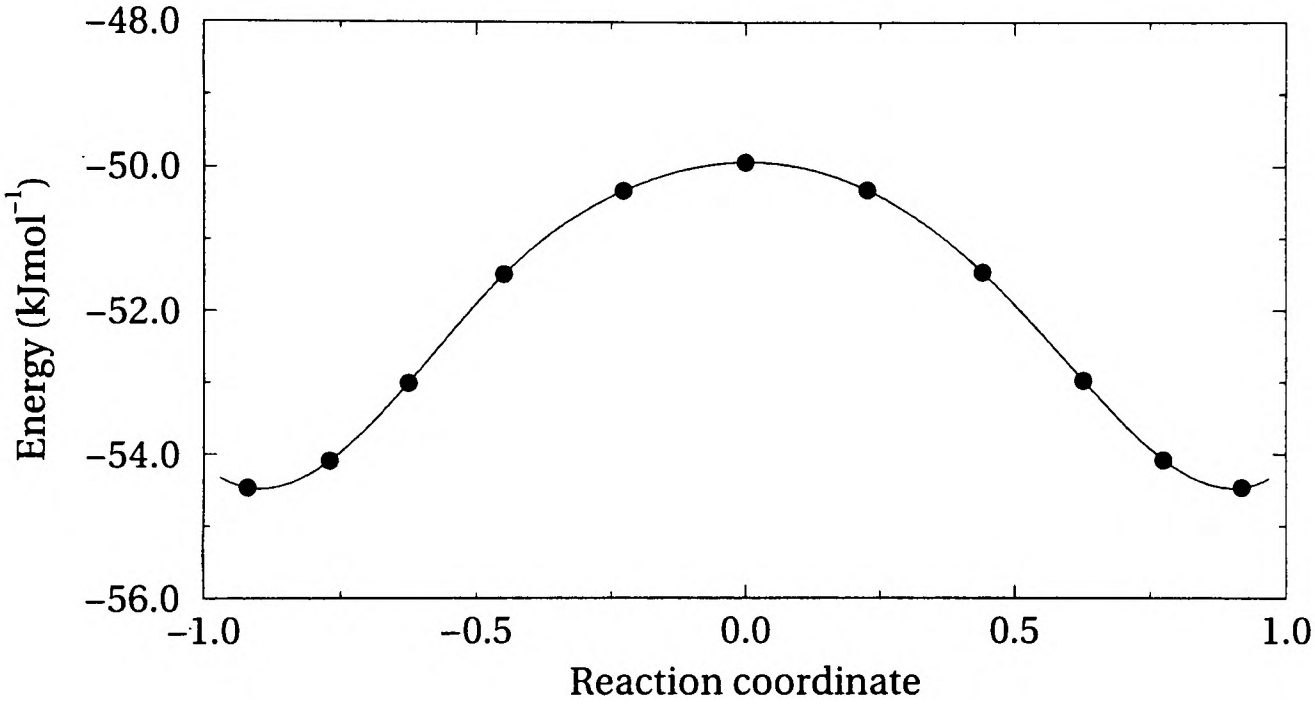


In all the following cases, the three-dimensional reaction coordinate, as defined previously, is used as the abscissa. The four-ring to four-ring hop consists of a simple sliding motion with the transition state occurring above the central four-ring. A schematic of the hop and energy profile is shown in Figure 8.9. The six-ring to four-ring hopping process is shown in Figure 8.10. This hop is interesting, in that since the two end point geometries differ by their relative rotational positions, the calculated trajectory necessarily includes the rotational barrier for conversion between the "parallel" and "perpendicular" four-ring binding sites as a consequence of the applied constraint. This can be seen clearly in the energy profile and represents only a small perturbation to the hop. Also there is hardly any barrier for the molecule leaving the six-ring site, indicating that this site is a very shallow minimum in the potential energy surface. The four-ring to window hopping process is shown in Figure 8.11. This process consists of a combined sliding and rotation process followed by a flip, and finally translation into the window. By analogy with Hammond's postulate, the transition state is "late" and therefore resembles the window binding site. Any attempt to calculate a trajectory from the six-ring site to the window results in a path going via the adjacent four-ring, again reflecting a shallow minimum. The final hopping process considered was the window-to-window hop (Figure 8.12). This is essentially a sliding mo-

Figure 8.9: The four-ring to four-ring hopping process



(a) calculated trajectory

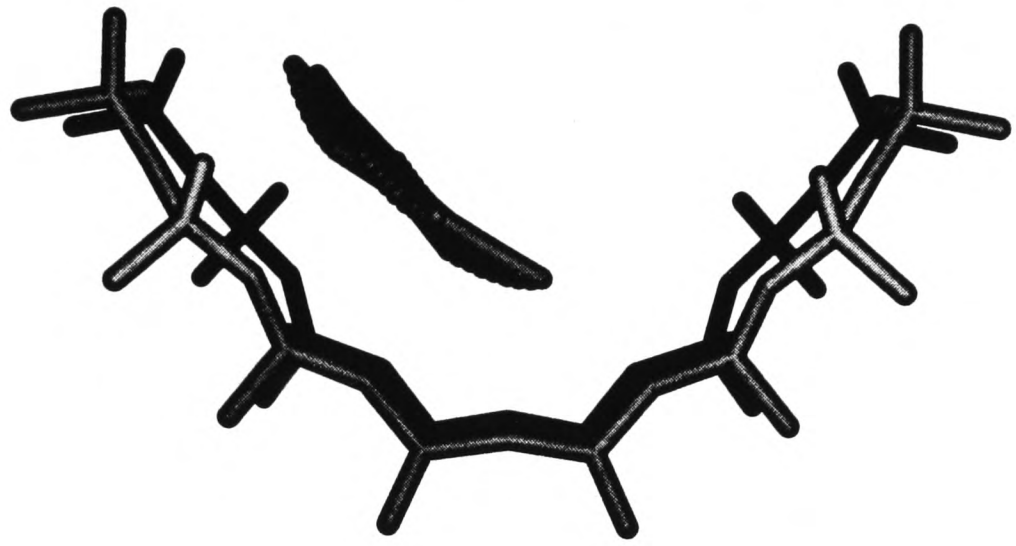


(b) energy profile

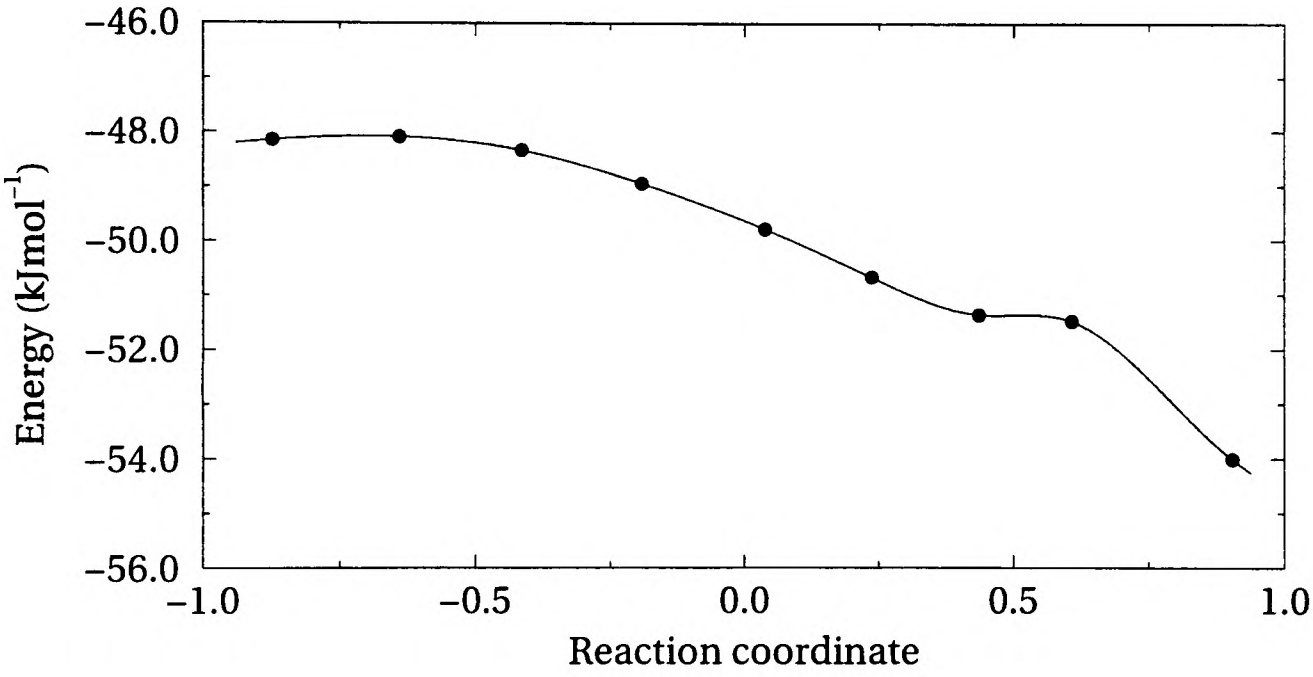
tion with the transition state lying above the central four-ring as for the four-ring to four-ring hop. The hop from a window-site to the opposite six-ring site via the supercage centre was also considered. However, once the constraint carries the benzene beyond the region of the window site it slides onto the wall of the supercage rather than exploring the centre of the cavity.

The barrier heights for each of the calculated trajectories are summarised in Table 8.6. In the case of intra-cage motion, this is controlled by the six-ring to four-ring hop and the activation energy for this process is similar to the low-temperature activation energy of the molecular dynamics simulation. Although the window to window hop has the high-

Figure 8.10: The six-ring to four-ring hopping process



(a) calculated trajectory

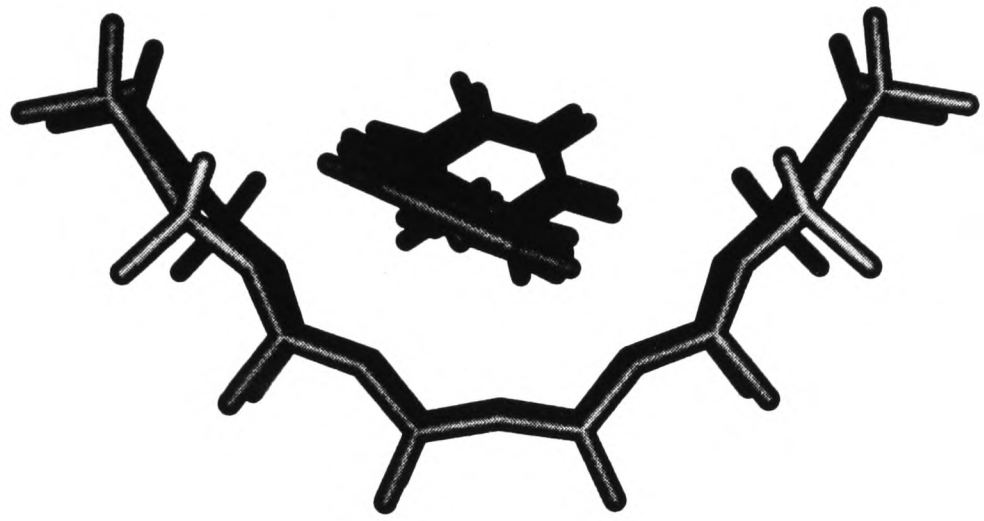


(b) energy profile

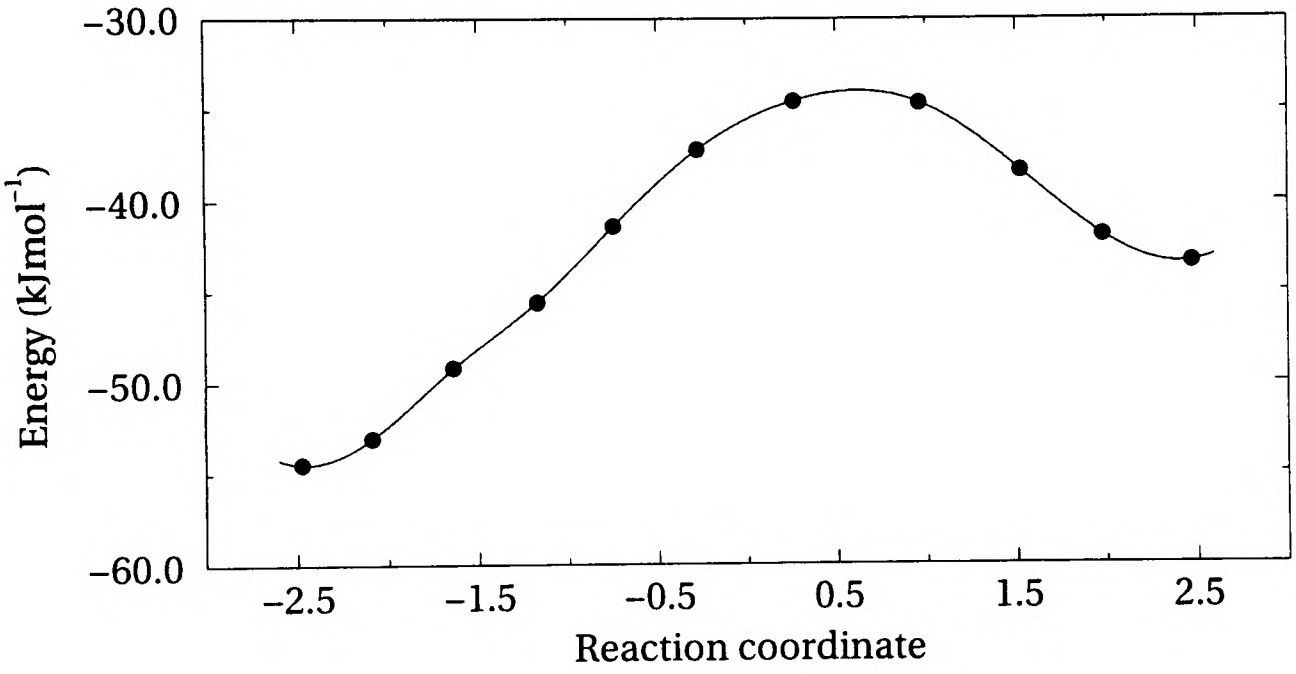
est activation energy of any intra-cage process, it is not essential for full motion around the wall of the supercage. The four-ring to window activation energy clearly controls the inter-cage transport process. There is once again good agreement between the activation energy for this process and the high-temperature molecular dynamics activation energy. The T_1 relaxation NMR activation energy lies approximately between the two different activation regimes, therefore suggesting contributions from both regimes. From the window, the benzene molecule can move to a four-ring in either an adjacent supercage or the original supercage with an activation energy of 9.2 kJmol^{-1}.

Recently calculations of the reorientational correlation function of benzene molecules

Figure 8.11: The four-ring to window hopping process



(a) calculated trajectory

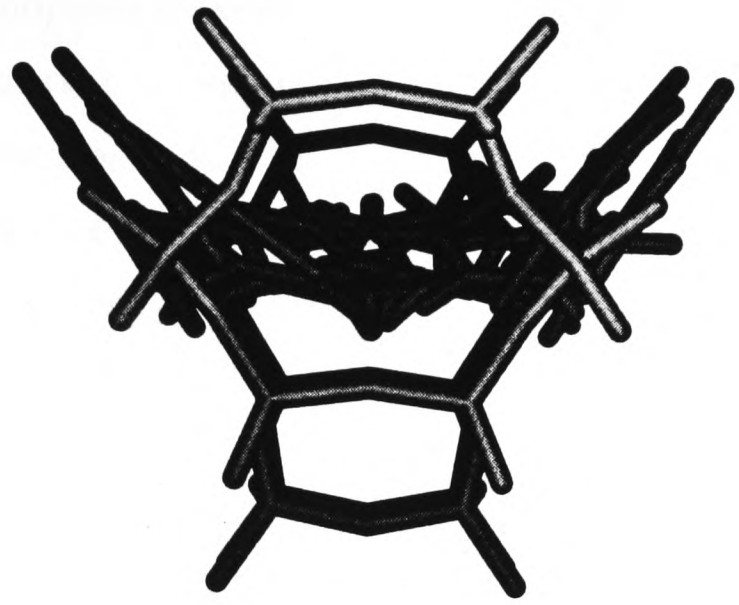


(b) energy profile

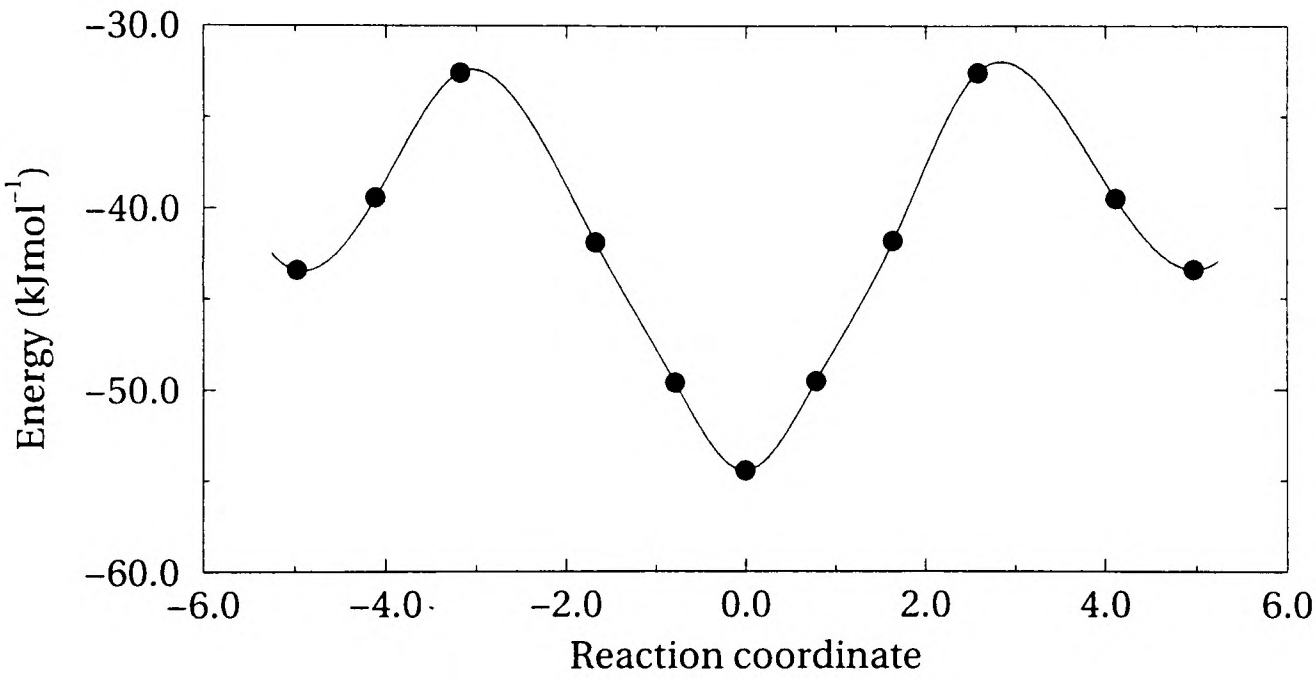
moving in a single supercage of siliceous faujasite have suggested activation energies for the process in ranging from 5 to 7 kJmol^{-1}[372] which correlate well with the hopping activation energies that are calculated here, adding further support to the idea that the NMR experiment is not measuring a diffusional process.

As outlined in the earlier part of this section, a plot of the three-dimensional reaction coordinate against the full-dimensional reaction coordinate can indicate motion involving significant rotation rather than translation. For all the hopping pathways considered above, the plots are straight lines with the notable exception of the six-ring to four-ring hop which has a slight discontinuity corresponding to the rotational conversion between

Figure 8.12: The window to window hopping process



(a) calculated trajectory



(b) energy profile

four-ring sites described above.

8.6 Conclusions

The calculations in this Chapter have shown that it is possible to make qualitative and semi-quantitative interpretations of experimental data for this system based on a simple model. Clearly the approach to obtaining a realistic potential could be improved since,

Table 8.6: Barrier heights for hopping processes for benzene in siliceous faujasite

hopping process	barrier height ($kJmol^{-1}$)
four-ring → four-ring	4.5
four-ring → six-ring	0.2
six-ring → four-ring	6.3
four-ring → window	20.5
window → four-ring	9.4
window → window	22.2
E_a (T_1 NMR)	10.2
E_a (PFG NMR)	38.6
E_a (MD - flexible lattice)	17.4, 3.4

despite fitting to both the heat of sorption and crystallographic structure, the experimental activation energies and pre-exponential factors can only be reproduced to within an order of magnitude. One possible explanation for this deficiency, aside from the choice of functional form for the potential, is that the fit was made to equilibrium properties of the system whereas a full dynamical description necessarily also requires an accurate representation of the region of the potential energy surface near to the transition state. An improved approach to the fitting procedure could include data from quantum mechanical calculations at both the stable binding sites and the transition state. In addition, the data from the shape of sorption isotherm could also be subsumed into the fit to further refine the potential.

The complementarity between the different approaches presented in this chapter is reassuring and gives confidence in applying the methods to calculate hypothetical trajectories to systems where a molecular dynamics calculation is infeasible due to the sluggishness of the transport process. This will be demonstrated in the next chapter.

Chapter Nine

Simulation of Benzene in Cation-Containing Faujasites

The majority of zeolite applications involve cation-containing zeolite systems rather than their siliceous analogues; the cations can be protons, as in acid catalysis, or metal cations, for example in gas separation and ion-exchange applications. The calculations in the previous three chapters have been limited to studies of the stability of siliceous systems and their interaction with sorbed species. In this chapter, the problems involved in the simulation of cation-containing zeolites will be addressed utilising Na-faujasite as a model system.

In the first part of this chapter, the problem of constructing realistic models for Na-faujasites for computational studies that are consistent with crystallographic data will be covered. Once appropriate models have been constructed, an investigation of the accuracy to which the chosen zeolite forcefield can reproduce crystallographically determined cation positions will be performed and the results analysed to assess to what extent the calculated relative cation site stabilities can be related to crystallographic occupancies. Finally, docking calculations and minimum energy pathways will be calculated for the behaviour of benzene in a number of Na-faujasite models representing different Si/Al ratios and cation occupancy patterns. The results will then be used to interpret and rationalise transport properties in analogous systems as measured by experiment.

9.1 Experimental Motivation: NMR Spin Lattice Relaxation

Bull and co-workers[89] and Vitale and co-workers[373] have performed ^{2}H NMR spin-lattice relaxation measurements on a series of faujasite samples with benzene as a sorbate. This experiment effectively measures the relaxation of the orientational correlation function of the C–D bond. A relaxation time for this process can be obtained by fitting the NMR line

Table 9.1: Activation energies (E_a), pre-exponential factors (D_o), and diffusivities at 298K (D_{298}) for transport of benzene in faujasite from ^2H NMR spin-lattice relaxation measurements

zeolite	D_o (m^2s^{-1})	E_a ($kJmol^{-1}$)	D_{298} (m^2s^{-1})
siliceous (Si/Al=∞)	$2.2\pm1.2x10^{-8}$	10.2 ± 0.8	$4.5\pm3.3x10^{-10}$
Na-Y (Si/Al=1.7)	$4.4\pm0.2x10^{-9}$	23.5 ± 0.9	$3.5\pm1.3x10^{-13}$
Na-X (Si/Al=1.2)	$5.1\pm1.3x10^{-9}$	14.0 ± 0.6	$2.0\pm0.9x10^{-11}$
Na-LSX (Si/Al=1.0)	$1.3\pm0.6x10^{-9}$	10.6 ± 0.9	$1.9\pm1.5x10^{-11}$

shape to an appropriate functional form. By assuming a characteristic jump length, an activation energy and pre-exponential factor can be obtained. The results of these experiments are shown in Table 9.1. The first observation is that the diffusion of benzene is reduced by over two orders of magnitude with the introduction of cations in the structure (Na-Y compared to siliceous faujasite). This rate reduction is mainly due to the binding site formed by the strong interaction of benzene with the *SII* Na^+ cation in the faujasite structure. The cations act as traps for any benzene molecule moving through the structure. This phenomenon also accounts for the increased activation energy for diffusion in the case of Na-Y. It might be expected that, as the concentration of cations in the structure increases, the diffusivity will be further reduced. However, this is clearly not the case since the diffusivity of benzene in Na-X is found to be enhanced compared to Na-Y and the activation energy reduced. It is interesting to note that in the case of the LSX sample, the activation approaches that in siliceous faujasite whereas the diffusion remains considerably slower.

Since the NMR spin-lattice relaxation experiment probes the reorientation of the benzene molecule, it would be expected that the activation energies that are measured by this technique are indicative of the most efficient benzene hopping process in the zeolite. In an attempt to explain this curious trend in diffusivity, computational methods will now be applied to this problem with the goal of calculating hypothetical hopping processes in representative models of the faujasite structure.

9.2 Methods and Models

As was detailed in Chapter 2, although there are many different experiments methods for the measurement of diffusivity, they often probe different diffusional time scales and can often measure different transport mechanisms. The NMR spin-lattice relaxation technique is one method that measures diffusional processes most analogous to those that can currently be simulated by standard computational techniques such as molecular dynamics. This compatibility of computational and experimental approaches is because the NMR measurement probes intracrystalline transport over a relatively small length scale comparable with the dimensions of the simulation cell.

9.2.1 Computational Methodology

The relatively few previous computational studies of the behaviour of organic molecules in cation-containing zeolites have focused on the faujasite system mainly because the cation sites are well determined by crystallographic methods and the zeolite is important in fluid catalytic cracking. The earliest study by Demontis and co-workers[242] was an attempt to perform molecular dynamics on benzene moving through Na zeolite-Y. The calculated diffusivity from this work was found to be four orders of magnitude faster than that measured by experiment. This discrepancy illustrates a common problem with the study of diffusion in a system where the transport is very slow; the simulation time of only 24ps was insufficient to sample enough of the transport process to accumulate statistically significant ensemble averages for the system.

Uytterhoeven and co-workers[374] studied the interaction of benzene with faujasite of varying Si/Al ratio and varying alkali-metal cation employing the electronegativity equalisation method to calculate the interactions. The benzene was moved along the three-fold axis of the structure to assess the relative stabilities of the binding sites at the *SII* cation and the window. These calculations represent a series of single-point energy calculations; no attempt was made to allow relaxation of the sorbate or the lattice. Interestingly, this work predicts that the window site becomes the most stable of the two sites in K-X, Rb-X and Cs-X, but not in Na-X. Unfortunately, the absolute values of the energies obtained by this method have little meaning and cannot therefore be compared with experiment.

Klein and co-workers[57] have combined X-ray diffraction measurements with computational methods to study the location and transport of a number of different aromatic molecules (benzene, toluene, xylenes, mesitylene, aniline, m-nitroaniline and m-dinitroaniline) in Na zeolite-Y. This study took potential parameters previously derived by Kiselev and co-workers,[333] and Demontis and co-workers[242] as a basis for their calculations, and calculated diffusion pathways with constrained energy minimisation. The calculated activation energies are in good agreement with experimental data. It is found that polar and non-polar aromatic molecules have subtly different binding site geometries and transport properties. This study represents one of the most detailed investigations of this system to date.

Schrimpf and co-workers[375] have recently challenged the conventional wisdom with regard to molecular dynamics studies on systems with slow diffusional processes by performing a calculation on the transport of *p*-xylene in Na-zeolite Y. In order to accelerate the calculations and allow a larger proportion of phase space to be accessed for the duration of the run, several approximations were made. Firstly, the zeolite lattice was held fixed. This is somewhat surprising since the same authors make a convincing case for allowing the lattice to flex for this type of system in an earlier publication.[376] Secondly, since the most time-consuming part of previous calculations is the computation of the electrostatic component of the energy via the Ewald summation, in this work the Coulombic contribution is calculated with a potential truncation function that significantly reduces the computational cost.[377] Finally, the molecular dynamics simulation were performed at elevated temperatures (between 500K and 1000K) in order to further accelerate the motion. These approximations allowed runs of an unprecedented length (100ns) to be performed, and trajectories clearly showed hopping processes between cation binding sites. Although only a few hopping events could be sampled even with this approach, it is nonetheless impressive that straight-lined Arrhenius plots were obtained for all loading models investigated. Further, the calculated activation energies show good agreement with NMR and uptake measurements.

In the work presented here, the first step is to verify that the chosen zeolite forcefield can adequately represent the cation sites of interest. This issue will be addressed by carrying out both periodic and defect lattice energy minimisation on a variety of models and

by observing how the cation positions differ compared to experiment. Once representative models for the two zeolites have been obtained, they will then be used as a basis for a Monte Carlo docking calculation as detailed in Chapter 8. The binding sites obtained will be utilised to compute minimum energy pathways for hypothetical hopping processes, and comparisons made with the NMR results.

9.2.2 Cation Sites in Faujasites

There has been a large number of crystallographic studies made on zeolites with the faujasite structure, both on aluminosilicates with various counter ions and silicoaluminophosphate derivatives. Regarding aluminosilicate derivatives of the faujasite structure, the nomenclature varies depending on the Si/Al ratio of the sample in question. It is generally accepted that samples with Si/Al<1.5 are referred to as X, whereas those above this value are known as Y. The special case of Si/Al=1 in which Si-Al alternation is observed is known as the LSX configuration.

There have been numerous crystallographic studies of sodium faujasite structures; however, for the purposes of these calculations it is important to consider only dehydrated structure determinations, since cation locations and occupancies are often heavily influenced by the presence of water.[378] In the case of Na-Y, the structure of Fitch and co-workers is considered as the basis for the constructed models. Until recently, the only available structural study on a dehydrated Na-X was that of Hseu.[379] However, recently two further works have appeared in the literature by Olson[380] and Vitale and co-workers.[381]

For Na-Y structural models, the important cation sites are listed below, shown schematically in Figure 9.1, and described in more detail in Table 9.2. In order to increase the Si/Al ratio beyond values typical in Na-Y, further sites (called *SIII* sites) must be occupied. In all three of the available structural studies on Na-X, the *SIII* sites are located in the region of the twelve-ring windows, although several different site geometries are observed. In the Hseu structure,[379] the *SIII* cations (dubbed *SIIIi*) are located above the four-rings. For each series of three rings joining adjacent six-rings in the supercage, there are two symmetry equivalent positions separated by 1.39 Å, which precludes simultaneous occupation. Each cation is four-coordinate and is sited at a distance of 2.83Å from two oxygen atoms in the

Figure 9.1: Cation sites in faujasites : showing *SI*, *SI'* and *SII* sites

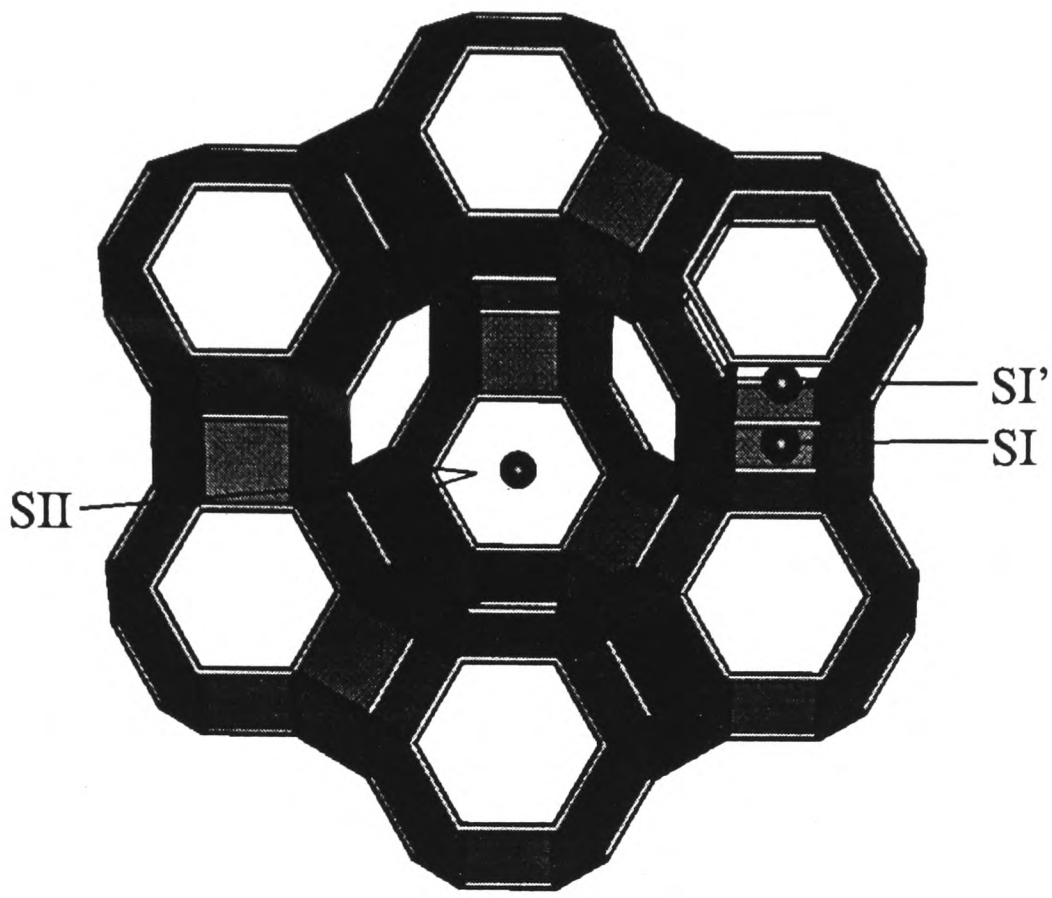
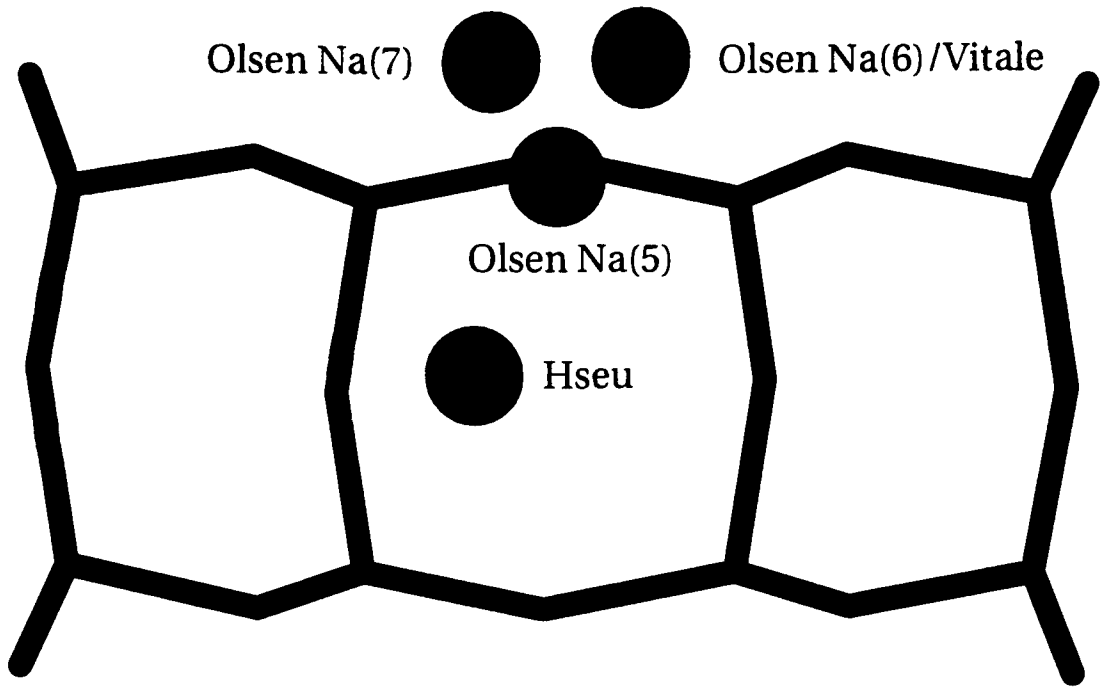


Table 9.2: Summary of Cation Sites in the Na-Y faujasite structure

site	site symmetry	description
SI	(16c)	centre of double six-ring
SI'	(32e)	above internal six-ring in sodalite cage
SII'	(32e)	above external six-ring in sodalite cage
SII	(32e)	above external six-ring in supercage

central four-ring, and also from two oxygens in the adjacent four-ring (Figure 9.2). Vitale and co-workers[381] determined the *SIII* cation site to be located further into the twelve-ring windows. There are six symmetry equivalent positions in each window are separated by 2.76Å. Each cation position has two close contacts with the oxygen atoms in the twelve-ring window at 2.58Å and 2.77Å. The Vitale work is notable in that it is the only structural study that refines Si and Al sites separately. Olson[380] found three *SIII* cation positions, which will be referred to as Na(5), Na(6) and Na(7) following Olson's notation. The Na(6) and Na(7) sites are approximately related via a centre of inversion at the centre of the cen-

Figure 9.2: *SIII* cation sites determined by crystallographic studies in relation to four-rings



tral four-ring. The Na(6) site has approximately the same geometry as the Vitale site. The Na(5) is approximately three-coordinate, making a close contact to a single four-ring oxygen atom at 2.23Å, and two more at adjacent oxygen atoms at 2.81Å. Each of the three sites is found to have similar occupancy (approximately one ninth).

There are several important questions to consider when attempting to construct realistic models for cation-containing zeolite from crystallographic data. Firstly, it is important to remember that the atomic positions from a structural refinement represent an average picture of the zeolite lattice without the effects of thermal vibration. In addition, the cation sites that are found tend to be partially occupied and therefore only give an idea of the actual cation site locations averaged over the entire structure, without giving any information on the local occupancy model within a single unit cell of the structure. In addition, it is rarely possible to determine the substitution positions for Al in the structure since disorder is very common.

9.3 Relative Cation Site Stability

9.3.1 Methods and Models

In a system in which thermodynamic equilibrium exists between each of the cation sites, the crystallographic occupancy would be entirely determined by the relative site stabilities and the temperature. However, since the formation of most zeolites is driven predominantly by kinetic, rather than thermodynamic, control, the site occupancies are influenced heavily by the mechanism of zeolite synthesis, and by templating effects.

Although ion-exchange is a popular method for producing zeolites with different extra-framework cations, the process is promoted by coordination of the cations with the relevant solvent and is performed under thermodynamic control. In the absence of a solvent, ion-exchange between different sites is very slow. In addition, it has been shown that the relative cation occupancies can also be influenced by the sorption of certain molecules. For example, this effect has been shown to occur in the H-Y/benzene system.[382] This can be thought of as a very weak solvation effect and is unlikely to be important with more inert sorbates such as normal hydrocarbons.

A theoretical study of the relative site energy is interesting in giving an indication of the importance of thermodynamic effects in a given zeolite structure, and an indication of the applicability of the current forcefield to the cation positions.

Previous Work

Earlier work on cation stability in faujasite has been reported by Sanders and Catlow[383] and Sanders[384] who looked at K^+-faujasite. This study performed simple Madelung energy calculations on a comprehensive set of cation configurations and paid particular attention to the effect of Al distribution on stability. The results have been summarised by Jackson and Catlow.[211] It was predicted that the *SII* cation site was the most energetically favoured. The most favourable configurations were then minimised with respect to the cation coordinate with the following main findings :-

- the most energetically favourable cation distributions have equal occupation of *SI* and *SI'* sites.

- the occupancy of adjacent *SI* and *SI'* sites is predicted for certain Al distributions
- the energies of structures with different Al distributions are very similar
- the energy minimised cation sites are reasonable close (within 0.2Å) of the crystallographically determined sites

No *SIII* cation sites were considered in this study.

Models for Framework and Non-Framework Positions in the Present Work

A basic structural model was constructed with the Olson work as the model for the framework sites since this provides the most representative selection of *SIII* cation positions. The Hseu *SIII* positions was transformed into this cell when needed, and since the Vitale *SIII* position is relatively close to the Olson Na(6) site it will not be considered separately.

Forcefield Models

Two forcefield models were considered, both the formal charge shell model of Sanders (used in Chapter 4 for the silica lattice calculations), and the partial charge model of Kramer (as employed in the forcefield fitted in Chapter 7). The functional forms for these forcefields have been detailed in earlier chapters; the parameters are given in Table 9.3 for completeness.

9.3.2 Results and Discussion

In this section, several different calculations will be performed on the cation positions in Na-faujasites. The calculations are designed to contrast a number of different methods of considering the cation sites rather than considering the large number of possible permutations of cation and Al sitings for a given Si/Al ratio.

Defect Lattice Energy Calculations

The first set of calculations consider the Na^+ cation site to be an isolated defect (an interstitial ion in the terminology of the defect calculation) in a siliceous structure, both with and without an associated Al substitution at an adjacent tetrahedral site with the Mott and

Table 9.3: Forcefield parameters for site stability calculations

formal charge				
interaction	A (eV)	ρ (Å)	C (eVÅ^6)	k (eVA^{-2})
Si–O	1283.9	0.3205	10.66	-
Al–O	1460.3	0.2991	0.0	-
Na–O	1226.84	0.3065	0.0	-
O–O	22764.0	0.1490	27.88	74.92
partial charge				
interaction	A (eV)	ρ (Å)	C (eVÅ^6)	
Si–O	18003.7572	0.205205	133.5381	
Al–O	16008.5345	0.208478	130.5659	
Na–O	3542.2072	0.241896	0.0	
O–O	1338.7730	0.362319	175.0	

Littleton formalism[187] as employed in Chapter 5 for the SAPO calculations. Full lattice relaxation is allowed for each of the configurations considered. In addition, the presence of *SIII* cation sites is also considered.

As in the case of the calculations on proton siting in SAPO-37 (Chapter 5), it is important to choose limits for the regions that are sufficient to give a realistic treatment of long-range effects. Several sets of region limits were considered ranging from 6.0/20.5Å to 13.0/24.0Å. It was found that the trends in the cation site stabilities had converged at the 11.0/22.0Å level. The comparison between the lowest limits and this level are shown in Table 9.4. In addition, it is to be noted that the same trends are observed regardless of the forcefield model employed. Therefore, since the Kramer model has been used as a basis for the forcefield considered in Chapters 7 and 8 it is employed exclusively in the remaining calculations on cation site stability. The region limits have a considerable effect in the case of the *SIII* cation site. This is due to the relatively low coordination of the cations in the twelve-ring window causing a smaller number of atoms to be defined within the inner 6Å region. The two different *SI'* cation sites are found to minimise to the same position. Of all the cation sites, the *SIII* positions are found to be the most energetically favourable, which

Table 9.4: Minimised energies (eV) for isolated cation defect calculations

	SI	*SI'(a)*	*SI'(b)*	*SII*	*SIII*			
					Na(5)	Na(6)	Na(7)	Hseu
6/20.5Å formal	-41.6	-49.9	-49.9	-39.6	-26.9	-29.8	-30.9	-30.6
11/22Å formal	-184.8	-173.4	-171.2	-169.6	-184.5	-191.2	-188.5	-191.9
11/22Å partial	-64.5	-60.6	-60.1	-59.4	-64.4	-67.5	-65.5	-66.5

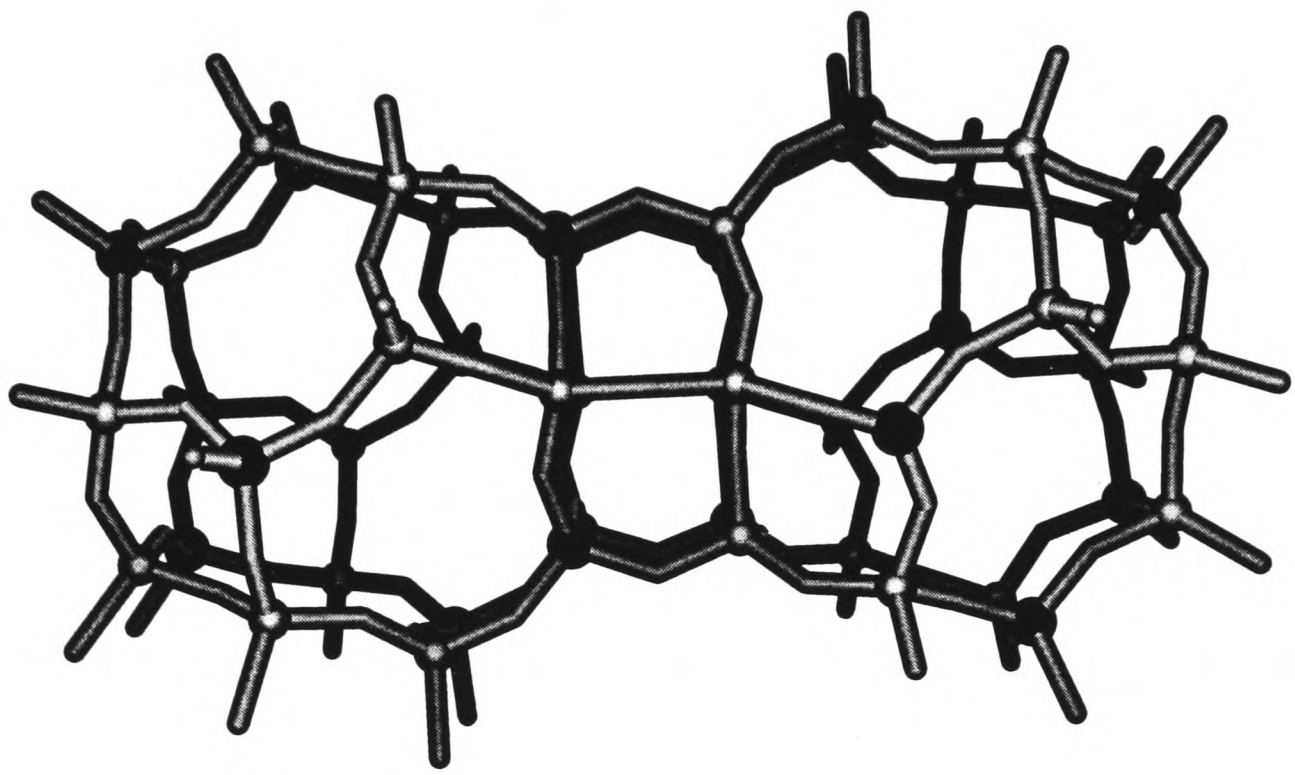
Table 9.5: Minimised energies (eV) for isolated cation defect calculations with concomitant Al substitution

	SI	*SI'(a)*	*SI'(b)*	*SII*	*SIII*			
					Na(5)	Na(6)	Na(7)	Hseu
11/22Å formal	-149.0	-137.9	-135.7	-135.0	-156.9	-156.9	-153.6	-156.7
11/22Å partial	-41.9	-37.5	-37.0	-36.9	-42.0	-45.3	-43.3	-43.1

may be a little surprising since they are the last cation position to be significantly occupied as a function of Si/Al ratio. In an attempt to investigate this further, the calculation was modified to assess the effect of Al on the site stability. Initially, a single Al substitutional defect was made on the nearest tetrahedral site to the cation site in question. The results of these calculations are shown in Table 9.5. As can be seen, the introduction of an Al atom makes no difference to the trends in energy. However, since it is known that certain cation sites only become occupied (and presumably energetically favourable) at lower Si/Al ratios, it is probable that a distribution of Al atoms is required to fully stabilise a given site. To address this question it is necessary to construct models for Al-substitution pattern in the faujasite unit cell. As has been mentioned previously, the only unambiguous determination of the siting of Al is in the case of the Vitale refinement of Na-X where Si-Al alternation is observed.[381] Although crystallographic data rarely provides evidence for Si/Al ordering with Si/Al > 1.0, NMR measurements have been analysed to suggest possible Al substitution patterns. Klinowski and co-workers[385] and Melchior and co-workers[386] have constructed models corresponding to a range of Si/Al ration that can reproduce ^{29}Si NMR spectra and are consistent with simple electrostatic arguments. For example, Klinowski

and co-workers suggested that the most favourable Si/Al distribution pattern for a faujasite with Si/Al=2.0 is that shown in Figure 9.3. This structural unit represents the primitive

Figure 9.3: A consistent Al-substitution pattern for faujasite with Si/Al=2.0 (Si is shown in grey, Al in black).



unit cell of the faujasite structure. It can be noted that each of the six-ring units have two Al substitutions (at Si/Al greater than these cases only one Al substitution can occur). Further, once the entire unit cell is constructed from this fundamental unit, all the six-rings that are located in the wall of the supercages have the two Al substitutions lying opposite each other i.e. the "meta" configuration by analogy with methyl substitutions in xylenes.

The defect calculation was repeated with this model for the faujasite lattice, and also in the case of fully ordered Na-X (Si/Al=1.0) where the Vitale unit cell was utilised as a basis for the framework model. In each case, charge neutrality was maintained by reducing the partial charge on the oxygen atoms in the framework with the approach of Sanders and Catlow.[383] The results are given in Table 9.6. Since this is the most sophisticated model considered in this section, the shift of the cation position on minimisation was also analysed. Since the crystallographic model is an average representation of the structure, a certain degree of discrepancy is expected. For example, the Olson structure has no explicit Al ordering, and therefore at the very least bond lengths in the region of the cation site will

Table 9.6: Minimised energies (eV) for isolated cation defect calculations with ordered Al substitution

	SI	*SI'(a)*	*SI'(b)*	*SII*	*SIII*			
					Na(5)	Na(6)	Na(7)	Hseu
Na-Y (Si/Al=2.0)	-1.65	-1.93	-1.93	-2.07	-2.49	-2.36	-2.51	-1.43
Na-X (Si/Al=1.0)	-12.62	-12.18	-12.03	-12.36	-13.38	-13.27	-13.44	-12.09

change significantly on minimisation. The *SI* site remains in the centre of the double six ring; however, the two *SI'* sites move significantly further out of plane into the sodalite cage. The *SII* site also moves further out of plane of the six-ring into the supercage on minimisation. The Na(5) and Na(7) sites move further into the plane of the window whereas the Na(6) site moves back towards the four-rings. In each case, the displacements are within 0.2Å of the crystallographic positions. However, the Hseu site is completely unstable in this model, and the cation moves away from the four-rings towards the centre of the supercage.

In addition to the ordered Na-Y model described above, calculations were also performed on a model with random Al substitution while maintaining Löwenstein's rule. The only difference in is the ability to have six-ring sites with only one Al substitution. In this case, the *SII* cation moves away completely from the region of the six-ring and assumes a position near to the twelve-ring window. Since this situation will become more common in faujasites with Si/Al $>$ 2.0, it would suggest that the *SII* site becomes destabilised in these cases.

Periodic Lattice Energy Calculations

To this point, the calculations have only considered the stability of a single cation site surrounded by a variety of models for the faujasite framework. Now the effect of cations interacting with each other will be addressed. Initially, periodic models of faujasite were constructed with full occupancy of a single cation site. The resulting charge imbalance was removed by reducing the charge on the tetrahedral sites. Full lattice energy minimisation was performed on each of the models. The results are presented in Table 9.7. Full occupancy of cation sites is clearly an unrealistic model in many cases since it is rarely observed

Table 9.7: Minimised energies (eV per tetrahedral site) for periodic models with a single cation site fully occupied

	SI	*SI'(a)*	*SI'(b)*	*SII*	*SIII*			
					Na(5)	Na(6)	Na(7)	Hseu
minimised energy	-35.5	-34.1	-34.1	-34.2	-29.2	-29.3	-29.2	-28.1

in crystallographic refinements. In many cases, this is due to the close contacts that would be created if two adjacent crystallographically equivalent positions were simultaneously occupied. These close contacts are listed in Table 9.8. This is more of a significant problem

Table 9.8: The closest contacts in Angstroms between adjacent cation position of the same type in the fully occupied models

	SI	*SI'(a)*	*SI'(b)*	*SII*	*SIII*			
					Na(5)	Na(6)	Na(7)	Hseu
distance	8.87	3.95	4.87	7.40	3.44	2.86	2.99	1.40

in the case of the *SIII* cation sites, since the contacts are much closer, and are probably the main reason for the dramatic differences in energy in Table 9.7. The relative stabilities of periodic models containing different cation sites which are occupied simultaneously are considered in the next section.

9.4 The Behaviour of Benzene in Na-Y

The forcefield fitted in Chapter 7 for the interaction of benzene in Na-Y will be used for the remainder of this chapter. The docking method was outlined in Chapter 7, whereas the technique for calculating minimum energy pathways was described in Chapter 8.

9.4.1 Models for Na-Y

In attempt to construct a model for Na-Y with the maximum crystallographic symmetry, a structure was built by filling all the *SI'* and *SII* sites in one unit cell. This produces a model with Si/Al=2.0. A similar structure could have been constructed by filling *SI* rather than

SI', however this gives a model of Si/Al=3.0 which differs from that considered in the NMR study. The framework structure of Fitch and co-workers[54] was considered as a basis for the model.

The model was modified further to produce both an average tetrahedral site and explicit Al-substituted structure. In the former, the tetrahedral atom partial charge was reduced from 2.4 to 2.066 to achieve charge neutrality and the structure minimised at constant pressure. The structure retained $Fd\bar{3}m$ symmetry on minimisation with the Si–O bond lengths adjusting slightly to accommodate the change in partial charge. A 0.99% reduction in cell volume was observed during the minimisation procedure. The Al-substituted was obtained by taking the Fitch structure and modifying it to allow the Al-substitution pattern of Klinowski outlined above. This reduces the symmetry to $C2/c$ symmetry based on a monoclinic cell. Minimisation of this structure at constant pressure results in a 3.52% reduction in cell volume. This cell represents the primitive cell of the centred tetragonal cell of symmetry $I4_1/a$; the tetragonal cell will be used for the docking calculations.

9.4.2 Docking Calculations

Average T-site Model

Utilising the minimised average-T site model as the starting point for the docking calculation, two binding sites were obtained, one at the *SII* cation site and the second in the twelve-ring window. The effect of lattice relaxation was assessed by performing a full lattice energy minimisation at constant volume for each of the minimised geometries. The results are summarised in Table 9.9. These results are consistent with the crystallographic

Table 9.9: Energetics of docked binding sites for benzene in Na-Y with average T-model

binding site	fixed lattice ($kJmol^{-1}$)	flexible lattice ($kJmol^{-1}$)
SII site	83.3	84.1
window site	50.0	50.4

data showing one dominant binding site at the *SII* cation position and a less favourable site in the twelve-ring window that only becomes significantly occupied at higher loading. The

results are not surprising since the forcefield were fitted to this structural model.

Explicit Al substitution

The introduction of Al into the Na-Y model has little effect on the nature of the binding sites obtained during the docking calculation. As before, both an *SII* cation binding site and a window binding site are found. The energies differ very slightly from those in the average T-site calculation and are given in Table 9.10. It can be noted that the binding energies are slightly less than for the average T-site model.

Table 9.10: Energetics of docked binding sites for benzene in Na-Y with the explicit-Al substituted model

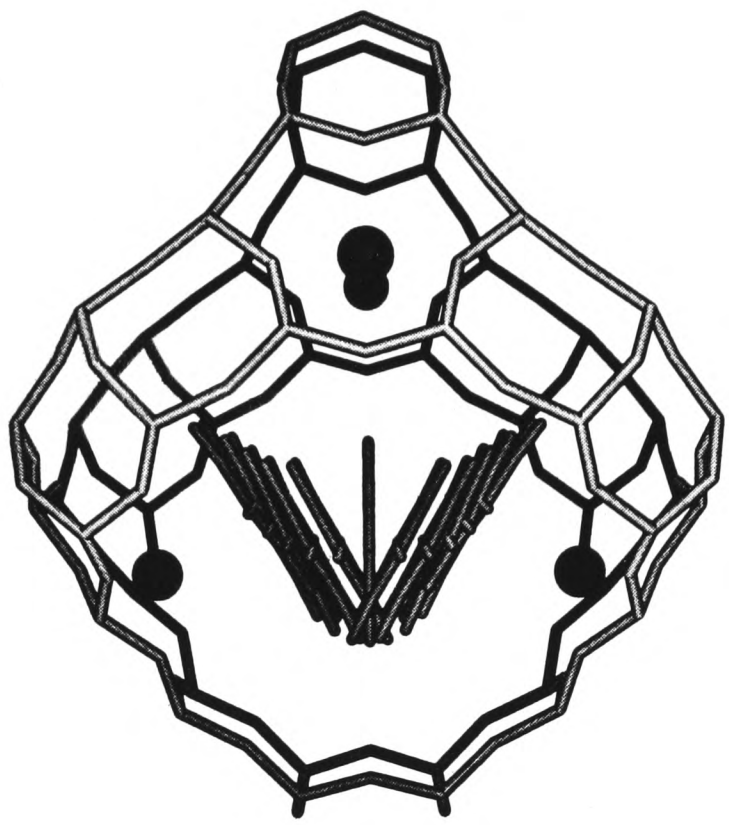
binding site	fixed lattice ($kJmol^{-1}$)	flexible lattice ($kJmol^{-1}$)
SII site	79.0	80.1
window site	47.2	47.6

9.4.3 Minimum Energy Pathways

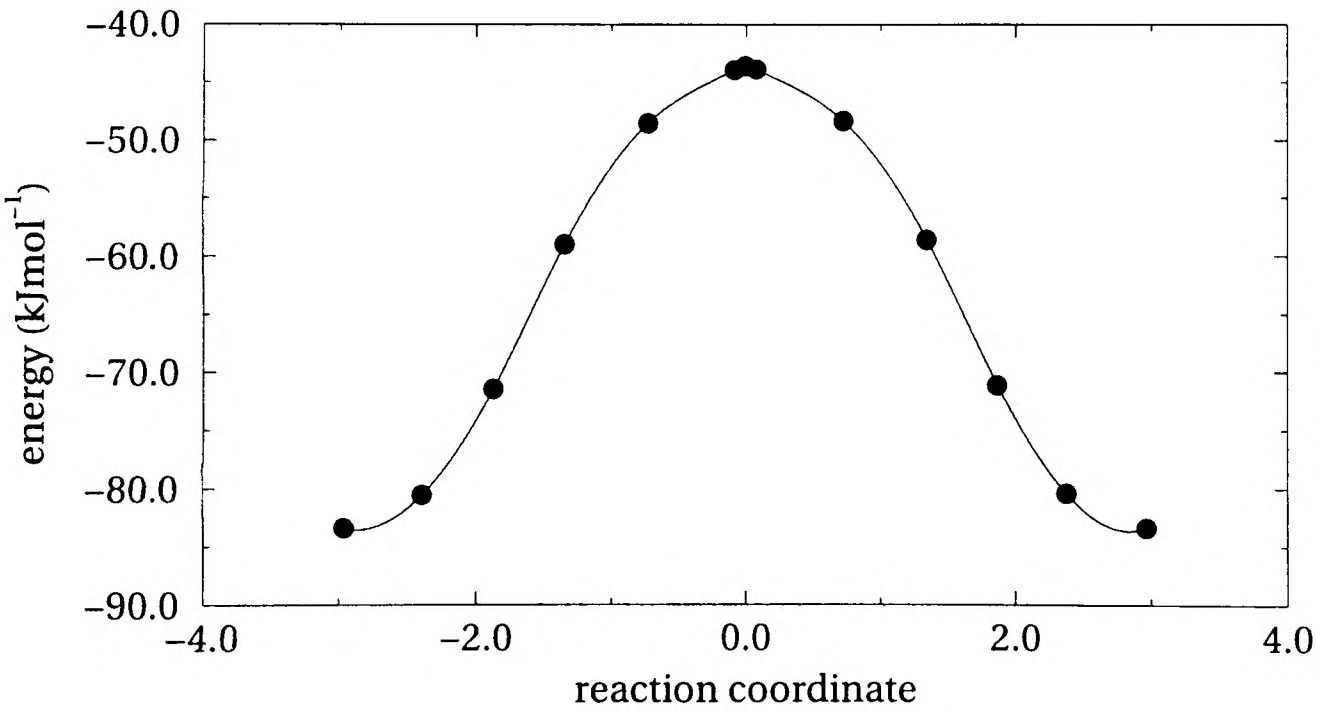
Since there are only two binding sites for benzene in the Na-Y model, this gives three possible hopping pathways: *SII* site→*SII* site, *SII*→window and window→window. The *SII*→*SII* hopping path is shown in Figure 9.4. This hopping pathway consists of a sliding motion down from the six-ring followed by a tilt into the transition state which places the benzene ring perpendicular to the middle four-ring. Previous work suggested the presence of an alternative pathway of similar energy with the transition state having the benzene ring parallel to the middle four-ring;[387] however, there is no evidence of such a pathway with this forcefield. Although it is possible to stabilise such a configuration at the transition state with the constraint applied, the binding energy is considerably higher than the perpendicular configuration (25.6 $kJmol^{-1}$). Any attempt to move the molecule away from this position produces a point on the minimum energy pathway for the parallel configuration. The activation energy for the hopping process in the figure is 39.8 $kJmol^{-1}$.

The *SII*→ window hopping path is shown in Figure 9.5. For this hopping pathway, there is significant hysteresis in the minimum energy surface depending on the choice of starting

Figure 9.4: The *SII*→*SII* hopping pathway in Na-Y (average T-site model)



(a) schematic hopping pathway



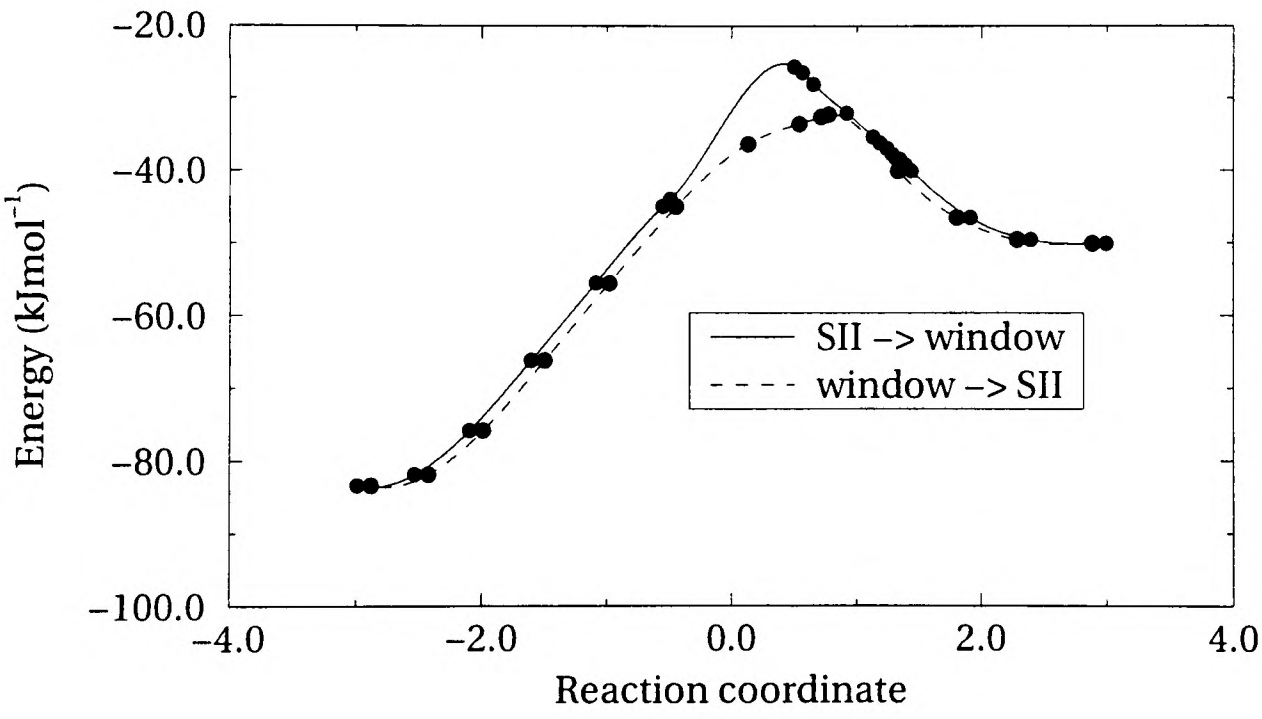
(b) minimum energy pathway

point. From the *SII* site, the pathway consisting of a sliding motion towards the window, followed by an abrupt tilt and the final translation into the window site. The position of the tilt from a "window-like" site to a "*SII*-like" site is the cause of the hysteresis in this case.

Figure 9.5: The *SII*→ window hopping pathway in Na-Y (average T-site model)



(a) schematic hopping pathway



(b) minimum energy pathway

The energy barrier varies from 39.3 kJmol^{-1} (window→ *SII*) to 50.8 kJmol^{-1} (*SII*→ window).

Attempts to model the window→ window hopping process were unsuccessful. Once the benzene molecule approaches the four rings, it was captured by one of the *SII* cation sites suggesting that this hopping process is unlikely.

Minimum energy pathways were also constructed for the explicit-Al model of Na-Y. The

energy barrier for the *SII* →*SII* hop was computed to be 38.5 kJmol^{-1}, whereas the barrier for the *SII* →window hop was 47.9 kJmol^{-1}. Unlike the case of the average-T site model, there was no hysteresis observed in the hopping pathway to the window site. The main cause of the reduction in the energy barriers is the lower stability of the docked sites in this model.

Since in both cases, the most efficient hopping pathway represents motion within a single supercage and therefore makes no contribution to intercage mobility, this suggest that the NMR experiment is simply measuring the mean residence time at the *SII* binding site. It must be noted that the activation energy for the important hopping process in Na-Y is predicted to be significantly higher than that for experiment. This was also observed in the previous chapter for benzene in siliceous faujasite and suggests that the fitted force-field needs to be further refined.

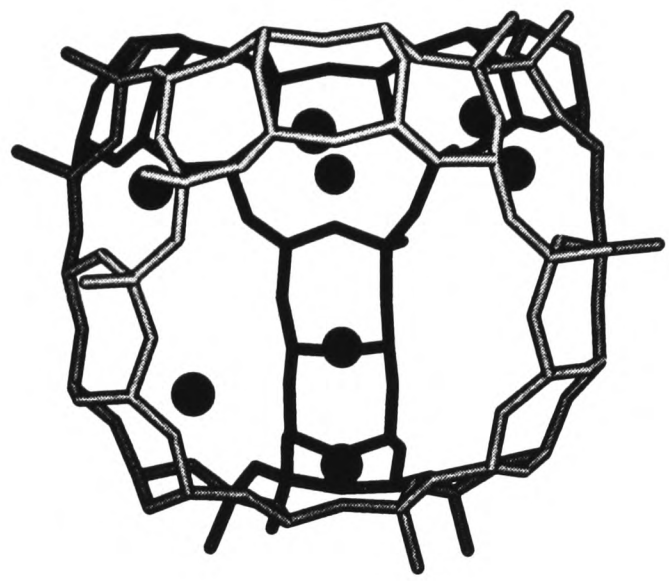
9.5 Behaviour of Benzene in Na-X

9.5.1 Models for Na-X

Models for Na-X were constructed using the Na-Y models as a basis. In order to simplify the question of Al-substitution, the Na-X structural determination of Vitale and co-workers[381] was chosen since this features Si–Al alternation. Models were constructed by filling only one type of *SIII* site in addition to the sites filled in the Na-Y model (all *SI'* and *SII* sites fully occupied) to examine the effect of the energetics of transport of each cation site.

The Hseu *SIII* cation site has site symmetry 96*i*. Using a Si/Al ratio of 1.0, and the Na-Y model as a starting point, 32 *SIII* cation sites need to be filled, which is four in each supercage. This corresponds to a third of the possible sites. One half of the 96 sites can be eliminated by removing one of every pair of *SIII* cations above each middle four-ring (see Figure 9.2). Two further *SIII* cations are then removed in each supercage such that of the six sets of three four-rings that bridge each six ring, only four have a *SIII* cation. This cation occupancy pattern is illustrated in Figure 9.6. From the point of view of each *SII* cation site, there are two pathways to adjacent *SII* sites: one that has an intermediate single *SIII* cation site and one that does not. For the two pathways with an intervening *SIII*, one *SIII* cation is slightly further from the *SII* cation than the other *SIII* cation. This produces a model of

Figure 9.6: The *SII* and *SIII* cation occupancy pattern in a single supercage for the Hseu model



$P\bar{4}$ crystallographic symmetry for an average T-site model, and a $P2$ model for the case of Si-Al alternation. Both models were energy minimised to produce a starting point for the docking calculation. Note that for the average-T site model, the partial charge on the tetrahedral atom reduces to 1.9 to accommodate the increased cation concentration. The $P\bar{4}$ model remains cubic after minimisation showing a 4.6% reduction in cell volume, whereas the $P2$ model shows a slight distortion to orthorhombic with a 1.7% reduction in cell volume (see Table 9.11).

The *SIII* cation site located by Olson are all very similar and models can be constructed for each with a similar method. Again the cations can be divided into pairs based on close contacts (see Table 9.8), and one of each pair deleted. As for the Hseu model, cations can then be deleted such that four remain in each supercage. There are several ways to achieve this. There are six symmetry equivalent cation sites in each window forming a hexagon when viewed perpendicular to the window plane, with each apex alternately on either side of the window plane. Therefore with the xylene substitution pattern nomenclature, there are three possible cation occupancy models for each window ("ortho", "meta" and "para"). The ortho and para models necessarily have their two cations in different supercages. However, for the meta model the choice of cations in windows common to a single supercage need to be correlated so as to ensure that four cations lie within each supercage. It would be expected that the different models will vary in stability mainly due to the interatomic distances between adjacent cations. To assess this effect, the Olson Na(5)

Table 9.11: Results of lattice energy minimisations of Na-X models. Comparison of minimised cell parameters and volumes with experimental determinations.

structure	a (Å)	b (Å)	c (Å)	change in cell volume (%)
Hseu expt. (Si/Al=1.37)	24.990	24.990	24.990	-
Olson expt. (Si/Al=1.18)	25.099	25.099	25.099	-
Vitale expt. (Si/Al=1.2)	25.033	25.033	25.033	-
Hseu model (average-T)	24.706	24.706	24.721	-4.6
Hseu model (Si-Al)	24.941	24.793	25.139	-1.7
Olson Na(5) (average-T)	24.937	25.012	24.909	-1.8
Olson Na(5) (Si-Al)	24.996	24.999	24.987	-1.3
Olson Na(6) (average-T)	24.982	24.995	24.935	-1.5
Olson Na(6) (Si-Al)	25.075	25.077	25.029	-0.5
Olson Na(7) (average-T)	25.016	25.016	24.857	-1.7
Olson Na(7) (Si-Al)	25.056	25.060	24.831	-1.4

site was chosen and model generated for each of the three cases, and the structures lattice energy minimised. The results of the calculations are summarised in Table 9.12. The

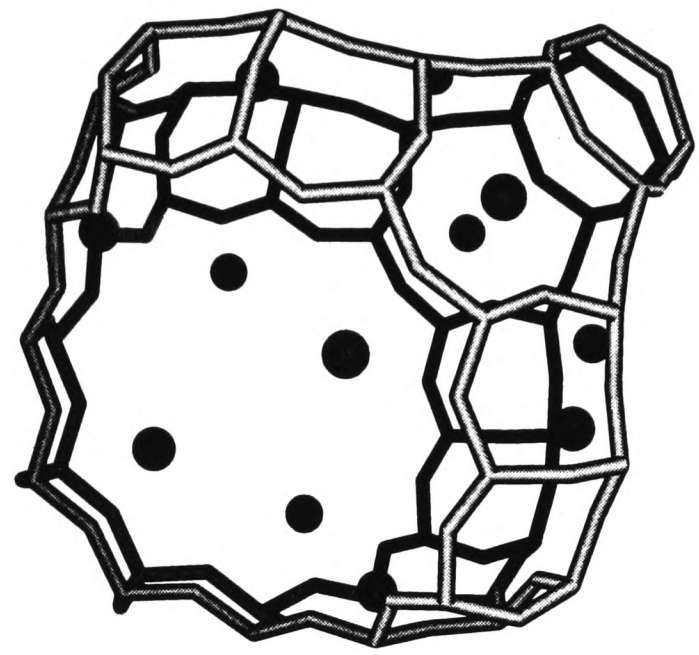
Table 9.12: Results of lattice energy minimisation of each of the three models for Na-X with the Olson Na(5) occupied

	minimised energy	closest Na–Na contact (Å)	
	(eV per tetrahedral atom)	starting model	minimised model
ortho model	-47.82	3.88	6.42
meta model	-47.80	5.98	7.07
para model	-47.82	7.13	7.10

minimised energies of each of the structures are very similar. However, it is important to note that in the case of ortho and meta models repulsions between the *SIII* cations cause a significant increase in the cation-cation separation, suggesting that this occupancy model is less likely to be stable. In general the cations shift to positions lying over the four-rings with a similar geometry to that of the Hseu *SIII* position. Consequently, the remainder of this section will focus on what appears to be the most stable model i.e., the para model.

The para model for the Olson Na(5) cation site is shown as an example in Figure 9.7.

Figure 9.7: The *SII* and *SIII* cation occupancy pattern in a single supercage for the Olson Na(5) model



Para models for each of the Olson *SIII* sites, and the structures were energy minimised both for the average T-site and for the Si-Al alternation case. The results of the energy minimisations are given in Table 9.11. In cases where two of the minimised cell parameters remain close after minimisation, it is possible to define a primitive tetragonal unit cell with half as many atoms as the cubic cell. The minimised models were then used to perform docking calculations. To date, there have been no previous crystallographic studies of benzene sorbed in a Na-X sample with which to compare the results obtained here.

9.5.2 Docking and Minimum Energy Pathways

Hseu Model: benzene docking and minimum energy pathways

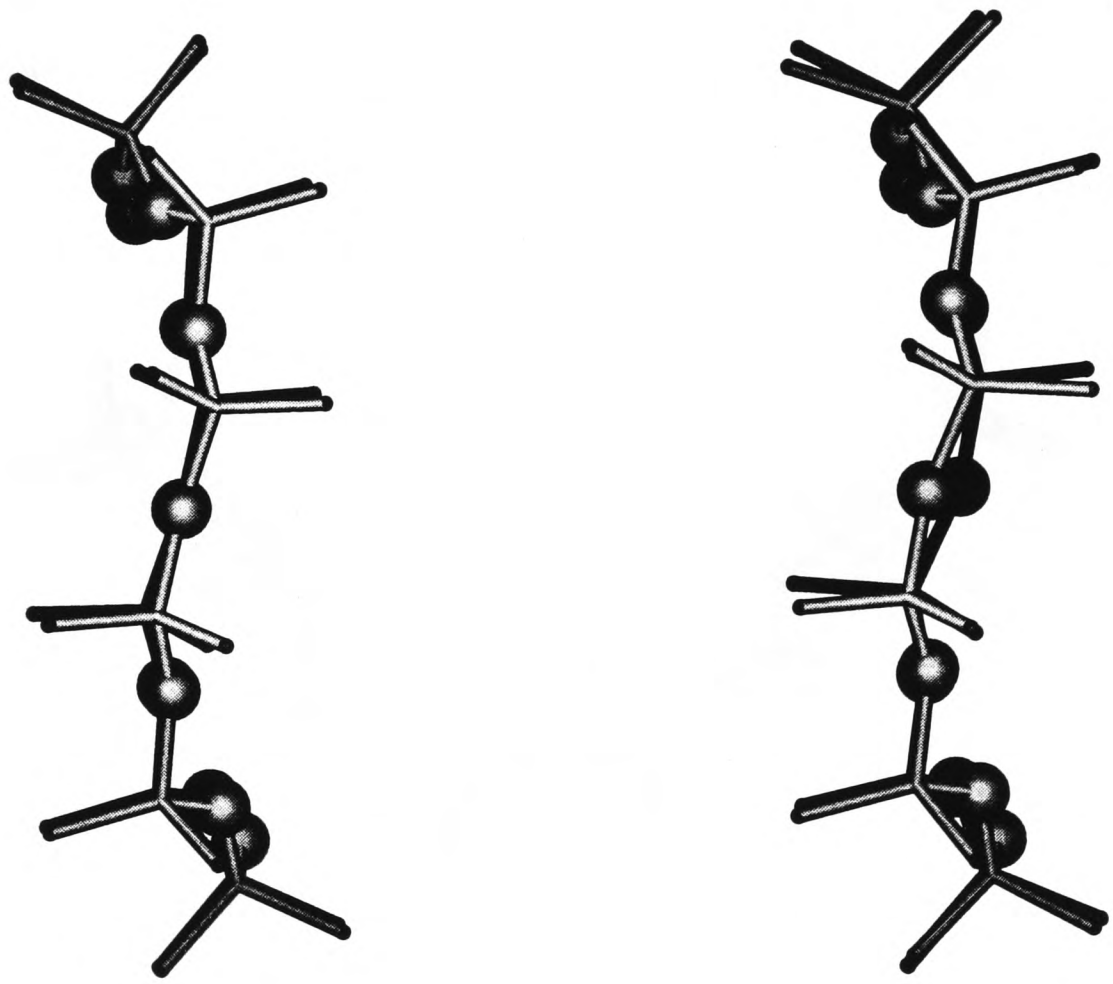
Docking calculations were performed on a Na-X model based on the Hseu structure, both with the average-T approximation and with Si-Al alternation. The presence of the *SIII* cation sites has several effects on the predicted binding sites.

Firstly, the binding site at the *SII* cation site is less favourable and is tilted slightly away from the geometry observed in Na-Y. This is mainly due to repulsive electrostatic interactions between the benzene hydrogens and the *SIII* cations. In addition, the presence of the *SIII* cation introduces a slight asymmetry into the supercage, which is evinced by slightly

different benzene-Na^+ distances and binding energies.

Secondly, the window site becomes more tightly bound due to favourable interactions between the benzene carbon atoms and the *SIII* cations. The shape of the twelve-ring window is somewhat different to that in siliceous faujasite in that the two sets of oxygen atoms in the ring no longer form the same in-plane and out-of-plane pairs (see Chapter 7). This can be seen in Figure 9.8 which is a side-on view of the window for both the average-T and explicit-Al models. In contrast to siliceous faujasite where an alternation of distances be-

Figure 9.8: Side-on views of the twelve ring window showing the ring oxygen atoms



(a) average-T model

(b) explicit-Al model

tween opposite oxygen atoms in the ring is observed, there is now a range of distances in the Na-X models. In both cases, the ring becomes more elliptical in nature. This is most pronounced for the average-T model which has a range of distances from 9.71Å to 12.14Å whereas for the explicit-Al model is the range of distances is reduced to 1.02Å. This has interesting consequences for the predicted binding sites in the window as will be seen later.

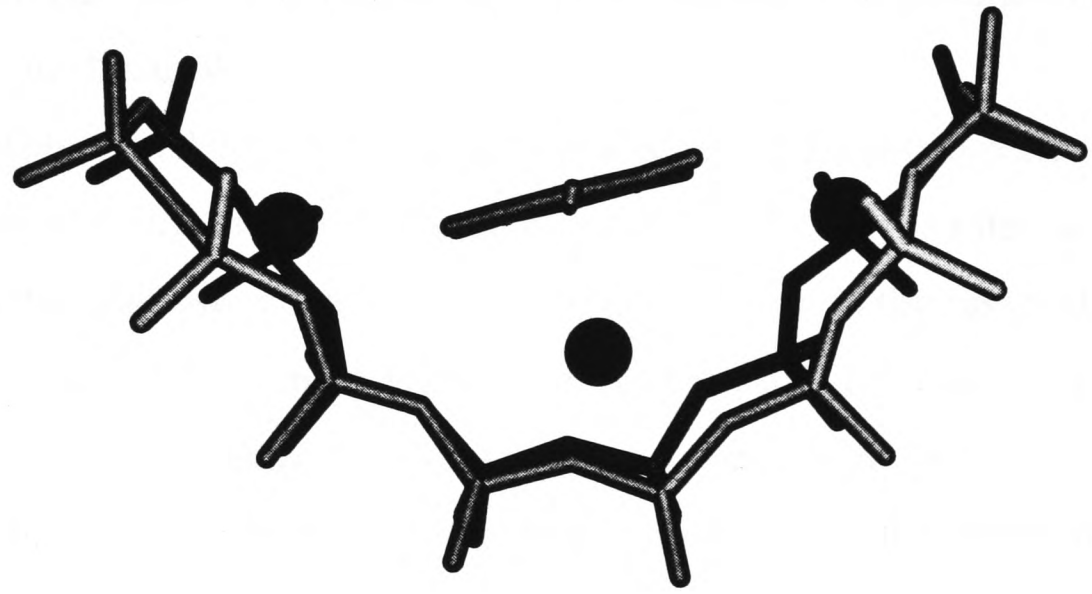
Finally, extra binding sites are observed with the benzene interacting directly with the *SIII* cation. The docking results are summarised in Table 9.13. The *SIII* binding site is the

Table 9.13: Summary of docking results for benzene in Na-X (Hseu model)

	average-T model		explicit-Al model	
	fixed lattice	flexible lattice	fixed lattice	flexible lattice
SII site	68.5	70.4	73.3	77.2
SIII site	74.3	76.2	75.2	75.9
window site	62.7	64.6	70.4	72.4

most stable of the three predicted sites, except in the case of the flexible lattice model with Al substitution, and its geometry is illustrated in Figure 9.9. In contrast to the Na-Y case,

Figure 9.9: The geometry of the benzene binding site at the *SIII* cation position in the Hseu model showing *SII* and *SIII* cations



the inclusion of Al into the Na-X models appears to stabilise all the different binding sites, whereas allowing the zeolite lattice to relax produces a similar stabilisation as before. In the case of the explicit-Al model, the bond lengths around the twelve-ring window alternate, distorting the ring such that the benzene molecule needs to tilt in order to fit into the window site. The two *SIII* cation positions shift about 0.25Å to accommodate the benzene molecule when the zeolite lattice is relaxed.

The question of whether the presence of *SIII* cations in a Na-faujasite increase or decrease the heat of sorption of benzene has been considered experimentally, although the

results are somewhat ambiguous. In order to minimise the effects of particle size and synthetic conditions, the comparison can be usefully limited to those studies considering both Na-X and Na-Y. Notable studies are the works of de Mallmann and Barthomeuf[364] and Dzhigit and co-workers.[326] The thermochemical results are summarized in Table 9.14. The

Table 9.14: Measured heats of sorption for benzene sorbed in Na-X and Na-Y

	Na-Y sample ($kJmol^{-1}$)	Na-X sample ($kJmol^{-1}$)
de Mallmann *et al.*[a]	78.7	73.2
Barthomeuf *et al.*[b]	79.5	83.5

[a]Na-Y (Si/Al=2.43), Na-X (Si/Al=1.23), T = 445K

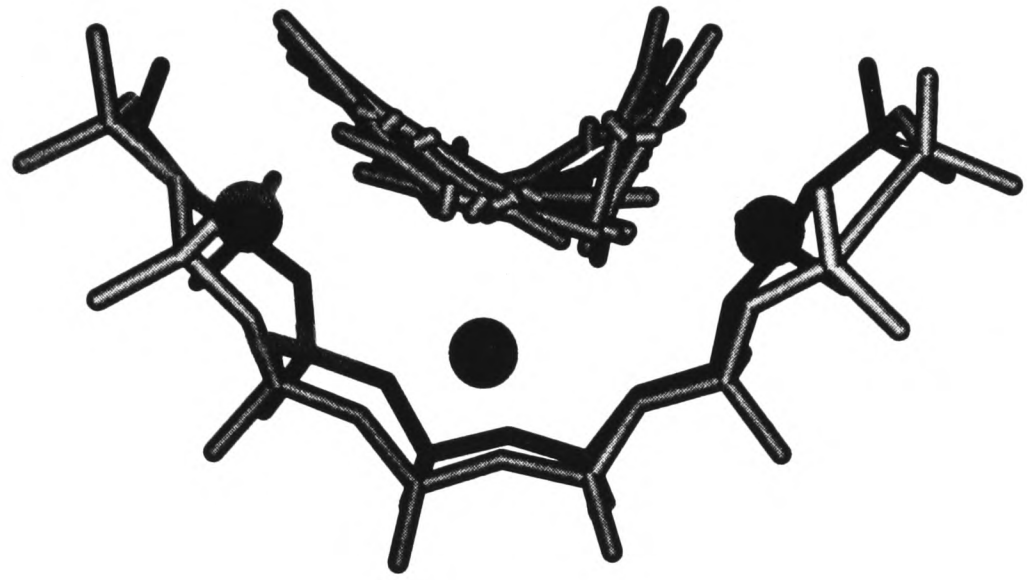
[b]Na-Y (Si/Al=2.27), Na-X (Si/Al=1.18), T = 323K

calculated binding energies from the Hseu model compare well with the experimental values, although additional experiments undoubtedly need to be performed before the correct trend in the heats of sorption is elucidated.

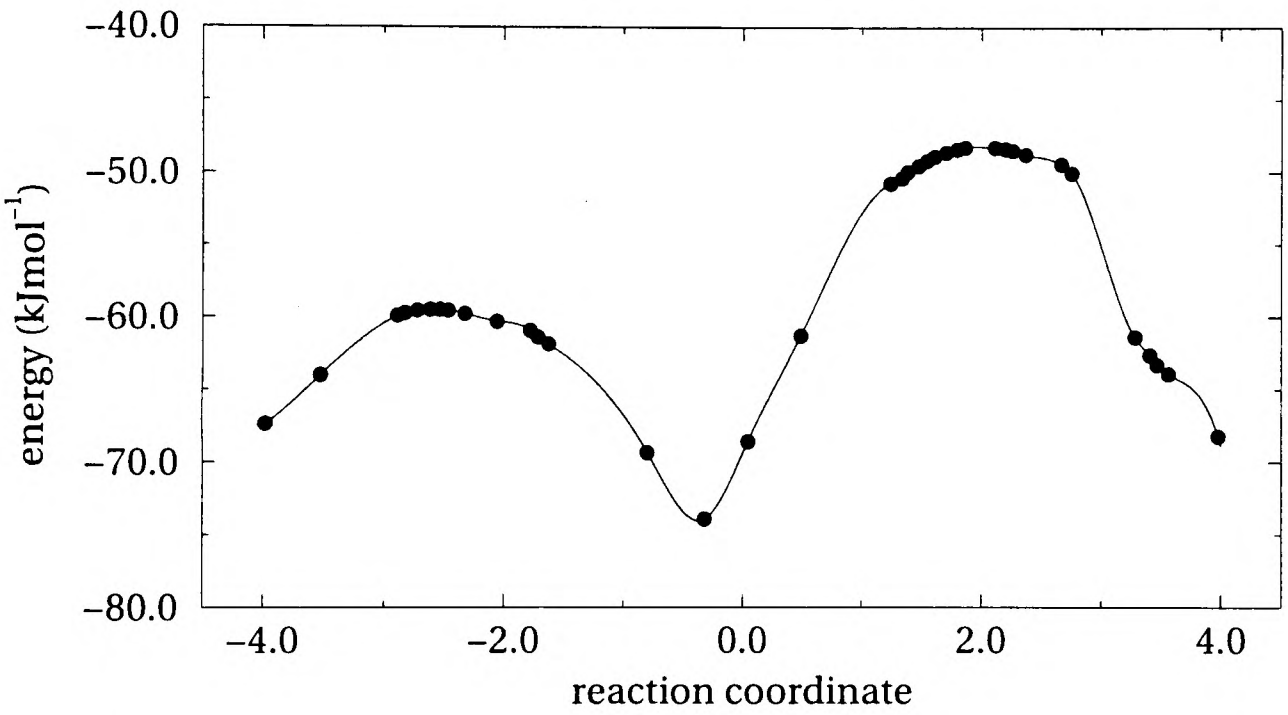
For the Hseu model, four hopping pathways were considered: two *SII* $\rightarrow$*SII* pathways, *SII* $\rightarrow$window and *SIII* $\rightarrow$window. The distinction between the two inter-*SII* hops depends on whether the intervening *SIII* cation is present or absent. In the case with no *SIII* cation although the pathway is similar to that observed in Na-Y; however the barrier is lower (25.9 $kJmol^{-1}$). This is mainly due to the binding energies at the two *SII* cations being less favourable than in Na-Y. The *SII* $\rightarrow$*SII* pathway via the *SIII* cation is illustrated in Figure 9.10. Two possibilities for this pathway are possible depending on whether the *SIII* cation is located far from or close to the *SII* cation from which the hopping pathway is initiated as explained above. The two pathways are related by mirror symmetry and therefore only one will be considered here. The two barriers associated with this pathway are 8.0 $kJmol^{-1}$ and 25.6 $kJmol^{-1}$ respectively. Since the larger barrier is very similar to that for the *SII* $\rightarrow$*SII* hop in the absence of the *SIII* cation, it would be expected that both of these pathways contribute to intra-cage motion.

The *SII* $\rightarrow$window hopping process is found to occur via the *SIII* site regardless of which *SII* site is chosen as the starting point, so it is more instructive to focus on the *SIII*

Figure 9.10: The *SII*→ *SII* hopping pathway via the *SIII* cation in Na-X (Hseu model)



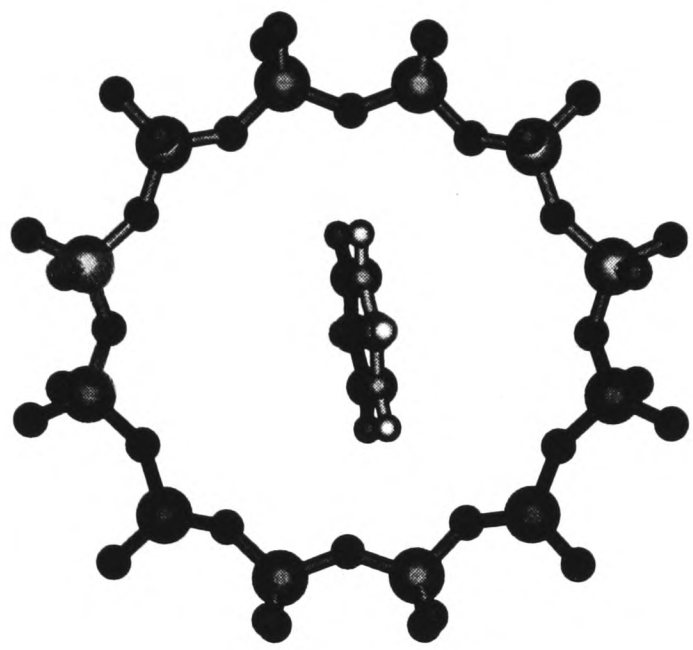
(a) schematic hopping pathway



(b) minimum energy pathway

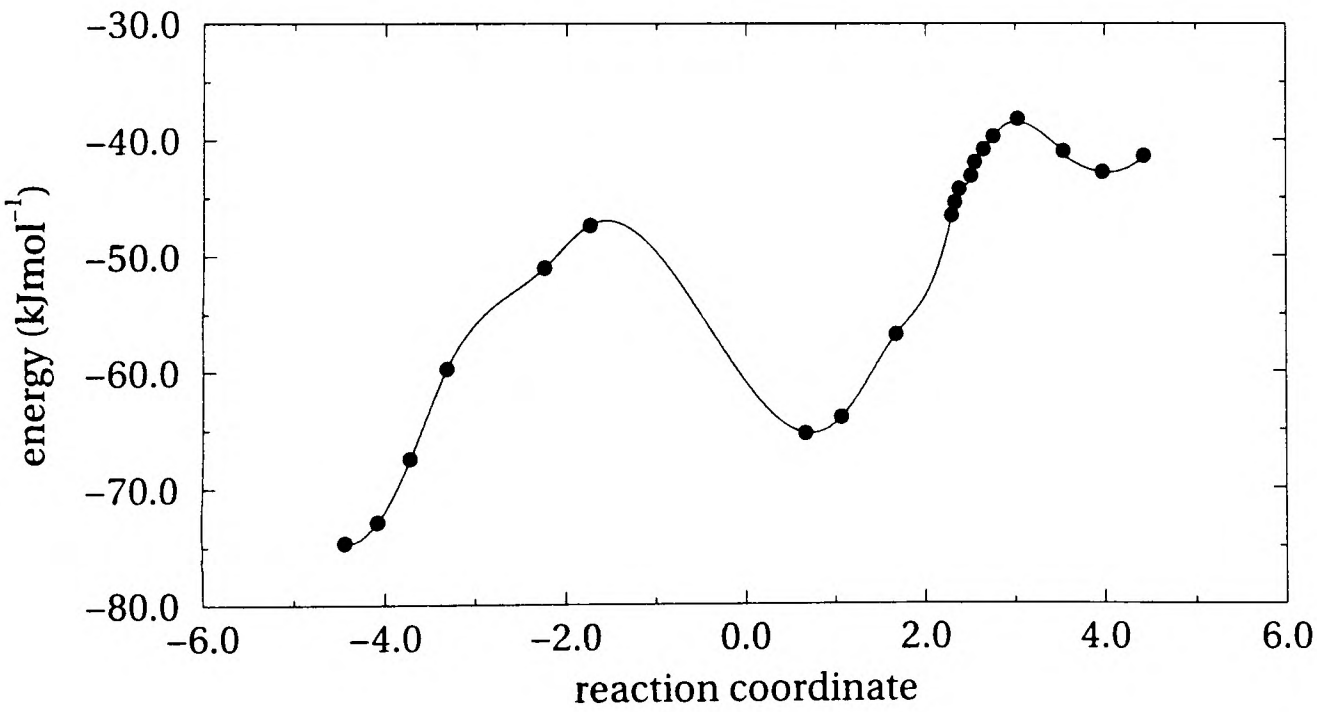
→window hop. The orientation of the *SIII* binding site is approximately perpendicular to the plane of the plane of the twelve-ring window. Therefore the benzene molecule must undergo significant rotational motion during the hopping process. In the absence of annealing, the benzene is forced into an unfavourable binding site in the window that lies perpendicular to the window plane with a binding energy of 42.8kJmol^{-1} (see Figure 9.11). This is probably due to the more elliptical nature of the window in the average-T model as

Figure 9.11: The perpendicular benzene binding site in the twelve-ring window of the Hseu Na-X model



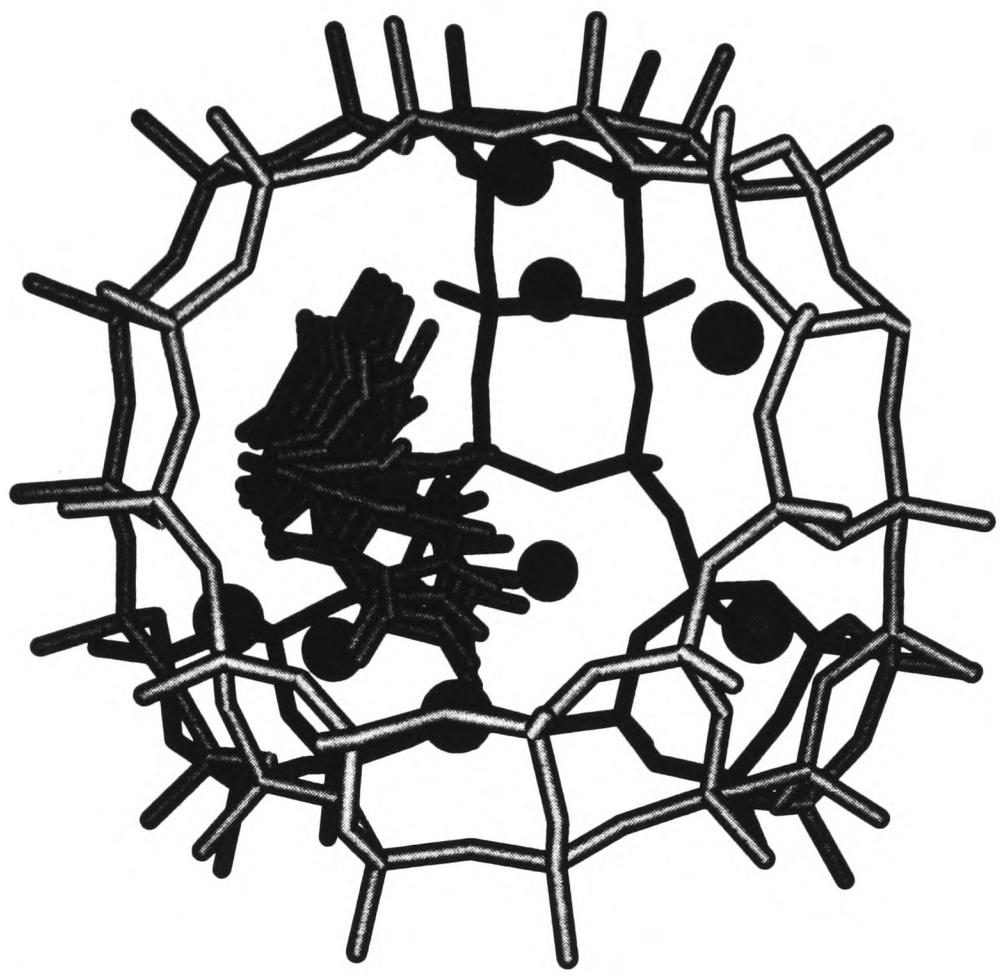
the benzene has its plane parallel to the long axis of the ellipse. The pathway has an intermediate site close to a second *SIII* site on the opposite side of the window and shows the window binding site minimum to be quite shallow. This is likely to be the reason that this site was not generated by the automated docking procedure. The energy barriers involved are comparable with those for the paths above (Figure 9.12) for inter-*SII* motion. However,

Figure 9.12: Minimum energy pathway for the non-annealed hop between the *SIII* cation and window site of the Hseu Na-X model

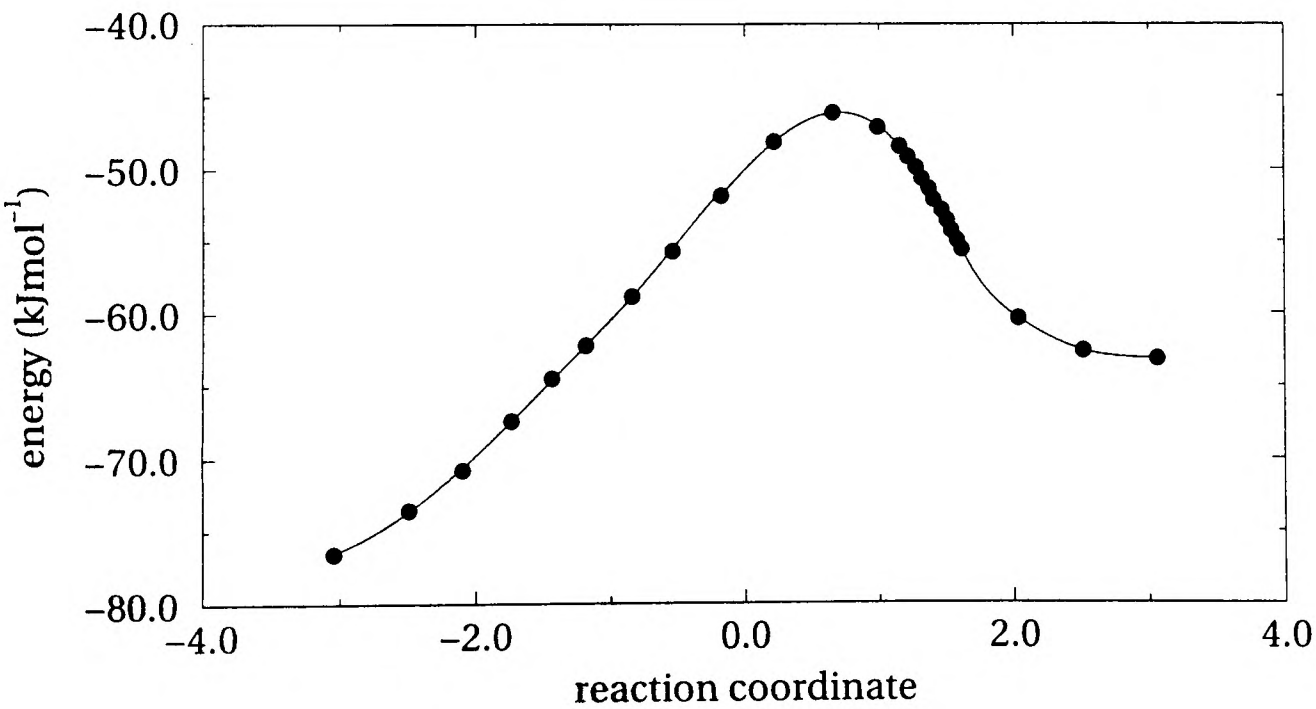


the annealed pathway shows a much smoother hopping trajectory and is shown in Figure 9.13. The barrier to reach the window site is 28.2 $kJmol^{-1}$, which is once again comparable

Figure 9.13: The *SIII*→ window hopping pathway in Na-X (Hseu model)



(a) schematic hopping pathway



(b) minimum energy pathway

with the other hopping pathways. The pathways considered suggest that intra-cage and inter-cage motion have approximately the same barrier and those barriers are lower than observed in the Na-Y models. This is consistent with the accelerated diffusivities observed by experiment.

In the case of the minimum energy pathways for the explicit-Al models, the results obtained are very similar with a few notable exceptions. In general, the energy barriers tend to be slightly higher reflecting mainly the increased stability of the binding sites. No benzene binding site perpendicular to the window is observed, presumably reflecting the less elliptical character of the twelve-ring. Also, separate pathways from both the *SII* cation and *SIII* cation sites to the window are observed. A comparison of the energy barriers for the two models is made in Table 9.15. In the explicit-Al model, there is a much lower barrier

Table 9.15: Comparison of the energy barriers ($kJmol^{-1}$) for hopping pathways in the average-T and explicit-Al models of Na-X (Hseu model)

path	average-T	explicit-Al
SII→*SII* (no *SIII*)	25.9	28.3
SII→*SII* (via *SIII*)	8.0,25.6	8.7,18.7
SII→window	via *SIII*	38.2
SIII→window	28.2	24.3
exit from window	14.7 (*SIII*)	19.8 (*SIII*),35.3 (*SII*)

to hop from the *SIII* site to the window than from the *SII* site. This is also the case when leaving the window site either to hop back into the original supercage, or into an adjacent one. This would suggest that both inter- and intra-cage motion are more facile when the benzene molecule hops via *SIII* cation sites.

In each case, the benzene molecule is able to completely reorientate itself either by motion in a single supercage or into an adjacent supercage with a maximum hopping activation energy of around 28 $kJmol^{-1}$. This is considerably less than the activation energy for Na-Y and would therefore be expected to allow faster diffusion in this zeolite.

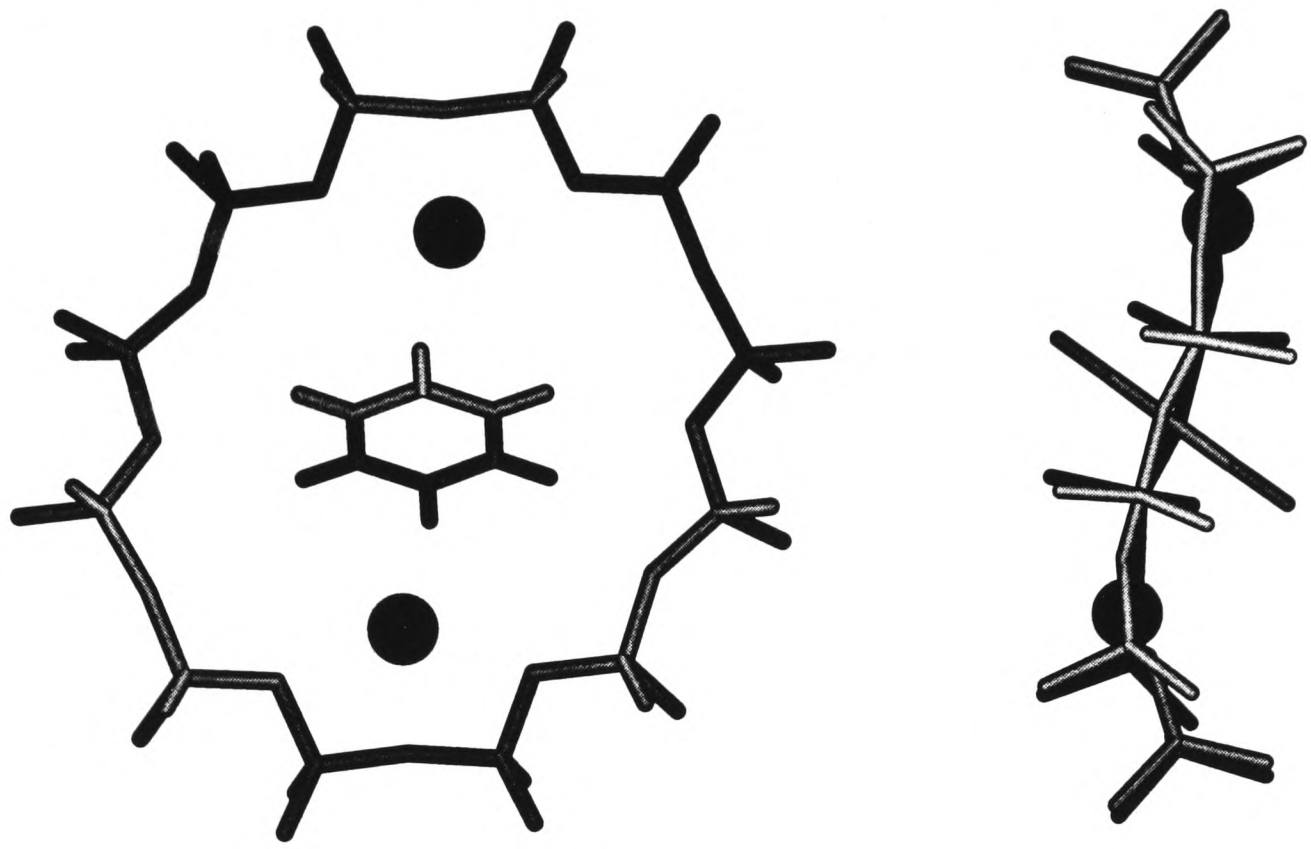
Table 9.16: Summary of docking results for benzene in Na-X (Olson Na(5) model)

	average-T model		explicit-Al model	
	fixed lattice	flexible lattice	fixed lattice	flexible lattice
SII site	54.0	57.9	55.9	58.8
SIII site (type I)	72.3	74.3	71.4	77.2
SIII site (type II)	70.4	77.2	72.3	73.3
dual *SIII* site	77.2	84.8	79.1	85.9

Olson Models: docking and minimum energy pathways

The docking binding sites in each of the Olson models for Na-X show several common features. Firstly, since the cation positions are located in the region of the twelve-ring window, the window site observed in other models is not present. Secondly, as with the Hseu model, sites involving direct interaction with *SII* and with *SIII* site are found. Finally, an unusual site is generated with the benzene molecule bounded approximately equidistant from the two *SIII* cations in a given window. The relative energies of these sites for the Olson Na(5) site and the effect of lattice relaxation is shown in Table 9.16. The *SII* site has benzene in a position in which it is interacting with both the *SII* site and a more distant *SIII* site. The benzene-*SII* cation distance is considerably longer than for the Hseu Na-X model and is tilted away from the plane of the six-ring. Two types of *SIII* site are possible depending on which side of the window plane the benzene is bound. It is interesting to note the considerable increase in binding energy afforded by lattice relaxation for the last two sites. This is mainly due to the *SIII* cations shifting up to 0.3Å away from their unrelaxed positions. These large shifts suggest that the low coordination of the *SIII* cations to framework oxygen allows relatively low activation energies for their motion in the presence of sorbates with strong interactions to the cations. The geometry of the dual *SIII* site is shown in Figure 9.14. Several possible pathways are possible between the determined docking sites. In contrast in the case of the Hseu model, all *SII* $\rightarrow$*SII* hops occur via an intermediate *SIII* cation site. In order to leave the cage, the benzene must visit the dual-*SIII* site in the window. It is possible to define a pathway moving from an *SII* to a dual-*SIII* site that contains all the relevant hopping pathways in one cage. This is shown is Figure 9.15. Although there

Figure 9.14: Geometry of the dual *SIII* binding site in Na-X (Olson Na(5) model)



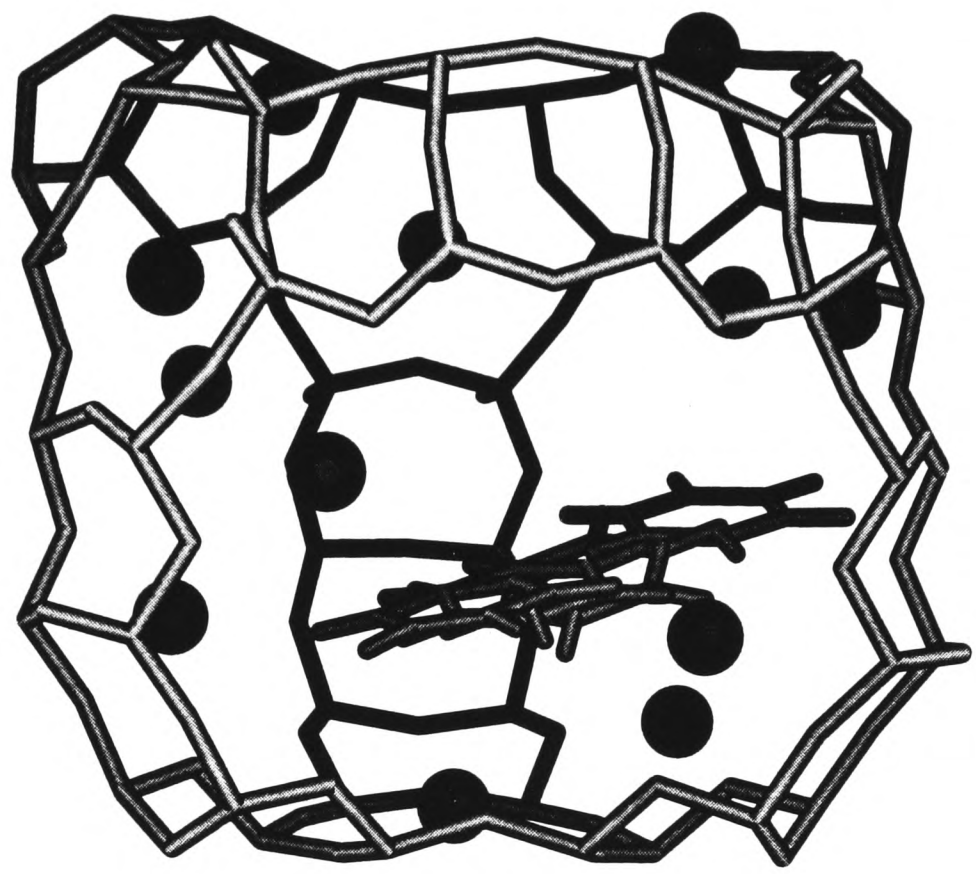
(a) front view (b) side view

are two types of *SIII* site, the binding energies and energy barriers are very close, so it is instructive to limit the calculations to this example pathway. The sites adopted and minimum energy pathways are similar for the explicit-Al model. The energy barriers for the hopping processes are summarised in Table 9.17. The sites and minimum energy pathways for models generated with different Olson *SIII* cation sites are very similar to those for the Na(5) model and therefore will not be detailed here. In each case, the activation energies for hopping are lower than that for the Na-Y models and therefore diffusion would expect to be enhanced.

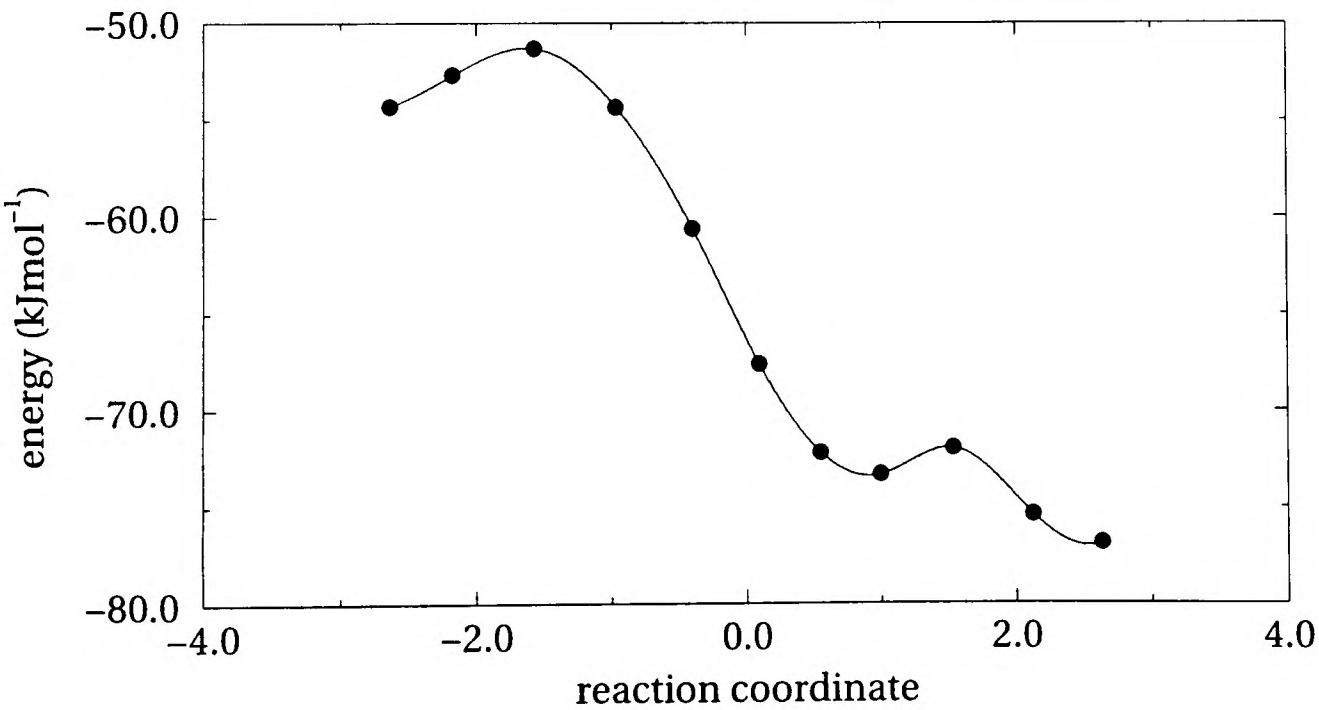
Table 9.17: Comparison of the energy barriers ($kJmol^{-1}$) for hopping pathways in the average-T and explicit-Al models of Na-X (Olson Na(5) model)

path	average-T	explicit-Al
SII→*SIII*	3.0	4.3
SIII→SII	22.0	20.2
SIII→dual *SIII*	1.3	0.7
dual *SIII*→*SIII*	4.9	7.8

Figure 9.15: The *SII*→ dual *SIII*-site hopping pathway in Na-X (Olson Na(5) model)



(a) schematic hopping pathway



(b) minimum energy pathway

9.5.3 Benzene Hopping in Highly Loaded Systems

All the previous calculations in this section have concerned sorption in the infinite dilution case. In this final set of calculations, the effect of loading on sorption sites and hopping pathways will be briefly investigated by taking a representative system, computing the energy barriers and comparing the results with the analogous infinite dilution case.

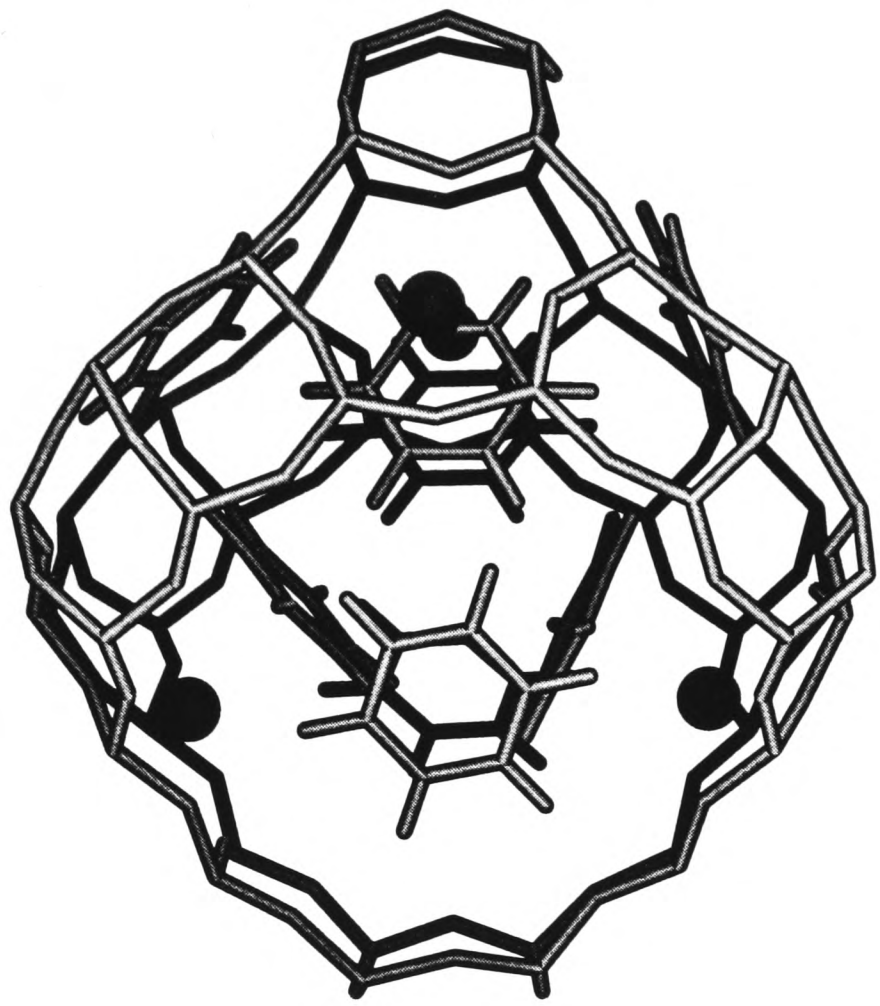
It is known from experimental sorption measurements that the maximum loading of benzene in Na-Y is around six molecules per supercage. A model with this loading level can be trivially constructed by occupying all the *SII* binding sites and all the window sites in one supercage with benzene molecules (the molecules in the window sites are shared with adjacent supercage, and therefore the total loading level is six). The explicit-Al Na-Y model was chosen for the zeolite model. The parameters for interactions between atoms in different benzene molecules were taken from Oie and co-workers[357] and are summarised in Table 9.18. The model with eight molecules was initially minimised with the zeolite

Table 9.18: Parameters for interactions between benzene molecules taken from the work of Oie and co-workers[357]

	σ_{ij} (Å)	ϵ_{ij} (meV)
C–C	3.207	4.156
C–H	2.780	3.047
H–H	2.405	2.564

fixed. The minimised geometry is shown in Figure 9.16. The minimised energy of the entire system is -619.3 kJmol^{-1}, which corresponds to an average energy of 77.4 kJmol^{-1} per molecule. Using the binding energy of the docked sites in the infinite dilution case, the predicted total energy in the absence of benzene-benzene interactions can be calculated to be -505.5 kJmol^{-1}. Therefore the contribution to the total sorption energy is approximately 14.2 kJmol^{-1} per molecule, which is 18% of the binding energy. From the minimised geometry, a single point energy calculation was performed with the benzene-benzene interaction neglected to assess the extent of destabilisation as a consequence of this highly loaded configuration. The energy can be compared to the infinite dilution case. The destabilisation is found to be only 1.1 kJmol^{-1} per molecule which is a negligible fraction of the

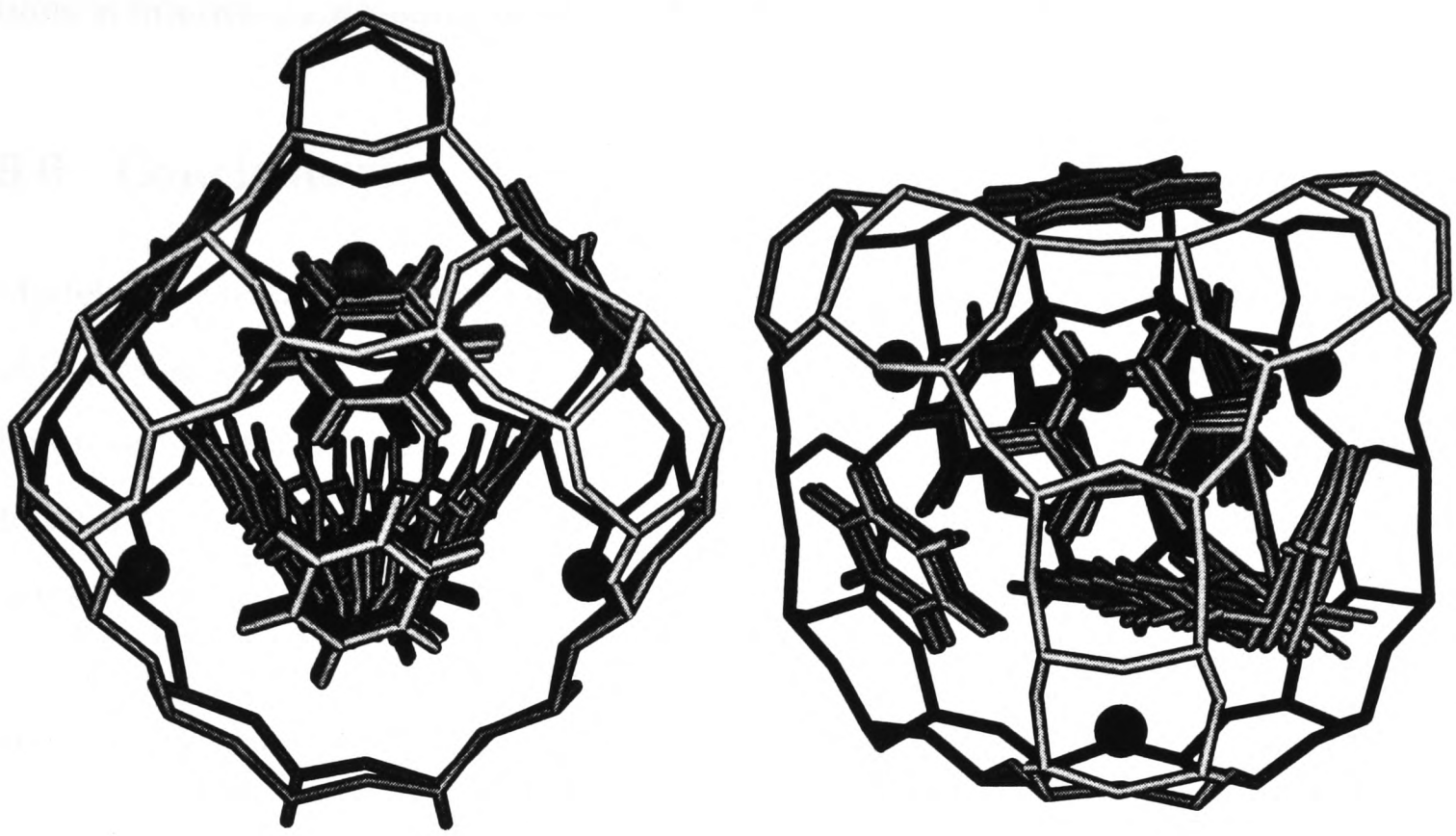
Figure 9.16: The minimised structure of a Na-Y model with eight benzenes sorbed in one supercage



total energy.

Two hopping pathways were considered. Firstly, a single benzene bound to an *SII* site was removed from the minimised configuration and a constrained minimum energy pathway calculated by moving an adjacent benzene molecule bound to an *SII* site to the empty site. A second pathway was constructed with the same method but with the removal of a benzene molecule in the window site. Although the zeolite lattice was held fixed during the minimisation, all other benzenes were allowed to relax their positions to accommodate the hopping molecule. The two hopping pathways are shown in Figure 9.17. The shapes of the minimum energy pathway curves are very similar to those in the infinite dilution case. A comparison of the energy barriers is given in Table 9.19. It is interesting to note that the barrier appears to be lower for the *SII* $\rightarrow$ *SII* hop in the highly loaded system which would suggest that the neighbouring benzene molecules somehow enhance the transport. It is likely that this occurs by the stabilisation of the transition state by the surrounding benzene molecules. In contrast, the energy barrier for the *SII* $\rightarrow$window hop is considerably higher. It can be noted that when a benzene molecule bound at the window site is

Figure 9.17: Hopping pathways in the high-loading model of Na-Y. Stationary benzene configurations superimposed from each hopping step to show displacement during hopping process



(a) *SII* → *SII* hop

(b) *SII* →window hop

Table 9.19: Comparison of the energy barriers (kJmol^{-1}) for the *SII* → *SII* and *SII* →window hopping processes in the infinite dilution and highly loaded models of Na-Y

	infinite dilution	high loading
SII → *SII*	38.5	30.9
SII →window	47.9	77.8

removed from the minimised model with eight molecules in a single supercage, the nearby molecules bound to *SII* sites rotate during relaxation. During the constrained energy minimisation, these molecules must rotate back to their original positions to accommodate the benzene in the window site. This significantly increases the barrier for the hopping process. This effect does not appear to be a important factor in the *SII* → *SII* hop.

There is some experimental evidence from the PFG NMR measurements of the dependence of the diffusivity benzene in Na-X on loading that suggests that the self-diffusivities remain approximately constant until reaching a critical loading level, after which the dif-

fusivities decrease by two orders of magnitude.[388] This is consistent with the dramatic increase in calculated activation energy in the high loading model, although more calculations at intermediate loading levels are needed to investigate this effect further.

9.6 Conclusions

Models have been constructed for Na-Y and Na-X faujasites that are consistent with available crystallographic data. Studies of the relative cation site stabilities suggest that no relation can be drawn to their crystallographic occupancies. The cation site positions tend to be more accurately reproduce when a model with an ordered Al-substitution pattern is employed. There is also evidence to suggest that at Si/Al ratios greater than 2.0, the *SII* cation site becomes slightly destabilised. In the case of Na-X, lattice energy minimisations suggest that cations in *SIII* geometry tend to occupy sites on the opposite sides of the same window to minimise repulsions. With regards to the behaviour of benzene in these systems, the fitted forcefield is found to correctly reproduce the trends in the diffusional behaviour as measured by NMR spin-lattice experiments. In addition, the calculated binding energies in each of the Na-X models are consistent with thermochemical measurements. However, the chosen forcefield tends to overestimate the hopping activation energy compared to experiment, which would suggest that the representation of the transition state configurations are inaccurate and therefore require further refinement. This could be achieved by performing quantum mechanical cluster calculations at the transition state geometry. In the case of highly loaded systems, it appears that the presence of other sorbed molecules in the region of hopping event can have a significant effect on the activation energy. This behaviour is yet to be confirmed by experiment.

References

1. A. F. Cronstedt. *Svenska Vetenskaps Akademiens Handlingar Stockholm,* **17**, 120–123 (1756).

2. J. L. Schlenker and G. H. Kühl. In *Proceeding from the Ninth International Zeolite Conference,* R. von Ballmoos, J. B. Higgins and M. M. J. Tracey, editors, volume 1, 3–9. Butterworth-Heinemann (1992).

3. S. T. Wilson, B. M. Lok, C. A. Messina, T. R. Cannan and E. M. Flanigen. *J. Am. Chem. Soc.,* **104**, 1146–1147 (1982).

4. B. L. Meyers, S. R. Ely, N. A. Kutz, J. A. Kaduk and E. van der Bossche. *J. Catal.,* **91**, 352–355 (1984).

5. J. M. Newsam and D. E. Vaughan. In *New Developments in Zeolite Science and Technology,* Y. Murakami, A. Iijima and J. W. Ward, editors, 457–464. Kodansha and Elsevier (1986).

6. B. M. Lok, C. A. Messina, R. L. Patton, R. T. Gajek, T. R. Cannan and E. M. Flanigen. *J. Am. Chem. Soc.,* **106**, 6092–6093 (1982).

7. E. M. Flanigen, B. M. Lok, R. L. Patton and S. T. Wilson. In *New Developments in Zeolite Science and Technology,* Y. Murakami, A. Iijima and J. W. Ward, editors, 103–112. Kodansha and Elsevier (1986).

8. M. E. Davis, C. Saldarriaga, C. Montes, J. Garces and C. Crowder. *Nature,* **331**, 698–699 (1988).

9. M. Estermann, L. B. McCusker, C. Baerlocher, A. Merrouche and H. Kessler. *Nature,* **352**, 320–323 (1991).

10. R. H. Jones, J. M. Thomas, J. S. Chen, R. R. Xu and A. M. Chippindale. *J. Solid State Chem.*, **102**, 204–208 (1993).

11. J. M. Newsam. In *Solid State Chemistry: Compounds*, A. K. Cheetham and P. Day, editors, 234–280. Oxford University Press (1992).

12. H. de. St. Claire Deville. *Comptes Rendus*, **54**, 324 (1862).

13. W. H. Taylor. *Z. Kristallogr.*, **74**, 1–19 (1930).

14. W. M. Meier and D. H. Olson. *Atlas of Zeolite Structure Types.* Butterworth-Heinemann (1992).

15. R. M. Barrer. *Pure and Appl. Chem.*, **51**, 1091–1100 (1979).

16. W. M. Meier. *Molecular Sieves.* Society of Chemical Industry (1968).

17. J. V. Smith. *Chem. Rev.*, **88**, 149–182 (1988).

18. D. E. Akporiaye and G. D. Price. *Zeolites*, **9**, 23–32 (1989).

19. M. E. Davis and R. F. Lobo. *Chem. Mater.*, **4**, 756–768 (1992).

20. G. O. Brunner and E. M. Meier. *Nature*, **337**, 147–147 (1989).

21. M. J. Annen, M. E. Davis, J. B. Higgins and J. L. Schlenker. *J. Chem. Soc. Chem. Comm.*, , 1175–1176 (1991).

22. C. T. Kresge, M. E. Leonowicz, W. J. Roth, J. C. Vartuli and J. S. Beck. *Nature*, **359**, 710–712 (1992).

23. W. Löwenstein. *Amer. Miner.*, **39**, 92–96 (1954).

24. J. Klinowski, S. W. Carr, S. E. Tarling and P. Barnes. *Nature*, **330**, 56–58 (1987).

25. P. E. Halstead and A. E. Moore. *J. Appl. Cryst.*, **12**, 413–417 (1962).

26. J. J. Pluth and J. V. Smith. *J. Am. Chem. Soc.*, **102**, 4704–4708 (1980).

27. D. H. Olsen. *J. Phys. Chem.*, **74**, 2758–2764 (1970).

28. E. Dempsey, G. H. Kühl and D. H. Olson. *J. Phys. Chem.*, **73**, 387–390 (1969).

29. K.-P. Schröder and J. Sauer. *J. Phys. Chem.*, **97**, 6579–6581 (1993).

30. M. Sato, K. Maeda and K. Hirasawa. *Chem. Lett.*, **8**, 1543–1546 (1994).

31. J. A. Hriljac, M. M. Eddy, A. K. Cheetham, J. A. Donohue and G. J. Ray. *J. Solid State Chem.*, **106**, 66–72 (1993).

32. A. K. Cheetham, M. M. Eddy and J. M. Thomas. *J. Chem. Soc. Chem. Comm.*, , 1337–1338 (1984).

33. J. Sauer. *Chem. Rev.*, **89**, 199–255 (1989).

34. L. J. Smith, A. K. Cheetham, R. E. Morris, P. A. Wright, L. Marchese, J. Chen and J. M. Thomas. *Science*, **271**, 799–802 (1996).

35. S. J. Weigel, J.-C. Gabriel, E. Guittierez Puebla, A. Monge Bravo, N. J. Henson, L. M. Bull and A. K. Cheetham. *J. Am. Chem. Soc. in press* (1996).

36. F. Delprato, L. Delmotte, J. L. Guth and L. Huve. *Zeolites*, **10**, 546–552 (1990).

37. D. M. Ginter, C. J. Radke and A. T. Bell. In *Zeolites: Facts, Figures, Future*, P. A. Jacobs and R. A. van Santen, editors, 161–168. Elsevier (1989).

38. E. M. Flanigen and R. L. Patton. *U. S. Patent No. 4,073,864* (1978).

39. J. L. Guth, H. Kessler and R. Wey. In *New Developments in Zeolite Science and Technology*, Y. Murakami, A. Iijima and J. W. Ward, editors, 121–128. Kodansha and Elsevier (1986).

40. J. L. Guth, H. Kessler, J. M. Higel, J. Lamblin, J. Patarin, A. Seive, J. M. Chezcau and R. Wey. In *Zeolite Synthesis*, M. L. Occelli and H. E. Robson, editors, 176–195. American Chemical Society, Washington (1989).

41. Q. S. Huo and R. R. Xu. *J. Chem. Soc. Chem. Comm.*, , 783–784 (1990).

42. A. Kupermann, S. Nadimi, S. Oliver, G. A. Ozin, J. M. Garces and M. M. Olken. *Nature*, **365**, 239–242 (1993).

43. S. Oliver, A. Kupermann, A. Lough, G. A. Ozin, J. M. Garces, M. M. Olken and P. Rudolph. In *Zeolites and Related Microporous Materials: State of the Art 1994*, J. Weitkamp, H. G. Karge, H. Pfeifer and W. Hölderich, editors, volume 1, 219–225. Butterworth-Heinemann (1994).

44. L. B. McCusker. *Acta Cryst.*, **A47**, 297–313 (1991).

45. L. B. McCusker. In *Zeolites and Related Microporous Materials: State of the Art 1994*, J. Weitkamp, H. G. Karge, H. Pfeifer and W. Hölderich, editors, 341–356. Elsevier (1994).

46. H. M. Rietveld. *J. Appl. Cryst.*, **2**, 65–71 (1969).

47. A. K. Cheetham, M. M. Eddy, D. A. Jefferson and J. M. Thomas. *Nature*, **299**, 24–26 (1982).

48. M. Czjzek, H. Jobic, A. N. Fitch and T. Vogt. *J. Phys. Chem.*, **96**, 1535–1542 (1992).

49. J. M. Bennett, J. W. Richardson, J. J. Pluth and J. V. Smith. *Zeolites*, **7**, 160–162 (1987).

50. J. W. Richardson, J. J. Pluth and J. V. Smith. *Acta Cryst.*, **C43**, 1469–1472 (1987).

51. L. B. McCusker. *J. Appl. Cryst.*, **21**, 305–310 (1988).

52. A. Simmen, L. B. McCusker, Ch. Baerlocher and W. M. Meier. *Zeolites*, **11**, 654–661 (1991).

53. P. A. Wright, J. M. Thomas, A. K. Cheetham and A. K. Nowak. *Nature*, **318**, 611–614 (1985).

54. A. N. Fitch, H. Jobic and A. Renouprez. *J. Phys. Chem.*, **90**, 1311–1318 (1986).

55. R. Goyal, A. N. Fitch and H. Jobic. *J. Chem. Soc. Chem. Comm.*, , 1152–1153 (1990).

56. C. Mellot, D. Espinat, , B. Rebours and Ch. Baerlocher. *Catal. Lett.* **27**, 159–169 (1994).

57. H. Klein, C. Kirschhock and H. Fuess. *J. Phys. Chem.*, **98**, 12345–12360 (1994).

58. J. M. Thomas. In *Zeolites: Facts, Figures, Futures*, P. A. Jacobs and R. A. van Santen, editors, 3–28. Elsevier (1989).

59. C. A. Fyfe, G. T. Kokotailo, H. Strobl and C. S. Pasztor. *Zeolites,* **9**, 531–534 (1989).

60. J. M. Newsam, M. M. J. Tracey, W. T. Koetsier and C. B. de Gruyer. *Proc. Roy. Soc. (London),* **A420**, 375–405 (1988).

61. Y. Y. Tong, J. J. Van der Klink, G. Clugnet and A. J. Renouprez. *Surf. Sci.,* **292**, 276–288 (1993).

62. R. F. Lobo and M. E. Davis. *J. Am. Chem. Soc.,* **117**, 3764–3779 (1995).

63. S. A. Axon, K. K. Fox, S. W. Carr and J. Klinowski. *Chem. Phys. Lett.,* **189**, 1–6 (1992).

64. D. W. Lewis, C. R. A. Catlow, G. Sankar and S. W. Carr. *J. Phys. Chem.,* **99**, 2377–2383 (1995).

65. E. M. Flanigen, H. Khatania and H. A. Szynanski. In *Molecular Sieves I,* E. M. Flanigen and L. B. Sand, editors, 201–229. American Chemical Society, Washington (1971).

66. P. A. Jacobs and R. A. von Ballmoos. *J. Phys. Chem.,* **86**, 3050–3052 (1982).

67. R. Vomsheid, M. Briend, M. J. Peltre and D. Barthomeuf. *J. Chem. Soc. Faraday Trans.,* **91**, 3281–3284 (1995).

68. B. L. Su and D. Barthomeuf. *Zeolites,* **15**, 470–474 (1995).

69. E. R. Andrew, A. Bradbury and R. G. Eades. *Nature,* **182**, 1659 (1959).

70. G. Engelhardt, V. Lohse, E. Lippmaa, M. Tarmak and M. A. Magi. *Z. Anorg. Allg. Chem.,* **482**, 49–64 (1981).

71. G. Engelhardt and D. Michel. *High-Resolution Solid-State NMR of Silicates and Zeolites.* Wiley (1987).

72. A. Bax, R. Freeman and S. P. Kempsall. *J. Am. Chem. Soc.,* **102**, 4849–4851 (1980).

73. A. Bax and R. Freeman. *J. Mag. Res.,* **44**, 542–561 (1981).

74. C. A. Fyfe, H. Gies and Y. Feng. *J. Am. Chem. Soc.,* **111**, 7702–7707 (1989).

75. A. Samoson, E. Lippmaa and A. Pines. *Mol. Phys.,* **65**, 1013–1018 (1988).

76. B. F. Chmelka, K. T. Mueller, A. Pines, J. Stebbins, Y. Wu and J. W. Zwaniger. *Nature,* **339**, 42–43 (1989).

77. A. Medek, J. S. Harwood and L. Frydman. *J. Am. Chem. Soc.*, **117**, 12779–12787 (1995).

78. J. P. Fraissard and T. Ito. *Zeolites,* **8**, 350–360 (1988).

79. J. Demarquay and J. Fraissard. *Chem. Phys. Lett.*, **136**, 314–318 (1987).

80. J. A. Ripmeester. *J. Chem. Soc. Faraday Trans. I,* **84**, 3731–3745 (1988).

81. B. F. Chmelka, J. G. Pearson, S. B. Liu, R. Ryoo, L. C. de Menorval and A. Pines. *J. Phys. Chem.*, **95**, 303–310 (1991).

82. M. W. Anderson and J. Klinowski. *J. Am. Chem. Soc.*, **112**, 1–16 (1990).

83. D. M. Ruthven. *Principles of Adsorption and Adsorption Processes.* Wiley Interscience (1984).

84. P. B. Weisz. *Chemtech,* **3**, 498–505 (1973).

85. W. M. Deen. *AIChE J.*, **33**, 1409–1425 (1987).

86. E. H. Kennard. *Kinetic Theory of Gases.* McGraw Hill (1938).

87. W. Heink, J. Kaerger, H. Pfeifer, P. Salverda, K. P. Datema and A. K. Nowak. *J. Chem. Soc. Faraday Trans.*, **99**, 515–519 (1992).

88. U. Hong, J. Kärger, B. Hunger, N. N. Feoktistova and S. P. Zhdanov. *J. Catal.*, **137**, 243–251 (1992).

89. L. M. Bull, N. J. Henson, A. K. Cheetham, J. M. Newsam and S. J. Heyes. *J. Phys. Chem.*, **97**, 11776–11780 (1993).

90. H. Jobic, M. Bee and G. J. Kearley. *Zeolites,* **9**, 312–317 (1989).

91. H. Jobic, M. Bee, J. Caro, M. Bülow and J. Kärger. *J. Chem. Soc. Faraday Trans. I,* **85**, 4201–4209 (1989).

92. H. G. Karge and W. Niessen. *Catalysis Today,* **8**, 451–465 (1991).

93. M. Eic and D. M. Ruthven. *Zeolites*, **8**, 40–45 (1988).

94. D. M. Ruthven. *Zeolites*, **13**, 594–594 (1993).

95. A. Torresan and Ph. Grenier. *Chem. Eng. J.*, **49**, 11–16 (1992).

96. Ph. Grenier, F. Meunier, P. G. Grey, L. M. Sun, J. Kärger, Z. Xu and D. M. Ruthven. *Zeolites*, **14**, 242–249 (1994).

97. L. V. C. Rees and D. Shen. In *Characterization of porous solids III*, J. Rouqerol, F. Rodríguez-Reinoso, K. S. W. Sing and K. K. Unger, editors, 563–571. Elsevier (1994).

98. A. G. Oblad. *Oil and Gas J.*, **70**, 84–87 (1972).

99. J. Haggin. *C&E News*, , 30–32 October 25 (1993).

100. M. Iwamoto, H. Yahiro, K. Tanda and N. Mizuno. *J. Phys. Chem.*, **95**, 3727–3730 (1991).

101. G. Pergo, C. Bellussi, C. Corno, M. Taramasso and F. Buonomo. In *New Developments in Zeolite Science and Technology*, Y. Murakami, I. Iijima and J. W. Ward, editors, 129–136. Kodansha and Elsevier (1986).

102. N. Y. Chen and W. Garwood. *J. Catal.*, **52**, 453–458 (1978).

103. P. E. Hathaway and M. E. Davis. *J. Catal.*, **116**, 253–287 (1988).

104. F. P. Gortsema, B. Beshty, J. J. Friedman, D. Matsumoto, J. J. Sharkey, G. Wildman, T. J. Blacklock and S. H. Pan. In *Catalysis of Organic Reactions*, J. R. Kosak and T. A. Johnson, editors, 445–459. Marcel Dekker (1994).

105. L. J. King, D. O. Campbell, E. D. Collins, J. B. Knauer and R. M. Wallace. In *Proceedings of the Sixth International Zeolite Conference*, D. H. Olsen and A. Bisio, editors, 660–672. Butterworth (1984).

106. N. Herron, Y. Wang, M. M. Eddy, G. D. Stucky, D. E. Cox, K. Moller and T. Bein. *J. Am. Chem. Soc.*, **111**, 530–540 (1989).

107. P. Enzel and T. Bein. *J. Phys. Chem.*, **93**, 6270–6272 (1989).

108. D. R. Hartree. *Proc. Cambridge Phil. Soc.*, **24**, 89–132 (1928).

109. V. Fock. *Z. Phys.*, **61**, 126–148 (1930).

110. C. C. J. Roothaan. *Rev. Mod. Phys.*, **23**, 69–89 (1951).

111. W. J. Hehre, R. F. Stewart and J. J. Pople. *J. Chem. Phys.*, **51**, 2657–2664 (1969).

112. M. J. Frisch, G. W. Trucks, M. Head-Gordon, P. M. W. Gill, J. B. Foresman, M. W. Wong, B. G. Johnston, H. B. Schlegel, M. A. Robb, E. S. Replogle, R. Gomperts, J. L. Andre, K. Raghavachari, J. S. Binkey, C. Gruzoly, R. L. Martins, D. J. Fox, D. J. DeFrees, J. Baker, J. J. P. Stewart and J. A. Pople. *GAUSSIAN 92.* Gaussian Inc., Pittsburg, PA (1992).

113. M. F. Guest and J. Kendrick. *GAMESS User Manual.* University of Manchester Computing Centre, UK (1986).

114. R. D. Amos and J. E. Rice. *Cambridge Analytical Derivatives Package 4.0.* Cambridge University, Cambridge (1987).

115. R. Ahlrichs, M. Bär, M. Häses, H. Horn and C. Kölmel. *Chem. Phys. Lett.*, **162**, 165–169 (1989).

116. R. P. Messmer and G. D. Watkins. *Phys. Rev. Lett.*, **25**, 656–659 (1970).

117. M. R. Haynes. *Phys. Rev. B*, **5**, 697–700 (1972).

118. M. J. S. Dewar, E. G. Zoebisch, E. F. Healy and J. J. P. Stewart. *J. Am. Chem. Soc.*, **107**, 3902–3909 (1985).

119. J. J. Stewart. *J. Comput. Chem.*, **10**, 209–220 (1989).

120. J. J. Stewart. *QCPE Bulletin No. 455* (1986).

121. P. Hohenberg and W. Kohn. *Phys. Rev.*, **136**, B864–B871 (1964).

122. W. Kohn and L. Sham. *Phys. Rev.*, **140**, A1133–A1138 (1965).

123. B. Delley. *J. Chem. Phys.*, **92**, 508–517 (1990).

124. J. Andzelm, E. Wimmer and D. R. Salahub. In *The Challenge of d and f Electrons: Theory and Computation,* D. R. Salahub and M. C. Zerner, editors, 228–245. American Chemical Society, Washington (1990).

125. R. Dovesi, C. Pisani, C. Roetti, M. Causa and V. R. Saunders. *CRYSTAL88, An ab initio All-Electron LCAO-Hartree-Fock program for Periodic Systems.* QCPE Program No. 577, Quantum Chemistry Program Exchange, Indiana University, Bllomington, Indiana (1988).

126. B. W. H. van Beest, J. Verbeek and R. A. van Santen. *Catal. Lett.* **1**, 147–154 (1988).

127. J. Sauer, C. M. Kölmel, J. R. Hill and R. Ahlrichs. *Chem. Phys. Lett.*, **164**, 193–198 (1990).

128. S. Beran. *J. Phys. Chem.*, **94**, 335–337 (1990).

129. J. Sauer, H. Horn, M. Häser and R. Ahlrichs. *Chem. Phys. Lett.*, **173**, 26–32 (1990).

130. P. J. O'Malley and J. Dwyer. *Zeolites*, **8**, 317–321 (1988).

131. G. J. Kramer, A. J. M. de Man and R. A. van Santen. *J. Am. Chem. Soc.*, **113**, 6435–6441 (1991).

132. S. Merlino. *Acta Cryst.*, **A37 (Suppl.)**, C189 (1981).

133. S. L. Lawton and W. J. Rohrbaugh. *Science*, **247**, 1319–1322 (1990).

134. K. D. Schmitt and G. J. Kennedy. *Zeolites*, **14**, 635–642 (1994).

135. J. C. White and A. C. Hess. *J. Phys. Chem.*, **97**, 8703–8706 (1993).

136. J. C. White and A. C. Hess. *J. Phys. Chem.*, **97**, 6398–6404 (1993).

137. E. Apra, R. Dovesi, C. Freyriafava and C. Pisani. *Modelling Simul. Mater. Sci. Engng.*, **1**, 297–306 (1993).

138. J. Sauer. *Modelling of Structure and Reactivity in Zeolites*, chapter 8, 183–216. Academic Press (1992).

139. H. V. Brand, L. A. Curtiss and L. E. Iton. *J. Phys. Chem.*, **96**, 7725–7732 (1992).

140. E. G. Derouane and J. G. Fripiat. *Zeolites*, **5**, 165–172 (1985).

141. A. E. Alvarado-Swaisgood, M. K. Barr, P. J. Hay and A. Redondo. *J. Phys. Chem.*, **95**, 10031–10036 (1991).

142. C. Pisani, R. Dovesi, R. Nada and L. N. Kantorwich. *J. Chem. Phys.*, **92**, 7448–7460 (1990).

143. S. J. Cook, A. K. Chakraborty, A. T. Bell and D. N. Theodorou. *J. Phys. Chem.*, **97**, 6679–6685 (1993).

144. S. P. Greatbanks, P. Sherwood and I. H. Hillier. *J. Phys. Chem.*, **98**, 8134–8139 (1994).

145. J. B. Nicholas and A. C. Hess. *J. Am. Chem. Soc.*, **116**, 5428–5436 (1994).

146. J. Sauer and P. Hobza. *Theor. Chim. Acta.*, **65**, 291–302 (1984).

147. A. Redondo and P. J. Hay. *J. Phys. Chem.*, **97**, 11754–11761 (1993).

148. J. D. Gale. *Computer Simulation of Zeolites and Pillared Clays.* PhD thesis, University of Oxford (1990).

149. J. Sauer, C. M. Kölmel, J.-R. Hill and Ahlrichs R. *Chem. Phys. Lett.*, **164**, 193–198 (1989).

150. M. Allavena, K. Seiti, E. Kassub, G. Ferenczy and J. G. Angyan. *Chem. Phys. Lett.*, **168**, 461–467 (1990).

151. R. Vetrivel, C. R. A. Catlow and E. A. Colbourne. *J. Phys. Chem.*, **93**, 4594–4598 (1989).

152. J. D. Gale, C. R. A. Catlow and A. K. Cheetham. *J. Chem. Soc. Chem. Comm.*, , 178–179 (1991).

153. E. Teunissen, R. A. van Santen, R. Dovesi and C. Roetti. In *CECAM Workshop, Orsay, Paris, Oct 10-18* (1991).

154. T. Mai and Kh. Dimitrov. *Kliment Okhridski*, **76**, 117 (1986).

155. S. Beran, P. Jiru and L. Kubelkova. *J. Mol. Catal.*, **12**, 341–349 (1981).

156. V. Srdanov, K. Haug, G. Stucky and H. Metiu. *J. Chem. Phys.*, **96**, 9039–9043 (1992).

157. C. P. Ursenbach, P. A. Madden, I. Sitch and M. C. Payne. *J. Phys. Chem.*, **99**, 6697–6714 (1995).

158. A. D. McLachlan. *Proc. Roy. Soc. (London)*, **A271**, 387 (1963).

159. J. C. Slater and J. G. Kirkwood. *Phys. Rev.*, **37**, 682–697 (1931).

160. J. G. Kirkwood. *Phys. Z.*, **33**, 57–60 (1932).

161. A. Müller. *Proc. Roy. Soc. (London)*, **A154**, 624–639 (1936).

162. P. W. Fowler. *Mol. Phys.*, **56**, 83–95 (1985).

163. J. E. Lennard-Jones. *Proc. Roy. Soc. (London)*, **A106**, 463–477 (1924).

164. I. D. Faux. *J. Phys. C.*, **9**, L211–L216 (1971).

165. B. G. Dick and A. W. Overhauser. *Phys. Rev.*, **112**, 90–103 (1958).

166. C. R. A. Catlow, I. D. Faux and M. J. Norgett. *J. Phys. C.*, **9**, 419–429 (1976).

167. U. Schröder. *Solid State Commun.*, **4**, 347–349 (1966).

168. M. J. Sangster, U. Schröder and R. M. Atwood. *J. Phys. C.*, **11**, 1523–1540 (1978).

169. H. M. Evjen. *Phys. Rev.*, **39**, 675–687 (1932).

170. E. Madelung. *Physik. Z.*, **19**, 524–533 (1918).

171. P. P. Ewald. *Ann. Physik.*, **64**, 253–287 (1921).

172. N. Anastasiou and D. Fincham. *Comp. Phys. Commun.*, **25**, 159–176 (1982).

173. C. R. A. Catlow and M. J. Norgett. *AERE Harwell Report M2936* (1976).

174. R. G. Gordon and Y. S. Kim. *J. Chem. Phys.*, **56**, 3122–3133 (1972).

175. W. C. Mackrodt and R. F. Stewart. *J. Phys. C.*, **10**, 1431–1446 (1977).

176. K. de Boer, A. P. J. Jansen and R. A. van Santen. *Chem. Phys. Lett.*, **223**, 46–53 (1994).

177. J. Purton, R. Jones, C. R. A. Catlow and M. Leslie. *Phys. Chem. Miner.*, **19**, 392–400 (1993).

178. J. D. Gale, C. R. A. Catlow and W. C. Mackrodt. *Modelling Simul. Mater. Sci. Engng,*. **1**, 73–81 (1992).

179. B. W. H. van Beest, G. J. Kramer and R. A. van Santen. *Phys. Rev. Lett.*, **64**, 1955–1958 (1990).

180. M. P. Allen and D. J. Tildesley. *Computer Simulation of Liquids.* Oxford University Press (1987).

181. M. Born and K. Huang. *Dynamical Theory of Crystal Lattices.* Oxford University Press (1954).

182. R. Fletcher and M. J. D. Powell. *Computer J.*, **6**, 163–169 (1963).

183. M. J. Powell. AERE Harwell Report TP372 (1969).

184. C. G. Broydon. *J. Inst. Maths. Appl.*, **6**, 222 (1970).

185. D. F. Shanno. *Math. Computing*, **24**, 647–656 (1970).

186. R. F. Fletcher and C. M. Reeves. *Computer J.*, **7**, 149–154 (1964).

187. N. F. Mott and M. J. Littleton. *J. Chem. Soc. Faraday Trans.*, **34**, 485–499 (1938).

188. G. D. Price, A. Wall and S. C. Parker. *Phil. Trans. Roy. Soc. London Ser.*, **328**, 391–407 (1989).

189. X. Zhang, C. R. A. Catlow, S. C. Parker and A. Wall. *J. Phys. Chem. Solids*, **53**, 761–770 (1992).

190. C. W. Gear. *The Numerical Differentiation of Ordinary Differential Equations of Various Orders.* Argonne National Laboratory Report ANL7126 (1966).

191. C. W. Gear. *Numerical Initial Value Problems in Ordinary Differential Equations.* Prentice Hall (1971).

192. L. Verlet. *Phys. Rev.*, **159**, 98–103 (1967).

193. D. Fincham and D. M. Heyes. *CCP5 Quarterly*, **6**, 4–10 (1982).

194. D. M. Heyes and K. Singer. *CCP5 Quarterly*, **6**, 11–23 (1982).

195. W. C. Swope, H. C. Andersen, P. H. Berens and K. R. Wilson. *J. Chem. Phys.*, **76**, 637–649 (1982).

196. H. C. Andersen. *J. Comput. Phys.*, **52**, 24–34 (1983).

197. J.-P. Ryckaert, G. Ciccotti and H. J. C. Berendsen. *J. Comput. Phys.*, **23**, 327–341 (1977).

198. H. C. Andersen, M. P. Allen, A. Bellemans, J. Board, J. H. R. Clarke, M. Ferrario, J. M. Haile, S. Nosé, J. V. Opheusden and J.-P. Ryckaert. *New Molecular Dynamics Methods for Various Ensembles.* Rapport d'activité scientifique du CECAM (1984).

199. H. J. C. Berendsen, J. P. M. Postma, W. F. van Gunsteren, A. DiNola and J. R. Haak. *J. Chem. Phys.*, **81**, 3684–3690 (1984).

200. M. Parinello and A. Rahman. *J. Appl. Phys.*, **52**, 7187–7190 (1981).

201. N. Metropolis, A. W. Rosenbluth, M. N. Rosenbluth, A. H. Teller and E. Teller. *J. Chem. Phys.*, **21**, 1087–1092 (1953).

202. W. W. Wood. *J. Chem. Phys.*, **48**, 415–434 (1968).

203. D. J. Adams. *Mol. Phys.*, **28**, 1241–1252 (1974).

204. D. J. Adams. *Mol. Phys.*, **29**, 307–311 (1975).

205. M. J. Sanders, M. Leslie and C. R. A. Catlow. *J. Chem. Soc. Chem. Comm.*, , 1271–1273 (1984).

206. G. J. Kramer, N. P. Farragher, B. W. H. van Beest and R. A. van Santen. *Phys. Rev. B*, **43**, 5068–5080 (1991).

207. E. de Vos Burchart, V. A. Verheij, H. van Bekkum and B. van de Graaf. *Zeolites*, **12**, 183–189 (1992).

208. J. B. Nicholas, A. J. Hopfinger, F. R. Trow and L. E. Iton. *J. Am. Chem. Soc.*, **113**, 4792–4800 (1991).

209. B. Vessal, M. Amini, D. Fincham and C. R. A. Catlow. *Phil. Mag*, **B60**, 753–775 (1989).

210. E. de Vos Burchart, H. van Bekkum, B. van de Graaf and E. T. C. Vogt. *J. Chem. Soc. Faraday Trans.*, **88**, 2761–2769 (1992).

211. R. A. Jackson and C. R. A. Catlow. *Mol. Sim.*, **1**, 207–224 (1988).

212. G. V. Lewis and C. R. A. Catlow. *J. Phys. C.*, **18**, 1149–1161 (1985).

213. C. R. A. Catlow, K. M. Diller and M. J. Norgett. *J. Phys. C.*, **10**, 1395–1412 (1979).

214. T. S. Bush, J. D. Gale, C. R. A. Catlow and P. D. Battle. *J. Mater. Chem.*, **4**, 831–837 (1994).

215. R. G. Bell, R. A. Jackson and C. R. A. Catlow. *J. Chem. Soc. Chem. Comm.*, , 782–783 (1990).

216. S. M. Tomlinson, R. A. Jackson and C. R. A. Catlow. *J. Chem. Soc. Chem. Comm.*, , 813–816 (1990).

217. M. D. Shannon, J. L. Casci, P. A. Cox and S. J. Andrews. *Nature,* **353**, 417–420 (1991).

218. P. A. Wright, S. Natarajan, J. M. Thomas, R. G. Bell, P. L. Gai-Boyes and R. H. Jones. *Angew. Chem. Intl. Ed. Engl.*, **31**, 1472–1475 (1992).

219. Z. Kaszkur, R. H. Jones, D. Waller, C. R. A. Catlow and J. M. Thomas. *J. Phys. Chem.*, **97**, 426–432 (1993).

220. B. P. Feuston and J. B. Higgins. *J. Phys. Chem.*, **98**, 4459–4462 (1994).

221. M. W. Deem and J. M. Newsam. *Nature,* **342**, 260–262 (1989).

222. C. M. Freeman, C. R. A. Catlow, J. M. Thomas and S. Brode. *Chem. Phys. Lett.*, **186**, 136–142 (1991).

223. D. S. Santilli, T. V. Harris and S. I. Zones. *Micro. Mater.*, **1**, 329–341 (1993).

224. P. A. Cox, A. P. Stevens, L. Banting and A. M. Gorman. In *Zeolites and Related Microporous Materials: State of the Art 1994*, J. Weitkamp, H. G. Karge, H. Pfeifer and W. Hölderich, editors, 2115–2122. Elsevier (1994).

225. P. R. van Tassel, H. T. Davis and A. V. McCormick. *Mol. Phys.*, **73**, 1107–1125 (1991).

226. P. R. van Tassel, H. T. Davis and A. V. McCormick. *Mol. Phys.*, **76**, 411–432 (1992).

227. R. L. June, A. T. Bell and D. N. Theodorou. *J. Phys. Chem.*, **94**, 1508–1516 (1990).

228. B. Smit and J. I. Siepmann. *J. Phys. Chem.*, **98**, 8442–8452 (1994).

229. G. B. Woods and J. S. Rowlinson. *J. Chem. Soc. Faraday Trans. II*, **85**, 765–781 (1989).

230. P. R. van Tassel, H. T. Davis and A. V. McCormick. *J. Chem. Phys.*, **98**, 8919–8928 (1993).

231. C. J. Jameson. *J. Chem. Phys.*, **100**, 5965–5987 (1994).

232. R. F. Cracknell and K. E. Gubbins. *Langmuir*, **9**, 824–830 (1993).

233. S. D. Pickett, A. K. Nowak, J. M. Thomas, B. K. Peterson, J. F. P. Swift, A. K. Cheetham, C. J. J. den Ouden, B. Smit and M. F. M. Post. *J. Phys. Chem.*, **94**, 1233–1236 (1990).

234. P. Santikary, S. Yashonath and G. Ananthakrishna. *J. Phys. Chem.*, **96**, 10469–10477 (1992).

235. W. Heink, J. Kaerger, H. Pfeifer and F. Stallmach. *J. Am. Chem. Soc.*, **112**, 2175–2178 (1990).

236. S. Yashonath and P. Santikary. *J. Phys. Chem.*, **98**, 6368–6376 (1994).

237. E. Hernandez, M. Kawano, A. A. Shubin, C. M. Freeman, C. R. A. Catlow, J. M. Thomas and K. I. Zamaraev. In *Proceedings of the Ninth International Zeolite Conference*, R. von Ballmoos, J. B. Higgins and M. M. J. Tracey, editors, volume 1, 695–702. Butterworth-Heinemann (1993).

238. R. L. June, A. T. Bell and D. N. Theodorou. *J. Phys. Chem.*, **96**, 1051–1060 (1992).

239. P. Demontis, E. S. Fois, G. B. Suffritti and S. Quartieri. *J. Phys. Chem.*, **94**, 4329–4334 (1990).

240. P. Demontis, G. B. Suffritti, E. S. Fois and S. Quartieri. *J. Phys. Chem.*, **96**, 1482–1490 (1992).

241. P. Demontis and G. B. Suffritti. *Modelling of Structure and Reactivity in Zeolites*, chapter 5. Academic Press (1992).

242. P. Demontis, S. Yashonath and M. L. Klein. *J. Phys. Chem.*, **93**, 5016–5019 (1989).

243. R. L. June, A. T. Bell and D. N. Theodorou. *J. Phys. Chem.*, **95**, 8866–8878 (1991).

244. N. Metropolis, J. Howlett and Gian-Carlo Ross. *A History of Computing in the Twentieth Century.* Academic Press (1980).

245. D. M. Beazely and P. S. Lomdahl. *Parallel Computing,* **20**, 173–195 (1994).

246. A. Geist, A. Beguelin, J. Dongarra, W. Jiang, R. Manchek and V. Sunderam. *PVM 3.0 User's Guide and Reference Manual.* Oak Ridge National Laboratory ORNL/TM-12187 (1993).

247. D. E. Tolmie and J. Renwick. *IEEE Network,* **7**, 28–32 (1993).

248. R. Bialek, W. M. Meier, M. Davis and M. J. Annen. *Zeolites,* **11**, 438–442 (1991).

249. R. E. Morris, S. J. Weigel, N. J. Henson, L. M. Bull, A. K. Cheetham, M. T. Janicke and B. F. Chmelka. *J. Am. Chem. Soc.,* **116**, 11849–11855 (1994).

250. I. Petrovic, A. Navrotsky, M. E. Davis and S. I. Zones. *Chem. Mater.,* **5**, 1805–1813 (1993).

251. B. Vessal. *cvff_aug Forcefield.* Catalysis Software Version 5.0, Biosym Technologies Inc., San Diego, CA 92121, U. S. A. (1994).

252. S. Tsuneyuki, M. Tsukada, H. Aoki and Y. Matsui. *Phys. Rev. Lett.,* **61**, 869–872 (1988).

253. S. Tsuneyuki, Y. Matsui and H. Aoki. *Nature,* **339**, 209–211 (1989).

254. C. R. A. Catlow, C. M. Freeman, B. Vessal, S. M. Tomlinson and M. Leslie. *J. Chem. Soc. Faraday Trans.,* **87**, 1947–1950 (1991).

255. B. P. Feuston and S. H. Garofalini. *J. Chem. Phys.,* **89**, 5818–5824 (1988).

256. J. R. Hill and J. Sauer. *J. Phys. Chem.,* **98**, 1238–1244 (1994).

257. J. R. Maple, U. Dinar and A. T. Hagler. *Proc. Nat. Acad. Sci. USA,* , 5350–5354 (1988).

258. J. R. Maple, T. S. Thacher, U. Dinar and A. T. Hagler. *Chem. Des. Auto. News,* **5**, 5–10 (1990).

259. *Discover version 95.0.* Biosym Technologies Inc., San Diego, CA 92121, U. S. A. (1995).

260. J. D. Gale. *GULP (General Utility Lattice Program).* Royal Institution/Imperial College, U. K. (1992-1995).

261. E. M. Flanigen, J. M. Bennett, R. W. Grose, J. P. Cohen, R. L. Patton, R. M. Kirchner and J. V. Smith. *Nature,* **271**, 512–516 (1978).

262. H. van Koningsveld, J. C. Jansen and H. van Bekkum. *Zeolites,* **10**, 235–242 (1990).

263. C. A. Fyfe, H. Gies, G. T. Kokotailo, C. Pasztor, H. Strobl and D. E. Cox. *J. Am. Chem. Soc.,* **111**, 2470 (1989).

264. C. A. Fyfe, H. Gies, G. T. Kokotailo, B. Marler and D. E. Cox. *J. Phys. Chem.,* **94**, 3718–3721 (1990).

265. W. H. Baur. *Acta Cryst.,* **B33**, 2615–2619 (1977).

266. R. E. Gibbs. *Proc. Roy. Soc. (London),* **A113**, 351–368 (1927).

267. W. A. Dollase. *Z. Krist. Bd.,* **121**, 369–377 (1965).

268. R. W. G. Wyckoff. *Crystal Structures.* Interscience (1964).

269. A. F. Wright and A. Leadbetter. *Phil. Mag,* **31**, 1391–1401 (1975).

270. J. M. Newsam, M. M. J. Tracey, D. E. W. Vaughan, K. G. Strohmaier and W. J. Mortier. *J. Chem. Soc. Chem. Comm.,* , 493–495 (1989).

271. G. Miehe and H. Graetsch. *Eur. J. Mineral,* **4**, 693–706 (1992).

272. W. H. Baur and A. A. Khan. *Acta Cryst.,* **B27**, 2133–2139 (1971).

273. J. W. Richardson and E. T. C. Vogt. *Zeolites,* **12**, 13–19 (1992).

274. R. Gramlich-Meier, V. Gramlich and W. M. Meier. *Amer. Miner.,* **80**, 619–623 (1985).

275. J. M. Bennett and R. M. Kirchner. *Zeolites,* **12**, 338–342 (1992).

276. V. Gramlich and W. M. Meier. *Z. Kristallogr., Kristallogeom., Kristallphys., Kristallchem.,* **133**, 134–149 (1971).

277. A. Alberti, P. Davoli and G. Vezzalini. *Z. Kristallogr.,* **175**, 249–256 (1986).

278. P. Behrens, G. van de Goor, M. Wiebcke, C. Braunbarth, A. M. Schneider, J. Felsche, G. Engelhardt, P. Fischer, K. Fütterer and W. Depmeier. *Proceedings of the 8th International Symposium on Molecular Recognition and Inclusion* (1994).

279. M. Calligaris, G. Nardin, L. Randaccio and P. C. Chiaramonti. *Acta Cryst.*, **B38**, 602–605 (1982).

280. P. R. Rudolph and C. E. Crowder. *Zeolites*, **10**, 163–168 (1990).

281. R. F. Lobo, M. Pan, I. Chan, R. C. Medrud, S. I. Zones, P. A. Crozier and M. E. Davis. *J. Phys. Chem.*, **98**, 12040–12052 (1994).

282. P. W. Fowler, P. J. Knowles and N. C. Pyper. *Mol. Phys.*, **56**, 83–95 (1985).

283. F. Liu, S. H. Garofalini and R. D. King-Smith. *Phys. Rev. Lett.*, **70**, 2750–2753 (1993).

284. CODATA Task Group (CODATA recommended key values for thermodynamics). *J. Chem. Thermodyn.*, **8**, 603–605 (1976).

285. P. Richet, Y. Bottinga, L. Denielou, J. P. Petitet and C. Tequi. *Geochim. Cosmochim. Acta.*, **46**, 2639–2658 (1982).

286. R. A. Robie, B. S. Hemingway and J. R. Fisher. *Geol. Survey Bull. No. 1452,* (1979).

287. P. A. Vaughan. *Acta Cryst.*, **21**, 983–990 (1966).

288. I. J. Pickering, P. J. Maddox, J. M. Thomas and A. K. Nowak. *J. Catal.*, **119**, 261–265 (1989).

289. M. P. Attfield. Unpublished results.

290. J. M. O. Lewis and J. B. Price. *U. S. Patent No. 4,873,390* (1989).

291. J. M. Bennett and B. K. Marcus. In *Innovation in Zeolite Materials Science*, P. J. Grobet, W. J. Mortier, E. F. Vansant and G. Schultz-Ekloff, editors, 269–279. Elsevier (1988).

292. H.-L. Zubowa, M. Richter, U. Roost, B. Parlitz and R. Fricke. *Catal. Lett.* **19**, 67–79 (1993).

293. A. J. M. de Man, W. P. J. H. Jacobs, J. P. Gilson and R. A. van Santen. *Zeolites,* **12**, 816–836 (1992).

294. A. J. M. de Man, R. A. van Santen and E. T. C. Vogt. *J. Phys. Chem.,* **96**, 10460–10466 (1992).

295. K. J. Choi, M. S. Jhon and K. T. No. *Bull. Korean Chem. Soc.,* **8**, 155 (1987).

296. H. He and J. Klinowski. *J. Phys. Chem.,* **97**, 10385–10388 (1993).

297. A. Navtrosky, I. Petrovic, Y. Hu, C.-Y. Chen and M. E. Davis. *Micro. Mater.,* **4**, 95–98 (1995).

298. C. R. A. Catlow, R. James, W. C. Mackrodt and R. F. Stewart. *Phys. Rev. B,* **25**, 1006–1026 (1982).

299. C. R. A. Catlow. *Proc. Roy. Soc. (London),* **A353**, 533–561 (1977).

300. N. Thong and D. Schwarzenbach. *Acta Cryst.,* **A35**, 658–664 (1979).

301. H. Wang, B. Xu, X. Liu, J. Han, S. Shan and H. Li. *J. Crystal Growth,* **79**, 227–231 (1986).

302. Z. P. Chang. *IEEE Trans. Sonics Ultrasonics,* **23**, 127–135 (1976).

303. R. M. Dessau, J. L. Schlenker and J. B. Higgins. *Zeolites,* **10**, 522–524 (1990).

304. J. W. Richardson, J. J. Pluth and J. V. Smith. *Acta Cryst.,* **B44**, 367–373 (1988).

305. J. L. Schlenker, J. J. Pluth and J. V. Smith. *Acta Cryst.,* **B33**, 3265–3268 (1977).

306. J. B. Parise. In *Zeolites: Synthesis, Structure, Technology and Application,* B. Držaj, S. Hočevar and S. Pejovnik, editors, 271–278. Elsevier (1985).

307. M. Ito, Y. Shimoyama, Y. Saito, Y. Tsurita and M. Otake. *Acta Cryst.,* **C41**, 1698–1700 (1985).

308. R. M. Kirchner and J. M. Bennett. *Zeolites,* **14**, 523–528 (1994).

309. J. J. Pluth, J. V. Smith and J. M. Bennett. *Acta Cryst.,* **C42**, 283–286 (1986).

310. J. W. Richardson, J. V. Smith and J. J. Pluth. *J. Phys. Chem.,* **93**, 8212–8219 (1989).

311. S. L. Qui, W. Q. Pang, H. Kessler and J. L. Guth. *Zeolites*, **9**, 440–444 (1989).

312. J. M. Bennett, J. P. Cohen, E. M. Flanigen, J. J. Pluth and J. V. Smith. In *Intrazeolite Chemistry*, G. D. Stucky and F. G. Dwyer, editors, 109–118. American Chemical Society (1983).

313. M. J. Annen, D. Young, M. E. Davis, O. B. Cavin and C. R. Hubbard. *J. Phys. Chem.*, **95**, 1380–1383 (1991).

314. M. P. J. Peeters, L. J. M. van de Ven, J. W. de Haan and J. H. C. van Hooff. *J. Phys. Chem.*, **97**, 8254–8260 (1993).

315. D. Demuth. *Synthese und Charakterisierung von modifizierten Alumophosphaten mit AFI-Struktur für neuartige Anwendungen.* PhD thesis, Universität Mainz (1994).

316. L. B. McCusker, Ch. Baerlocher, E. Jahn and M. Bülow. *Zeolites*, **11**, 308–313 (1991).

317. M. E. Davis, C. Montes, P. E. Hathaway, J. P. Arhancet, D. L. Hasha and J. M. Garces. *J. Am. Chem. Soc.*, **111**, 3919–3924 (1989).

318. R. C. Mooney. *Acta Cryst.*, **9**, 728–733 (1956).

319. J. M. Bennett, R. M. Kirchner and S. T. Wilson. In *Zeolites: Facts, Figures, Future*, P. A. Jacobs and R. A. van Santen, editors, 731–739. Elsevier (1989).

320. E. B. Keller, W. M. Meier and R. M. Kirchner. *Solid State Ionics*, **43**, 93–102 (1990).

321. P. A. Wright, R. H. Jones, S. Natarajan, R. G. Bell, J. Chen, M. B. Hursthouse and J. M. Thomas. *J. Chem. Soc. Chem. Comm.*, , 633–635 (1993).

322. K.-P. Schröder, J. Sauer, M. Leslie, C. R. A. Catlow and J. M. Thomas. *Chem. Phys. Lett.*, **188**, 320–325 (1992).

323. P. Saul and C. R. A. Catlow. *Phil. Mag B*, **51**, 107–117 (1985).

324. K.-P. Schröder, J. Sauer, M. Leslie and C. R. A. Catlow. *Zeolites*, **12**, 20–23 (1992).

325. L. M. Bull, A. K. Cheetham, P. D. Hopkins and B. M. Powell. *J. Chem. Soc. Chem. Comm.*, , 1196–1198 (1993).

326. S. Dzwigaj, M. Briend, A. Shikholeslami, M. J. Peltre and D. Barthomeuf. *Zeolites,* **10**, 157–162 (1990).

327. G. V. Gibbs, M. P. Meagher, J. V. Smith and J. J. Pluth. In *Molecular Sieves II,* J. R. Katzer, editor, 19–29. American Chemical Society, Washington (1977).

328. T. Ito and J. Fraissard. *J. Chem. Soc. Faraday Trans. I,* **83**, 451–462 (1987).

329. P. A. Wright, J. M. Thomas, S. Ramdas and A. K. Cheetham. *J. Chem. Soc. Chem. Comm.,* , 1338–1339 (1984).

330. R. H. Jones, P. Lightfoot and R. M. Ormerod. *J. Chem. Soc. Chem. Comm.,* , 783–784 (1995).

331. R. H. Jones, P. Lightfoot and R. M. Ormerod. *J. Phys. Chem. Solids,* **56**, 1377–1381 (1995).

332. A. V. Kiselev, A. A. Lopatkin and A. A. Shulga. *Zeolites,* **5**, 261–267 (1985).

333. A. G. Bezus, A. V. Kiselev, A. A. Lopatkin and P. Q. Du. *J. Chem. Soc. Faraday Trans. II,* **74**, 367–379 (1978).

334. S. Yashonath, P. Demontis and M. L. Klein. *Chem. Phys. Lett.,* **153**, 551–556 (1988).

335. R. L. June, A. T. Bell and D. N. Theodorou. *J. Phys. Chem.,* **94**, 8232–8240 (1990).

336. I. S. Kerr. *Nature,* **210**, 294–295 (1966).

337. N. J. Henson. *DIZZY computational chemistry program, version 6.3.* University of Oxford and University of California Santa Barbara (1991-95).

338. L. Verlet. *Phys. Rev.,* **159**, 98 (1967).

339. E. G. Derouane, J. B. Nagy, C. Fernandez, Z. Gabelica, E. Laurent and P. Maljean. *Appl. Catal.,* **40**, L1–L10 (1988).

340. E. G. Derouane, J.-M. Andre and A. A. Lucas. *J. Catal.,* **110**, 58–73 (1988).

341. E. G. Derouane. In *Guidelines for Mastering the Properties of Molecular Sieves,* D. Barthomeuf, editor, 225–239. Plenum Press (1990).

342. J. G. Tsikoyiannis and J. Wei. *Chem. Engr. Sci.*, **46**, 233–253 (1991).

343. J. G. Tsikoyiannis and J. Wei. *Chem. Engr. Sci.*, **46**, 255–264 (1991).

344. S. J. Weiner, P. A. Kollman, D. A. Case, U. C. Singh, C. Ghio, G. Alagona, Jr. Profeta and P. Weiner. *J. Am. Chem. Soc.*, **106**, 765–784 (1984).

345. B. R. Brooks, R. E. Bruisoleiv, B. D. Olafson, D. J. States, S. Swaminathan and M. Karplus. *J. Comp. Chem.*, **4**, 187–217 (1983).

346. N. L. Allinger. *J. Am. Chem. Soc.*, **99**, 8127–8134 (1977).

347. N. L. Allinger, Y. H. Yuh and J. A. Li. *J. Am. Chem. Soc.*, **111**, 8551–8566 (1989).

348. R. J.-M. Pellenq and D. Nicholson. *J. Chem. Soc. Faraday Trans.*, **89**, 2499–2508 (1993).

349. R. J.-M. Pellenq and D. Nicholson. *J. Phys. Chem.*, **98**, 13339–13349 (1994).

350. J. M. Hutson and P. W. Fowler. *Surf. Sci.*, **173**, 337–350 (1986).

351. P. W. Fowler and J. M. Hutson. *Phys. Rev. B*, **33**, 3724–3735 (1986).

352. M. I. McCarthy and A. C. Hess. *J. Chem. Phys.*, **96**, 6010–6017 (1992).

353. R. J.-M. Pellenq, A. Pellegatti, D. Nicholson and C. Minot. *J. Phys. Chem.*, **99**, 10175–10180 (1995).

354. R. S. Mulliken. *J. Chem. Phys.*, **23**, 1833–1840 (1955).

355. A. S. Chiang, A. G. Dixon and Y. H. Ma. *Chem. Eng. Sci.*, **39**, 1451–1459,1461–1468 (1984).

356. R. E. Richards and L. V. C. Rees. *Langmuir*, **3**, 335–340 (1987).

357. T. Oie, G. M. Maggiora, R. E. Christoffersen and D. D. Duchamp. *Int. J. Quant. Chem., Quan. Biol. Supp.*, **1**, 1–47 (1981).

358. R. Q. Snurr, A. T. Bell and D. N. Theodorou. *J. Phys. Chem.*, **98**, 5111–5119 (1994).

359. D. E. Williams and T. L. Starr. *Comp. and Chem.*, **1**, 173–177 (1977).

360. A. G. Bezus, M. Kocirik, A. V. Kiselev, A. A. Lopatkin and E. A. Vasilyeva. *Zeolites,* **6**, 101–106 (1986).

361. P. J. O'Malley and C. J. Braithwaite. *Zeolites,* **15**, 198–201 (1995).

362. M. Stockenhuber. Unpublished results.

363. D. Barthomeuf and B.-H. Ha. *J. Chem. Soc. Faraday Trans. I,* **69**, 2147–2157 (1973).

364. A. de Mallmann and D. Barthomeuf. *J. Phys. Chem.,* **27**, 5636–5637 (1989).

365. A. Redondo. Unpublished results.

366. H. K. Chae, W. G. Klemperer, D. A. Payne, C. T. A. Suchictel, D. R. Wake and S. R. Wilson. In *Materials for Nonlinear Optics,* S. R. Marder, J. E. Sohn and G. D. Stucky, editors, volume 455, 528–540. ACS Symposium Series (1991).

367. G. J. Nesbitt and M. D. Mann. Unpublised results.

368. J. A. Snymann. *Comp. Math. Appl.,* **17**, 1369–1377 (1989).

369. P. Pechukas. *The Dynamics of Molecular Collisions, Part B,* chapter 6, 269–320. Plenum, New York (1976).

370. Z. Y. Zhang, K. Haug and H. I. Metiu. *J. Chem. Phys.,* **93**, 917 (1990).

371. S. M. Auerbach. Unpublished results.

372. S. M. Auerbach. Unpublished results.

373. G. Vitale, L. M. Bull, R. E. Morris, A. K. Cheetham, B. H. Toby, C. G. Coe and J. E. MacDougall. *J. Phys. Chem.,* **99**, 16087–16092 (1995).

374. L. Uytterhoeven, D. Dompas and W. J. Mortier. *J. Chem. Soc. Faraday Trans.,* **88**, 2753–2760 (1992).

375. G. Schrimpf, B. Tavitian and D. Espinat. *J. Phys. Chem.,* **99**, 10932–10941 (1995).

376. G. Schrimpf, M. Schlenkrich, J. Brickmann and P. Bopp. *J. Phys. Chem.,* **96**, 7404–7410 (1992).

377. H. Dufner, M. Schlenkrich and J. Brickmann. *submitted to J. Comput. Chem.* (1996).

378. H. Klein, H. Fuess and M. Hunger. *J. Chem. Soc. Faraday Trans.*, **91**, 1813–1824 (1995).

379. T. Hseu. PhD thesis, University of Washington, University Microfilm number 73-13835, Ann Arbor, Michigan, U. S. A. (1972).

380. D. H. Olsen. *Zeolites*, **16**, 439–443 (1995).

381. G. Vitale. Unpublished results.

382. G. Vitale, L. M. Bull, B. M. Powell and A. K. Cheetham. *J. Chem. Soc. Chem. Comm.*, , 2253–2254 (1995).

383. M. J. Sanders and C. R. A. Catlow. In *Proceedings from the Sixth International Zeolite Conference*, D. Olsen and A. Bisio, editors, 131–140. Butterworths, Guildford (1984).

384. M. J. Sanders. *Computer Simulation of Framework Structured Minerals.* PhD thesis, University of London (1984).

385. J. Klinowski, S. Ramdas and J. M. Thomas. *J. Chem. Soc. Faraday Trans. II*, **78**, 1025–1050 (1982).

386. M. T. Melchior, D. E. W. Vaughan and A. J. Jacobson. *J. Am. Chem. Soc.*, **104**, 4859–4864 (1982).

387. S. M. Auerbach, N. J. Henson, A. K. Cheetham and H. I. Metiu. *J. Phys. Chem.*, **99**, 10600–10608 (1994).

388. J. Kärger and D. M. Ruthven. *Zeolites*, **9**, 267–281 (1989).

389. J. A. Snymann. *Appl. Math. Modelling*, **6**, 449–462 (1982).

390. J. A. Snymann. *Appl. Math. Modelling*, **7**, 216–218 (1983).

Appendix A

The LFOPC minimisation method

Snymann[368,389,390] has proposed several algorithms for unconstrained minimisation of functions which operate via the solution of the associated dynamical problem with the equations of motion :-

$$\ddot{\boldsymbol{r}}(t) = -\boldsymbol{\nabla} E(\boldsymbol{r}(t)) \tag{A.1}$$

subject to the conditions :-

$$\boldsymbol{r}(0) = \boldsymbol{x}_0 \tag{A.2}$$

$$\dot{\boldsymbol{r}}(0) = \boldsymbol{v}_0 = 0 \tag{A.3}$$

where $\boldsymbol{r}_0$ is an arbitrary starting point. $E(\boldsymbol{r}(t))$ is considered to represent the potential energy of a particle of unit mass at the point $\boldsymbol{r}(t)$ in a n-dimensional force field at time t. The most efficient method that Snymann proposed (LFOPC) used the leap-frog method to solve the equations of motion with a variable time step that ensures the system reaches a minimum. This method can be summarised as follows.

Given $\boldsymbol{r}_0$, $\boldsymbol{v}_0$ and a time step $\Delta t > 0$, compute for $k = 0, 1, 2\ldots$

$$\boldsymbol{r}_{k+1} = \boldsymbol{r}_k + \boldsymbol{r}_k \Delta t \tag{A.4}$$

$$\boldsymbol{v}_{k+1} = \boldsymbol{v}_k + \boldsymbol{a}_{k+1} \Delta t \tag{A.5}$$

where

$$\boldsymbol{a}_k = -\boldsymbol{\nabla} E(\boldsymbol{r}_k) = -\boldsymbol{\nabla} E_k \tag{A.6}$$

It can be shown that for a trajectory computed by equation A.6 the following relationship holds :-

$$\frac{1}{2} \parallel \boldsymbol{v}_{k+1} \parallel^2 + E_{k+1} = \frac{1}{2} \parallel \boldsymbol{v}_k \parallel^2 + E_k + \frac{1}{2} \parallel \boldsymbol{a}_{k+1} \parallel^2 (\Delta t)^2 - \frac{1}{2} \Delta \boldsymbol{r}_k^T H(\tilde{\boldsymbol{r}}) \Delta \boldsymbol{r}_k \quad \text{(A.7)}$$

where H is the Hessian matrix = $[\, \partial^2 E / \partial r_i \partial r_j \,]$, $\Delta \boldsymbol{r}_k = \boldsymbol{r}_{k+1} - \boldsymbol{r}_k$ and $\tilde{\boldsymbol{r}} = \boldsymbol{r}_{k+1} - \theta \Delta \boldsymbol{r}_k$, $0 \leq \theta \leq 1$. This expression may be rewritten as :-

$$\Delta E_k = \frac{1}{2} \parallel \boldsymbol{v_k} \parallel^2 + \frac{1}{2} \parallel \boldsymbol{a_{k+1}} \parallel^2 (\Delta t)^2 - \frac{1}{2} \parallel \boldsymbol{v_{k+1}} \parallel^2 - \frac{1}{2} \boldsymbol{\Delta r_k^T} H(\tilde{\boldsymbol{r}}) \Delta \boldsymbol{r}_k \quad \text{(A.8)}$$

Since $\boldsymbol{v_{k+1}} = \boldsymbol{v_k} + \boldsymbol{a_{k+1}} \Delta t$, equation A.8 may be further simplified to :-

$$\Delta E_k = -\boldsymbol{v_k^T a_{k+1}} \Delta t - \frac{1}{2} \boldsymbol{\Delta r_k^T} H(\tilde{\boldsymbol{r}}) \Delta \boldsymbol{r}_k \quad \text{(A.9)}$$

Now clearly, since $\Delta t > 0$, if H is positive semidefinite then a sufficient condition for descent to the minimum i.e. $\Delta E_k < 0$, is :-

$$\boldsymbol{v_k^T a_{k+1}} > 0 \quad \text{(A.10)}$$

To investigate how to achieve this condition, consider the following steepest descent step :-

$$\tilde{\boldsymbol{v}} = \boldsymbol{a}_k \Delta t \quad \text{(A.11)}$$

$$\tilde{\boldsymbol{r}} = \boldsymbol{r}_k + \tilde{\boldsymbol{v}} \Delta t \quad \text{(A.12)}$$

Also set :-

$$\tilde{\boldsymbol{a}} = -\boldsymbol{\nabla} E(\tilde{\boldsymbol{r}}) \quad \text{(A.13)}$$

There are three possibilities based on equation A.10 :-

(i) $\boldsymbol{v_k^T a_{k+1}} > 0$. In this case, the condition is satisfied, and the trajectory can be propagated according to equation A.6.

(ii) $\boldsymbol{v_k^T a_{k+1}} \leq 0$ and $\tilde{\boldsymbol{v}}^T \boldsymbol{a} > 0$. The condition is not met along the leap-frog trajectory but it is satisfied along the steepest descent path. A step must be taken intermediate between $\boldsymbol{\Delta x_k}$ and $\tilde{\boldsymbol{x}} - \boldsymbol{x_k}$ but with the certainty of achieving descent. This may be achieved by setting $\boldsymbol{v_{k-1}}$=$\boldsymbol{v_{k-1}}/2$, recomputing $\boldsymbol{v_k}$ and restarting the step.

(iii) $\boldsymbol{v_k^T a_{k+1}} \leq 0$ and $\tilde{\boldsymbol{v}}^T \boldsymbol{a} \leq 0$. For both steps the descent condition is not met. In this case, it is necessary to halve the time step and restart the step with the original velocity $\boldsymbol{v_k}$.

A more detailed treatment of the convergence of the LFOPC method has been reported.[368] Unlike other methods such as conjugate gradients, this method requires no line searches or function evaluations to operate. The method has been shown to compete quite well with standard minimisation procedures especially in cases of functions with very high dimensionality.

The method can be implemented using the following algorithm :-

1. assume $\boldsymbol{x_0}$, Δt, and ϵ given, $k = -1$.
2. compute $\boldsymbol{a_0} = -\boldsymbol{\nabla} E(\boldsymbol{r_0})$, set $\boldsymbol{v_0}$=$\boldsymbol{a_0}\Delta t$.
3. set $k = k + 1$.
4. set $\boldsymbol{r_{k+1}} = \boldsymbol{r_k} + \boldsymbol{v_k}\Delta t$.
5. compute $\boldsymbol{a_{k+1}} = -\boldsymbol{\nabla} E(\boldsymbol{r_{k+1}})$.
6. if $\| \boldsymbol{a_{k+1}} \| < \epsilon$, stop; otherwise go to 7.
7. if $\boldsymbol{v_k^T a_{k+1}} > 0$, set $\boldsymbol{v_{k+1}} = \boldsymbol{v_k} + \boldsymbol{a_{k+1}}\Delta t$ and go to 3; otherwise go to 8.
8. set $\tilde{\boldsymbol{v}} = \boldsymbol{a_k}\Delta t$, $\tilde{\boldsymbol{r}} = \boldsymbol{r_k} + \tilde{\boldsymbol{v}}\Delta t$ and compute $\tilde{\boldsymbol{a}} = -\boldsymbol{\nabla} E(\tilde{\boldsymbol{r}})$.
9. if $\tilde{\boldsymbol{v}}^T \boldsymbol{a} \leq 0$, set $\Delta t = \frac{1}{2}\Delta t$, $\boldsymbol{v_{k+1}} = \boldsymbol{v_k}$, $\boldsymbol{r_{k+1}} = \boldsymbol{r_k}$, and go to 3; otherwise go to 10.
10. set $\boldsymbol{r_{k+1}} = \boldsymbol{r_k}$, $\boldsymbol{v_k} = \frac{1}{2}\boldsymbol{v_k} - \boldsymbol{a_k}\Delta t$ and go to 3.

The algorithm terminates when :-

$$\| \boldsymbol{\nabla} E_k = \| \boldsymbol{a_k} \| < \epsilon \tag{A.14}$$

where ϵ is a small specified positive number.

Appendix B

The DIZZY program

The DIZZY (Dynamics and Docking in Zeolites) program[337] was written as a multi-purpose simulation code for the study of the behaviour of sorbates in zeolites and was used for the work detailed in Chapters 6-9. The current version of the program is available from the author on request. The latest README file for the current distribution of the program (version 6.3) is reproduced below :-

```
*****************************************************************
*                DIZZY Computational Chemistry Program          *
*           Computer Simulation of Sorbates in Zeolite Pores    *
*               Neil Henson, Materials Department, UCSB         *
*                            Version 6.3                        *
*****************************************************************

Welcome to the wonderful world of DIZZY (release 6.3)

This short file will tell you how to install the program and run
the test suite to demonstrate its capabilities.

1. Scope
--------

The package consists of two programs : GENCONFIG, which allows the
building of crystal structures given the asymmetric unit and space
group to generate an input file for DIZZY, and DIZZY itself which
does the actual simulation.

GENCONFIG takes the asymmetric unit and space group and generates the
cell. All the standard space group settings from International Tables
are recognised. Non-standard setting can be accessed by specifying
symmetry operators.

DIZZY can currently perform the following types of runs :

1) Molecular dynamics on :

    a) a liquid with one component
    b) a zeolite structure
    c) a zeolite and a guest

   in the NVE or NVT (scaled velocities or Nose method) ensembles.
```

2) Minimisation of the above systems at constant volume

3) Constrained energy minimisation with the guest molecule limited to a defined plane.

4) Monte-Carlo docking calculations to probe the interior of a zeolite for sorbate binding sites with or without annealing of the minimum energy position.

5) Basic Metropolis Monte Carlo calculations to probe a local region of a zeolite for binding sites or to obtain an estimate for the heat of sorption at a specified temperature.

6) Grand Canonical Monte Carlo calculations to obtain sorption isotherms.

2. Installation

Inventory

```
README              : This file!
Makefile            : The common system makefile
*.f                 : Source code
dizzy.help
genconfig.help      : Text files used by on-line help
eledata             : Tables of atomic labels, covalent radii and masses
dizzy_run
genconfig_run       : C-shell scripts to run the programs
symm*
pars*               : example input files
GENTAGS, RATTAGS    : development only!
force.database      : archive of forcefield parameters
```

Compiling the program

DIZZY was written to operate in the following (default) environment which can be modified quite easily via the Makefile.

If ROOT is the root-file name of your environment use :

$ROOT/=source for the source code

the executables will be placed in $ROOT/=execute

To compile, type the following :

```
% make <machine_name>

in the directory containing the source code, where <machine_name> is
one of the following :

sgir3000      for Silicon Graphics R3000 Indigo/Personal Iris
sgir4000      for Silicon Graphics R4000 Indigo/Indigo 2/Indy
sgir4400      for Silicon Graphics Challenge
sgir4600      for Silicon Graphics R4600 Indy
sgir8000      for Silicon Graphics Power Challenge
aix           for IBM RS-6000 Series
hp700         for Hewlett Packard 9000/700 Series
convex        for Convex 9.0
sun           for Sun Sparcstation running Solaris 5.3

There are two scripts :

genconfig_run and dizzy_run

which are the front-end to the program. They set up the various to the
files that the programs use and call the executables. They both take a
single argument which is used as the root name of the output files.

Place these files somewhere in your path and modify them to point to
the place where the executable is located.

3. Testing the program
----------------------

Several example files are provided :-

symm_tb_dynamics.dat
pars_tb_dynamics.dat            : Example molecular dynamics run

symm_tb_minimise.dat
pars_tb_minimise.dat            : Example minimisation run

symm_tb_minregion.dat
pars_tb_minregion.dat           : Minimisation of a spherical region of the
                                  system only.

symm_tb_constrainedmin.dat
pars_tb_constrainedmin.dat      : Example constrained minimisation run

pars_tb_docking.dat             : Example docking run

pars_tb_mddocking.dat           : Example MD docking run

symm_tb_anglecorr.dat           : Example NMR angle correlation calculation
```

```
symm_tb_mc.dat                  : Example NVT-ensemble Metropolis
pars_tb_mc.dat                    Monte Carlo calculation

symm_tb_gcmc.dat                : Example GCMC calculation
pars_tb_gcmc.dat
```

GENCONFIG takes its input from filenames of the form symm_xxxx.dat. To run the program type :

```
% genconfig_run xxxx
```

where xxxx specifies the root name of the symm_xxxx.dat file. Output will be generated in the genconfig_xxxx.out file. GENCONFIG also generates a dump.old file which DIZZY reads to begin the simulation.

Similarly for DIZZY, type :

```
% dizzy_run xxxx
```

to run the simulation. The log file will be called xxxx.log .

4. Files generated and their uses

suffix	Description
GENCONFIG	
genconfig.car	Built structure as a Biosym .car file
genconfig.xtl	Built structure as a Biosym .xtl file
genconfig.cssr	Built structure as a Chem-X .cssr file
genconfig.out	Log file for GENCONFIG
genconfig.fgs	Built structure as a Fungus input filr
genconfig.gpt	Angle correlation function. GNUPLOT input file.
genconfig.gdat	Angle correlation function. ASCII data file.
genconfig.dis	Distance/angles calculation
DIZZY	
.arc	Biosym archive file
.spl	Details of splines
.vel	Velocities of atoms and molecules
.ene	Instantaneous energy of system
.com	Molecular centres of mass

.dis	Distances of molecules from arbitrary starting point
.grd	Grid file containing possible molecular insertion points for docker
.ave	Average quantities
.flc	Fluctuations in the averages
.nrv	Normal vectors
.mle	Molecular energies
.dmp	Restart file

5. Utilities

Several utility programs are provided to analyse data obtained from a simulation run :

rc : Calculates a suitable reaction coordinate from the output of a constrained energy minimisation run. An example input file is provided "test_rc.arc". Questions about this program should be directed at S. M. Auerbach.

calc_distrib : Calculates a pairwise distribution for molecules in a zeolite based on the molecular centre of mass.

calc_msd : Calculates the mean squared displacement as a function of time from the contents of a .com file.

calc_vacf : Calculates the velocity autocorrelation function as a function of time from the contents of a .vel file.

calc_mle : Calculates the molecular energy distribution function from the contents of a .mle file.

6. On-line help

To access on-line help, type the name of the executable directly and then type help and follow the instructions. This works for both DIZZY and GENCONFIG.

NJH
September 1995.